

## Machine learning and randomness in mechanical metamaterials

Pahlavani, H.

**DOI**

[10.4233/uuid:662b7fa8-5154-464f-bf7e-6ae5bf15c828](https://doi.org/10.4233/uuid:662b7fa8-5154-464f-bf7e-6ae5bf15c828)

**Publication date**

2023

**Document Version**

Final published version

**Citation (APA)**

Pahlavani, H. (2023). *Machine learning and randomness in mechanical metamaterials*. [Dissertation (TU Delft), Delft University of Technology]. <https://doi.org/10.4233/uuid:662b7fa8-5154-464f-bf7e-6ae5bf15c828>

**Important note**

To cite this publication, please use the final published version (if applicable). Please check the document version above.

**Copyright**

Other than for strictly personal use, it is not permitted to download, forward or distribute the text or part of it, without the consent of the author(s) and/or copyright holder(s), unless the work is under an open content license such as Creative Commons.

**Takedown policy**

Please contact us and provide details if you believe this document breaches copyrights. We will remove access to the work immediately and investigate your claim.

# **Machine learning and randomness in mechanical metamaterials**



# **Machine learning and randomness in mechanical metamaterials**

## **Proefschrift**

ter verkrijging van de graad van doctor  
aan de Technische Universiteit Delft,  
op gezag van de Rector Magnificus, Prof.dr.ir. T.H.J.J. van der Hagen,  
voorzitter van het College voor Promoties,  
in het openbaar te verdedigen op dinsdag 20 juni 2023 om 10:00 uur.

door

**Helda PAHLAVANI**

Master of Science in Civil Engineering,  
Sharif University of Technology, Iran,  
geboren te Torbatehedarieh, Iran

Dit proefschrift is goedgekeurd door de promotor.

Samenstelling promotiecommissie bestaat uit:

Rector magnificus,	Voorzitter
Prof.dr. A.A. Zadpoor	Technische Universiteit Delft, promotor
Dr. J. Zhou	Technische Universiteit Delft, promotor
Dr. M.J. Mirzaali Mazandarani	Technische Universiteit Delft, copromotor

Onafhankelijke leden:

Prof.dr. M.L. van Hecke	Universiteit Leiden, Nederland
Prof.dr. M.J. Santofimia Navarro	Technische Universiteit Delft, Nederland
Prof.dr.ir. J. Harlaar	Technische Universiteit Delft/ Amsterdam UMC/ Erasmus MC, Nederland
Prof.dr.ir. P. Breedveld	Technische Universiteit Delft, Nederland



The research leading to these results was part of the 3DMed project that received funding from the Interreg 2 Seas program 2014-2020, co-funded by the European Regional Development Fund under subsidy contract No. 2S04-014.

Keywords: Randomness, mechanical metamaterials, machine learning, additive manufacturing.

Cover designed by: Maede Shakeri | <https://maedeshakeri1393.wixsite.com/maede>

Printed by: Gildeprint | [www.gildeprint.nl](http://www.gildeprint.nl)

Copyright © 2023 by H. Pahlavani

ISBN 978-94-6419-838-6

An electronic version of this dissertation is available at <http://repository.tudelft.nl/>





# Summary

In recent years, the advances in additive manufacturing techniques as well as the interest in the unusual properties of mechanical metamaterials have ignited a spike of attention to these architected materials whose unprecedented properties originate from their designs at the micro-scale. The unusual properties of these materials make them a suitable choice for numerous applications in high-tech industries, such as soft robotics and biomedical engineering. However, for the real-world applications of such designer materials, their mechanical properties should be tuned for the intended application. The common approach to designing mechanical metamaterials is to create specific geometric patterns at the micro-scale, which are repeated in a highly ordered manner. However, it is not always possible to find the right geometries for unit cells to achieve the desired combinations of mechanical properties. Furthermore, the purposely designed materials with extreme Poisson's ratios tend to have low elastic moduli, making it difficult to independently control the elastic properties of the designed structures. Moreover, there are additional design requirements besides mechanical properties, such as spatial dimensions and uniform stress distribution within the designed structure, that should also be considered. The main objective of this thesis is to rationally design mechanical metamaterials with various combinations of mechanical properties (including rare-event designs) while satisfying additional design requirements. To achieve this goal, we have leveraged the advantages of randomness to broaden the range of design possibilities. We have introduced two sources of randomness, including randomness in the material choice by spatially distributing materials with different properties within lattice structures (Chapters 2 and 3), and randomness in the geometry by designing disordered micro-architectures (Chapter 4). The integration of randomness into the rational design of mechanical metamaterials is a less explored approach, despite its potential benefits, such as robustness against the presence of (manufacturing) imperfections in the structure of the material. Our results show that



both approaches could be used to obtain a wide range of elastic properties as well as rare-event properties, such as double-auxetic yet stiff structures.

Advanced additive manufacturing techniques allow for the creation of metamaterials with intricate shapes and a variety of material properties. However, finding rare designs that result in unusual material properties, such as double-auxeticity and high stiffness, remains a challenging task. Towards this aim, we have employed machine learning techniques to not only predict the mechanical properties of the designed structures much faster than computational models but also to inversely design structures with predefined mechanical properties, including rare-event elastic properties. In the research presented in Chapter 5, deep learning (DL) algorithms were utilized to investigate the correlation between the mechanical properties and random combinations of hard and soft phases in three types of planar lattices, and to pinpoint unusual designs. By developing the correlations between the design parameters and mechanical properties, the time required for evaluating each design was significantly reduced to  $\approx 2.4 \times 10^{-6}$  s, and the process of evaluating different designs was made highly parallelizable. In the next step, we leveraged the abilities of DL algorithms to predict the elastic properties of multi-material mechanical metamaterials and to generate new designs, while also considering other design requirements beyond mechanical properties, to create a modular approach titled “Deep-DRAM” for solving this complex, multi-objective inverse design problem (Chapter 6). Deep-DRAM, which stands for Deep learning for the Design of RAndom-network Metamaterials, is composed of four separate modules, including two deep learning models (DLM), a deep generative model (DGM), and finite element (FE) simulations. The approach receives the desired elastic properties and specimen dimensions, generates candidate designs, filters them based on the closeness of the generated properties to the desired ones, and uses FE simulations to identify the designs with minimal peak stresses within the lattice structure. It allows for the creation of metamaterials with specific elastic properties that correspond to

the specific dimensions provided to Deep-DRAM and can be used for a wide range of applications.

Taken together, this work explores a new frontier in the design of mechanical metamaterials by introducing randomness in the material choice as well as randomness in the geometry. DL techniques were then utilized to accelerate the material discovery within the broad design space. The approach proposed in this study paves ways for extracting mechanical metamaterials with defined elastic properties (including rare properties) that are independent of the overall dimension of the metamaterial and are suitable for various applications.



# Samenvatting

In de afgelopen jaren hebben de ontwikkelingen in additive manufacturing-technieken en de interesse in de ongebruikelijke eigenschappen van mechanische metamaterialen geleid tot een piek in de aandacht voor deze ontworpen materialen met ongekeerde eigenschappen die voortkomen uit hun ontwerpen op microschaal. De ongebruikelijke eigenschappen van deze materialen maken ze geschikt voor tal van toepassingen in hightechindustrieën, zoals zachte robotica en biomedische technologie. Voor de reële toepassingen van dergelijke ontworpen materialen moeten hun mechanische eigenschappen echter worden afgestemd op de beoogde toepassing. De gebruikelijke benadering voor het ontwerpen van mechanische metamaterialen is het creëren van specifieke geometrische patronen op microschaal, die op een zeer geordende manier worden herhaald. Het is echter niet altijd mogelijk om de juiste geometrieën voor eenheidscellen te vinden om de gewenste combinaties van mechanische eigenschappen te bereiken. Bovendien hebben de gericht ontworpen materialen met extreme Poisson-factoren vaak lage elasticiteitsmoduli, waardoor het moeilijk wordt om de elastische eigenschappen van de ontworpen structuren onafhankelijk te regelen. Naast de mechanische eigenschappen zijn er ook aanvullende ontwerpeisen, zoals bijvoorbeeld ruimtelijke afmetingen en uniforme spanningsverdelingen binnen de ontworpen constructie. Het hoofddoel van dit proefschrift is het rationeel ontwerpen van mechanische metamaterialen met verschillende combinaties van mechanische eigenschappen (waaronder “rare-event” ontwerpen) en tegelijkertijd te voldoen aan aanvullende ontwerpeisen. Om dit doel te bereiken, hebben we gebruik gemaakt van de voordelen van willekeur om het scala aan ontwerpmogelijkheden te verbreden. We hebben twee bronnen van willekeur geïntroduceerd, waaronder willekeur in de materiaalkeuze door materialen met verschillende eigenschappen ruimtelijk te verdelen binnen roosterstructuren (Hoofdstuk 2 en 3), en willekeur in de geometrie door ongeordende micro-architecturen te ontwerpen (Hoofdstuk 4). De integratie van willekeur in het

rationele ontwerp van mechanische metamaterialen is een minder onderzochte benadering, ondanks de potentiële voordelen ervan, zoals robuustheid tegen de aanwezigheid van (fabricage) imperfecties in de structuur van het materiaal. Onze resultaten laten zien dat beide benaderingen kunnen worden gebruikt om een breed scala aan elastische eigenschappen te verkrijgen, evenals ongebruikelijke eigenschappen, zoals dubbel-auxetische maar toch stijve structuren.

Geavanceerde additive manufacturing-technieken maken het creëren van metamaterialen met ingewikkelde vormen en een verscheidenheid aan materiaaleigenschappen mogelijk. Het vinden van zeldzame ontwerpen die resulteren in ongebruikelijke materiaaleigenschappen, zoals dubbele auxeticiteit met hoge stijfheid, blijft echter een uitdagende taak. Vandaar hebben we machine learning-technieken gebruikt om niet alleen de mechanische eigenschappen van de ontworpen structuren veel sneller te voorspellen dan computationele modellen, maar ook om omgekeerde structuren te ontwerpen met vooraf gedefinieerde mechanische eigenschappen, waaronder ongebruikelijke elastische eigenschappen. In het onderzoek in Hoofdstuk 5 werden de deep learning (DL) -algoritmen gebruikt om de correlatie tussen de mechanische eigenschappen en willekeurige combinaties van harde en zachte fasen in drie soorten vlakke roosters te onderzoeken en om ongebruikelijke ontwerpen te bepalen. Door de correlaties tussen de ontwerpparameters en mechanische eigenschappen te ontwikkelen, werd de tijd die nodig is voor het evalueren van elk ontwerp aanzienlijk verlaagd tot  $\approx 2,4 \times 10^{-6}$  s, en het evaluatieproces werd zeer parallel uitvoerbaar gemaakt. In de volgende stap hebben we gebruik gemaakt van de mogelijkheden van DL algoritmen om de elastische eigenschappen van mechanische metamaterialen met meerdere materialen te voorspellen en nieuwe ontwerpen te genereren, terwijl we ook andere ontwerpeisen buiten mechanische eigenschappen hebben meegewogen, om een modulaire benadering te creëren, getiteld “Deep-DRAM”, voor het oplossen van dit complexe multi-doel omgekeerde ontwerpprobleem (Hoofdstuk 6). Deep-DRAM, dat staat voor “Deep learning for the Design of RANdom-network Metamaterials”,

bestaat uit vier afzonderlijke modules, waaronder twee deep learning modellen (DLM), een diep generatief model (DGM) en eindige element (FE) simulaties. Deze aanpak krijgt de gewenste elastische eigenschappen en specimenafmetingen, genereert kandidaatontwerpen, filtert ze op basis van de nabijheid van de gegenereerde eigenschappen voor de gewenste en gebruikte FE-simulaties om de ontwerpen te identificeren met minimale piekspanningen binnen de roosterstructuur. Het voorziet in de creatie van metamaterialen met specifieke elastische eigenschappen die overeenkomen met de specifieke afmetingen die aan Deep-DRAM worden verstrekt en die voor een breed scala aan toepassingen kunnen worden gebruikt.

Alles bij elkaar verkent dit werk een nieuwe opkomst in het ontwerp van mechanische metamaterialen door zowel willekeur in de materiaalkeuze als willekeur in de geometrie te introduceren. DL-technieken werden gebruikt om de materiaalontdekking binnen de brede ontwerpruimte te versnellen. De benadering die in deze studie wordt voorgesteld, baant de weg voor het creëren van mechanische metamaterialen met gedefinieerde elastische eigenschappen (inclusief ongebruikelijke eigenschappen) die onafhankelijk zijn van de algehele dimensie van het metamateriaal en geschikt zijn voor verschillende toepassingen.



# Contents

Summary.....	vii
Samenvatting .....	xi
Contents.....	xv
List of abbreviations.....	xix
<b>1. Introduction .....</b>	<b>1</b>
1.1. Background.....	2
1.2. Objective of the thesis .....	5
1.3. Thesis outline.....	6
References .....	9
<b>2. Multi-material 3D printed mechanical metamaterials.....</b>	<b>13</b>
Abstract .....	14
2.1. Introduction .....	15
2.2. Materials and methods.....	15
2.2.1. Computational modeling .....	16
2.2.2. Fabrication and experimental testing.....	17
2.3. Results and discussion.....	20
2.4. Conclusion.....	25
2.5. Supplementary document .....	27
References .....	28
<b>3. Non-affinity in multi-material mechanical metamaterials.....</b>	<b>31</b>
Abstract .....	32
3.1. Introduction .....	33
3.2. Materials and methods.....	35
3.2.1. Design and computational modeling .....	35
3.2.2. Fabrication and experimental testing.....	37
3.3. Results and discussion.....	39
3.4. Conclusion.....	47



3.5. Supplementary document .....	49
References .....	54
<b>4. Auxeticity and stiffness of random networks .....</b>	<b>59</b>
Abstract .....	60
4.1. Introduction .....	61
4.2. Materials and methods.....	61
4.2.1. Numerical simulations.....	63
4.2.2. Statistical analyses.....	64
4.2.3. Fabrication and experimental testing.....	64
4.3. Results and discussion.....	65
4.4. Conclusion.....	75
4.5. Supplementary document .....	76
References .....	84
<b>5. Rare-event multi-material mechanical metamaterials.....</b>	<b>87</b>
Abstract .....	88
5.1. Introduction .....	89
5.2. Materials and methods.....	91
5.2.1. Computational models.....	92
5.2.2. Deep learning.....	94
5.2.3 Experiments.....	97
5.3. Results and discussion .....	98
5.3.1. Training and performance of the deep learning models .....	98
5.3.2. Single unit cell deep learning model .....	100
5.3.4. Role of multi-material design .....	102
5.3.5. Stiff double-auxetic structures.....	103
5.3.6. Tiled and transformed structures .....	105
5.3.7. Uniformity of stress distribution.....	108
5.4. Conclusion.....	112
5.5. Supplementary document .....	113

5.5.1. Supplementary methods .....	116
References .....	126
<b>6. Size-agnostic inverse design of random networks .....</b>	<b>131</b>
Abstract .....	132
6.1. Introduction .....	133
6.2. Materials and methods.....	136
6.2.1. Computational models.....	136
6.2.2. Deep learning.....	138
6.2.3. Experiments.....	143
6.3. Results and discussion.....	144
6.3.1. Elastic properties of RN unit cells.....	144
6.3.2. Generative inverse design framework .....	148
6.3.3. Unit cells with requested rare elastic properties .....	149
6.3.4. Elastic properties of combinatorial designs.....	152
6.3.5. Inverse design of lattice structures with requested elastic properties and dimensions.....	155
6.3.6. Stress distribution .....	157
6.4. Discussion and future outlook .....	160
6.5. Conclusion.....	161
6.6. Supplementary document .....	162
6.6.1. Supplementary methods .....	166
6.6.2. Supplementary movies .....	182
References .....	183
<b>7. General discussion and future outlook .....</b>	<b>187</b>
7.1. General discussion.....	188
7.1.1. Multi-material mechanical metamaterials .....	188
7.1.2. RN mechanical metamaterials .....	190
7.1.3. Deep learning for the design of rare-event multi-material mechanical metamaterials.....	192

7.1.4. Deep-DRAM framework: Deep learning for the design of random-network mechanical metamaterials .....	194
7.2. Future outlook .....	195
References .....	198
<b>Acknowledgements.....</b>	<b>201</b>
<b>Publications.....</b>	<b>205</b>
A. Journals.....	205
B. Conferences .....	206
<b>Curriculum Vitae.....</b>	<b>207</b>

# list of abbreviations

AM	Additive Manufacturing
ANN	Artificial Neural Network
CNN	Convolutional Neural Network
CV	Cross Validation
CVAE	Conditional Variational AutoEncoder
DGM	Deep Generative Model
DIC	Digital Image Correlation
DL	Deep Learning
DLM	Deep Learning Model
DOF	Degrees Of Freedom
FDM	Fused Deposition Modeling
FE	Finite Element
GAN	Generative Adversarial Network
KL	Kullback–Leibler
MAE	Mean Absolute Error
ML	Machine Learning
MSE	Mean Squared Error
PLA	PolyLactic Acid
RMSE	Root Mean Squared Error
RN	Random-Network
SD	Standard Deviation
SGD	Stochastic Gradient Descent
SLS	Selective Laser Sintering
STL	Standard Tessellation Language
VAE	Variational AutoEncoder



# 1

## Introduction

## 1.1. Background

Mechanical metamaterials are a class of advanced engineered materials whose unprecedented properties originate from their rational design at smaller scales<sup>1-3</sup>. Some of the examples of these unusual properties include a negative Poisson's ratio (*i.e.*, auxetic metamaterials)<sup>4-8</sup>, shape morphing<sup>9,10</sup>, negative compressibility<sup>11-13</sup>, negative stiffness<sup>14</sup>, and tunable negative thermal expansion<sup>15</sup>. Because of their unusual properties, these artificial materials are being increasingly used in various areas of application, including biomedical engineering<sup>16-18</sup>, soft robotics<sup>19-21</sup>, automobile and aerospace industries<sup>22</sup>, and other advanced technologies<sup>23-25</sup>. Mechanical metamaterials can be produced either by 3D printing them directly<sup>6,26,27</sup> or by applying the crumpling<sup>28</sup>, origami<sup>29,30</sup>, or mechanism-based<sup>31</sup> approach.

An important aim in the design of mechanical metamaterials is independent tailoring of their elastic properties, including the elastic modulus and Poisson's ratio<sup>32</sup>. Adjusting the Poisson's ratio of mechanical metamaterials over a wide range of negative and positive values allows for devising a rich set of new functionalities. For example, negative values of Poisson's ratios (*i.e.*, auxetic mechanical metamaterials<sup>33</sup>) can be combined with positive values (*i.e.*, conventional mechanical metamaterials) to design orthopedic implants with improved longevity<sup>34</sup> and to enable complex local actuations in soft robotics using a single far-field force<sup>35</sup>. At the same time, tailoring the stiffness values of mechanical metamaterials allows for the adjustment of their load-bearing capability and compliance. For example, mechanical metamaterials with extremely high negative or positive values of the Poisson's ratio often lack high elastic moduli. Rational design approaches are, therefore, required to increase (or decrease) the elastic modulus of architected materials regardless of their Poisson's ratio.

The common approach to the rational design of mechanical metamaterials has been to create specific geometric patterns (*i.e.*, unit cells) at the micro-level which are repeated in a highly ordered manner to achieve desired macro-level properties.

## 1.1. Background

However, it is difficult and challenging to find out what unit cell geometry must be used in order to attain a specific combination of mechanical properties. Furthermore, designs with extremely high or low values of the Poisson's ratio typically exhibit low elastic moduli. It is, therefore, important to independently tune the elastic properties of mechanical metamaterials. Incorporating randomness in the design of mechanical metamaterials is an alternative approach to tackle some of these challenges<sup>36–39</sup>. For instance, the spatial distribution of materials with different material properties within lattice structures (*i.e.*, randomness in material distribution), random-network (RN) unit cells consisting of stretch- and bending-dominated beamlike structures (*i.e.*, randomness in geometry), or a combination of both approaches can be used to achieve the desired set of elastic properties. In addition, randomness allows designers to achieve a continuous range of elastic properties while also affording the designed architected materials with a certain degree of robustness against manufacturing imperfections<sup>40,41</sup>.

Advanced 3D printing techniques that allow for the creation of micro-architectures with intricate structures have recently been developed. Moreover, these structures can be made from multiple materials that possess differing mechanical properties. However, due to the “curse of dimensionality”<sup>42</sup> caused by the different ways of incorporating randomness in the distribution of material properties and geometrical designs, the number of possible designs is extremely large. Therefore, optimizing the designs and especially discovering designs with rare-event mechanical properties are exceedingly challenging and are associated with formidably high computational costs. Given the inadequacy of conventional computational models for dealing with such a vast design space, alternative approaches based on machine learning (ML) techniques are needed to comprehensively explore the design space and uncover the most appropriate designs.

In general, the applications of ML in the field of material and architected structures can be categorized into three major categories: (i) prediction of structure performance, (ii) discovering of new materials, and (iii) design of materials with



target properties<sup>43,44</sup>. Supervised ML techniques have received more attention than unsupervised ML approaches when dealing with types of research problems<sup>44</sup>. Regression methods are commonly employed in the first category to forecast the mechanical properties of lattice structures with complex micro-architectures<sup>45,46</sup>. Probabilistic methods are often employed to tackle problems of the second kind in which one seeks to identify micro-architectures that result in a particular set of mechanical properties<sup>47,48</sup>. The third category involves utilizing a combination of regression and probabilistic algorithms to find the materials that exhibit optimal performance<sup>49-51</sup>.

Deep learning (DL) as one of the most advanced ML techniques has garnered substantial interest in the field of materials science<sup>45</sup>. DL employs the notion of artificial neural networks with several hidden layers to progressively extract higher-level characteristics from raw data. Different variants of DL models (*e.g.*, convolutional neural networks (CNN) and fully-connected artificial neural networks (ANN)) can be used to predict the mechanical response of metamaterials without the need for time-consuming tests or iterative numerical simulations<sup>45,52-54</sup>. The ultra-fast prediction of mechanical properties can then be used to find designs with rare mechanical properties<sup>45,55</sup>.

Considering the real-world applications of mechanical metamaterials, the inverse design of architected materials with predefined properties, especially rare-event properties, is of particular interest. Additionally, and given the limited resolution of available additive manufacturing (AM) techniques, we need to solve such inverse problems for specific dimensions of architected structures. The primary challenge, therefore, lies in the inverse design of mechanical metamaterials with predefined mechanical properties as well as specific dimensions. It should be also noted that such design problems typically have multiple solutions. This set of requirements makes probabilistic generative models (*e.g.*, generative adversarial networks (GAN)<sup>56</sup> and variational autoencoders (VAE)<sup>57</sup>) particularly interesting for tackling such complex, multi-faceted, and multi-objective design problems<sup>49,50,54,58</sup>.

## 1.2. Objective of the thesis

An advantage of such probabilistic generative models is that they can find several solutions to the above-mentioned inverse design problem. The availability of several solutions makes it possible to apply additional design requirements and select the most well-performing design. For instance, resistance to fatigue and fracture is a crucial design requirement for architected metamaterials, which rational design approaches have rarely considered. Stress concentration can lead to premature failure by initiating and growing cracks. It is, therefore, important to select designs with as uniform of a stress distribution and as small a stress peak as possible. To enable the selection of such structurally superior designs from a pool of possible designs, one can complement the ML techniques with direct finite element simulations.

## 1.2. Objective of the thesis

The background information provided in the previous section highlights the importance of finding designs for mechanical metamaterials with independently tailored elastic properties. The main objective of this thesis, therefore, is to rationally design mechanical metamaterials with desired elastic properties (including rare-event designs) while satisfying additional design requirements. We first made use of the benefits of randomness in the expansion of the design possibilities by incorporating it into both the material distribution and the geometrical design of lattice structures. We then employed computational models, machine learning, and advanced AM techniques to determine the elastic properties of the designed lattices and optimize their performance. Finally, we developed a modular platform titled “Deep-DRAM” which uses deep learning techniques for the inverse design of mechanical metamaterials with predefined elastic properties and spatial dimensions while also minimizing the peak stress within the structure. The main objectives and achievements of this thesis are discussed as follows: The first three chapters of the thesis (*i.e.*, Chapters 2-4) focus on the role of randomness in the design of architected metamaterials. While the first two of those chapters deal with the multi-material aspect of random designs, the third one is dedicated to the effects of random

geometries. These three chapters are followed by two chapters which apply ML techniques in general and DL methods in particular to design architected materials with rare combinations of elastic properties (Chapter 5) and to solve multi-objective inverse design problems pertaining to the multi-objective design of RN mechanical metamaterials with a desired set of elastic properties and specific dimensions (Chapter 6). A more detailed description of these chapters is presented in the following section.

### 1.3. Thesis outline

This thesis consists of seven chapters including this introductory chapter. The outlined research objective is reflected in the following chapters.

**Chapter 2.** In this chapter, computational models and an advanced multi-material 3D printing technique were employed to rationally design multi-material mechanical metamaterials using the spatial distribution of a hard phase within an originally soft lattice structure. The main objective of the study is to independently tailor the Poisson's ratio and elastic modulus of these multi-material mechanical metamaterials. Towards this aim, three types of unit cells (*i.e.*, auxetic, zero Poisson's ratio, and conventional), different levels of the elastic modulus of the hard phase to that of the soft phase ( $E_h/E_s$ ), and different levels of the ratio of the volume of the hard phase to that of the soft phase ( $\rho_h$ ) were considered to explore the achievable envelope of elastic properties (*i.e.*, Poisson's ratio and elastic modulus). In addition, several specimens with designed patterns of hard phase were fabricated and mechanically tested to validate the computational results.

**Chapter 3** uses computational models and mechanical tests to study the degree of non-affinity in the dual-phase multi-material mechanical metamaterial presented in Chapter 2. In multi-material mechanical metamaterials, the presence of hard and soft phases resulted in an additional non-affinity of deformations that had not been studied before. To decouple the non-affinity caused by the presence of different material phases from that of geometrical design, we determined the degree of non-

### 1.3. Thesis outline

affinity by comparing the deformations taking place in the designed multi-material mechanical metamaterials with those taking place in the same lattice structure but made from one single material (*i.e.*, with properties corresponding to a mixture of hard and soft phases). In addition, this chapter extensively discusses the correlation between the degree of non-affinity and elastic properties (*i.e.*, Poisson’s ratio and elastic modulus) as well as design parameters (*i.e.*, type of unit cell,  $E_h/E_s$ , and  $\rho_h$ ).

**Chapter 4** uses computational models and advanced 3D printing techniques to explore the elastic properties of two general types of disordered networks, namely lattice-restricted and unrestricted networks. These networks were composed of nodal points and beam-like elements where the nodes can be randomly connected to their adjacent nodes using beam-like elements with a mean nodal connectivity ranging between 2.5 and 7. In the case of lattice-restricted networks, the locations of the nodal points were restricted in space while the nodal points were chosen randomly in unrestricted networks, but only within predetermined boundaries. Finally, several representative networks were selected, and 3D printed to corroborate the results of our computational models.

**Chapter 5.** The objective of this chapter is to use computational models and DL algorithms to predict the elastic properties of multi-material mechanical metamaterials and identify the rare-event designs that exhibit highly desirable combinations of elastic properties (*e.g.*, high stiffness and highly negative values of the Poisson’s ratio). We used planar lattices (also called “tiled design”) based on the re-entrant, cubic, and honeycomb unit cells and various ranges of  $\rho_h$  and studied the relationship between the random distributions of the hard and soft phases in these structures and the resulting values of the elastic properties. We also studied various combinations of tiled designs (*e.g.*, four-tile and nine-tile structures) to learn how combining multiple instances of these random lattices into a hybrid, tiled lattice can expand the range of achievable elastic properties.

Moreover, this chapter discusses the training of two DL models (*i.e.*, single unit cell model, and four-tile model) that can accurately predict the elastic properties of the tiled designs and the combinations of four tiles. To validate the results of the prediction models, several specimens were fabricated using a multi-material 3D printer based on the Polyjet technology to be mechanically tested. We also used digital image correlation (DIC) to measure the full-field strain patterns during the mechanical testing of the fabricated specimens.

**Chapter 6.** This chapter presents a modular approach titled “Deep-DRAM” that aims to find many solutions to the multi-objective inverse design problem of finding RN mechanical metamaterials that give rise to a desired set of elastic properties while satisfying certain dimension requirements. Deep-DRAM (deep learning for the design of RN metamaterials) incorporates four decoupled models, including two deep learning models (DLM), a deep generative model (DGM) based on conditional variational autoencoders (CVAE), and direct finite element (FE) simulations. Deep-DRAM receives the desired elastic properties and dimensions and returns a set of candidate designs. After a filtering step based on the closeness of the actual properties of the generated designs to the initial desired properties, the last step uses direct FE simulations to identify the designs with the minimum peak stresses. The approach proposed in this chapter paves the way for the development of mechanical metamaterials with well-defined elastic properties (including rare-event properties) that can be found regardless of the overall dimensions of the metamaterial and are suitable for a broad range of applications.

**Chapter 7.** This chapter provides a summary of the main findings of this thesis. Moreover, a number of recommendations for future research directions are made.

## References

1. Surjadi, J. U. *et al.* Mechanical metamaterials and their engineering applications. *Adv. Eng. Mater* **21**, 1800864 (2019).
2. Yu, X., Zhou, J., Liang, H., Jiang, Z. & Wu, L. Mechanical metamaterials associated with stiffness, rigidity and compressibility: a brief review. *Prog. Mater. Sci.* **94**, 114–173 (2018).
3. Zadpoor, A. A. Mechanical meta-materials. *Mater. Horizons* **3**, 371–381 (2016).
4. Alderson, A. & Alderson, K. L. Auxetic materials. *Proc. Inst. Mech. Eng. Part G J. Aerosp. Eng.* **221**, 565–575 (2007).
5. Duncan, O. *et al.* Review of auxetic materials for sports applications: expanding options in comfort and protection. *Appl. Sci.* **8**, 941 (2018).
6. Mirzaali, M. J. *et al.* Multi-material 3D printed mechanical metamaterials: Rational design of elastic properties through spatial distribution of hard and soft phases. *Appl. Phys. Lett.* **113**, (2018).
7. Rayneau-Kirkhope, D., Zhang, C., Theran, L. & Dias, M. A. Analytic analysis of auxetic metamaterials through analogy with rigid link systems. *Proc. R. Soc. A* **474**, 20170753 (2018).
8. Ren, X., Das, R., Tran, P., Ngo, T. D. & Xie, Y. M. Auxetic metamaterials and structures: a review. *Smart Mater. Struct.* **27**, 23001 (2018).
9. Mirzaali, M. J., Janbaz, S., Strano, M., Vergani, L. & Zadpoor, A. A. Shape-matching soft mechanical metamaterials. *Sci. Rep.* **8**, 1–7 (2018).
10. Neville, R. M., Scarpa, F. & Pirrera, A. Shape morphing kirigami mechanical metamaterials. *Sci. Rep.* **6**, 31067 (2016).
11. Dudek, K. K., Gatt, R., Dudek, M. R. & Grima, J. N. Negative and positive stiffness in auxetic magneto-mechanical metamaterials. *Proc. R. Soc. A* **474**, 20180003 (2018).
12. Lakes, R. S., Lee, T., Bersie, A. & Wang, Y. C. Extreme damping in composite materials with negative-stiffness inclusions. *Nature* **410**, 565 (2001).
13. Nicolaou, Z. G. & Motter, A. E. Mechanical metamaterials with negative compressibility transitions. *Nat. Mater.* **11**, 608–613 (2012).
14. Moore, B., Jaglinski, T., Stone, D. S. & Lakes, R. S. Negative incremental bulk modulus in foams. *Philos. Mag. Lett.* **86**, 651–659 (2006).
15. Wang, Q. *et al.* Lightweight mechanical metamaterials with tunable negative

- thermal expansion. *Phys. Rev. Lett.* **117**, (2016).
16. Kolken, H. M. A. *et al.* Rationally designed meta-implants: a combination of auxetic and conventional meta-biomaterials. *Mater. Horizons* **5**, 28–35 (2018).
  17. Koons, G. L., Diba, M. & Mikos, A. G. Materials design for bone-tissue engineering. *Nat. Rev. Mater.* **5**, 584–603 (2020).
  18. Zadpoor, A. A. Meta-biomaterials. *Biomater. Sci.* **8**, 18–38 (2020).
  19. Rafsanjani, A., Bertoldi, K. & Studart, A. R. Programming soft robots with flexible mechanical metamaterials. *Sci. Robot.* **4**, 2–5 (2019).
  20. Lee, H. *et al.* 3D-printed programmable tensegrity for soft robotics. *Sci. Robot.* **5**, 1–12 (2020).
  21. Wu, S. *et al.* Symmetry-breaking actuation mechanism for soft robotics and active metamaterials. *ACS Appl. Mater. Interfaces* **11**, 41649–41658 (2019).
  22. Yuan, S., Chua, C. K. & Zhou, K. 3D-printed mechanical metamaterials with high energy absorption. *Adv. Mater. Technol.* **4**, 1–9 (2019).
  23. Surjadi, J. U. *et al.* Mechanical metamaterials and their engineering applications. *Adv. Eng. Mater.* **21**, 1800864 (2019).
  24. Wu, W. *et al.* Mechanical design and multifunctional applications of chiral mechanical metamaterials: a review. *Mater. Des.* **180**, 107950 (2019).
  25. Mirzaali, M. J. *et al.* Curvature induced by deflection in thick meta-plates. *Adv. Mater.* **33**, 2008082 (2021).
  26. Hedayati, R., Leeflang, A. M. & Zadpoor, A. A. Additively manufactured metallic pentamode meta-materials. *Appl. Phys. Lett.* **110**, 91905 (2017).
  27. van Manen, T., Janbaz, S. & Zadpoor, A. A. Programming 2D/3D shape-shifting with hobbyist 3D printers. *Mater. Horizons* **4**, 1064–1069 (2017).
  28. Mirzaali, M. J., Habibi, M., Janbaz, S., Vergani, L. & Zadpoor, A. A. Crumpling-based soft metamaterials: the effects of sheet pore size and porosity. *Sci. Rep.* **7**, 13028 (2017).
  29. Lv, C., Krishnaraju, D., Konjevod, G., Yu, H. & Jiang, H. Origami based mechanical metamaterials. *Sci. Rep.* **4**, 5979 (2014).
  30. Silverberg, J. L. *et al.* Using origami design principles to fold reprogrammable mechanical metamaterials. *Science* **345**, 647–650 (2014).
  31. Coulais, C., Kettenis, C. & van Hecke, M. A characteristic length scale causes anomalous size effects and boundary programmability in mechanical

## References

- metamaterials. *Nat. Phys.* **14**, 40 (2018).
32. Mirzaali, M. J. *et al.* Rational design of soft mechanical metamaterials: Independent tailoring of elastic properties with randomness. *Appl. Phys. Lett.* **111**, 51903 (2017).
  33. Evans, K. E. & Alderson, A. Auxetic materials: functional materials and structures from lateral thinking! *Adv. Mater.* **12**, 617–628 (2000).
  34. Kolken, H. M. A. *et al.* Rationally designed meta-implants: a combination of auxetic and conventional meta-biomaterials. *Mater. Horizons* **5**, 28–35 (2018).
  35. Hedayati, R., Mirzaali, M. J., Vergani, L. & Zadpoor, A. A. Action-at-a-distance metamaterials: distributed local actuation through far-field global forces. *APL Mater.* **6**, 36101 (2018).
  36. Hanifpour, M., Petersen, C. F., Alava, M. J. & Zapperi, S. Mechanics of disordered auxetic metamaterials. *Eur. Phys. J.* **91**, 1–8 (2018).
  37. Rayneau-Kirkhope, D., Bonfanti, S. & Zapperi, S. Density scaling in the mechanics of a disordered mechanical meta-material. *Appl. Phys. Lett.* **114**, 111902 (2019).
  38. Hagh, V. F. & Thorpe, M. F. Disordered auxetic networks with no reentrant polygons. *Phys. Rev. B.* **98**, 100101(2018).
  39. Reid, D. R. *et al.* Auxetic metamaterials from disordered networks. *Proc. Natl. Acad. Sci. U. S. A.* **115**, E1384–E1390 (2018).
  40. Hanifpour, M., Petersen, C. F., Alava, M. J. & Zapperi, S. Mechanics of disordered auxetic metamaterials. *Eur. Phys. J. B* **91**, 271 (2018).
  41. Rayneau-Kirkhope, D., Bonfanti, S. & Zapperi, S. Density scaling in the mechanics of a disordered mechanical meta-material. *Appl. Phys. Lett.* **114**, 111902 (2019).
  42. Köppen, M. The curse of dimensionality. *In Proc. of the 5th Online Conference on Soft Computing in Industrial Applications (WSC5)*, 4–8 (2000).
  43. Jiao, P. & Alavi, A. H. Artificial intelligence-enabled smart mechanical metamaterials: advent and future trends. *Int. Mater. Rev.* **66**, 365-393 (2021).
  44. Liu, Y., Zhao, T., Ju, W. & Shi, S. Materials discovery and design using machine learning. *J. Mater.* **3**, 159–177 (2017).
  45. Yang, C., Kim, Y., Ryu, S. & Gu, G. X. Using convolutional neural networks to predict composite properties beyond the elastic limit. *MRS Commun.* **9**, 609–617 (2019).



46. Yang, C., Kim, Y., Ryu, S. & Gu, G. X. Prediction of composite microstructure stress-strain curves using convolutional neural networks. *Mater. Des.* **189**, 108509 (2020).
47. Sardeshmukh, A., Reddy, S., GauthamB., P. & Bhattacharyya, P. TextureVAE: learning interpretable representations of material microstructures using variational autoencoders. *AAAI Spring Symp. MLPS* (2021).
48. Xue, T., Wallin, T. J., Menguc, Y., Adriaenssens, S. & Chiaramonte, M. Machine learning generative models for automatic design of multi-material 3D printed composite solids. *Extrem. Mech. Lett.* **41**, 100992 (2020).
49. Ma, W., Cheng, F., Xu, Y., Wen, Q. & Liu, Y. Probabilistic representation and inverse design of metamaterials based on a deep generative model with semi-supervised learning strategy. *Adv. Mater.* **31**, (2019).
50. Wang, L. *et al.* Deep generative modeling for mechanistic-based learning and design of metamaterial systems. *Comput. Methods Appl. Mech. Eng.* **372**, 1–41 (2020).
51. Kim, Y. *et al.* Exploration of optimal microstructure and mechanical properties in continuous microstructure space using a variational autoencoder. *Mater. Des.* **202**, 109544 (2021).
52. Wilt, J. K., Yang, C. & Gu, G. X. Accelerating auxetic metamaterial design with deep learning. *Adv. Eng. Mater.* **22**, 1–7 (2020).
53. Liu, T., Sun, S., Liu, H., An, N. & Zhou, J. A predictive deep-learning approach for homogenization of auxetic kirigami metamaterials with randomly oriented cuts. *Modern Phys. Lett. B* **35**, 2150033 (2021)
54. Kollmann, H. T., Abueidda, D. W., Koric, S., Guleryuz, E. & Sobh, N. A. Deep learning for topology optimization of 2D metamaterials. *Mater. Des.* **196**, 109098 (2020).
55. Kailkhura, B., Gallagher, B., Kim, S., Hiszpanski, A. & Han, T. Y. J. Reliable and explainable machine-learning methods for accelerated material discovery. *npj Comput. Mater.* **5**, 1–9 (2019).
56. Goodfellow, I. *et al.* Generative adversarial networks. *Commun. ACM* **63**, 139–144 (2020).
57. Kingma, D. P. & Welling, M. Auto-encoding variational bayes. Preprint at arXiv:1312.6114 (2013)
58. Kumar, S., Tan, S., Zheng, L. & Kochmann, D. M. Inverse-designed spinodoid metamaterials. *npj Comput. Mater.* **6**, 1–10 (2020).

# 2

## Multi-material 3D printed mechanical metamaterials

Published as:

Mirzaali, M. J., Caracciolo, A., Pahlavani, H., Janbaz, S., Vergani, L., & Zadpoor, A. A. Multi-material 3D printed mechanical metamaterials: rational design of elastic properties through spatial distribution of hard and soft phases. *Applied Physics Letters* 113(24), 241903 (2018).

## Abstract

Up until recently, the rational design of mechanical metamaterials has usually involved devising geometrical arrangements of micro-architectures that deliver unusual properties on the macro-scale. A less explored route to rational design is spatially distributing materials with different properties within lattice structures to achieve the desired mechanical properties. Here, we used computational models and advanced multi-material 3D printing techniques to rationally design and additively manufacture multi-material cellular solids for which the elastic modulus and Poisson's ratio could be independently tailored in different (anisotropic) directions. The random assignment of a hard phase to originally soft cellular structures with an auxetic, zero Poisson's ratio, and conventional designs allowed us to cover broad regions of the elastic modulus-Poisson's ratio plane. Patterned designs of the hard phase were also used and were found to be effective in the independent tuning of the elastic properties. Close inspection of the strain distributions associated with different types of materials distributions suggests that locally deflected patterns of deformation flow and strain localizations are the main underlying mechanisms driving the above-mentioned adjustments in the mechanical properties.

## 2.1. Introduction

### 2.1. Introduction

The vast majority of the mechanical metamaterials<sup>1-3</sup> presented to date have used various types of geometrical designs to achieve their unusual properties such as negative Poisson's ratios<sup>4</sup> and bistability<sup>5</sup>, shape-morphing mechanical metamaterials<sup>6</sup>, negative compressibility<sup>7</sup>, negative stiffness<sup>8</sup>, crumpled metamaterials<sup>9</sup>, and tunable negative thermal expansion<sup>10</sup>. However, the rational design of mechanical metamaterials is not limited to their small-scale geometry and includes rationally designing the spatial distribution of the mechanical properties as well as a combination with geometrical design and spatial distribution of mechanical properties. The research into both latter rational design approaches has just started, as the multi-material 3D printing (= AM) techniques required for achieving complex spatial distributions of mechanical properties and combining that with complex geometries are just emerging. A few recent studies on 3D lattices with high Poisson's ratio properties<sup>11</sup>, topology optimization of multi-material mechanical metamaterials with negative Poisson's ratio<sup>12</sup> or multifunctionality<sup>13</sup>, and controlling instabilities<sup>14</sup> are examples of the applications of dual-phase materials<sup>15,16</sup> for achieving new ranges of properties and new types of functionalities in mechanical metamaterials.

Here, we used complex spatial distributions of the mechanical properties realized through advanced multi-material 3D printing processes and combined that with architected geometrical designs to independently tailor the Poisson's ratio and elastic modulus of dual-phase (*i.e.*, soft-hard) mechanical metamaterials. We used computational models for the rational design of the mechanical metamaterials. A large number of the designed specimens were then fabricated and were subjected to mechanical loading to characterize their mechanical behavior.

### 2.2. Materials and methods

In our designs, we used three unit cells, representing lattice structures with negative ( $\theta = 60^\circ$ ), intermediate (*i.e.*, zero) ( $\theta = 90^\circ$ ) and positive ( $\theta = 120^\circ$ ) Poisson's ratios (Figure 1a). The unit cells had a similar height ( $c$ ) and width ( $w$ )

while differing in  $h$  and  $l$  (Figure 1a). Keeping a specific set of design parameters constant, allowed us to design lattice structures with an equal overall width ( $W$ ) and length ( $L$ ). The in-plane ( $t$ ) and out-of-plane thicknesses ( $b$ ) of the unit cells with different angles were similar as well. All design parameters are listed in Supplementary Table 1.

### 2.2.1. Computational modeling

To create the computational models, the geometry of each lattice structure was created as an input file in MATLAB (R2011b) and later was handled with the finite element modeling software (Abaqus 6.14). In-plane Timoshenko beam elements (B21, Abaqus) with a rectangular cross-section were used to model the lattice structures. A hyperelastic material model (Neo Hookean,  $C_{10} = 0.106$  MPa,  $D_1 = 0.03$  MPa<sup>-1</sup>) was applied as the constitutive equation of the soft phase. Three levels of the elastic modulus of the hard phase were selected with one, two, or three orders of magnitude higher elastic moduli as compared to the soft phase (*i.e.*,  $E_h/E_s = 10, 100, \text{ or } 1000$ ). Furthermore, two levels of the fraction of the hard phase with respect overall volume (*i.e.*,  $\rho_h = 25\%$  and  $50\%$ ) were chosen when spatially distributing both phases in the lattice structures.

A large number of finite element models of the lattice structures were created in which the hard phase replaced the soft elements of the lattice structures at random locations. The replacement of the soft phase with the hard phase continued until the intended fraction of the hard phase was achieved. To adequately sample the stochastic space of possible designs, one thousand simulations were performed for each combination of the hard phase fraction and  $E_h/E_s$ , resulting in a total of 18000 simulations.

Moreover, the simulations were performed in two directions, *i.e.*, 1 and 2, in order to investigate the anisotropic behavior of these metamaterials. A displacement boundary condition equal to 10% longitudinal/transverse strain was applied to simulate a tensile test. The boundary conditions were applied to a reference point,

## 2.2. Materials and methods

which was kinematically coupled to the corresponding nodes of the lattice structures. For instance, for the simulation in the 1-direction (Figure 1a), a displacement was applied on a top reference point. Another reference node was created at the bottom of the structure, which was clamped. A non-linear static simulation was performed. The stresses ( $\sigma_{11}, \sigma_{22}$ ) and strains ( $\varepsilon_{11}, \varepsilon_{22}$ ) in both directions were respectively calculated based on the ratio of the reaction force to the cross section area and the ratio of the displacement to the free length of the structure in the longitudinal (transverse) direction. The elastic stiffnesses ( $E_{11}, E_{22}$ ) of the structure was calculated as the slope of the stress-strain curve at 1% strain.

The Poisson's ratio in direction 1 was calculated as  $\nu_{12} = -\frac{\varepsilon_{22}}{\varepsilon_{11}}$ , where  $\varepsilon_{11}$  is the applied strain in direction 1, and  $\varepsilon_{22}$  is the sum of the transverse deformation of the structure under this displacement at every  $i^{\text{th}}$  node ( $U_{22,i}$ ) with  $\varepsilon_{22} = \frac{\sum_{i=1}^n U_{22,i}}{W}$  and  $n$  =total number of lateral nodes along direction 2. Likewise, the Poisson's ratio in direction 2 was defined as  $\nu_{21} = -\frac{\varepsilon_{11}}{\varepsilon_{22}}$  where  $\varepsilon_{22}$  is the applied strain in direction 2 and  $\varepsilon_{11} = \frac{\sum_{i=1}^p U_{11,i}}{L}$  with  $p$  is equal to the total number of the lateral nodes in direction 1. The Poisson's ratios in both directions were measured at 1% longitudinal (transverse) strain.

### 2.2.2. Fabrication and experimental testing

For the experimental study, fifteen specimens were directly fabricated using a multi-material 3D printer (Object500 Connex3 3D printer, Stratasys) working on the basis of material jetting (the Polyjet technology). Of those specimens, 6 and 9 samples were tested in directions 1 and 2, respectively. Among the specimens mentioned above, 5 were purely soft while the rest were multi-material. The hard and soft phases were respectively printed with VeroCyan (RGD841, shore hardness (D) 83-86) and Agilus30 Black (FLX985, shore hardness (A) 30-35). These materials were selected to achieve  $E_h/E_s$  values up to  $\approx 1000$ .

The specimens tested in direction 1 had an extra hard part to make it possible to attach it to the gripper while the ones tested in direction 2 were directly attached to the gripper via pins. Two gripping systems and their pins were designed and additively manufactured using a fused deposition modeling (FDM) 3D printer (Ultimaker 2+, Geldermalsen, The Netherlands) from polylactic acid (PLA) filaments (MakerPoint PLA 750 gr Natural).

Tensile mechanical testing was performed under displacement control using an LLOYD instrument (LR5K) mechanical testing machine with a 100 N load cell and a stroke rate of 2 mm/min. The time, force, and displacement were recorded at a sampling rate of 20 Hz. The force and displacement were used to calculate the stress and strain with respect to the initial cross-section area and the initial free length of the specimens. The stiffness of the structure was determined using the measured stress and strain values. The deformation of the specimens was also captured by a digital camera that was later used to calculate the Poisson's ratios in both directions using image analysis (see the supplementary document, Supplementary Figure 1).

We validated the accuracy of our numerical simulations for the purely soft lattice structures by comparing them with the experimental and theoretical models (Figure 1b). Equation 1 shows the existing theoretical relations for the calculation of the elastic properties of homogenized lattice structures<sup>17</sup>.

$$E_{11} = \frac{k_f(h/l + \sin \theta)}{b \cos^3 \theta}, \quad E_{22} = \frac{k_f \cos \theta}{b(h/l + \sin \theta) \sin \theta} \quad (1)$$

$$v_{12} = \frac{\sin \theta (h/l + \sin \theta)}{\cos^2 \theta}, \quad v_{21} = \frac{\cos^2 \theta}{\sin \theta (h/l + \sin \theta)}$$

where  $k_f = E_b b (t/l)^3$  is the flexure force constant and  $E_b$  is the elastic modulus of the solid constituent. The elastic modulus,  $E_s$ , of our soft materials is 0.6 MPa.

## 2.2. Materials and methods

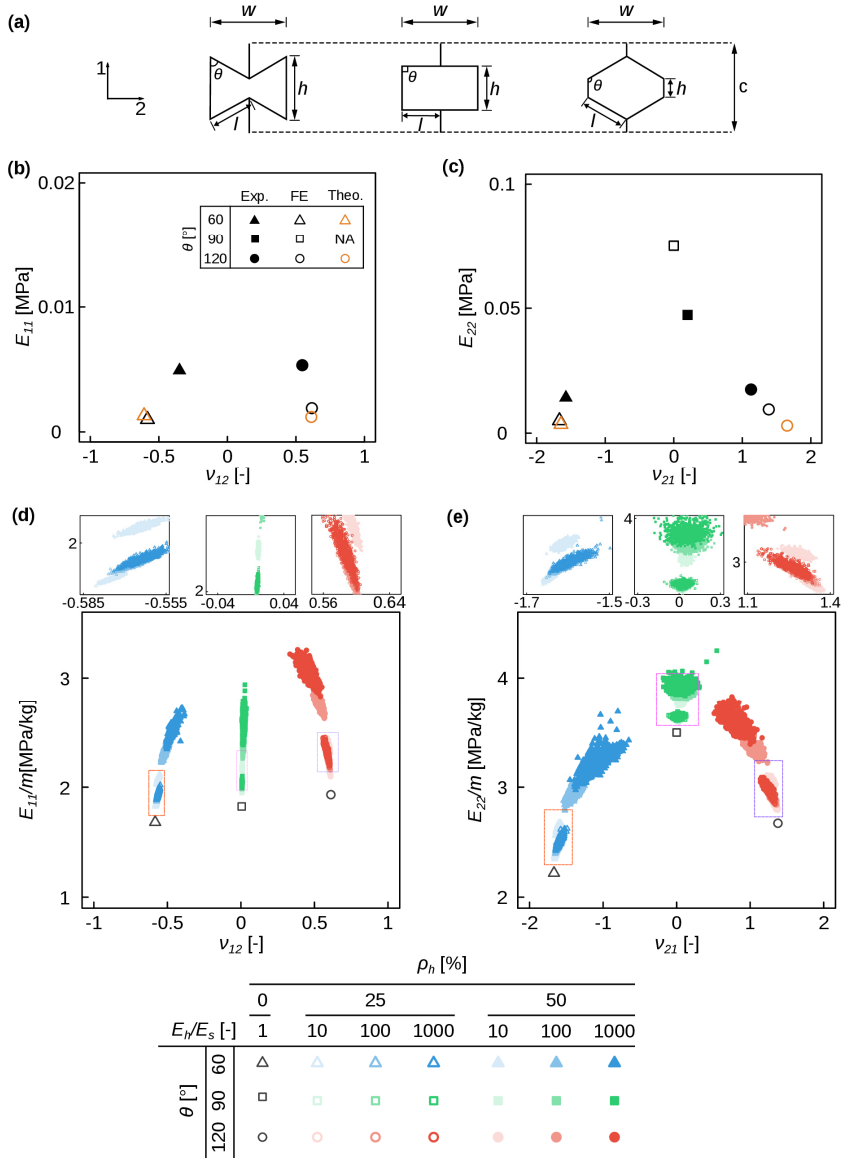


**Figure 1.** (a) Three unit cell geometries ( $\theta = 60^\circ, 90^\circ, 120^\circ$ ) used for the fabrication of lattice structures. A comparison of the numerical results, experimental observations, and theoretical predictions for the lattice structures made from a uniform (soft) material and tested in directions 1 (b) and 2 (c). The regions covered by the mechanical properties of multi-material mechanical metamaterials with three geometries and random assignment of a hard phase to the elements of the lattice structure until two fractions of the hard material,  $\rho_h = 25\%$  and  $50\%$ , were achieved. Moreover, three different values of  $E_h/E_s$  were used to calculate the elastic modulus and Poisson's ratio in directions 1 (d) and 2 (e). The specific elastic stiffnesses (*i.e.*, normalized by the mass,  $m$ , of the sample) are presented in (d) and (e).



We found that the elastic properties obtained from our computational models for the homogeneously soft materials are within the range of those calculated using Equation 1 (Theo.) and experimental observations (Exp.) (Figure 1b-c).

### 2.3. Results and discussion

The random assignment of the hard phase to the elements of the lattice structures considered here resulted in drastic changes in both the Poisson's ratio and elastic modulus (Figure 1d-e). Specific regions, therefore, emerged within the elastic modulus-Poisson's ratio plane within which the Poisson's ratio and elastic modulus could be independently adjusted (Figure 1d-e). Generally speaking, the changes in both Poisson's ratio and elastic modulus were larger in direction 2 as compared to direction 1 (Figure 1d-e, and Figure 2). Moreover, the elastic properties of lattice structures with  $\theta = 60^\circ$  and  $\theta = 120^\circ$  were much more sensitive to the presence of a second, harder phase, as compared to the lattice structures with  $\theta = 90^\circ$  (Figure 1d-e). This trend was particularly clear for the Poisson's ratio in direction 1 and elastic modulus in direction 2 (Figure 1d-e). Random assignment of a hard phase ( $E_h/E_s=10-1000$ ) to up to 50% of the elements of the considered lattice structures resulted in up to  $\approx 2$  orders of magnitude increase in elastic modulus (Figure 1d-e). Combining the hard and soft phases shifted the Poisson's ratio of the lattice structures towards higher values in the case of  $\theta = 60^\circ$  and towards lower values in the case of  $\theta = 120^\circ$  (Figure 1d-e, Figure 2a-d). The distribution of the Poisson's ratio of the original value (*i.e.*, the Poisson's ratio of a single-material lattice structure) was more or less symmetric in the case of  $\theta = 90^\circ$  (Figure 1d-e).

As expected, the effects of a second phase on the Poisson's ratio was amplified for higher values of  $E_h/E_s$  (Figure 2a-d). The same held for the fraction of the hard phase (Figure 2a-d). Stress and strain localizations were clearly present in the case of multi-material designs (Figure 2a-d). In addition, the stress and strain localizations were clearly intensified in the case of a higher fraction of the hard phase (*i.e.*,  $\rho_h = 50\%$ ) (Figure 2a-d). Assigning a hard phase to a random place within a soft lattice

### 2.3. Results and discussion

structure could also affect the global deformation of the lattice structure and lead to an asymmetric deformation pattern (Figure 2), as the harder elements of the lattice structure deflect or block the deformation flow.

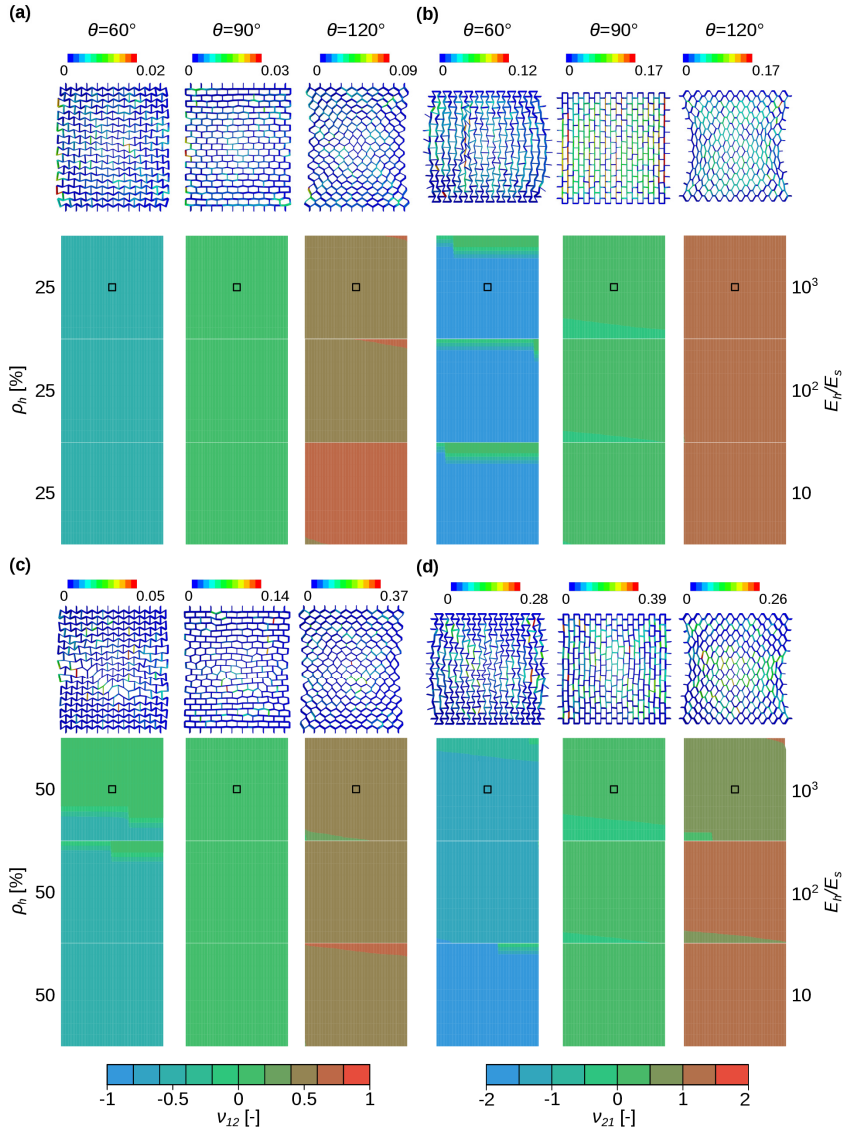


**Figure 2.** The Poisson's ratios of the random multi-material lattice structures made with three unit cell geometries, three values of  $E_h/E_s$ , and two fractions of the hard material ( $\rho_h$ ). The values were calculated for directions 1 (a, c), and 2 (b, d). The strain distributions presented at the top of the Poisson's ratio contours show the principal strains obtained from the numerical simulations at 10% applied strain and for the data points indicated with boxes.

In addition to randomly assigning the second (*i.e.*, hard) phase material to a number of the elements of the lattice structure, we rationally designed the placement of the hard phase such that the elements to which the hard phase were assigned collectively created either a re-entrant (*i.e.*, auxetic) or honeycomb (*i.e.*, conventional) shape (Figure 3). All designs were both 3D printed and analyzed using our computational models. Such rational placements of the second phase resulted in drastic changes in the elastic properties of the mechanical metamaterials (Figure 3a-b). For example, when we started from an auxetic lattice structure (legend:  $\Delta$ ) and assigned the hard phase to specific elements of the structure in such a way that they created a global re-entrant shape, the Poisson's ratio remained largely unchanged while the stiffness was increased by  $> 10$  times in direction 1 (Figure 3). Choosing a honeycomb shape for the hard elements assigned to the same type of the lattice structure (*i.e.*, auxetic, legend: O) pushed the Poisson's ratio towards 0, while not significantly changing the stiffness in direction 1 and substantially increasing the stiffness in direction 2 (Figure 3). Various types of drastic evolutions in the stiffness and Poisson's ratio in both directions were observed for the other types of lattice structures and using different types of designs of the hard phase elements (see the arrows in Figure 3a-b).

Interestingly, in the case of the lattice structures with a zero Poisson's ratio (legend:  $\square$ ), introducing hard unit cells with a global re-entrant or honeycomb shape resulted in lattice structures with relatively large (negative or positive) values of the Poisson's ratio (Figure 3). This shows that, in addition to the geometrical design, one could benefit from the spatial distribution of the mechanical properties as an effective tool to independently tailor the elastic properties of mechanical metamaterials.

### 2.3. Results and discussion

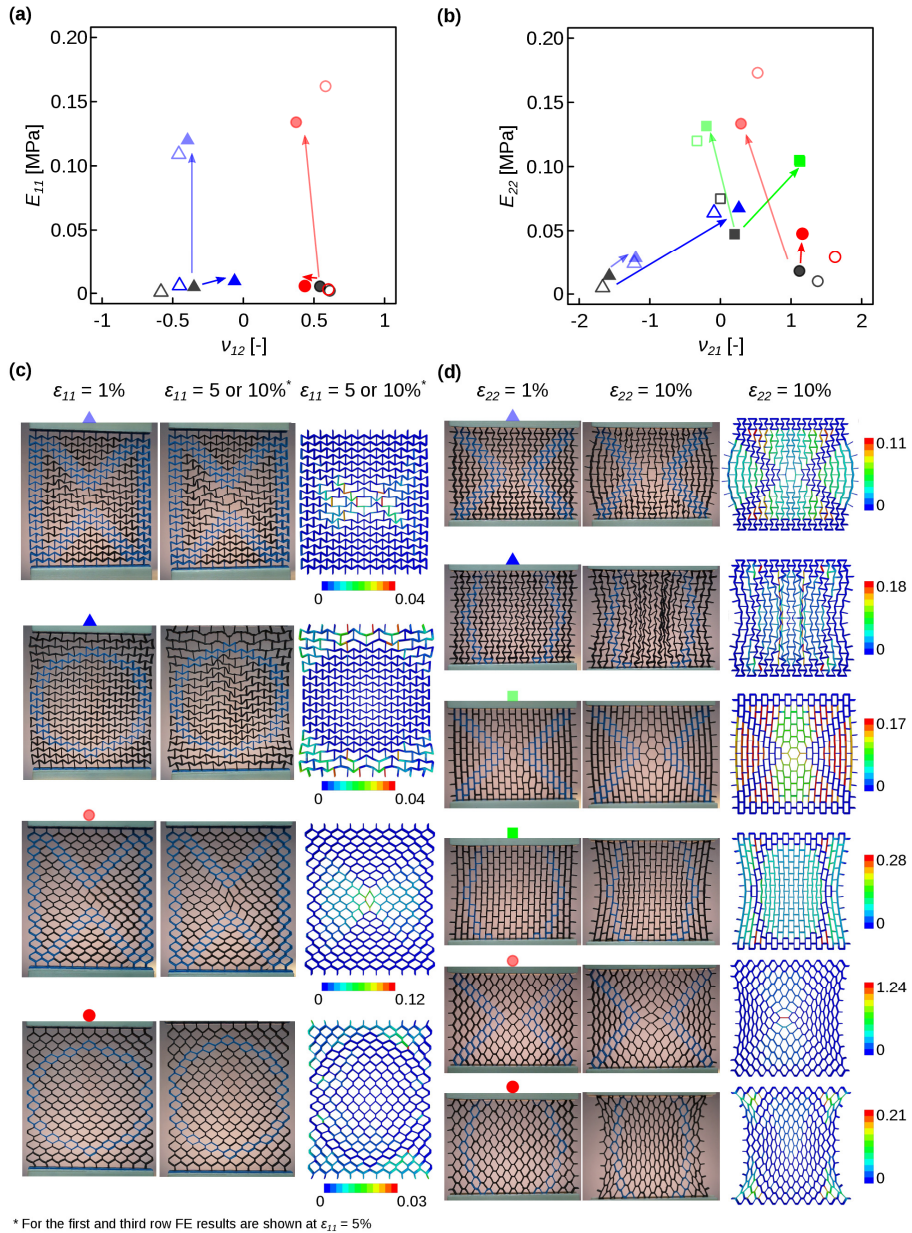


**Figure 3.** The numerical (hollow markers) and experimental (solid markers) results for the elastic properties of multi-material lattice structures with rationally designed hard phases and tested in directions 1 (a) and 2 (b). The arrows compare the results of a corresponding lattice structure with a single soft material with those of the multi-material designs. The experimental and numerical deformation patterns are also compared with each other in directions 1 (c) and 2 (d). The strain distributions show the principal strains obtained using the computational models.

Here, we assumed constant thickness for the beam elements of the lattice structures and increased the rigidity of each beam only by increasing individual stiffnesses. Since the rigidity of each beam in these lattice structures is defined as  $EI$ , where  $E$  is the elastic stiffness and  $I$  is the second moment of inertia, one could increase beam's rigidity by changing the second moment of inertia. In this case, it means using various beam thicknesses for each element. This is again mapping the elastic properties by manipulating the geometrical features of the lattice structures, although there is a limitation on the maximum thickness considered for such designs. We also used the dual-material for the construction of these metamaterials. However, different hard-soft elastic ratios or even a gradient in the mechanical properties can be taken into account for the construction of these materials.

The results of this study clearly show that both random and rational distributions of a hard phase could be used for independent tailoring of the elastic modulus and Poisson's ratio of a soft mechanical metamaterial. The spatial distribution of the mechanical properties could also be used for independent tailoring of the elastic properties in different directions, thereby allowing for the rational design of anisotropic mechanical metamaterials. Our computational models clearly show that, at the micro-scale, nonhomogeneous strain distributions and localized deformations are responsible for the observed behavior on the macro-scale including not only the effective elastic properties but also such phenomena as asymmetric deformations. From the mechanistic viewpoint, the assignment of a hard phase to *random* elements within the lattice structure locally deflects the flow of deformation, thereby disrupting the uniform deformation flow resulting from the geometrical design of the lattice structure. As the stiffness of the hard phase or its fraction increases, this effect will be stronger. For lattice structures whose Poisson's ratio is already largely positive or negative, this random disruption of the deformation is unlikely to increase the Poisson's ratio further, which is why the absolute value of the Poisson's ratio tends to decrease when a hard phase is randomly assigned to lattice structure with  $\theta = 60^\circ$  or  $\theta = 120^\circ$ . In the case of  $\theta = 90^\circ$ , the Poisson's ratio is already perfectly

## 2.4. Conclusion

zero, meaning that any random defelctions of the deformation flow will likely increase the Poisson's ratio. However, there is an equal chance that this random disruption of the deformation flow results in a positive or negative Poisson's ratio. That explains the more or less symmetric region of the elastic modulus-Poisson's ratio covered by random multi-material lattice strucutres with  $\theta = 90^\circ$ . When the assignment of the hard phase is rationally designed (*e.g.*, in the global shape of a re-entrant structure of a honeycomb), very big jumps in the values of the Poisson's ratio are possible. Regarding the elastic modulus, an addition of a hard phase clearly increases the resistance to deformation, thereby resulting in a higher elastic modulus. The level of the increase in the elastic modulus is, however, dependent on how effectively the hard phase is used for increasing the load-bearing capacity of the lattice strucutre in a specific direction. Adjusting the effectiveness of the hard phase in a specific direction could, therefore, be used for tuning the elastic modulus of the lattice strucutre with the upper bound given by the most efficient distribution of the hard phase. Together, all above-mentioned mechanisms allow for independent tailoring of the elastic modulus and Poisson's ratio of the lattice strucutre regardless of the geometrical design. Keeping the geometrical design intact might be particularly useful when designing multiphysics metamaterials, for which the geometrical design also determines other physical properties of the material (*e.g.*, thermal expansion or mass transport properties).

## 2.4. Conclusion

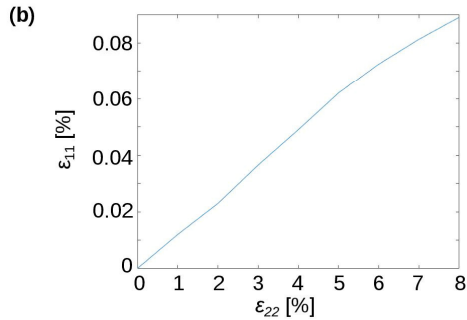
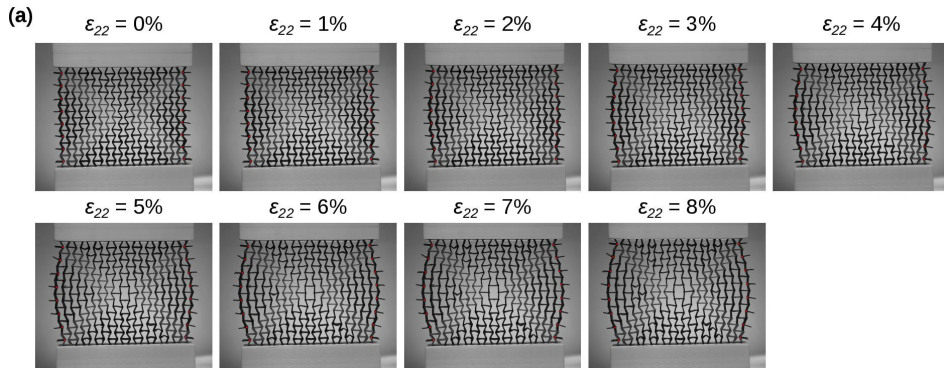
Here, we showed that spatial distribution of materials with different mechanical properties (*i.e.*, soft and hard phases) could be used to tailor the elastic properties of cellular structures. However, the trade-off for the use of such combinations is the creation of local stress concentrations in the resulting lattices. The level of the stress concentrations can significantly increase with a higher mismatch between the hard and soft phases. Moreover, the presence of these stress riser regions can result in the formation of local buckling or local damage. Those can eventually facilitate crack

initiation and propagation in the cellular structure, leading to pre-mature failure particularly under repetitive loading. One way to address this challenge would be to introduce intermediate phases with specific gradients in their mechanical properties to decrease the severity of the stress concentrations. Here, we performed monotonic quasi-static tensile tests, as we were primarily interested in the elastic properties of these structures. Systematic study of the failure and fatigue mechanisms would, however, require extensive fatigue tests that are suggested to be pursued in future research.

## 2.5. Supplementary document

**Supplementary Table 1.** Design parameters of lattice structures.

$\theta$ [°]	$W$ [mm]	$L$ [mm]	$w$ [mm]	$h$ [mm]	$l$ [mm]	$c$ [mm]	$t$ [mm]	$b$ [mm]
60	112.5	124.3	11.25	9.17	6.50	11.85	0.75	7.5
90	112.5	124.3	11.25	5.92	5.63	11.85	0.75	7.5
120	112.5	124.3	11.25	2.67	6.50	11.85	0.75	7.5



**Supplementary Figure 1.** (a) Image analysis steps during tensile testing at different longitudinal strain levels. The lateral strains ( $\epsilon_{11}$ ) were calculated with respect to the intact condition. The evolution of lateral strain under progressive longitudinal strain ( $\epsilon_{22}$ ) is shown in (b).



## References

1. Alderson, A. & Alderson, K. L. Auxetic materials. *Proc. Inst. Mech. Eng. Part G J. Aerosp. Eng.* **221**, 565–575 (2007).
2. Evans, K. E. & Alderson, A. Auxetic materials: functional materials and structures from lateral thinking! *Adv. Mater.* **12**, 617–628 (2000).
3. Ren, X., Das, R., Tran, P., Ngo, T. D. & Xie, Y. M. Auxetic metamaterials and structures: a review. *Smart Mater. Struct.* **27**, 23001 (2018).
4. Lakes, R. Negative Poisson's ratio materials: response. *Sci.* **238**, 551 (1987).
5. Yasuda, H. & Yang, J. Reentrant origami-based metamaterials with negative Poisson's ratio and bistability. *Phys. Rev. Lett.* **114**, 185502 (2015).
6. Mirzaali, M. J., Janbaz, S., Strano, M., Vergani, L. & Zadpoor, A. A. Shape-matching soft mechanical metamaterials. *Sci. Rep.* **8**, 1–7 (2018).
7. Nicolaou, Z. G. & Motter, A. E. Mechanical metamaterials with negative compressibility transitions. *Nat. Mater.* **11**, 608–613 (2012).
8. Dudek, K. K., Gatt, R., Dudek, M. R. & Grima, J. N. Negative and positive stiffness in auxetic magneto-mechanical metamaterials. *Proc. R. Soc. A Math. Phys. Eng. Sci.* **474**, 20180003 (2018).
9. Mirzaali, M. J., Habibi, M., Janbaz, S., Vergani, L. & Zadpoor, A. A. Crumpling-based soft metamaterials: the effects of sheet pore size and porosity. *Sci. Rep.* **7**, 13028 (2017).
10. Wang, Q. et al. Lightweight mechanical metamaterials with tunable negative thermal expansion. *Phys. Rev. Lett.* **117**, (2016).
11. Chen, D. & Zheng, X. Multi-material additive manufacturing of metamaterials with giant, tailorable negative Poisson's ratios. *Sci. Rep.* **8**, (2018).
12. Vogiatzis, P., Chen, S., Wang, X., Li, T. & Wang, L. Topology optimization of multi-material negative Poisson's ratio metamaterials using a reconciled level set method. *Comput. Des.* **83**, 15–32 (2017).
13. Wang, Y., Gao, J., Luo, Z., Brown, T. & Zhang, N. Level-set topology optimization for multimaterial and multifunctional mechanical metamaterials. *Eng. Optim.* **49**, 22–42 (2017).
14. Janbaz, S., McGuinness, M. & Zadpoor, A. A. Multimaterial control of instability in soft mechanical metamaterials. *Phys. Rev. Appl.* **9**, 64013 (2018).
15. Mirzaali, M. J. et al. Length-scale dependency of biomimetic hard-soft composites. *Sci. Rep.* **8**, 12052 (2018).

## References

16. Wang, K., Chang, Y.-H., Chen, Y., Zhang, C. & Wang, B. Designable dual-material auxetic metamaterials using three-dimensional printing. *Mater. Des.* **67**, 159–164 (2015).
17. Masters, I. G. & Evans, K. E. Models for the elastic deformation of honeycombs. *Compos. Struct.* **35**, 403–422 (1996).



# 3

## Non-affinity in multi-material mechanical metamaterials

Published as:

Mirzaali, M. J., Pahlavani, H., Yarali, E., & Zadpoor, A. A. Non-affinity in multi-material mechanical metamaterials. *Scientific Reports*, 10(1), 1-10 (2020).

## Abstract

Non-affine deformations enable mechanical metamaterials to achieve their unusual properties while imposing implications for their structural integrity. The presence of multiple phases with different mechanical properties results in additional non-affinity of the deformations, a phenomenon that has never been studied before in the area of extremal mechanical metamaterials. Here, we studied the degree of non-affinity,  $\Gamma$ , resulting from the random substitution of a fraction of the struts,  $\rho_h$ , that made up a lattice structure and were printed using a soft material (elastic modulus =  $E_s$ ) by those printed using a hard material ( $E_h$ ). Depending on the unit cell angle (*i.e.*,  $\theta = 60^\circ, 90^\circ$ , or  $120^\circ$ ), the lattice structures exhibited negative, near-zero, or positive values of the Poisson's ratio, respectively. We found that the auxetic structures exhibit the highest levels of non-affinity, followed by the structures with positive and near-zero values of the Poisson's ratio. We also observed an increase in  $\Gamma$  with  $E_h/E_s$  and  $\rho_h$  until  $E_h/E_s = 10^4$  and  $\rho_h = 75\%-90\%$ , after which  $\Gamma$  saturated. The dependency of  $\Gamma$  upon  $\rho_h$  was, therefore, found to be highly asymmetric. The positive and negative values of the Poisson's ratio were strongly correlated with  $\Gamma$ . Interestingly, achieving extremely high or extremely low values of the Poisson's ratio required highly affine deformations. In conclusion, our results clearly show the importance of considering non-affinity when trying to achieve a specific set of mechanical properties and underscore the structural integrity implications in multi-material mechanical metamaterials.

## 3.1. Introduction

A simple mechanical load (*e.g.*, uniaxial compression, tension, or shear) applied to a geometrically simple (*e.g.*, square-shaped) piece of what is traditionally considered a material (*e.g.*, metals, polymers) leads to a simple deformation that is highly predictable at large enough length scales and is homogeneously distributed within the material. Such a homogenous deformation is formally called an ‘affine’ deformation and can be fully described using an affine transformation (*i.e.*, a linear transformation plus a rigid body translation) applied to the coordinates of the points constituting the material<sup>1,2</sup>.

All this simplicity, predictability, and homogeneity may be lost when a simple mechanical load is applied to an architected material<sup>3</sup>. Architected materials, which are sometimes referred to as mechanical metamaterials<sup>4-6</sup>, possess complex small-scale geometries that are engineered to give rise to unusual mechanical properties at the macroscale. In a way, the whole point of rationally designing<sup>7</sup> the small-scale geometry of architected materials, may be to break the affinity of the deformations in an exact way so as to achieve unusual macroscale properties. Non-affine deformations can, for example, be exploited to achieve negative values of the Poisson’s ratio<sup>8,9</sup>, action-at-a-distance actuation behaviors<sup>10</sup>, and independent tailoring of the elastic properties<sup>11</sup>. Some other functionalities of mechanical metamaterials such as shape morphing<sup>12,13</sup> are ‘per definition’ dependent on the non-affinity of the induced deformation. Non-affine deformations can also be observed in other systems. For example, random networks<sup>14-17</sup> that are found in biological systems such as the filamentous proteins that make up the cytoskeleton and extracellular matrix<sup>18-22</sup>, as well as flexible polymer networks<sup>23</sup> and polymer hydrogels<sup>24</sup> exhibit highly non-affine deformations.

From the structural integrity viewpoint, however, non-affine deformations could be troublesome, as they may give rise to stress concentrations and, thus, decreased fatigue lives and premature failures. It is, therefore, crucial to understand

the non-affinity of deformations in architected materials because both advanced functionalities and structural performance of these materials are dependent on the proper management of non-affine deformations. Even though non-affine deformations can be studied at different length scales<sup>15,25–27</sup>, the most relevant scale in the case of mechanical metamaterials is the length scale of the constituting structural elements (*i.e.*, struts)<sup>28</sup>. We will, therefore, be focusing on this length scale.

Non-affine deformation can be characterized in terms of a degree of non-affinity ( $\Gamma$ ) or non-affine correlation functions<sup>14,29,30</sup>. The degree of non-affinity is a scalar parameter that depends on the length scale<sup>31</sup> and applied strain<sup>15,19,21</sup>. There are also other metrics of non-affinity that are based on strain energy<sup>15,19,31,32</sup> or a comparison of the local deformations with affine deformations<sup>14,29,30,33–39</sup>.

The degree of non-affinity is an important determinant of the inhomogeneous deformation of metamaterials. However, its relationship with the elastic properties (*e.g.*, elastic modulus and Poisson's ratio) of mechanical metamaterials remains elusive. Recent advances in multi-material additive manufacturing (also called 3D printing) techniques have enabled the fabrication of 'multi-material' mechanical metamaterials<sup>40–42</sup> whose unusual properties and advanced functionalities are as much dependent on the spatial distribution of multiple phases with different mechanical properties as they are on the small-scale geometrical design of the constituting unit cells. Essentially, the complex distributions of the multiple phases are alternative ways of creating non-affine deformations so as to expand the range of achievable macroscale properties<sup>41</sup>. From the structural integrity viewpoint, the presence of multiple phases with highly different mechanical properties creates stress concentrations that underscore the importance of studying the non-affinity of the deformations even more. However, non-affine deformations in multi-material mechanical metamaterials have never been studied before.

Here, using computational models and experimental tests, we studied the non-affinity of the deformations taking place in a special class of multi-material

## 3.2. Materials and methods

mechanical metamaterials that are made from two distinct phases, namely a hard phase and a soft phase. We aimed to separate the non-affinity caused by the presence of multiple materials from that of geometrical design.

Towards this aim, the degree of non-affinity was determined by comparing the deformations taking place in the multi-material mechanical metamaterials (*i.e.*, heterogeneous structures) with those of reference materials with monolithic properties (*i.e.*, homogeneous structures) using computational models. The properties of the homogeneous structure equivalent to each heterogeneous structure were calculated using the rule-of-mixture, the properties of the soft and hard phases, and their ratios. Moreover, three different structures with cell angles of  $60^\circ$ ,  $90^\circ$ , and  $120^\circ$  and with different mechanical properties were fabricated using an advanced multi-material 3D printing technique. Finally, the elastic properties of multi-material mechanical metamaterials and the degree of non-affinity were quantified and discussed in both quantitative and qualitative terms.

## 3.2. Materials and methods

### 3.2.1. Design and computational modeling

We used already existing geometrical designs<sup>8,43</sup> to create our mechanical metamaterials. The specimens were fabricated based on three types of unit cells with negative ( $\theta = 60^\circ$ ), near-zero ( $\theta = 90^\circ$ ), and positive ( $\theta = 120^\circ$ ) values of the Poisson's ratio (Figure 1a). The dimensions of the unit cells ( $w, c$ ) and the overall dimensions of the structures ( $W, C$ ) were kept constant in all designs. The angle ( $\theta$ ) changed the height ( $h$ ) and length ( $l$ ) of the unit cells. Similar in-plane ( $t$ ) and out-of-plane ( $T$ ) thicknesses were considered for the unit cells with different angles. The design parameters are listed in Supplementary Table 1.

The geometry of each lattice structures was created in MATLAB (R2017b) and was then used as an input file for numerical simulations in a nonlinear finite element solver (Abaqus Standard 6. 14). We used the linear Timoshenko beam elements



(B21) with a rectangular cross-section because these elements can capture axial deformations, bending, and shear. We assumed a plane stress condition in our computational models. The constitutive behavior of the soft phase was described using a hyperelastic material model (Neo-Hookean,  $C_{10} = 0.106$  MPa,  $D_1 = 0.03$  MPa<sup>-1</sup>). We also used a hyperelastic material model for the hard phase and adjusted the parameters of the model correspondingly. For example, for the hard phase with 100 times stiffer elastic properties the Neo-Hookean material parameters were adjusted assuming the following parameters:  $100 \times C_{10} = 10.6$  MPa,  $D_1/100 = 0.0003$  MPa<sup>-1</sup>.

The multi-material lattice structures were created by considering multiple levels of the elastic modulus of the hard phase,  $E_h$ , to that of the soft phase,  $E_s$  (*i.e.*,  $E_h/E_s = 10, 100, \text{ and } 1000$ ). To spatially distribute the hard phase in the lattice structures, we chose three levels of the ratio of the volume of the hard phase (*i.e.*,  $\rho_h = 25\%, 50\%, \text{ and } 75\%$ ). A random process was then used to assign the hard phase to randomly select struts of the unit cells constituting the lattice structures. First, a vector containing the random permutation of numbers from 1 to the total number of struts of the structure was generated. Then, a percentage of the first elements of the vector, equaling  $\rho_h$ , were selected. The selected elements specified to which struts the hard phase was to be assigned.

For the special case of  $E_h/E_s = 10^3$ , we extended our simulations by considering a wider range of  $\rho_h$  values (*i.e.*,  $\rho_h = 1\%, 5\%, 25\%, 50\%, 75\%, 90\%, 95\%, \text{ and } 99\%$ ). We also performed further numerical simulations for  $E_h/E_s$  values of  $10^4, 10^5, \text{ and } 10^6$ , while keeping  $\rho_h$  constant at 50%. For every above-mentioned combination of the design parameters, we performed 1000 simulations, resulting in a total of 51000 simulations. This means that, for each batch of 1000 simulations, the geometry,  $\rho_h$  and  $E_h/E_s$  were kept constant among the specimens while the distribution of the hard phase within the structure was modified.

## 3.2. Materials and methods

A uniaxial displacement-controlled stretch test in the direction 2 (Figure 1a) was simulated in all models. Two reference points were defined on the right and left sides of the lattice structure, which were kinematically coupled with the corresponding nodes of the structure (Supplementary Figure 3). A displacement boundary condition (corresponding to 10% strain) was applied to one reference point, while constraining all the degrees of freedom of the other reference point (Supplementary Figure 3).

The normal stress,  $\sigma = F/A$ , was defined as the ratio of the reaction force,  $F$ , to the initial cross-section area,  $A = W \times T$ . The longitudinal strain,  $\varepsilon_{22} = \frac{\delta W}{W}$ , was calculated as the ratio of the displacement along the direction 2,  $\delta W$ , to the initial length of the structure in that direction,  $W$ . The elastic modulus,  $E$ , was computed as the instantaneous slope of the stress-strain curve. The Poisson's ratio was calculated as  $\nu = -\frac{\varepsilon_{11}}{\varepsilon_{22}}$ , where  $\varepsilon_{11}$  is the lateral strain measured by the average of the displacements taking place in the direction 1 ( $U_{i1}$ ) with respect to the transverse length of the structure ( $C$ ) (i.e.,  $\varepsilon_{11} = \frac{\sum_{i=1}^n U_{i1}}{C}$ , where  $n$  is the total number of nodes at the lateral side of the structure along the direction 1).

The degree of non-affinity was defined as  $\Gamma = \frac{1}{\varepsilon_{22}^2 N} \sum_{i=1}^N (u_i^{non-affine} - u_i^{affine})^2$  where  $N$  is the total number of nodes in the structure,  $u_i^{non-affine}$  is the local displacement of the  $i$ th node of the multi-material structure, and  $u_i^{affine}$  is the corresponding displacement of the  $i$ th node of a corresponding single-material lattice structure (Figure 1d). The elastic modulus of that single material was determined as the rule-of-mixture combination of the elastic moduli of the phases constituting the corresponding multi-material lattice structure (i.e.,  $E' = \frac{\rho_h \times E_h + \rho_s \times E_s}{\rho_h + \rho_s}$ ).

### 3.2.2. Fabrication and experimental testing

For our experimental study, we selected three representative cases for each angle of the unit cells. We manually segmented their geometry in Solidworks to

create different hard and soft phases, which were later converted into STL (standard tessellation language) files. The STL files were then inputted into a multi-material 3D printer (Object500 Connex3, Stratasys), which works on the basis of material jetting (the Polyjet technology) and were directly 3D printed using commercially available materials, namely VeroCyan (hard phase, RGD841, shore hardness (D) = 83–86) and Agilus30 Black (soft phase, FLX985, shore hardness (A) = 30–35) (Figure 1c). The Young's modulus of the hard and soft phases were respectively  $726.36 \pm 59.77$  MPa and  $0.60 \pm 0.05$  MPa<sup>44,45</sup>. The selection of the materials was made to achieve  $E_h/E_s \approx 1000$  (see Figure 1 and Supplementary Table 2).

To attach the specimens to the mechanical testing machine, a gripping system and pins were designed and additively manufactured using a fused deposition modeling (FDM) 3D printer (Ultimaker 2+, Geldermalsen, The Netherlands) from polylactic acid (PLA) filaments (MakerPoint PLA 750 gr Natural). Monotonic uniaxial tensile tests were performed under displacement control (stroke rate = 2 mm/min) using a LLOYD instrument (LR5K, load cell = 100 N) mechanical testbench. The time, force, and displacement were recorded at a sampling rate of 20 Hz. The stress and strain were obtained correspondingly by dividing the force to the initial cross-section area and dividing the displacement to the initial free length of the specimens. The stiffness of the structure was measured from the stiffest slope of the stress-strain curve. Using a digital camera, the deformations of the specimens were captured, which were then used to calculate the Poisson's ratio. We manually positioned a couple of points at the borders of the specimens in the digital images. We manually positioned 20 points around the periphery of the specimens captured in the digital images. We developed a MATLAB code to trace the movement of individual points in those images. The Poisson's ratio was calculated based on the changes in the coordinates of those points during the deformation. We repeated the mechanical tests for each specimen three times.

## 3.3. Results and discussion

A wide range of the elastic moduli (*i.e.*, 0.1 – 10 MPa) and Poisson's ratios (*i.e.*, –1.6 to 1.4) could be obtained using the multi-material design approach, followed in the current study (Figure 1b). The duos of the elastic modulus and Poisson's ratio (at 1% strain) corresponding to the auxetic (*i.e.*,  $\theta = 60^\circ$ ) and honeycomb (*i.e.*,  $\theta = 120^\circ$ ) structures approached the values resulting from the orthogonal unit cells (*i.e.*,  $\theta = 90^\circ$ ) as  $\rho_h$  increased (Figure 1b). A similar trend was observed for the higher values of the applied strain (*i.e.*, 10%) (Figure 1b).

The deformation patterns and the elastic properties predicted using our numerical simulations agreed with the experimentally observed deformation patterns and experimentally determined values of the elastic modulus and Poisson's ratio (Figure 1c, and Supplementary Table 2). The small differences between the numerical and experimental results could be due to the imperfections induced during the manufacturing process as well as the pre-stretching of the soft ligaments when attaching the specimens to the clamps. We also performed a mesh sensitivity analysis for the models shown in Figure 1c. Each strut in our reference computational models consisted of one element. For the mesh sensitivity analysis, we doubled the number of elements per strut. Then, we compared the values of elastic modulus and Poisson's ratio obtained from the models with finer mesh and reference models. That comparison resulted in less than 3% difference. We also used higher-order 2D elements (B22) in our computational models. That resulted in less than 4% difference in the values of the elastic modulus and Poisson's ratios, as compared to our reference model. A number of unit cells showed very clear non-affine deformations, as compared to geometrically identical lattice structures made from a single material (Figure 1c, right side). Similar non-affine deformations were observed in our experiments and captured by our simulations (Figure 1c-d).

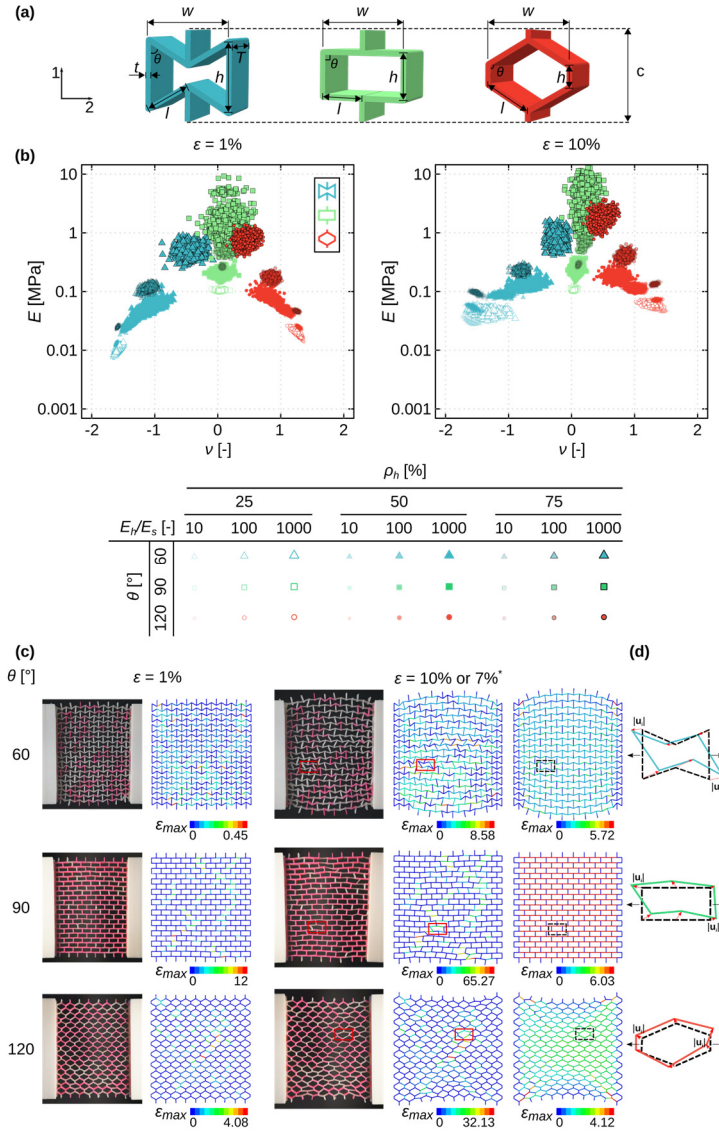


**Figure 1.** The three types of unit cells used in this study (a). The duos of the elastic modulus and Poisson's ratio calculated from the numerical simulations at two levels of the applied strain (*i.e.*, 1% and 10%) (b). The multi-material 3D printed specimens were mechanically tested under tensile loading and were compared with the finite element simulations (c). The quantitative data pertaining to this comparison are presented in Supplementary Table 2. For the specimen with  $\theta = 60^\circ$ , the applied strain was 10%, while it was 7% for the specimens with  $\theta = 90^\circ, 120^\circ$ . The insets in subfigure (c) show the maximum strain distribution. Subfigure (d) shows the deformation of a homogenous lattice with an elastic modulus equal to the rule-of-mixture combination of the elastic moduli of the hard and soft phases.  $|u_i|$  in (d) stands for the difference between the deformation of the  $i^{\text{th}}$  node of a homogeneous lattice structure and the deformation of the exact same node in a multi-material specimen.

### 3.3. Results and discussion

For the same values of  $\rho_h$  and  $E_h/E_s$ , the auxetic structures (*i.e.*,  $\theta = 60^\circ$ ) always showed the maximum mean values of  $\Gamma$ , which were up to several times higher than those corresponding to the honeycomb (*i.e.*,  $\theta = 120^\circ$ ) and orthogonal (*i.e.*,  $\theta = 90^\circ$ ) lattice structures (Figure 2a, Supplementary Table 3, and Supplementary Figure 1a). Except for the case where the hard phase was not much stiffer than the soft phase (*i.e.*,  $E_h/E_s = 10$ ), the honeycomb lattice structures exhibited a higher degree of non-affinity as compared to the orthogonal ones (Figure 2a, Supplementary Table 3 and Supplementary Figure 1a). There were significant overlaps between the range of the  $\Gamma$  values found for the lattice structures with different values of  $\rho_h$  (Figure 2b, Supplementary Table 4 and Supplementary Figure 1b). This observation suggests that the degree of non-affinity is more dependent on how the hard phase is distributed in the lattice than on the amount of the hard phase (Figure 2b, Supplementary Table 4 and Supplementary Figure 1b). Inspecting the deformations exhibited by the different types of the lattice structures clearly showed that those based on the re-entrant unit cell were more susceptible to the inhomogeneous deformations that result from the presence of high-stiffness struts (Figure 2c). This is expected given the fact that the deformation of the re-entrant unit cell is dominated by the high stresses concentrated around its sharp corners, whereas stresses are generally more homogeneously distributed in the honeycomb and particularly orthogonal unit cells where the stress gradients within one single unit cell are relatively low (see Supplementary Figure 4). Moreover, performing thousands of simulations with the random distribution of the hard phase within the lattice structure allows for determining the envelope within which the degree of non-affinity could change for a given value of  $\rho_h$ . Therefore, this envelope shows the possible range within which degree of non-affinity can change by the different spatial distribution of the hard phases in the lattices.

The degree of non-affinity initially increased with  $E_h/E_s$  regardless of the type of the unit cell until  $E_h/E_s = 10^4$  after which it saturated (Figure 3a-top). A hard phase with a higher stiffness value disrupts the stress flow to a greater extent than a

hard phase with a lower level of stiffness, which explains the initial increasing trend. For large enough values of  $E_h/E_s$ , however, the hard phase is so much stiffer than the soft phase so that it practically behaves as a rigid material. Therefore, a further increase in  $E_h$  does not noticeably affect the stress flow in the lattice structure and eventually, the degree of non-affinity saturates. In other words, up to a certain value of  $E_h/E_s$ , the deformation experienced by heterogeneous structures increasingly deviates from the one experienced by equivalent homogeneous structures.

The degree of non-affinity increased with  $\rho_h$  until a maximum value was reached for  $\rho_h = 75\% - 90\%$  (Figure 3b-top). For the larger values of  $\rho_h$ , the degree of non-affinity is decreased such that it reaches  $\Gamma = 0$  for  $\rho_h = 100\%$  (*i.e.*, a monolithically hard material), (Figure 3b-top). The maximum value of  $\Gamma$  occurred around the same  $\rho_h$  value regardless of the type of the unit cell and the level of the applied strain (Figure 3b-top). The same general trends were also valid for the higher levels of applied strain (*e.g.*, 10%) (Figure 3b-bottom). The plot of  $\Gamma$  vs.  $\rho_h$  was, therefore, highly asymmetric in all cases considered here (Figure 3b). The initial increase in  $\Gamma$  as  $\rho_h$  increased is expected, given that a higher  $\rho_h$  value translates into a larger number of highly stiff struts that block the deformation of their surrounding low-stiffness struts. Moreover, the high stiffness struts can more effectively affect the stress flow in the lattice structures made from mostly low stiffness struts than the other way around. This explains the asymmetry in the plot of  $\Gamma$  vs.  $\rho_h$ .

### 3.3. Results and discussion

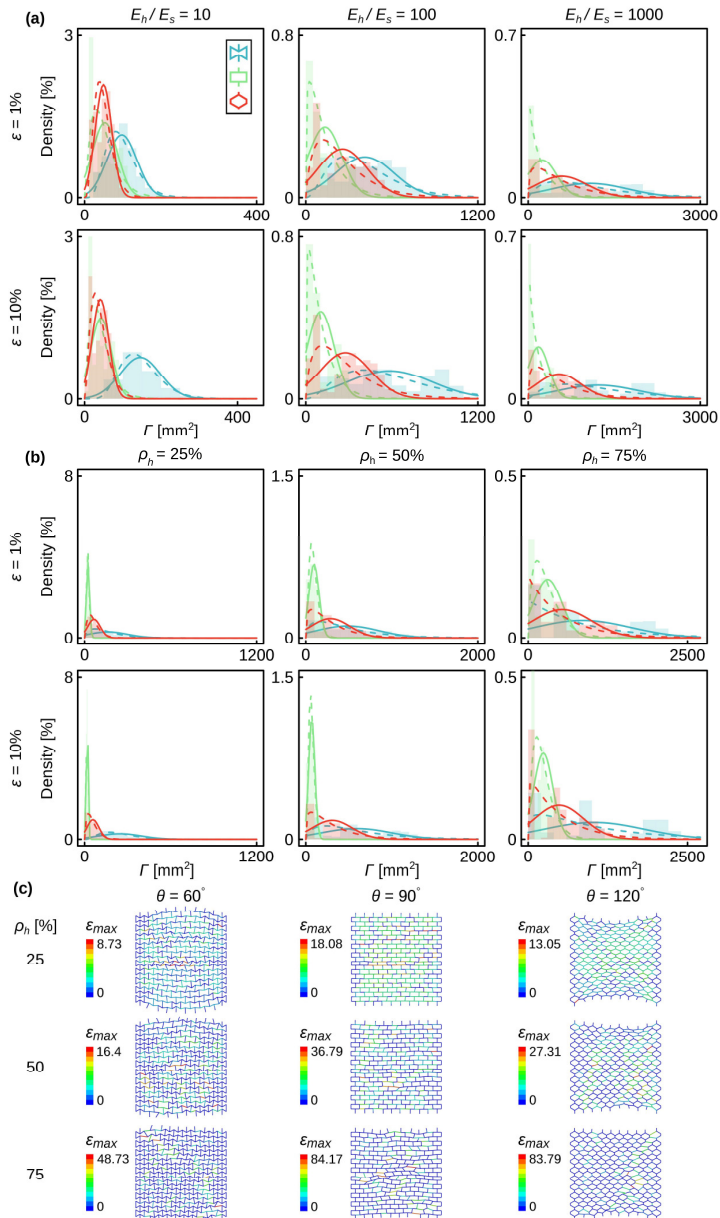


**Figure 2.** The Gaussian (solid lines) and gamma distributions (dashed lines) describing the change in the degree of non-affinity as functions of  $E_h/E_s$  with pooled data (*i.e.*,  $\rho_h = 25\%$ ,  $50\%$  and  $75\%$ ) (a) and  $\rho_h$  with pooled data ( $E_h/E_s = 10, 100$ , and  $1000$ ) (b). The parameters of these distributions are listed in Supplementary Table 3 and Supplementary Table 4. The degree of non-affinity for the representative cases shown in (c) is equal to the mean value of the corresponding group with  $E_h/E_s = 1000$  at  $10\%$  strain. The design parameters for each of the specimens presented in (c) are listed in Supplementary Table 5. The color bars in subfigure (c) show the maximum strain distribution.



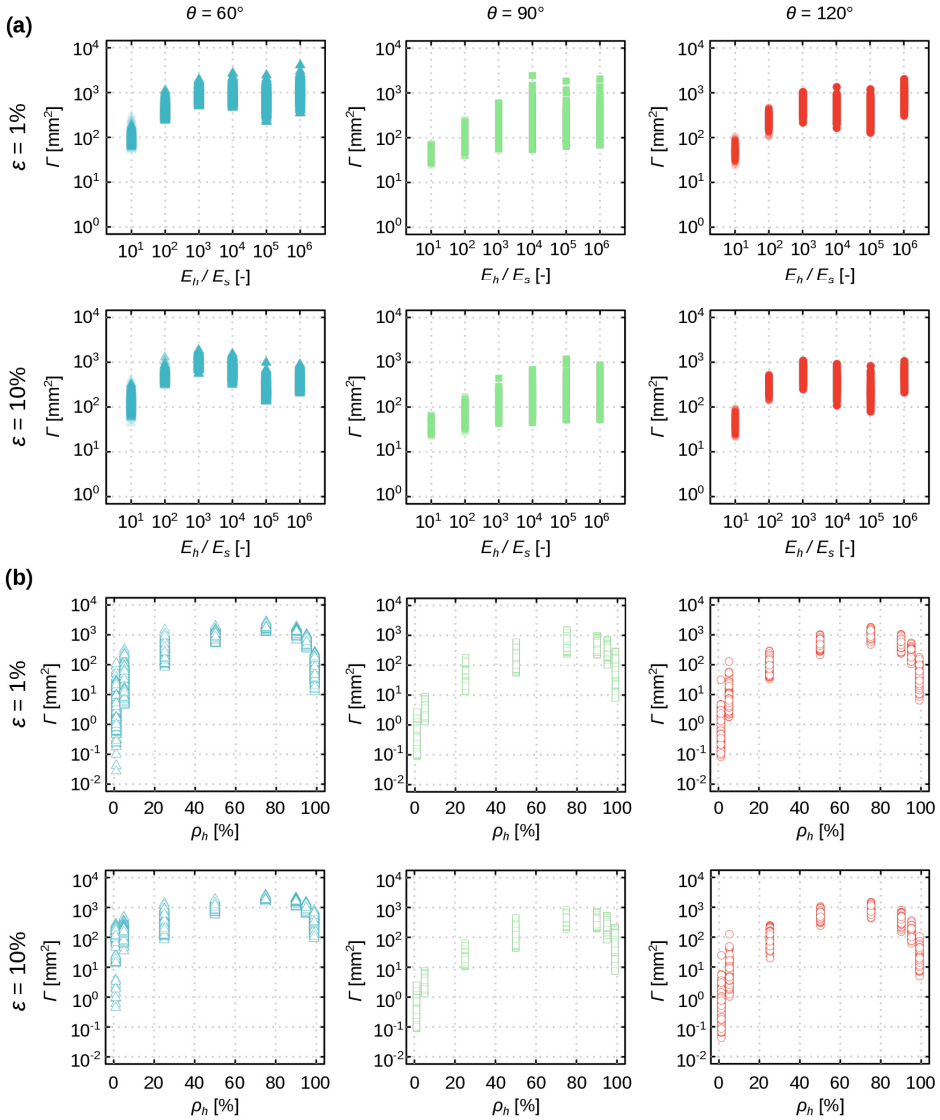


**Figure 3.** (a) The changes in the degree of non-affinity for different values of  $E_h/E_s$  and for the three different types of the unit cell geometries (*i.e.*,  $\theta = 60^\circ, 90^\circ, 120^\circ$ ) but the same value of  $\rho_h = 50\%$ . (b) The change in the degree of non-affinity for different hard volume fractions and for three types of unit cell geometries (*i.e.*,  $\theta = 60^\circ, 90^\circ, 120^\circ$  with  $E_h/E_s = 1000$ ).

For both auxetic and honeycomb unit cells, there was a very clear (power-law) relationship between the Poisson's ratio and the degree of non-affinity of the lattice structures (Supplementary Figure 2). In general, the degree of non-affinity was up to

### 3.3. Results and discussion

2 orders of magnitude lower for the lattice structures with the extreme absolute values of the Poisson's ratio (Figure 4a-left). This relationship was even stronger (*i.e.*, less scatter around the power-law trend line) for the higher levels of applied strain (Figure 4a-right, and Supplementary Figure 2). No such relationship was, however, observed for the lattice structures with near-zero Poisson's ratios (*i.e.*,  $\theta = 90^\circ$ ) (Figure 4a). These observations explain that achieving highly negative and highly positive values of the Poisson's ratio requires that all or most of the struts contribute towards the targeted type of deformation. A homogenous (*i.e.*, highly affine) distribution of the deformations among the different unit cells of the lattice structure is particularly efficient in achieving large lateral deformations that are needed for large absolute values of the Poisson's ratio. That is because similar deformations exhibited by all unit cells add up instead of (partially) canceling each other out (Figure 4c).

The relationship between the elastic modulus and the degree of non-affinity was less clear (Figure 4b). For each type of the unit cells, the degree of non-affinity was generally higher for the stiffer lattice structures (Figure 4b). This is, however, attributed to the fact that a higher value of  $\rho_h$  both increases the degree of non-affinity and the stiffness of the lattice structure.

In the present study, we excluded the geometrical and topological complexities that are relevant to the design of mechanical metamaterials. Those parameters have shown to influence the degree of non-affinity<sup>33</sup>. In addition, we used a limited number of unit cells (*i.e.*,  $10 \times 10$ ) to minimize the effects of boundary conditions on our computational models. We believe that increasing the number of unit cells will not change the trend of non-affinity that we found here. However, the effects of geometrical and topological parameters on non-affinity need to be further studied.

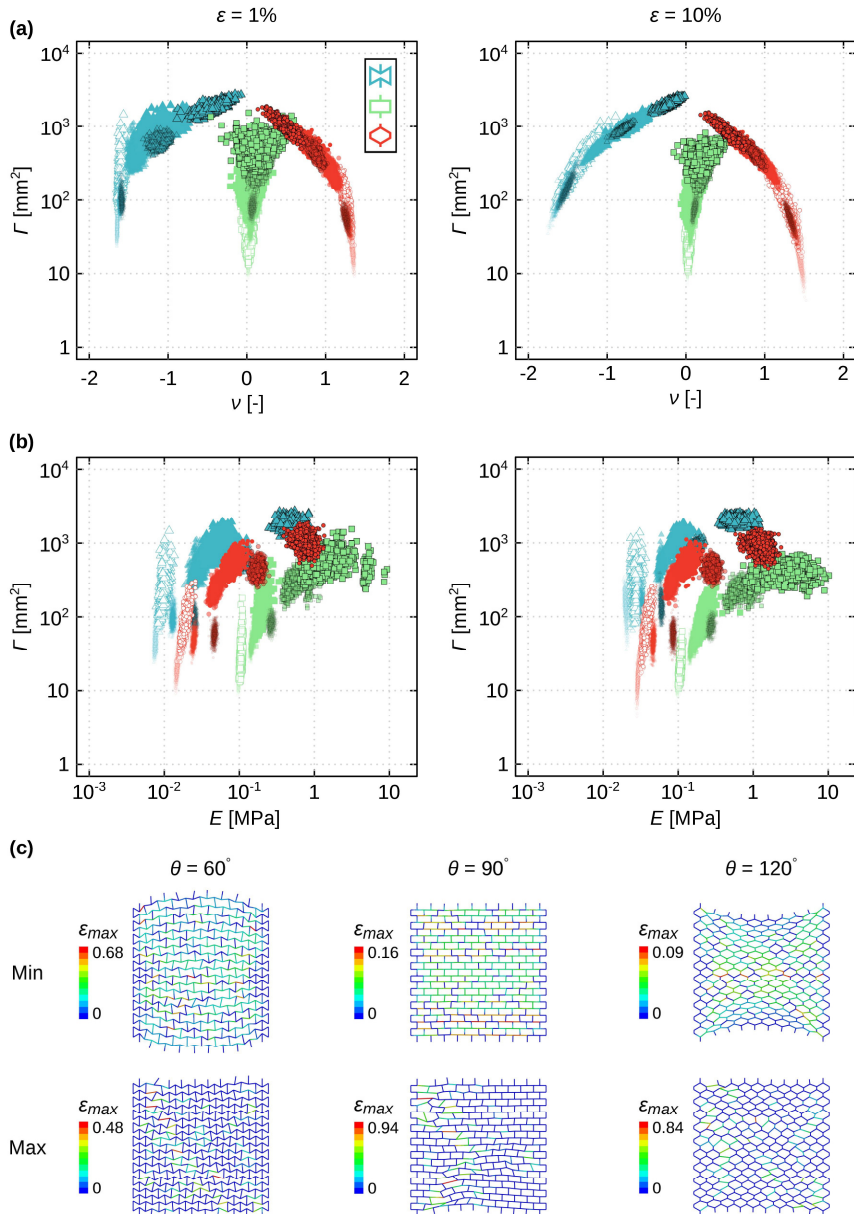


**Figure 4.** The changes in the degree of non-affinity as functions of the Poisson's ratio (a) and the elastic modulus (b) at two levels of the applied strain (1% and 10%). A selected number of cases are depicted in (c), representing the lattice structures with the minimum and maximum values of  $\Gamma$  with  $E_h/E_s = 1000$ . The design parameters for each of the specimens presented in (c) are listed in Supplementary Table 6. The color bars in subfigure (c) show the maximum strain distribution.

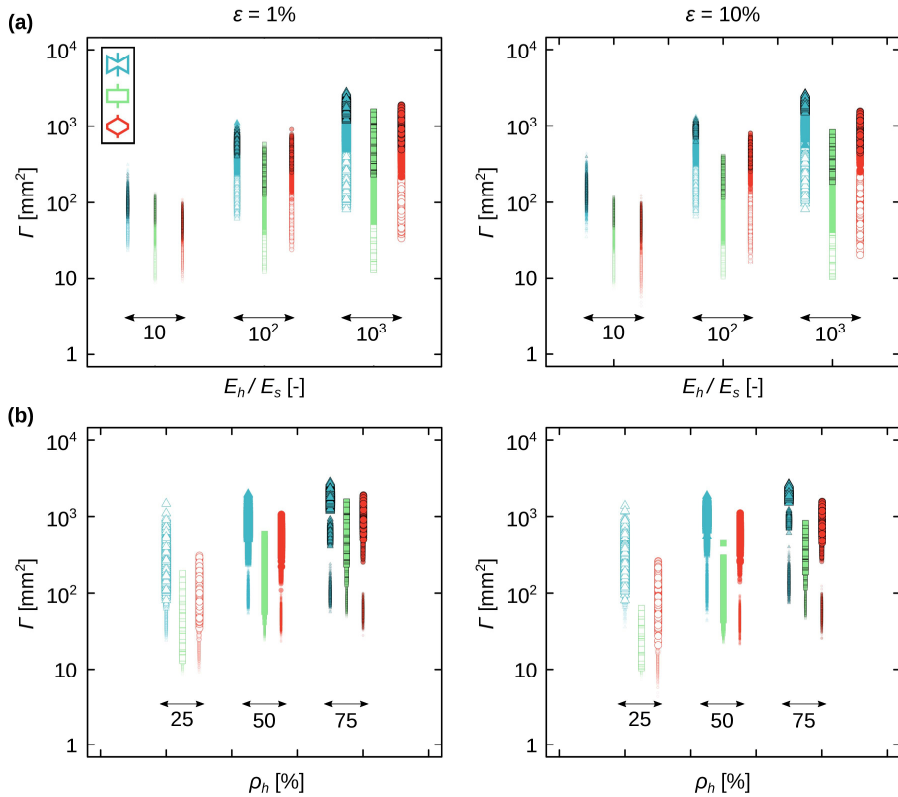
### 3.4. Conclusion

## 3.4. Conclusion

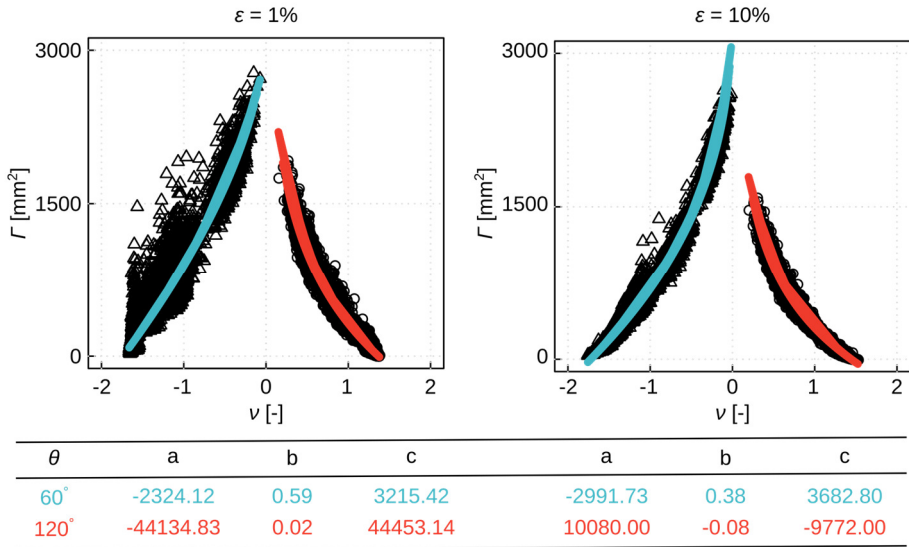
We studied here, for the first time in the area of extremal mechanical metamaterials, the non-affinity of the deformations experienced by multi-material mechanical metamaterials with random distributions of a hard phase within a lattice structure made of a soft material. We isolated the effects of multi-material design from those of geometry by comparing the deformation observed in our lattice structures with those of geometrically identical lattice structures that were made from one single material. Our results clearly show that a multi-material design approach could lead to both a wide range of elastic properties, and a wide range of non-affine deformations. We found that the degree of non-affinity is strongly correlated with the design parameters including  $\theta$ ,  $\rho_h$ , and  $E_h/E_s$ . In addition, the degree of non-affinity is highly correlated to the mechanical properties particularly the Poisson's ratio. Interestingly, achieving extremely high levels of auxeticity (or highly positive Poisson's ratios) seems to require highly affine deformations in multi-material mechanical metamaterials. On the other hand, achieving high values of the elastic modulus with multi-material mechanical metamaterials is associated with high levels of non-affine deformations. This is a new type of incompatibility between the very high values of the elastic modulus and very high absolute values of the Poisson's ratio. It is important to realize that this incompatibility is different from the other types of such incompatibilities observed in the past (*e.g.*, see<sup>46</sup>), as this incompatibility pertains to the spatial distribution of the mechanical properties within the lattice structure but not to the geometrical design of the unit cells (*i.e.*, bending-dominated *vs.* stretch-dominated unit cells). The high levels of non-affinity observed here for multi-material mechanical metamaterials are expected to have clear implications for the structural integrity of the lattice structures. That is due to the high level of stress concentrations that are created as a result of such non-affine deformations. The high-stress concentration zones could accelerate crack initiation and propagation and ultimately lead to premature structural failure. The use of

functional gradients may, therefore, be required to mitigate the structural effects of non-affine deformations.

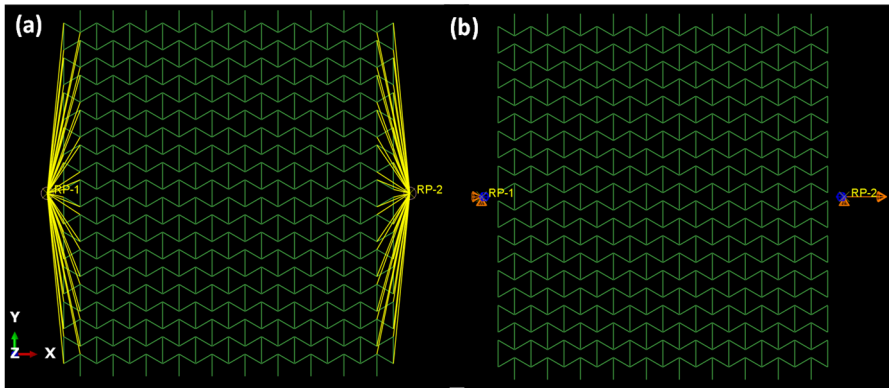
## 3.5. Supplementary document



**Supplementary Figure 1.** The changes in the degree of non-affinity with  $E_h/E_s$  (a) and the volume fraction of the hard material,  $\rho_h$ , (b) for the three different types of unit cell geometries and two levels of the applied strain (*i.e.*, 1% and 10%). Pooled data (*i.e.*,  $\rho_h = 25\%$ , 50% and 75%, and  $E_h/E_s = 10, 100$ , and 1000) are shown in this figure.

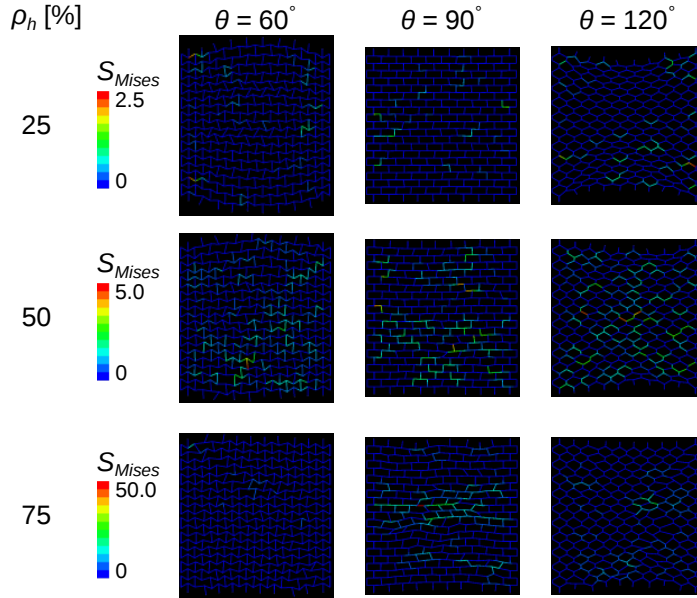


**Supplementary Figure 2.** Both for the auxetic and honeycomb types of the unit cells, the degree of non-affinity and the Poisson's ratio were related to each other through a power law (*i.e.*,  $\Gamma = av^b + c$ ). The parameters of the fits for both types of the geometries are presented as well. The pooled data (*i.e.*,  $\rho_h = 25\%$ ,  $50\%$  and  $75\%$ , and  $E_h/E_s = 10, 100$ , and  $1000$ ) are presented in this figure.



**Supplementary Figure 3.** A schematic of applied kinematic coupling constraints (a) and boundary conditions (b) in our computational models.

### 3.5. Supplementary document



**Supplementary Figure 4.** The distribution of the von-Mises stress in the selected designs presented in Figure 2c. The hard-soft stiffness ratio was set to 1000. The presented results correspond to an applied strain of 10%.

**Supplementary Table 1.** The design parameters of the lattice structures.

$\theta$ [°]	$W$ [mm]	$L$ [mm]	$w$ [mm]	$h$ [mm]	$l$ [mm]	$c$ [mm]	$t$ [mm]	$b$ [mm]
60	112.5	124.3	11.25	9.17	6.50	11.85	0.75	7.5
90	112.5	124.3	11.25	5.92	5.63	11.85	0.75	7.5
120	112.5	124.3	11.25	2.67	6.50	11.85	0.75	7.5

**Supplementary Table 2.** A comparison between the experimentally measured (Exp) and computationally determined (FEA) values of the elastic properties (*i.e.*, elastic modulus and Poisson's ratio) with  $E_h/E_s = 1000$ . The data are reported at 1% strain.

$\theta$ [°]	$\rho_h$ [%]	$E_{Exp}$ [MPa]	$E_{FEA}$ [MPa]	$\nu_{Exp}$ [-]	$\nu_{FEA}$ [-]	$\Gamma$ [mm <sup>2</sup> ]
60	25	$0.03 \pm 0.002$	0.01	$-1.31 \pm 0.08$	-1.61	400.41
90	75	$0.77 \pm 0.13$	1.14	$0.01 \pm 0.06$	-0.06	402.36
120	50	$0.10 \pm 0.01$	0.09	$0.89 \pm 0.05$	0.99	395.00



**Supplementary Table 3.** The parameters of the Gaussian distributions (*i.e.*, mean and standard deviation (SD)) and the gamma distributions (*i.e.*, shape, rate, and skewness) of the non-affinity parameter,  $\Gamma$  [ $\text{mm}^2$ ] presented in Figure 2a and Supplementary Figure 1a. The pooled data (*i.e.*,  $\rho_h = 25\%$ ,  $50\%$  and  $75\%$ ) are presented in this table.

$\theta$ [ $^\circ$ ]	$E_h/E_s$	$\varepsilon$ [%] =1					$\varepsilon$ [%] =10				
		Mean	SD	Shape	Rate	Skewness	Mean	SD	Shape	Rate	Skewness
60	10	86.6	34.6	6.0	0.1	0.8	145.6	52.3	8.3	0.1	0.7
90	10	47.0	29.0	2.4	0.1	1.3	42.9	26.6	2.4	0.1	1.3
120	10	44.0	19.1	4.6	0.1	0.9	41.4	21.7	3.0	0.1	1.2
60	100	411.3	200.9	3.2	0.0	1.1	585.2	291.2	3.2	0.0	1.1
90	100	133.6	115.5	1.2	0.0	1.8	104.0	92.4	1.2	0.0	1.8
120	100	256.7	167.7	1.9	0.0	1.5	276.1	176.1	1.7	0.0	1.5
60	1000	1075.9	666.0	1.9	0.0	1.4	1218.7	693.7	2.2	0.0	1.4
90	1000	244.7	247.9	0.9	0.0	2.1	179.3	178.4	0.9	0.0	2.1
120	1000	586.8	443.0	1.3	0.0	1.7	534.2	376.6	1.3	0.0	1.7

**Supplementary Table 4.** The parameters of the Gaussian distributions (*i.e.*, mean and standard deviation (SD)) and the gamma distributions (*i.e.*, shape, rate, and skewness) of the non-affinity metric  $\Gamma$  [ $\text{mm}^2$ ] presented in Figure 2b and Supplementary Figure 1b. The pooled data ( $E_h/E_s = 10, 100,$  and  $1000$ ) are presented in this table.

$\theta$ [ $^\circ$ ]	$\rho_h$ [%]	$\varepsilon$ [%] =1					$\varepsilon$ [%] =10				
		Mean	SD	Shape	Rate	Skewness	Mean	SD	Shape	Rate	Skewness
60	25	162.9	135.8	1.8	0.0	1.5	247.1	148.0	3.4	0.0	1.1
90	25	24.0	10.8	6.7	0.3	0.8	18.8	5.8	11.7	0.6	0.6
120	25	65.3	43.7	2.2	0.0	1.3	58.3	41.6	1.8	0.0	1.5
60	50	485.9	363.8	1.5	0.0	1.6	590.5	406.6	1.6	0.0	1.6
90	50	95.3	58.6	3.2	0.0	1.1	69.5	35.7	4.6	0.1	0.9
120	50	286.0	225.3	1.3	0.0	1.7	306.5	230.1	1.3	0.0	1.8
60	75	853.0	745.8	1.0	0.0	2.0	1034.1	774.7	1.2	0.0	1.8
90	75	306.1	220.7	1.8	0.0	1.5	237.8	151.1	2.3	0.0	1.3
120	75	533.6	458.8	1.0	0.0	2.0	485.1	383.7	1.1	0.0	1.9

### 3.5. Supplementary document

**Supplementary Table 5.** The specifications of the sample finite element models depicted in Figure 2c. The hard-soft stiffness ratio (*i.e.*,  $E_h/E_s$ ) was 1000.

$\theta$ [°]	$\rho_h$ [%]	$\Gamma$ [mm <sup>2</sup> ]	$\nu$ [-]	$E$ [MPa]
60	25	345.57	-1.31	0.03
	50	1087.50	-0.75	0.08
	75	2014.10	-0.31	0.47
90	25	22.30	0.03	0.11
	50	102.49	0.06	0.20
	75	412.77	0.28	2.57
120	25	94.60	1.24	0.04
	50	575.24	0.75	0.12
	75	954.31	0.51	1.10

**Supplementary Table 6.** The specifications of the sample finite element models depicted in Figure 4c. The hard-soft stiffness ratio (*i.e.*,  $E_h/E_s$ ) was 1000.

$\theta$ [°]	$\rho_h$ [%]	$\Gamma$ [mm <sup>2</sup> ]	$\nu$ [-]	$E$ [MPa]
60	25	81.24	-1.65	0.03
	75	2639.14	-0.11	0.67
90	25	10.52	0.04	0.10
	75	816.69	0.25	1.83
120	25	21.24	1.44	0.04
	75	1596.61	0.30	1.11

## References

1. Truesdell, C. & Noll, W. The non-linear field theories of mechanics. *Non-Linear F. Theor. Mech.* 1–579 (2004).
2. Wu, H. C. Continuum mechanics and plasticity. *Contin. Mech. Plast.* 1–685 (2004).
3. Schaedler, T. A. & Carter, W. B. Architected cellular materials. *Annu. Rev. Mater. Res.* **46**, 187–210 (2016).
4. Barchiesi, E., Spagnuolo, M. & Placidi, L. Mechanical metamaterials: a state of the art. *Math. Mech. Solids* **24**, 212–234 (2019).
5. Yu, X., Zhou, J., Liang, H., Jiang, Z. & Wu, L. Mechanical metamaterials associated with stiffness, rigidity and compressibility: a brief review. *Prog. Mater. Sci.* **94**, 114–173 (2018).
6. A. Zadpoor, A. Mechanical meta-materials. *Mater. Horizons* **3**, 371–381 (2016).
7. Van Hecke, M. Jamming of soft particles: geometry, mechanics, scaling and isotaticity. *J. Phys. Condens. Matter* **22**, 033101 (2009).
8. Lakes, R. Negative Poisson’s ratio materials: response. *Sci.* **238**, 551 (1987).
9. Lakes, R. S., Lee, T., Bersie, A. & Wang, Y. C. Extreme damping in composite materials with negative-stiffness inclusions. *Nat.* **410**, 565–567 (2001).
10. Hedayati, R., Mirzaali, M. J., Vergani, L. & Zadpoor, A. A. Action-at-a-distance metamaterials: distributed local actuation through far-field global forces. *APL Mater.* **6**, 36101 (2018).
11. Mirzaali, M. J. *et al.* Rational design of soft mechanical metamaterials: Independent tailoring of elastic properties with randomness. *Appl. Phys. Lett.* **111**, 51903 (2017).
12. Bertoldi, K., Vitelli, V., Christensen, J. & Van Hecke, M. Flexible mechanical metamaterials. *Nat. Rev. Mater.* **2**, (2017).
13. Mirzaali, M. J., Janbaz, S., Strano, M., Vergani, L. & Zadpoor, A. A. Shape-matching soft mechanical metamaterials. *Sci. Rep.* **8**, 1–7 (2018).
14. DiDonna, B. A. & Lubensky, T. C. Nonaffine correlations in random elastic media. *Phys. Rev. E* **72**, 66619 (2005).
15. Hatami-Marbini, H. & Picu, R. C. Effect of fiber orientation on the non-affine deformation of random fiber networks. *Acta Mech.* **205**, 77–84 (2009).

## References

16. Mirzaali, M. J., Pahlavani, H. & Zadpoor, A. A. Auxeticity and stiffness of random networks: lessons for the rational design of 3D printed mechanical metamaterials. *Appl. Phys. Lett.* **115**, 021901 (2019).
17. Wilhelm, J. & Frey, E. Elasticity of stiff polymer networks. *Phys. Rev. Lett.* **91**, 108103 (2003).
18. Burkel, B., Proestaki, M., Tyznik, S. & Notbohm, J. Heterogeneity and nonaffinity of cell-induced matrix displacements. *Phys. Rev. E* **98**, 52410 (2018).
19. Hatami-Marbini, H. Simulation of the mechanical behavior of random fiber networks with different microstructure. *Eur. Phys. J. E* **41**, 65 (2018).
20. Head, D. A., Levine, A. J. & MacKintosh, F. C. Deformation of cross-linked semiflexible polymer networks. *Phys. Rev. Lett.* **91**, 108102 (2003).
21. Head, D. A., Levine, A. J. & MacKintosh, F. C. Distinct regimes of elastic response and deformation modes of cross-linked cytoskeletal and semiflexible polymer networks. *Phys. Rev. E* **68**, 61907 (2003).
22. Janmey, P. A. Mechanical properties of cytoskeletal polymers. *Curr. Opin. Cell Biol.* **3**, 4–11 (1991).
23. Basu, A. *et al.* Nonaffine displacements in flexible polymer networks. *Macromolecules* **44**, 1671–1679 (2011).
24. Wen, Q., Basu, A., Janmey, P. A. & Yodh, A. G. Non-affine deformations in polymer hydrogels. *Soft Matter* **8**, 8039–8049 (2012).
25. Hatami-Marbini, H. Nonaffine behavior of three-dimensional semiflexible polymer networks. *Phys. Rev. E* **93**, 1–7 (2016).
26. Shaofan Li, B. S. Advances in soft matter mechanics. (2012).
27. Heussinger, C. & Frey, E. Floppy modes and nonaffine deformations in random fiber networks. *Phys. Rev. Lett.* **97**, 1–4 (2006).
28. Coulais, C., Kettenis, C. & van Hecke, M. A characteristic length scale causes anomalous size effects and boundary programmability in mechanical metamaterials. *Nat. Phys.* **14**, 40 (2018).
29. Hatami-Marbini, H. & Shriyan, V. Topology effects on nonaffine behavior of semiflexible fiber networks. *Phys. Rev. E* **96**, 62502 (2017).
30. Mathesan, S., Tripathy, M., Srivastava, A. & Ghosh, P. Non-affine deformation of free volume during strain dependent diffusion in polymer thin films. *Polymer (Guildf)*. **155**, 177–186 (2018).

31. Broedersz, C. P., Sheinman, M. & MacKintosh, F. C. Filament-length-controlled elasticity in 3D fiber networks. *Phys. Rev. Lett.* **108**, 78102 (2012).
32. Liu, J., Nie, Y., Tong, H. & Xu, N. Realizing negative Poisson's ratio in unstressed spring networks. Preprint at arXiv1810.10768 (2018).
33. Cioroianu, A. R., Spiesz, E. M. & Storm, C. Disorder, pre-stress and non-affinity in polymer 8-chain models. *J. Mech. Phys. Solids* **89**, 110–125 (2016).
34. Falk, M. L. & Langer, J. S. Dynamics of viscoplastic deformation in amorphous solids. *Phys. Rev. E* **57**, 7192 (1998).
35. Huisman, E. M., Storm, C. & Barkema, G. T. Monte Carlo study of multiply crosslinked semiflexible polymer networks. *Phys. Rev. E* **78**, 51801 (2008).
36. Iyer, S. S., Tripathy, M. & Srivastava, A. Fluid phase coexistence in biological membrane: insights from local nonaffine deformation of lipids. *Biophys. J.* **115**, 117–128 (2018).
37. Janbaz, S., Bobbert, F. S. L., Mirzaali, M. J. & Zadpoor, A. A. Ultra-programmable buckling-driven soft cellular mechanisms. *Mater. Horizons* **6** (2019).
38. Leonforte, F., Tanguy, A., Wittmer, J. P. & Barrat, J.-L. Continuum limit of amorphous elastic bodies II: linear response to a point source force. *Phys. Rev. B* **70**, 14203 (2004).
39. Van Doorn, J. M., Lageschaar, L., Sprakel, J. & van der Gucht, J. Criticality and mechanical enhancement in composite fiber networks. *Phys. Rev. E* **95**, 42503 (2017).
40. Janbaz, S., McGuinness, M. & Zadpoor, A. A. Multimaterial control of instability in soft mechanical metamaterials. *Phys. Rev. Appl.* **9**, 64013 (2018).
41. Mirzaali, M. J. *et al.* Multi-material 3D printed mechanical metamaterials: rational design of elastic properties through spatial distribution of hard and soft phases. *Appl. Phys. Lett.* **113**, (2018).
42. Mirzaali, M. J. *et al.* Length-scale dependency of biomimetic hard-soft composites. *Sci. Rep.* **8**, 12052 (2018).
43. Gibson, L. J., Ashby, M. F. & Harley, B. A. Cellular materials in nature and medicine. (Cambridge University Express, 2010).
44. Mirzaali, M. J. *et al.* Multi-material 3D printing of functionally graded hierarchical soft–hard composites. *Adv. Eng. Mater.* **22**, (2020).
45. Mirzaali, M. J. *et al.* Mechanics of bioinspired functionally graded soft-hard

## References

- composites made by multi-material 3D printing. *Compos. Struct.* **237**, (2020).
46. Mitschke, H. *et al.* Geometry: The leading parameter for the Poisson's ratio of bending-dominated cellular solids. *Int. J. Solids Struct.* **100**, 1–10 (2016).



# 4

## Auxeticity and stiffness of random networks

Published as:

Mirzaali, M. J., Pahlavani, H., & Zadpoor, A. A. Auxeticity and stiffness of random networks: Lessons for the rational design of 3D printed mechanical metamaterials. *Applied Physics Letters* 115, 021901 (2019).



## Abstract

The emergence of advanced 3D printing techniques and the recent interest in architected materials have sparked a surge of interest in mechanical metamaterials whose unusual properties are defined by their highly ordered micro-architectures. Mechanical metamaterials with disordered micro-architectures have, however, not received as much attention despite their inherent advantages, such as robustness against the precise arrangement and design parameters of individual unit cells. Here, we computationally studied the elastic properties of two general types of disordered networks, namely lattice-restricted and unrestricted networks that were made of beam-like elements and possessed mean connectivity values,  $Z$ , ranging between 2.5 and 7. We also additively manufactured a number of representative networks using selective laser sintering and showed that their deformations are consistent with our computational predictions. Unrestricted networks exhibited several advantages over the lattice-restricted ones including a broader range of achievable elastic modulus-Poisson's ratio duos as well as a higher probability of exhibiting auxetic and double-auxetic (*i.e.*, auxetic behavior in both orthogonal directions) behaviors. Most interestingly, we could find unrestricted auxetic networks for high connectivity levels of up to 4.5, while no lattice-restricted auxetic networks were found for any connectivity level beyond 3.5. Given the fact that, according to the Maxwell's criterion, 3.5 is the highest  $Z$  for which both of our lattice-restricted and unrestricted networks are bending-dominated, we concluded that unrestricted networks exhibit auxetic behavior well into their stretch-dominated domain. This is a promising observation that underlines the potential of unrestricted networks for the challenging task of designing stiff auxetic metamaterials in the stretch-dominated domain (*i.e.*,  $Z = 4 - 4.5$ ).

### 4.1. Introduction

Mechanical metamaterials are often composed of repeating unit cells that are rationally arranged in a highly ordered manner. The local and/or global interactions of these unit cells define the anomalous properties of metamaterials at the macroscale<sup>1-3</sup>. Such building blocks of engineered cellular metamaterials are often made of beam-like structural elements, and, depending on their level of connectivity, may be stretch-dominated, bending-dominated, or a mixture of both<sup>4,5</sup>. The proper positioning of stretch- or bending-dominated unit cells can create heterogeneous stress and strain distributions in these structures with asymmetric deformations that can eventually lead to novel properties<sup>6</sup>. Therefore, devising the geometrical and topological design of these unit cells is essential in developing metamaterials with advanced functionalities and properties.

In addition to the regular arrangement of unit cells in space, the geometry of cellular metamaterials can be created using random processes. Nature uses irregular micro-architectures such as disordered networks in the design of architected materials, such as trabecular bone and wood<sup>7-9</sup>, polymer gels<sup>10,11</sup>, protein networks<sup>12</sup>, cytoskeletal structures<sup>13</sup>, and collagenous extracellular matrix<sup>14,15</sup>. The advantage of such random tessellation is that a wide range of possible properties can be created without any need for precise and centralized control over the micro-architecture. This allows for spatial and temporal changes in properties, as a living organism may require high levels of such variations to fulfill its functions. Moreover, unlike mechanical metamaterials with regular unit cells, the mechanical properties of disordered mechanical metamaterials are less sensitive to the precise arrangement of the individual building blocks and their geometric cell parameters<sup>2,16-19</sup>. Random networks can be also tuned or created so as to achieve specific properties. Examples of such tunings include the pruning of random networks to achieve auxetic behavior<sup>20</sup>, controlling brittle-ductile transitions<sup>21</sup>, and controlling the mechanical properties of random metamaterials<sup>16,22</sup>.

Random networks also have potential applications in the design of porous (bio)materials<sup>23,24</sup>. One of the critical aspects in the design of such materials is independent tailoring of the elastic properties (*e.g.*, the elastic modulus and Poisson's ratio)<sup>18</sup> through a random or disordered arrangement of beam-like elements. Here, we studied the elastic properties of mechanical metamaterials based on random networks through a computational study of half a million arrangements as well as experiments on 3D printed models of a number of selected designs. Our networks covered a wide range of connectivity values,  $Z$ , ranging between 2.5 and 7.

## 4.2. Materials and methods

Two types of networks were considered, namely lattice-restricted and unrestricted. In the case of lattice-restricted structures, the nodal points of the beam-like elements were restricted to a pre-determined square lattice, while the nodes of unrestricted networks were randomly picked within box-restricted limits (Figure 1). The geometrical parameters of each type of network are presented in Figure 1a-b and Supplementary Table 1. The total size of the networks ( $W, L$ ) and the total number of nodes ( $n = 21 \times 21$ ) were the same for both types of structures. In both cases, the nodes could be randomly connected to their adjacent nodes, if their normal distances were below an upper limit (*i.e.*, 12 mm). The upper limit was chosen such that, in the case of lattice-restricted networks, diagonal connections were admissible.

The network connectivity was defined as the ratio of the sum of the connectivity of all nodes to the total number of the nodes in the structure. The minimum connectivity for each node was set to 2. Moreover, if the random positioning of the elements resulted in islands (*i.e.*, isolated or disconnected sub-structures), the corresponding designs were discarded. Ten levels of connectivity were considered between 2.5 and 7. The in-plane and out-of-plane thicknesses of both lattice-restricted and unrestricted networks were similar and were respectively 1 mm and 10 mm. Detailed information on the numerical simulations and statistical analyses are given in the supplementary document.

## 4.2. Materials and methods

### 4.2.1. Numerical simulations

The geometry of each network was created as an input file in MATLAB (R2017b), which was later imported into a finite element modeling software package (Abaqus 6.14) to perform computational modeling using a nonlinear implicit solver. In-plane beam elements (B21, Abaqus) based on the Timoshenko beam theory with a rectangular cross-section were used. This allowed us to take the effects of axial deformation, bending, and shear into account. A hyperelastic material model (Neo-Hookean,  $C_{10} = 0.106$  MPa,  $D_1 = 0.03$  MPa<sup>-1</sup>) was used for all simulations. The models, therefore, included both geometrical and material nonlinearities. For each level of connectivity, 10,000 finite element simulations were performed. The number of simulations was increased to 100,000 (per connectivity) in the case of unrestricted networks with low connectivity (*i.e.*,  $Z = 2.5, 3, \text{ and } 3.5$ ). In order to investigate the effects of the network size on the elastic properties, we simulated larger (*i.e.*, 300 mm × 300 mm) and smaller (*i.e.*, 75 mm × 75 mm) networks and compared their properties with the reference networks (*i.e.*, 150 mm × 150 mm) (Supplementary Table 1).

Moreover, the networks were loaded in both orthogonal directions (*i.e.*, 1 and 2) to investigate their anisotropic behavior. These two effects (*i.e.*, the size effect and anisotropy) were analyzed by running 1,000 additional simulations for both lattice-restricted and unrestricted networks ( $Z = 2.5, 3.5, 4.5, 5.5, \text{ and } 6.5$ ). Additional vertical (horizontal) elements were added to the upper and lower (left and right) sides of the networks to uniformly apply the loads (Figure 1 and Supplementary Figure 2). To simulate a tensile test, a displacement boundary condition equal to 10% longitudinal (transverse) strain was applied to a reference point. The reference point was kinematically coupled with the corresponding nodes of the networks. For example, to apply a displacement in the direction 2 (Figure 1), the displacement was applied to a reference point defined at the top of the network while a clamp boundary condition was applied to another reference point placed at the bottom of the network.

The stresses ( $\sigma_{11}, \sigma_{22}$ ) were defined as the ratio of the reaction force to the initial cross-section area. The strains ( $\varepsilon_{11}, \varepsilon_{22}$ ) were calculated as the ratio of the deformation to the free lengths of the networks in the lateral (longitudinal) directions. The elastic modulus ( $E_{11}, E_{22}$ ) of the networks was calculated as the slope of the stress-strain curve at 1% strain.

The Poisson's ratio in the direction 1 was calculated as  $\nu_{12} = -\frac{\varepsilon_{11}}{\varepsilon_{22}}$ , where  $\varepsilon_{11}$  is the strain at the direction of the applied load (*i.e.*, direction 1), while  $\varepsilon_{22}$  is the lateral strain calculated by summing up the deformations ( $U_{22}$ ) at every  $i^{\text{th}}$  node as  $\varepsilon_{22} = \frac{\sum_{i=1}^m U_{22,i}}{L}$ , and  $m$  = total number of side nodes along the direction 2. Likewise, the Poisson's ratio in the direction 2 was defined as  $\nu_{21} = -\frac{\varepsilon_{22}}{\varepsilon_{11}}$ , where  $\varepsilon_{22}$  is the strain along the loading direction (*i.e.*, direction 2) and  $\varepsilon_{11} = \frac{\sum_{i=1}^m U_{11,i}}{W}$ , where  $U_{11,i}$  is the deformation at the  $i^{\text{th}}$  node along the direction 1. The Poisson's ratios in both directions were measured at 1% longitudinal (transverse) strain.

### 4.2.2. Statistical analyses

We performed statistical analyses in R<sup>25</sup>. The `fitdistrplus` package<sup>26</sup> was used for fitting normal and gamma distributions to the simulation results and for calculating the corresponding statistical parameters of the fits. The statistical significance of the differences between various groups was analyzed using either parametric (*i.e.*, Student's t-test) or non-parametric (*i.e.*, Wilcoxon<sup>27</sup>) tests depending on the results of a Shapiro–Wilk normality test<sup>28</sup>. A  $p$ -value below 0.05 was assumed to indicate a statistically significant difference.

### 4.2.3. Fabrication and experimental testing

We also 3D printed 8 specimens of selected networks using selective laser sintering (SLS, EOS Formiga P100). We used commercially available materials (*i.e.*, Oceanz Flexible, PrimePart<sup>®</sup> ST PEBA 2301 from EOS GmbH) for fabrication of these specimens. To be able to attach the specimens to the testing machine, they

### 4.3. Results and discussion

included two additional parts that were designed and 3D printed together with the networks. The specimens were then attached to a mechanical testing machine via grippers and pins. The gripping systems and their pins were designed and additively manufactured using a fused deposition modeling (FDM) 3D printer (Ultimaker 2+, Geldermalsen, The Netherlands) from polylactic acid (PLA) (MakerPoint PLA 750 gr Natural). Displacement-controlled mechanical testing (stroke rate: 2 mm/min) was performed under tension using a LLOYD instrument (LR5K) machine equipped with a 100 N load cell. The deformations of the specimens at strain levels equivalent to those applied in the numerical models were captured using a digital camera.

### 4.3. Results and discussion

The distributions of the elastic modulus-Poisson's ratio duos exhibited similar trends for both lattice-restricted and unrestricted networks (Figure 1, Supplementary Figures 1 and 2). However, the variations in the elastic properties were much larger for the unrestricted networks as compared to the lattice-restricted networks (Figure 1a). Instead, lattice-restricted networks reached higher values of the elastic modulus as compared to unrestricted networks (Figure 1b). In both groups, the variations in the elastic properties were higher for the lower values of connectivity (Figure 1). Auxetic behavior could be only observed for the smaller values of connectivity (Figure 1). The maximum level of connectivity for which auxetic behavior could be observed was higher (*i.e.*,  $Z = 4.5$ , Figure 1b, and Figure 3d) for the unrestricted networks as compared to the lattice-restricted networks (*i.e.*,  $Z = 3.5$ , Figure 1a and Figure 3c). For both lattice-restricted and unrestricted networks, the deformation observed in the networks appeared to be highly non-affine with high levels of localized strain concentrations in certain regions of the network, while some other regions hardly deformed (Figure 1).

The Maxwell stability number,  $M$ ,<sup>5,29</sup> is defined as  $M = 2b - j + 3$ , where  $b$  and  $j$  are respectively the numbers of the struts and joints in a 2D frame. The Maxwell number can be used as a criterion to determine whether a network is stretch-

dominated (for  $M \geq 0$ ) or bending-dominated (for  $M < 0$ ). For each connectivity value, the Maxwell number was exactly the same for lattice-restricted and unrestricted networks (Supplementary Table 1). The maximum connectivity for which the networks were still bending-dominated was  $Z = 3.5$  (Supplementary Table 1). In the case of lattice-restricted networks, that  $Z$  value was coincident with the highest connectivity for which auxetic structures could be still found. In the case of unrestricted networks, however, auxetic structures could be found for networks with much higher connectivity values (*i.e.*, up to  $Z = 4.5$ ) and highly positive Maxwell numbers (Supplementary Table 1), indicating that they were stretch-dominated. Given that stretch-dominated networks exhibit higher stiffness values, this clearly shows the utility of unrestricted random networks for expanding the range of the elastic properties that could be achieved including stiffer auxetics.

### 4.3. Results and discussion

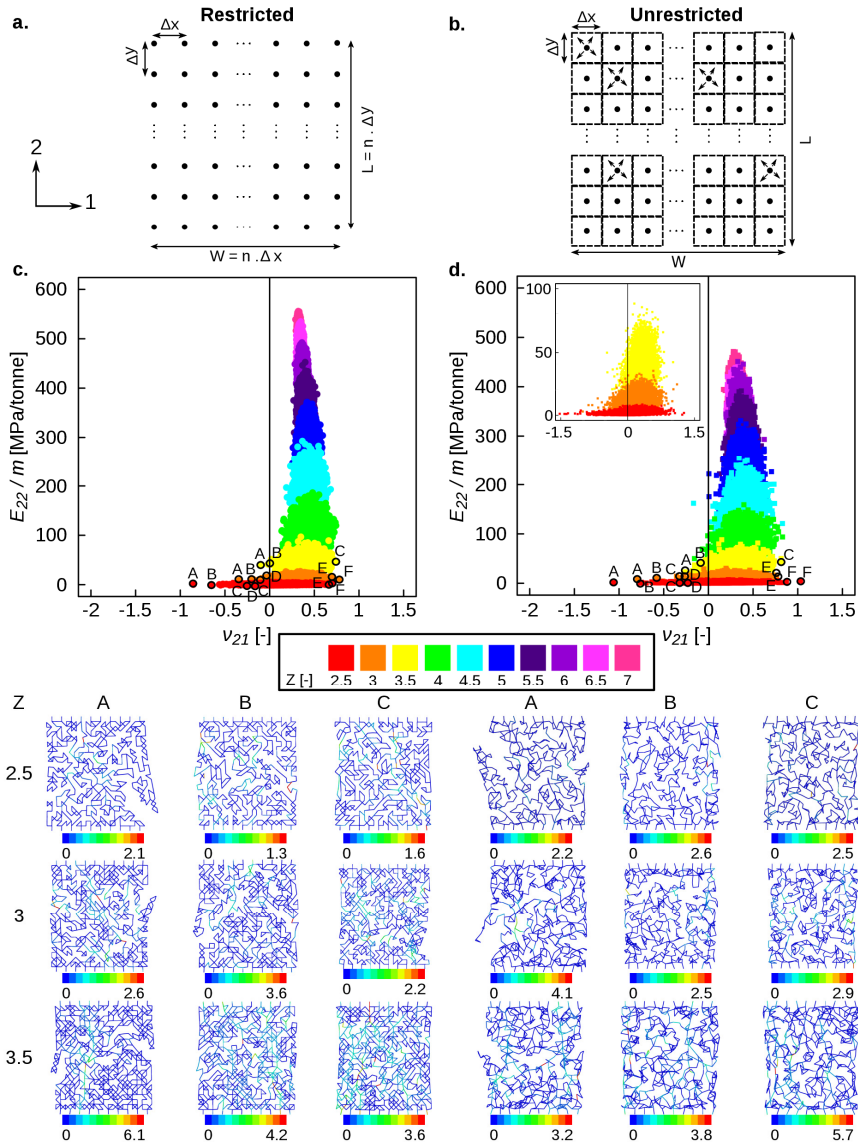


**Figure 1.** Schematic drawings of lattice-restricted (a) and unrestricted (b) networks. The placement of the nodes for lattice-restricted networks is pre-determined ( $\Delta x = \Delta y = 7.5$  mm,  $W = L = 150$  mm), while in the case of unrestricted networks nodes can be placed randomly within a box shown in (b). The elastic modulus-Poisson's ratio duos calculated for lattice-restricted (c) and unrestricted (d). The strain distributions below each graph (A-C) belong to some representative cases with low connectivity values (*i.e.*,  $Z = 2.5, 3$ , and  $3.5$ ). For each level of connectivity, 10,000 simulations were performed. In the case of unrestricted random networks, 100,000 simulations were performed for the lower connectivity values (*i.e.*,  $2.5, 3$ , and  $3.5$ ). These simulations are presented as an inset in sub-figure (d). More representative cases are presented in Supplementary Figures 1 and 2.



The level of anisotropy was highly dependent on the size of the networks (Figure 2 and Supplementary Table 2). In all cases, the level of anisotropy decreased as the size of the networks increased (Figure 2 and Supplementary Table 2). This is expected, given the random nature of the networks that increases the directional similarity for the larger sizes of networks. As far as the anisotropy of the stiffness values is concerned, the lattice-restricted and unrestricted networks showed different types of dependency on the connectivity value (Figure 2- left sub-figures). In the case of lattice-restricted networks, the maximum level of anisotropy in the stiffness values was observed for the intermediate values of connectivity (*i.e.*,  $Z = 4.5, 5.5$ ). In contrast, the level of anisotropy appeared to increase with connectivity in the case of unrestricted networks up to a certain point (*i.e.*,  $Z = 5.5$ ), after which it remained more or less constant (Figure 2). The change in the level of anisotropy was the opposite in the case of the Poisson's ratio: it decreased with connectivity both for lattice-restricted and unrestricted networks (Figure 2- right sub-figures). For all sizes of networks, the probability of finding auxetic networks was higher in the case of unrestricted networks as compared to lattice-restricted networks (Figure 2). Moreover, the probability of exhibiting an auxetic behavior was lower for the networks with larger sizes as compared to the smaller networks, as the Poisson's ratio in both directions converged to 0.33 for the largest networks (Figure 2, Supplementary Tables 2 and 3). The probability of finding networks with double-auxetic behavior (*i.e.*, auxetic behavior in both directions) was small (ranging between 0.4% and 1.62%) and decreased with the size of the networks (Figure 2- right sub-figures).

### 4.3. Results and discussion

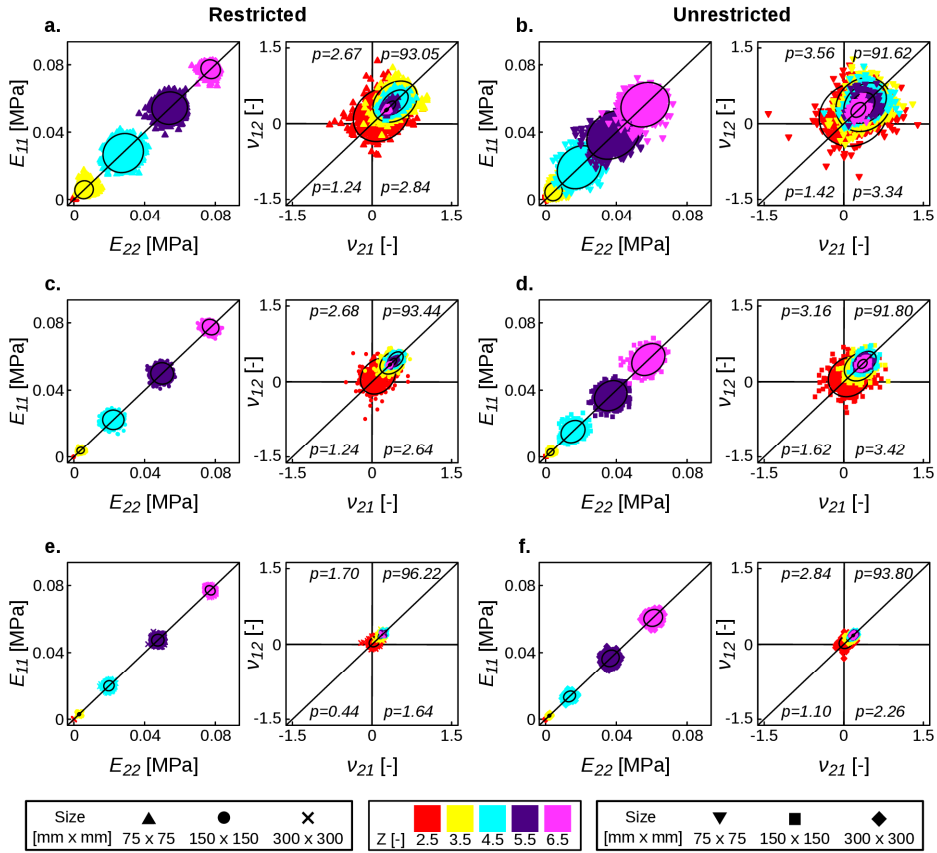


**Figure 2.** The effects of the network size on the (anisotropic) elastic properties of lattice-restricted and unrestricted networks. Three different sizes were considered for the simulations, namely 75 mm  $\times$  75 mm (lattice-restricted (a) and unrestricted (b)), 150 mm  $\times$  150 mm (lattice-restricted (c) and unrestricted (d)), and 300 mm  $\times$  300 mm (lattice-restricted (e) and unrestricted (f)). The anisotropic properties were tested in the directions 1 and 2. The numerical simulations were performed for networks with 5 different levels of connectivity (*i.e.*, 2.5, 3.5, 4.5, 5.5, and 6.5). The 95% confidence ellipses are added to each cluster of data. The principal radii of the confidence ellipses are listed in Supplementary Table 2.

As the connectivity increased, the mean value of the stiffness increased in both lattice-restricted and unrestricted networks (Figure 3- left sub-figures). The highest amount of variation in the stiffness values was observed for the intermediate values of connectivity (*i.e.*,  $Z = 4.5 - 5.5$ ) in the cases of both lattice-restricted and unrestricted networks (Figure 3- left sub-figures). The mean value of the Poisson's

ratio initially increased with connectivity until a maximum was reached at  $Z = 4.5$  for lattice-restricted networks (Supplementary Table 4) and at  $Z = 4.5 - 5.5$  for unrestricted networks (Supplementary Table 5). Further increase in connectivity reduced the Poisson's ratio with a mean converging to  $0.33 - 0.34$  for both lattice-restricted and unrestricted networks (Supplementary Tables 4 and 5). Comparing the Poisson's ratio of lattice-restricted and unrestricted networks showed that lattice-restricted structures converge faster than unrestricted networks (Supplementary Figure 3a-j, right sub-figures). The stiffness values exhibited significant positive-skewness in the case of low connectivity values (*i.e.*,  $Z = 2.5$ ), which gradually decreased as connectivity increased (Supplementary Figure 3a-b, left sub-figures, Supplementary Tables 4 and 5). There was no significant skewness in the values of the Poisson's ratio regardless of the connectivity value (Supplementary Figure 3a-j, right sub-figures). The mean value of the Poisson's ratio was positive for all connectivity values (Supplementary Tables 4 and 5). The probability of finding an auxetic network was  $p = 26\%$  for unrestricted and  $p = 20\%$  for restricted networks in the case of  $Z = 2.5$  and gradually decreased to zero for the higher values of connectivity (Supplementary Table 3).

The changes in the elastic modulus with the relative density,  $\phi$ , followed a similar nonlinear trend for both lattice-restricted and unrestricted networks. The range of the elastic moduli achieved here is within the theoretical limits given by the Hashin–Shtrikman bounds<sup>1,30–32</sup> for the positive values of the Poisson's ratio (Fig 3a, b):

$$0 < E(v) < -2C_1v + 2C_1, 0 < E(v) < 2C_2v + 2C_2,$$

$$C_1 = \frac{E_b}{2(1 - \nu_b)} + \frac{E_b(1 - \phi)}{\phi(1 - \nu_b^2) - 2(1 - \nu_b)},$$

$$C_2 = \frac{E_b}{2(1 + \nu_b)} + \frac{1 - \phi}{\frac{\phi}{2}(3 - \nu) - \frac{2(1 + \nu_b)}{E_b}}$$

### 4.3. Results and discussion

where the bulk properties of the material, from which beam-like structural elements are made, are given as  $E_b = 0.6$  MPa and  $\nu_b = 0.3$ .

The local values of connectivity in unrestricted lattices varied between 2 and 10, while the maximum local connectivity at each node was limited to 8 in the case of lattice-restricted networks (Figure 3c, d). We divided the range of the Poisson's ratios into four regions (*i.e.*,  $\nu < -0.5$ ,  $-0.5 < \nu < 0$ ,  $0 \leq \nu < 0.5$  and  $\nu > 0.5$ ) and compared the statistical distributions of the local connectivity values for both types of networks. We found no statistically significant differences between the local connectivity values of those four groups (Figure 3c, d). This suggests that the statistical distribution of the local connectivity values does not control the level of auxeticity.

We performed further statistical analyses to study the statistical distributions of the (bond) angles in lattice-unrestricted networks (Supplementary Figures 4 and 5). We calculated the angles of all the ligaments reaching individual nodes (with respect to the horizontal direction,  $x$ ). In a different definition, we defined the bond angle as the angle between the highest and lowest ligaments connected to each node. All the specimens with connectivity values between 2.5 and 4.5 were pooled and were divided into four groups according to the value of their Poisson's ratio (*i.e.*,  $\nu < -0.5$ ,  $-0.5 < \nu < 0$ ,  $0 \leq \nu < 0.5$ , and  $\nu > 0.5$ ). We used a non-parametric test (Wilcoxon test) to compare whether the statistical distributions of these four groups were significantly different from each other. We also used a Benjamini–Hochberg method to adjust the  $p$ -value. For both definitions of the bond angle in unrestricted networks, we found significant differences between the statistical distributions corresponding to the negative and positive ranges of the Poisson's ratio.

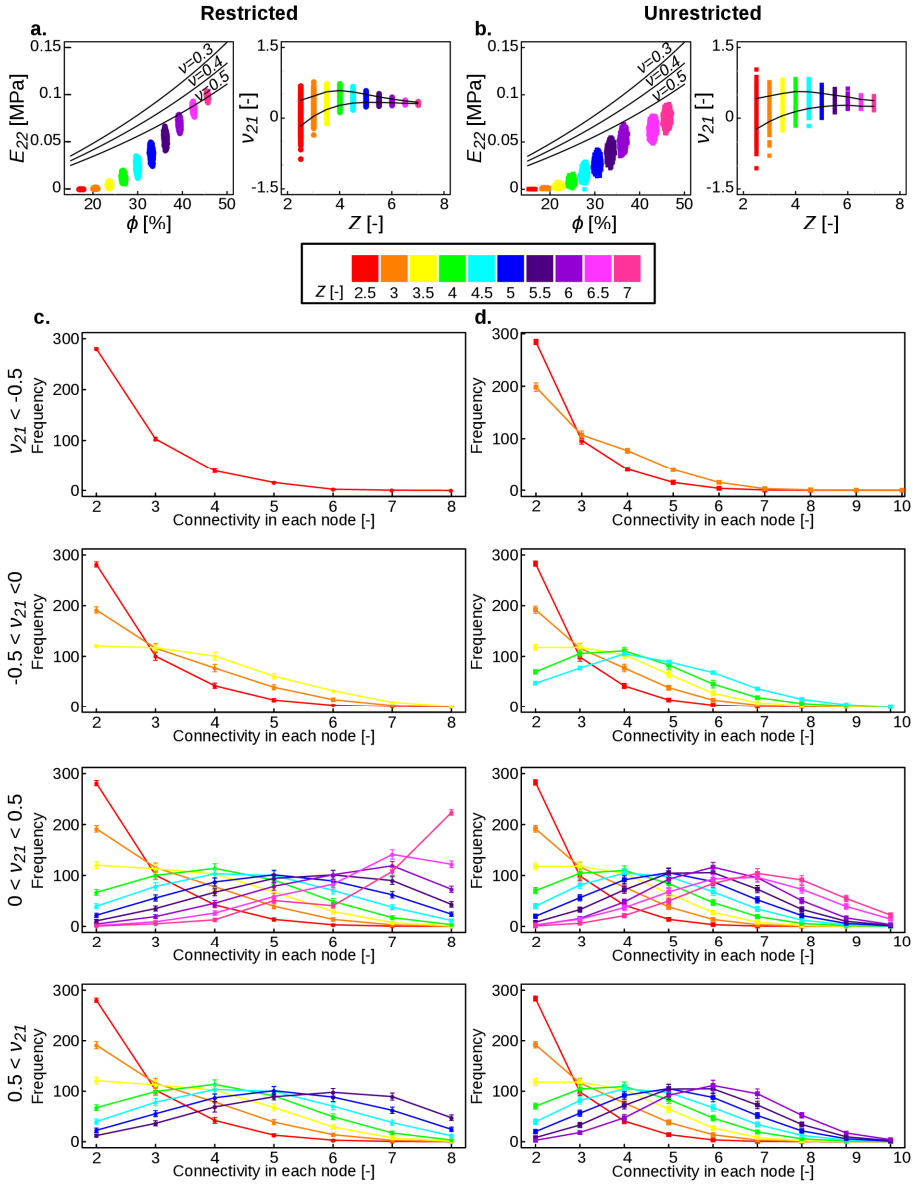


**Figure 3.** The change in the elastic modulus and relative density for lattice-restricted (a, right) and unrestricted (b, right) networks. The solid lines in the right sub-figures (a, and b) show the Hashin–Shtrikman bounds for three values of the relative density. The Poisson’s ratios of lattice-restricted (a, left) and unrestricted (b, left) networks as functions of the connectivity values. The trend lines show 95% confidence intervals in the left sub-figures (a and b). The histograms of the local connectivity values for restricted (c) and unrestricted (d) networks with different levels of the Poisson’s ratio.

### 4.3. Results and discussion

We performed numerical simulations for regular (*i.e.*, non-random, unit cells=re-entrant) lattices with values of negative Poisson's ratio that were comparable with those calculated for unrestricted networks. We compared the specific elastic moduli of the ordered lattices with those of the unrestricted networks presented here (Supplementary Table 6). We could clearly see that the mean ratio of the elastic modulus of the unrestricted random networks to that of ordered lattices always exceeded unity and increased with the degree of connectivity (Supplementary Table 6). That is due to the fact that unrestricted networks exhibit auxetic behavior also for higher degrees of connectivity, which is well into the stretch-dominated range of deformations, whereas the deformation of regular auxetic lattices is dominated by bending.

Some of the most negative values of the Poisson's ratio were observed for the networks that exhibited large lateral openings due to limited connectivity on their sides (Figure 4). Plotting the time history of the position of the nodes that moved the most in such networks showed that very diverse movement trajectories could be achieved using random network designs (Figure 4). Comparing the results of computational simulations with experimental observations indicated a good agreement between them, confirming that the applied 3D printing technique is capable of fabricating the studied random networks and that the behavior exhibited by the actual specimens is comparable with computational predictions even in the case of the very large deformations observed here (Figure 4). For this particular type of networks (*i.e.*, those with large lateral openings), the boundary between mechanical metamaterials and compliant mechanisms<sup>33–35</sup> whose displacements are driven by the elastic deformation of their constituting linkages (but not their rigid body movements) is blurred. The random networks studied here could, therefore, be also seen as some type of compliant mechanisms particularly when multiple networks are combined with each other to create more complex movement patterns than those observed in Figure 4.

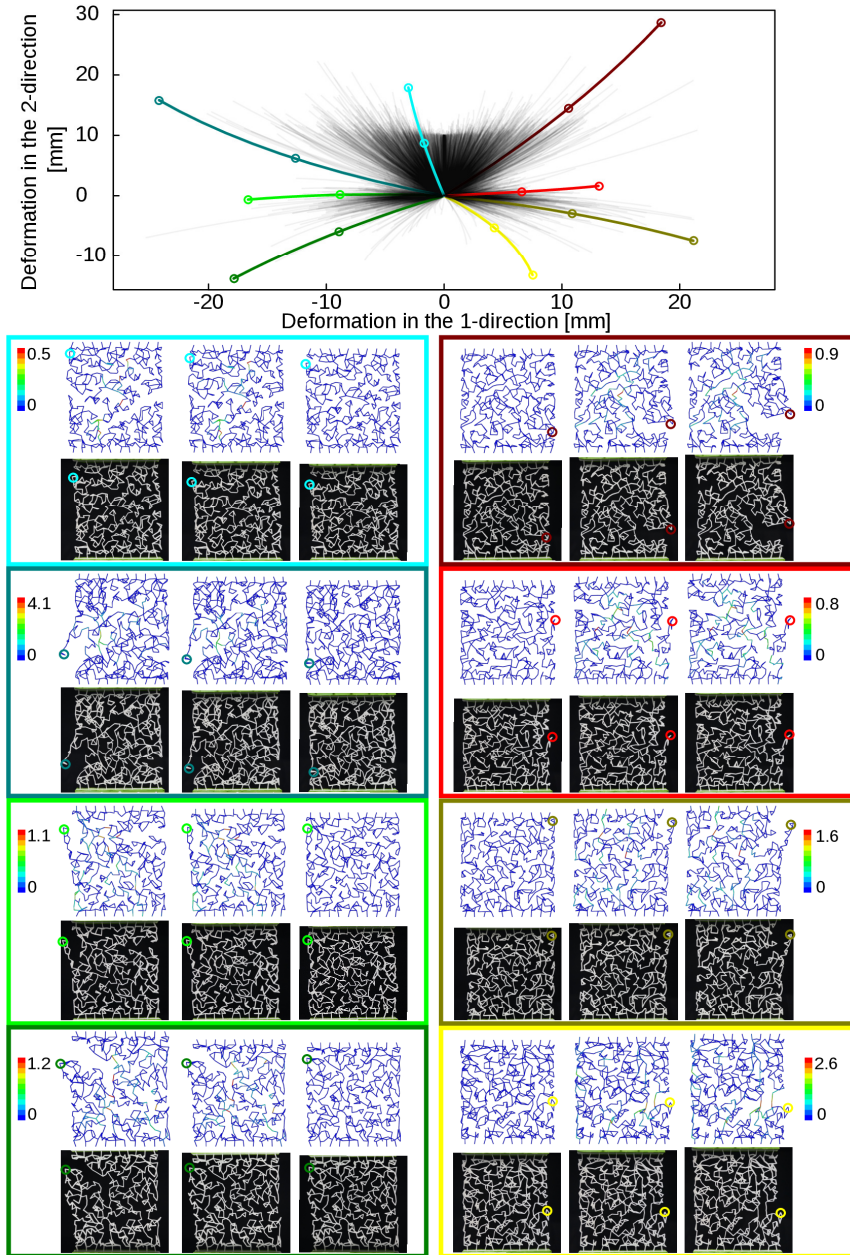


**Figure 4.** The trajectories of the lateral node that exhibited the maximum displacement in unrestricted random networks ( $Z = 2.5 - 3.5$ ). The deformation trajectories for eight representative cases are highlighted with different colors in the graph. The corresponding deformation patterns obtained from numerical simulations and experiments are presented for three levels of applied strain (*i.e.*, 0, 5%, and 10%). A comparison between the finite element simulations and experimental data is presented in Supplementary Table 7. The test setup is shown in Supplementary Figure 6.

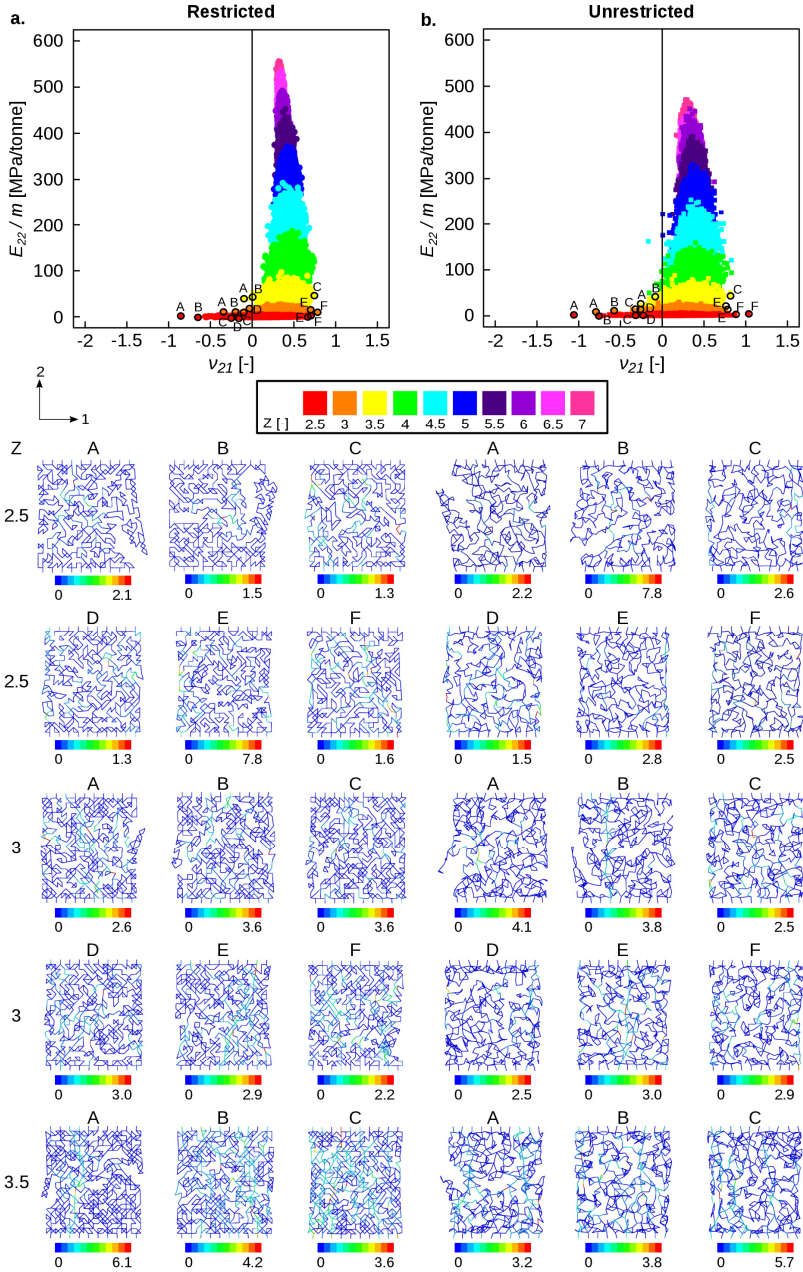
## 4.4. Conclusion

### 4.4. Conclusion

In summary, we studied the elastic properties of lattice-restricted and unrestricted random networks with different levels of connectivity to gain a better understanding that could aid us in the design of disordered mechanical metamaterials. Our results show that unrestricted networks have a number of clear advantages over lattice-restricted networks, which make them particularly attractive for that purpose. That includes a much wider range of elastic modulus-Poisson's ratio duos as well as a higher probability of exhibiting auxetic and double-auxetic behaviors. Interestingly, as opposed to lattice-restricted networks that do not exhibit any auxetic behavior in their stretch-dominated range (*i.e.*, positive values of the Maxwell metric), unrestricted networks could exhibit auxetic behavior also when in the stretch-dominated domain. This is another advantage of unrestricted networks that makes them particularly useful for the design of stiff auxetic metamaterials.

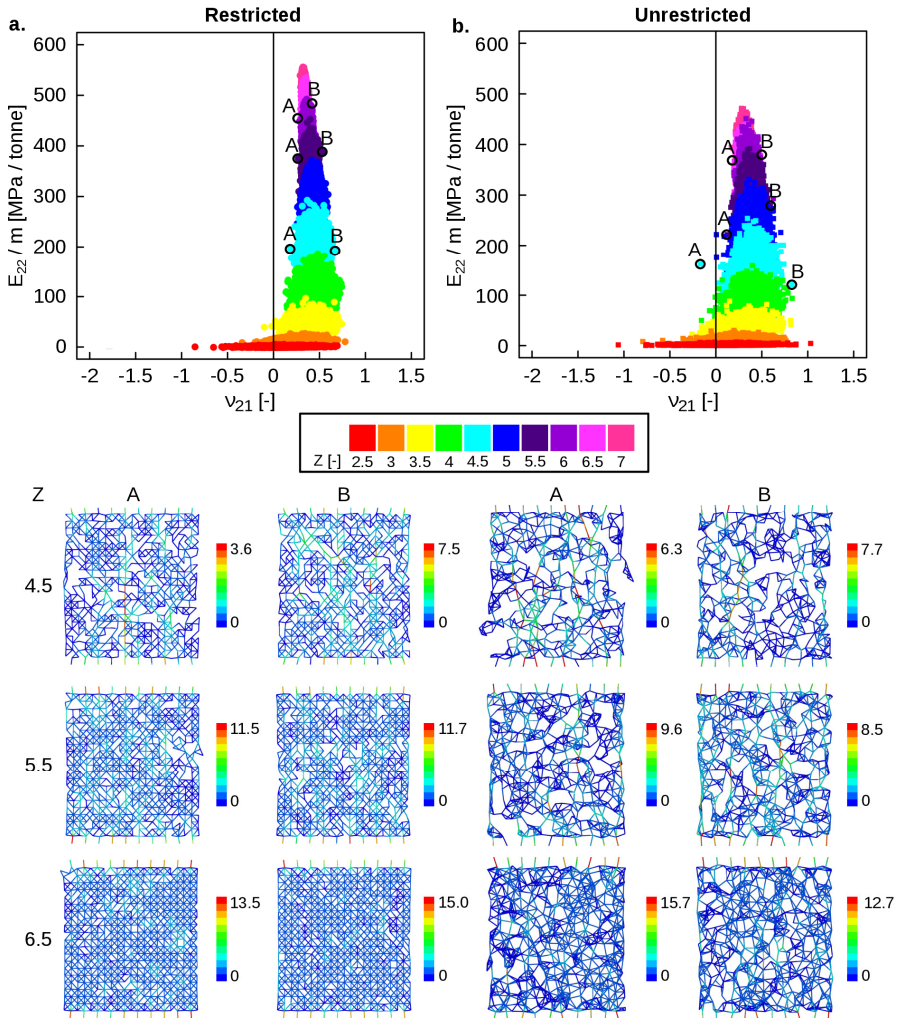


## 4.5. Supplementary document

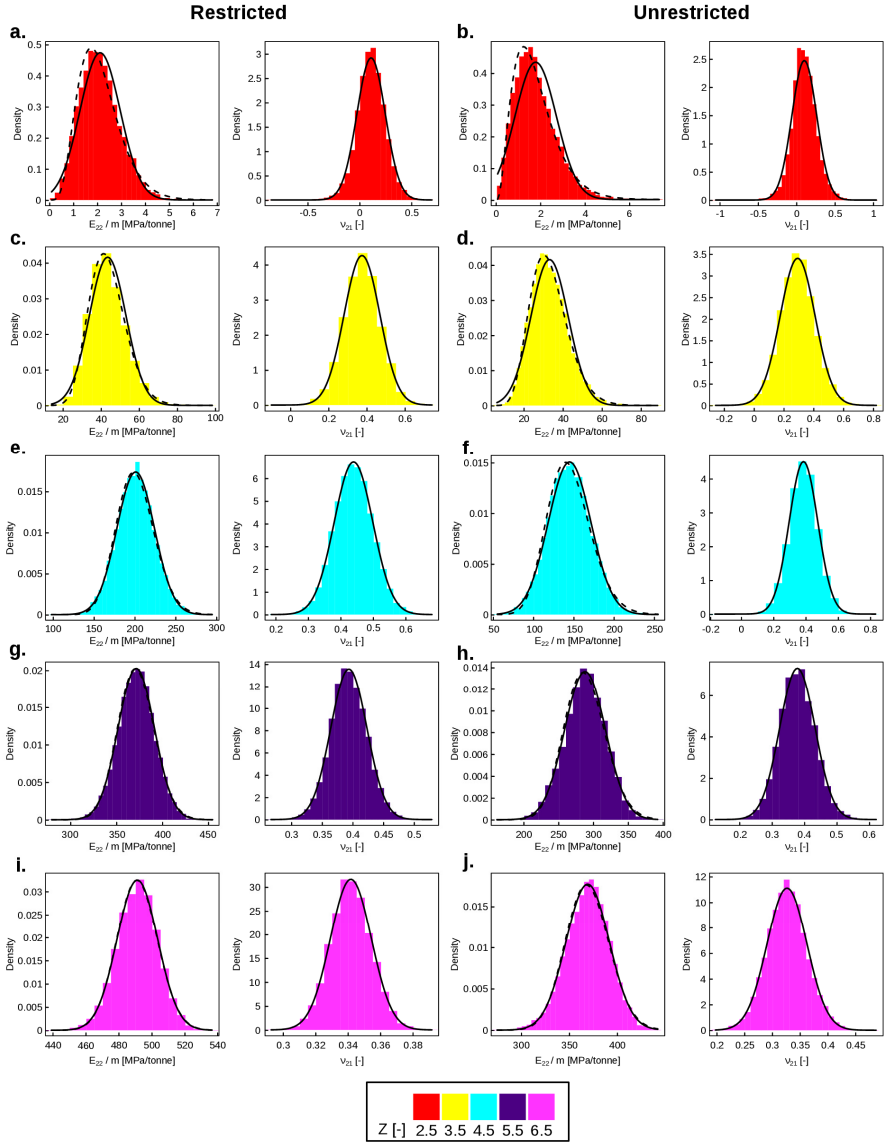


**Supplementary Figure 1.** The plane of the elastic modulus and Poisson's ratio values for lattice-restricted (a) and unrestricted (b) networks. The strain distributions below each graph (A-F) belong to some representative cases with connectivity values of 2.5, 3, and 3.5.

## 4.5. Supplementary document

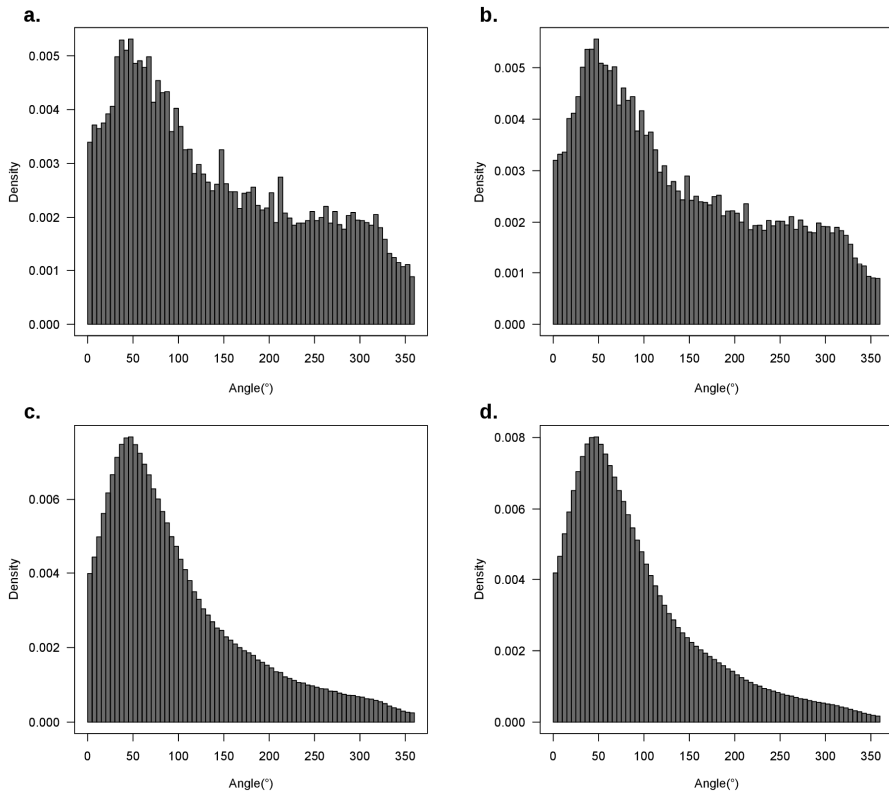


**Supplementary Figure 2.** The plane of the elastic modulus and Poisson's ratio values for lattice-restricted (a) and unrestricted (b) networks. The strain distributions of representative cases with connectivity values of 4.5, 5.5, and 6.5 are presented for both cases as well.

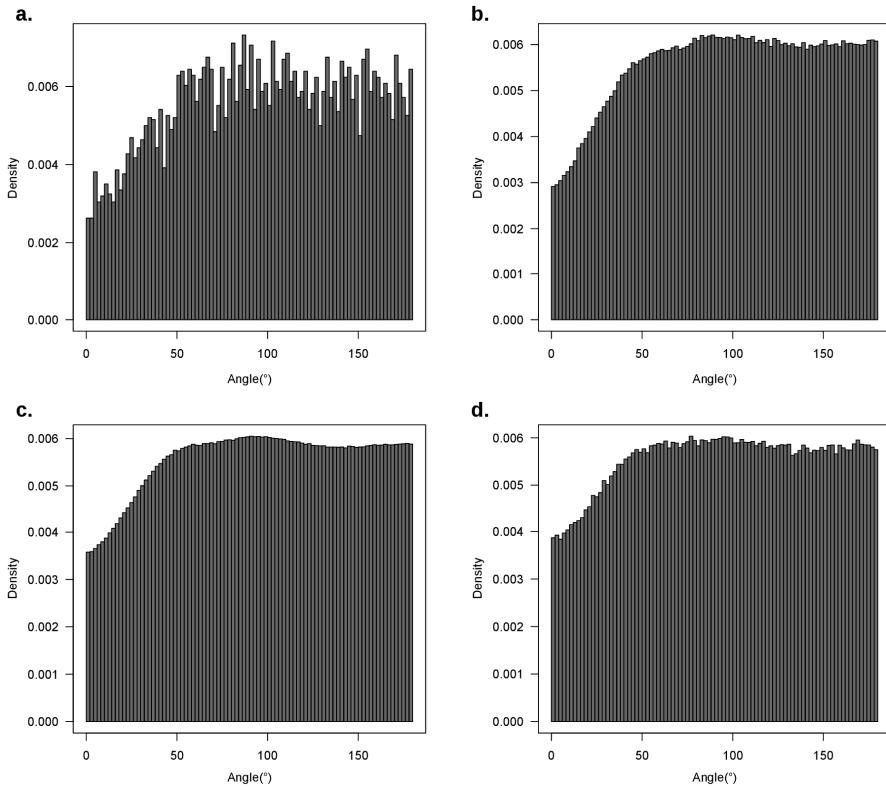


**Supplementary Figure 3.** The distribution of the elastic modulus and Poisson's ratio for the networks with connectivity levels of 2.5 (lattice-restricted (a), unrestricted (b)), 3.5 (lattice-restricted (c), unrestricted (d)), 4.5 (lattice-restricted (e), unrestricted (f)) 5.5 (lattice-restricted (g), unrestricted (h)), and 6.5 (lattice-restricted (i), unrestricted (j)) are presented. Gaussian distributions were fit to the elastic modulus and Poisson's ratio data (solid lines). We also fit gamma distributions to the elastic modulus data (dash-lines). The parameters of the probability distributions are listed in Supplementary Tables 4 and 5.

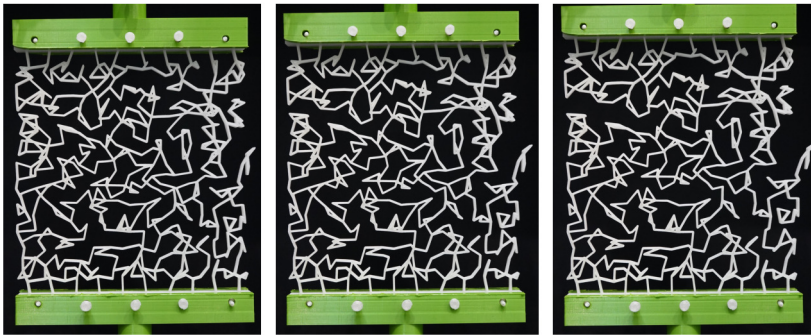
## 4.5. Supplementary document



**Supplementary Figure 4.** The density distribution of the bond angles for unrestricted networks with (a)  $\nu < -0.5$ , (b)  $-0.5 < \nu < 0$ , (c)  $0 \leq \nu < 0.5$ , and (d)  $\nu > 0.5$ .



**Supplementary Figure 5.** The density distribution of the bond angles for unrestricted networks with (a)  $\nu < -0.5$ , (b)  $-0.5 < \nu < 0$ , (c)  $0 \leq \nu < 0.5$  and (d)  $\nu > 0.5$ .



**Supplementary Figure 6.** The test setup for the monotonic tensile testing of the 3D printed networks.

#### 4.5. Supplementary document

**Supplementary Table 1.** The number of nodes ( $n$ ), elements ( $NE$ ), and Maxwell number ( $M$ ) for lattice-restricted and unrestricted networks with different sizes.

Z	The size of lattice-restricted or unrestricted networks								
	75 × 75			150 × 150			300 × 300		
	n	NE	M	n	NE	M	n	NE	M
2.5	121	151	-89	441	551	-329	1681	2101	-1259
3	121	181	-59	441	661	-219	1681	2521	-839
3.5	121	211	-29	441	771	-109	1681	2941	-419
4	121	242	2	441	882	2	1681	3362	2
4.5	121	272	32	441	992	112	1681	3782	422
5	121	302	62	441	1102	222	1681	4202	842
5.5	121	332	92	441	1212	332	1681	4622	1262
6	121	363	123	441	1323	443	1681	5043	1683
6.5	121	393	153	441	1433	553	1681	5463	2103
7	121	423	183	441	1543	663	1681	5883	2523

**Supplementary Table 2.** The principal radii of the confidence ellipses presented in Figure 2.

Size	Z	Lattice-restricted				Unrestricted			
		$E_{22}$ [MPa]		$\nu_{21}$ [-]		$E_{22}$ [MPa]		$\nu_{21}$ [-]	
		$r_1$	$r_2$	$r_1$	$r_2$	$r_1$	$r_2$	$r_1$	$r_2$
75 × 75	2.5	0.0004	0.0004	0.5768	0.4795	0.0005	0.0005	0.6738	0.5965
	3.5	0.0054	0.0052	0.4634	0.3519	0.0055	0.0049	0.5613	0.4881
	4.5	0.0120	0.0110	0.3015	0.1875	0.0137	0.0114	0.4513	0.3423
	5.5	0.0101	0.0096	0.1360	0.0743	0.0162	0.0130	0.2771	0.2026
	6.5	0.0058	0.0053	0.0427	0.0245	0.0143	0.0125	0.1631	0.1180
150 × 150	2.5	0.0001	0.0001	0.3783	0.2992	0.0001	0.0001	0.4220	0.3657
	3.5	0.0021	0.0019	0.2701	0.1876	0.0021	0.0019	0.3213	0.2509
	4.5	0.0061	0.0058	0.1721	0.1166	0.0074	0.0061	0.2416	0.1727
	5.5	0.0065	0.0063	0.0831	0.0532	0.0099	0.0082	0.1478	0.1026
	6.5	0.0049	0.0044	0.0355	0.0223	0.0105	0.0082	0.1016	0.0742
300 × 300	2.5	0.0001	0.0000	0.1206	0.0873	0.0001	0.0000	0.1413	0.1134
	3.5	0.0009	0.0008	0.0777	0.0496	0.0009	0.0008	0.0901	0.0614
	4.5	0.0031	0.0029	0.0490	0.0322	0.0036	0.0030	0.0687	0.0460
	5.5	0.0036	0.0035	0.0239	0.0152	0.0052	0.0046	0.0408	0.0290
	6.5	0.0030	0.0025	0.0111	0.0070	0.0055	0.0048	0.0274	0.0205

**Supplementary Table 3.** The probability of finding different ranges of the Poisson's ratio for each connectivity value and both types of networks (*i.e.*, lattice-restricted and unrestricted).

-	Z	$\nu < -0,5$	$-0,5 \leq \nu < 0$	$0 \leq \nu < 0,5$	$(\nu \geq 0,5)$
Lattice-restricted	2.5	0.07	20.33	79.24	0.36
	3	0.01	1.12	97.73	1.14
	3.5	0	1.12	91.42	8.55
	4	0	0	82.37	17.63
	4.5	0	0	85.32	14.68
Unrestricted	2.5	0.19	26.13	72.53	1.15
	3	0.03	5.93	92.38	1.66
	3.5	0	0.78	95.24	3.98
	4	0	0.11	91.71	8.18
	4.5	0	0.02	91.22	8.76

**Supplementary Table 4.** The parameters of the Gaussian distributions (*i.e.*, mean and standard deviation (SD)) of the elastic modulus and Poisson's ratio for the lattice-restricted networks (Figure 3a). In the case of the elastic modulus, the parameters of the gamma distribution (*i.e.*, shape, rate, and skewness) are presented as well.

Z	Lattice-restricted						
	$E_{22}/m$ [MPa/tonne]					$\nu_{21}[-]$	
	Gaussian		Gamma			Normal	
	Mean	SD	Shape	Rate	Skewness	Mean	SD
2.5	2.09	0.84	5.59	2.67	0.85	0.10	0.14
3.5	43.18	9.60	20.37	0.47	0.44	0.37	0.09
4.5	200.38	22.96	74.88	0.37	0.23	0.44	0.06
5.5	370.91	19.70	351.98	0.95	0.11	0.39	0.03
6.5	490.91	12.30	1589.17	3.24	0.05	0.34	0.01

**Supplementary Table 5.** The parameters of the Gaussian distributions (*i.e.*, mean and standard deviation (SD)) for the elastic modulus and Poisson's ratio of the unrestricted networks (Figure 3b). In the case of the elastic modulus, the parameters of the gamma distribution (*i.e.*, shape, rate, and skewness) are presented.

Z	Unrestricted						
	$E_{22}/m$ [MPa/tonne]					$\nu_{21}[-]$	
	Gaussian		Gamma			Normal	
	Mean	SD	Shape	Rate	Skewness	Mean	SD
2.5	1.73	0.93	3.18	1.84	1.12	0.09	0.16
3.5	32.85	9.60	11.53	0.35	0.59	0.29	0.12
4.5	144.19	26.48	28.64	0.20	0.37	0.38	0.09
5.5	287.31	29.28	94.21	0.33	0.21	0.38	0.05
6.5	368.62	22.56	263.53	0.71	0.12	0.33	0.04

#### 4.5. Supplementary document

**Supplementary Table 6.** The mean ratio of specific stiffness of lattice-unrestricted networks (with the values of connectivity between 3.5 and 4.5) to regular (*i.e.*, non-random) lattices.

Z	$\left(\frac{E_{22}}{m}\right)_{unrestricted} / \left(\frac{E_{22}}{m}\right)_{Ordered}$
	Mean
3.5	1.41
4	2.91
4.5	8.31

**Supplementary Table 7.** Comparison of the elastic moduli obtained from numerical simulations and experimental results. The elastic modulus of the material used in finite element simulations was set to 70 MPa.

Sample number	$E_{22}$ [kPa]		Error (%)
	Simulation	Experiment	
1	16.13	14.80	8.95
2	9.38	10.30	8.98
3	9.50	8.50	11.76
4	3.75	3.76	0.27
5	0.50	0.46	9.17
6	69.88	65.00	7.50
7	5.00	5.45	8.26
8	70.38	76.20	7.64



## References

1. Berger, J. B., Wadley, H. N. G. & McMeeking, R. M. Mechanical metamaterials at the theoretical limit of isotropic elastic stiffness. *Nature* **543**, 533 (2017).
2. Hedayati, R., Mirzaali, M. J., Vergani, L. & Zadpoor, A. A. Action-at-a-distance metamaterials: distributed local actuation through far-field global forces. *APL Mater.* **6**, 036101 (2018).
3. Mitschke, H. *et al.* Finding auxetic frameworks in periodic tessellations. *Adv. Mater.* **23**, 2669–2674 (2011).
4. Buxton, G. A. & Clarke, N. “Bending to stretching” transition in disordered networks. *Phys. Rev. Lett.* **98**, 238103 (2007).
5. Deshpande, V. S., Ashby, M. F. & Fleck, N. A. Foam topology: bending versus stretching dominated architectures. *Acta Mater.* **49**, 1035–1040 (2001).
6. Bertoldi, K., Vitelli, V., Christensen, J. & Van Hecke, M. Flexible mechanical metamaterials. *Nat. Rev. Mater.* **2**, (2017).
7. Bauer, J., Schroer, A., Schwaiger, R. & Kraft, O. Approaching theoretical strength in glassy carbon nanolattices. *Nat. Mater.* **15**, 438 (2016).
8. Gibson, L. J. & Ashby, M. F. Cellular solids: structure and properties. (Cambridge university press, 1999).
9. Gibson, L. J., Ashby, M. F. & Harley, B. A. Cellular materials in nature and medicine. (Cambridge University Express, 2010).
10. Head, D. A., Levine, A. J. & MacKintosh, F. C. Distinct regimes of elastic response and deformation modes of cross-linked cytoskeletal and semiflexible polymer networks. *Phys. Rev. E* **68**, 61907 (2003).
11. Wilhelm, J. & Frey, E. Elasticity of stiff polymer networks. *Phys. Rev. Lett.* **91**, 108103 (2003).
12. Thorpe, M. F. Comment on elastic network models and proteins. *Phys. Biol.* **4**, 60 (2007).
13. Head, D. A., Levine, A. J. & MacKintosh, F. C. Deformation of cross-linked semiflexible polymer networks. *Phys. Rev. Lett.* **91**, 108102 (2003).
14. Fratzl, P. Collagen: structure and mechanics, an introduction. in *Collagen 1–13* (Springer, 2008).
15. Licup, A. J. *et al.* Stress controls the mechanics of collagen networks. *Proc. Natl. Acad. Sci.* **112**, 9573–9578 (2015).

## References

16. Hanifpour, M., Petersen, C. F., Alava, M. J. & Zapperi, S. Mechanics of disordered auxetic metamaterials. *Eur. Phys. J. B* **91**, 1–8 (2018).
17. Hagh, V. F. & Thorpe, M. F. Disordered auxetic networks with no reentrant polygons. *Phys. Rev. B* **98**, 100101(2018).
18. Mirzaali, M. J. *et al.* Rational design of soft mechanical metamaterials: Independent tailoring of elastic properties with randomness. *Appl. Phys. Lett.* **111**, 051903 (2017).
19. Rayneau-Kirkhope, D., Bonfanti, S. & Zapperi, S. Density scaling in the mechanics of a disordered mechanical meta-material. *Appl. Phys. Lett.* **114**, 111902 (2019).
20. Reid, D. R. *et al.* Auxetic metamaterials from disordered networks. *Proc. Natl. Acad. Sci.* **115**, E1384-E1390 (2018).
21. Berthier, E. *et al.* Rigidity percolation control of the brittle-ductile transition in disordered networks. *arXiv Prepr. arXiv1812.07466* (2018).
22. Vermeulen, M. F. J., Bose, A., Storm, C. & Ellenbroek, W. G. Geometry and the onset of rigidity in a disordered network. *Phys. Rev. E* **96**, 53003 (2017).
23. Carleton, J. B., D'Amore, A., Feaver, K. R., Rodin, G. J. & Sacks, M. S. Geometric characterization and simulation of planar layered elastomeric fibrous biomaterials. *Acta Biomater.* **12**, 93–101 (2015).
24. Karageorgiou, V. & Kaplan, D. Porosity of 3D biomaterial scaffolds and osteogenesis. *Biomaterials* **26**, 5474–5491 (2005).
25. R Core Team. R: A language and environment for statistical computing. (2013).
26. Delignette-Muller, M. L., Dutang, C. & others. fitdistrplus: An R package for fitting distributions. *J. Stat. Softw.* **64**, 1–34 (2015).
27. Hollander, M. & Wolfe, D. A. Nonparametric Statistical Methods (Wiley, 1973).
28. Shapiro, S. S. & Francia, R. S. An approximate analysis of variance test for normality. *J. Am. Stat. Assoc.* **67**, 215–216 (1972).
29. Ashby, M. F. Hybrids to fill holes in material property space. *Philos. Mag.* **85**, 3235–3257 (2005).
30. Hashin, Z. The elastic moduli of heterogeneous materials. *J. Appl. Mech.* **29**, 143–150 (1962).
31. Hashin, Z. & Shtrikman, S. A variational approach to the theory of the elastic behaviour of multiphase materials. *J. Mech. Phys. Solids* **11**, 127–140 (1963).

32. Ostanin, I., Ovchinnikov, G., Tozoni, D. C. & Zorin, D. A parameteric class of composites with a large achievable range of effective elastic properties. *J. Mech. Phys. Solids* **118**, 204-217 (2018).
33. Ion, A. *et al.* Metamaterial mechanisms. in *Proceedings of the 29th Annual Symposium on User Interface Software and Technology*. 529–539 (2016).
34. Lee, J., Kim, K., Ju, J. & Kim, D.-M. Compliant cellular materials with elliptical holes for extremely high positive and negative Poisson's ratios. *J. Eng. Mater. Technol.* **137**, 11001 (2015).
35. Meza, L. R. *et al.* Resilient 3D hierarchical architected metamaterials. *Proc. Natl. Acad. Sci.* **112**, 11502–11507 (2015).

# 5

## Rare-event multi-material mechanical metamaterials

Published as:

Pahlavani, H., Amani, M., Saldívar, M. C., Zhou, J., Mirzaali, M. J., & Zadpoor, A. A. Deep learning for the rare-event rational design of 3D printed multi-material mechanical metamaterials. *Communications Materials* 3, 1-11 (2022).

## Abstract

Emerging multi-material 3D printing techniques enables the rational design of metamaterials with not only complex geometries but also arbitrary distributions of multiple materials within those geometries, yielding unique combinations of elastic properties. However, discovering the rare designs that lead to highly unusual combinations of material properties, such as double-auxeticity and high elastic moduli, remains a non-trivial crucial task. Here, we use computational models and deep learning algorithms to identify rare-event designs. In particular, we study the relationship between random distributions of hard and soft phases in three types of planar lattices and the resulting mechanical properties of the two-dimensional networks. By creating a mapping from the space of design parameters to the space of mechanical properties, we are able to reduce the computational time required for evaluating each design to  $\approx 2.4 \times 10^{-6}$  s, and to make the process of evaluating different designs highly parallelizable. We then selected ten designs to be 3D printed, mechanically tested them, and characterized their behavior using digital image correlation (DIC) to validate the accuracy of our computational models. Our simulation results show that our deep learning-based algorithms can accurately predict the mechanical behavior of the different designs and that our modeling results match experimental observations.

### 5.1. Introduction

The rational design of architected materials with anisotropic properties enables them to offer optimal, multi-functional performance. For example, nature uses evolutionarily optimized micro-architectures to combine extremely high stiffness (in selected directions) with a light weight (*e.g.*, in wood and bone<sup>1-3</sup>) or to combine ultrahigh stiffness values with ultrahigh toughness (*e.g.*, in nacre<sup>4-6</sup>). In man-made designer materials that are also known as metamaterials, other combinations of mechanical properties may be sought, as they allow for devising novel functionalities. For example, a combination of auxetic behavior in various orthogonal directions and high stiffness is instrumental for the structural applications of auxetic materials<sup>7-9</sup>.

To achieve a desired combination of material properties, the primary challenge is to find the specific micro-architectures that give rise to the desired properties. Once the micro-architecture is determined, the metamaterial can be fabricated using additive manufacturing (=3D printing) techniques. The recent emergence of powerful multi-material 3D printing techniques means that the micro-architecture not only consists of rationally designed, complex geometries but can also combine multiple materials with different mechanical properties. Many other design features found in nature, such as hierarchical micro-architectures<sup>10-13</sup>, functional gradients (in terms of both geometries and material properties)<sup>14,15</sup>, and soft-hard composites (similar to the organic and mineral phases in bone<sup>11,16,17</sup>) can be also realized to expand the range of the achievable properties.

Given such a wide range of possibilities for the fabrication of metamaterials with complex (multi-scale) geometries and complex spatial distributions of material properties, the space of possible design parameters is formidably large. Optimizing the design parameters is, therefore, challenging and requires an excessively large number of computational models to be solved. Such simulations are required not only to understand how the design parameters relate to the anisotropic elastic

properties but, more importantly, to discover the very rare designs that give rise to the desired properties. For example, double-auxeticity (*i.e.*, auxetic properties in two orthogonal directions) is very rare (*i.e.*, as little as  $< 1.6\%$  of the possible designs) in two-dimensional lattices<sup>18</sup>. Combining the double-auxeticity with the additional requirement of possessing high stiffness values in (both) directions results in the excessive rarity of micro-architectures that satisfy the design requirements.

Computational models, therefore, need to scan a vast design space to find rare events. Due to the “curse of dimensionality”<sup>19</sup>, the number of designs that need to be evaluated is so large ( $\approx 7.7 \times 10^{43}$ , see Supplementary Table 1) that extremely fast models and highly parallelizable algorithms are required. Computational models, such as finite element (FE) models, are not fast enough for that purpose. Here, we used deep learning to establish a mapping from the space of design parameters to that of the anisotropic elastic properties, thereby decreasing the solution time to  $\approx 2.4 \times 10^{-6}$  s while also making the evaluation process extremely parallelizable. Recent progress in machine learning has led to significant achievements in different scientific fields<sup>20</sup>, including the design of composites and metamaterials<sup>21-28</sup>, prediction of material properties<sup>29-31</sup>, the prediction of elasticity distributions to circumvent the inverse problem of elasticity imaging<sup>32,33</sup>, and optimization of manufacturing processes<sup>34,35</sup>. However, the advantages of such artificial intelligence approaches have not yet been demonstrated in the case of designing multi-material mechanical metamaterials to achieve very rare target properties.

The main objective of the present research was to use computational models and deep learning models to predict the mechanical properties of multi-material mechanical metamaterials, allowing us to discover very rare designs that exhibit highly desirable combinations of elastic properties (*e.g.*, high stiffness and highly negative Poisson’s ratio). We used planar lattices based on the re-entrant, cubic, and honeycomb unit cells (corresponding to the cell angles of  $60^\circ$ ,  $90^\circ$ , and  $120^\circ$ , respectively) with random distributions of hard and soft phases. The ratio of the hard phase volume to the soft phase volume was varied as well (*i.e.*,  $\rho_h(\%) =$

## 5.2. Materials and methods

5, 10, 20, 30, 40, 50, 60, 70, 80, 90, and 95). FE models were then created to generate the training dataset required for the training of a deep learning model (*i.e.*, the single unit cell model). Moreover, we selected three designs (one from each unit cell angles of  $60^\circ$ ,  $90^\circ$ , and  $120^\circ$ ) to be fabricated using an advanced multi-material 3D printing technique and applied digital image correlation (DIC) to measure the full-field strain patterns during the mechanical testing of the fabricated specimens. After training, the deep learning model was used to predict the elastic properties of a wide range of lattices ( $1.5 \times 10^9$  different designs), given their design parameters. We also studied various combination of tiled designs (*e.g.*, four-tile and nine-tile structures) to show how combining multiple instances of these random lattices into a hybrid, tiled lattice can boost the possible range of mechanical properties. We also trained another deep learning model (*i.e.*, the four-tile model) which predicts the mechanical properties resulting from the various combinations of four tiles with different mechanical properties. A fabrication and mechanical testing procedure similar to the one mentioned above (but without DIC) was applied to experimentally characterize seven additional tiled designs (*i.e.*, four four-tile structures and three nine-tile structures).

## 5.2. Materials and methods

We considered planar lattices with three groups of unit cell angles representing the negative (re-entrant,  $\theta = 60^\circ$ ), zero (orthogonal,  $\theta = 90^\circ$ ), and positive (honeycomb,  $\theta = 120^\circ$ ) values of the Poisson's ratio (Figure 1a). We kept the overall dimensions of each design ( $W, C$ ) as well as the dimensions of the constituent unit cells ( $w, c$ ) unchanged. All three groups of designs were composed of  $5 \times 5$  unit cells with similar in-plane ( $t$ ) and out-of-plane ( $T$ ) thicknesses. The geometrical parameters of the designed lattice structures are presented in Supplementary Table 5. The hard and soft phases were randomly assigned to the struts of the structure so as to achieve various ratios of the volume of the hard phase to that of the soft phase ( $\rho_h$  (%) = 5, 10, 20, 30, 40, 50, 60, 70, 80, and 95). To further expand the space of



possible mechanical properties, we studied the various combination of the unit cells. Moreover, we studied the stress distribution within the soft and hard elements of the unit cells and used a more uniform distribution of stresses as the criterion for selecting the best designs among all the designs with similar elastic properties.

### 5.2.1. Computational models

All FE models were created using MATLAB (MATLAB R2018b, Mathworks, USA) codes. The codes were used to design the three groups of lattice structures (composed of unit cells with the three different cell angles of  $60^\circ$ ,  $90^\circ$ , and  $120^\circ$ ), to randomly assign the hard and soft phases to the struts of each design, and to perform the FE simulations that estimate their mechanical properties (*i.e.*, elastic modulus and Poisson's ratio in two orthogonal directions). Our codes were further extended to combine single unit cell designs into four-tile and nine-tile lattice structures. In each structure, the adjacent designs were connected using a row of struts made of the hard material.

We used three-node quadratic beam elements (Timoshenko beam elements) with rectangular cross-sections and with two translational (*i.e.*,  $u_x$ ,  $u_y$ ) and one rotational (*i.e.*,  $u_z$ ) degrees of freedom (DOF) at each node. We assigned elastic materials to both soft and hard phases with a similar Poisson's ratio of 0.48 but vastly different Young's moduli of 0.6 and 60 MPa (*i.e.*,  $E_h/E_s = 100$ ), respectively. To estimate the mechanical properties of each structure in both the x- and y-directions, a strain of 3% in each direction was separately applied to the structure. Towards this aim, in one model, the top nodes were subjected to a strain of 3% in the y-direction ( $u_x = u_z = 0$  and  $u_y = 3\%$  strain), while all the degrees of freedom of the bottom nodes were constrained ( $u_x = u_y = u_z = 0$ ). In the other model, the right nodes were subjected to 3% strain in the x-direction ( $u_y = u_z = 0$ , and  $u_x = 3\%$  strain), while all the degrees of freedom of the left nodes were constrained ( $u_x = u_y = u_z = 0$ ). The element stiffness matrix transferred to the global coordinate ( $K^e$ ) was calculated as<sup>36,37</sup>:

## 5.2. Materials and methods

$$K^e = Q^T \bar{K}^e Q, \quad (1)$$

$$\bar{K}^e = \frac{E}{(1+\mu)} \times \quad (2)$$

$$\begin{bmatrix} A(1+\mu)/L & 0 & 0 & -A(1+\mu)/L & 0 & 0 \\ 0 & 12I/L^3 & 6I/L^2 & 0 & -12I/L^3 & 6I/L^2 \\ 0 & 6I/L^2 & 4I(1+\mu/4)/L & 0 & -6I/L^2 & 2I(1-\mu/2)/L \\ -A(1+\mu)/L & 0 & 0 & A(1+\mu)/L & 0 & 0 \\ 0 & -12I/L^3 & -6I/L^2 & 0 & 12I/L^3 & -6I/L^2 \\ 0 & 6I/L^2 & 2I(1-\mu/2)/L & 0 & -6I/L^2 & 4I(1+\mu/4)/L \end{bmatrix},$$

$$\mu = \frac{12EI}{L^2 GAK_s}, \quad (3)$$

$$Q = \begin{bmatrix} n_{x\bar{x}} & n_{y\bar{x}} & 0 & 0 & 0 & 0 \\ n_{x\bar{y}} & n_{y\bar{y}} & 0 & 0 & 0 & 0 \\ 0 & 0 & 1 & 0 & 0 & 0 \\ 0 & 0 & 0 & n_{x\bar{x}} & n_{y\bar{x}} & 0 \\ 0 & 0 & 0 & n_{x\bar{y}} & n_{y\bar{y}} & 0 \\ 0 & 0 & 0 & 0 & 0 & 1 \end{bmatrix}, \quad (4)$$

where  $\bar{K}^e$  is the local element stiffness matrix, and  $E, A, I$ , and  $L$  are the elastic modulus, the cross-section area, the moment of inertia ( $I = Tt^3 / 12$ ), and the length of the element, respectively.  $\mu$  is a dimensionless coefficient that characterizes the importance of shear-related parameters including  $G$  (shear modulus) and  $K_s$  (shear correction factor = 0.85).  $Q$  is the transformation matrix and contains the direction cosines:

$$n_{x\bar{x}} = n_{y\bar{y}} = \frac{x_2 - x_1}{L}, n_{y\bar{x}} = -n_{x\bar{y}} = \frac{y_2 - y_1}{L}, \quad (5)$$

where  $x_1, y_1, x_2$ , and  $y_2$  are the element nodal coordinates.

The element load vector  $f^e$  is obtained as follows <sup>37</sup>:

$$f^e = Q^T \bar{f}_l^e \quad (6)$$

$$\bar{f}_l^e = \begin{bmatrix} q_{\bar{x}}L/2 \\ q_{\bar{y}}L/2 \\ q_{\bar{y}}L^2/12 \\ q_{\bar{x}}L/2 \\ q_{\bar{y}}L/2 \\ -q_{\bar{y}}L^2/12 \end{bmatrix} \quad (7)$$

The stiffness matrix and load vectors of all the elements were calculated and were assembled into a global stiffness matrix ( $K$ ) and a global load vector ( $F$ ). Finally, all the forces and displacements were calculated using Hook's law ( $F = Kd$ ).

To calculate the Young's moduli of the structure ( $E_{11} = \sigma_{11}/\varepsilon_{11}$  and  $E_{22} = \sigma_{22}/\varepsilon_{22}$ ), the normal stresses in the directions 1 and 2 ( $\sigma_{11} = \bar{F}_1/A_2$ ,  $\sigma_{22} = \bar{F}_2/A_1$ , where  $A_1$  and  $A_2$  are the cross-section areas of the structure on the 1-3 and 2-3 planes (Figure 1a)) were divided by the strain applied along the same direction ( $\varepsilon_{11} = \varepsilon_{22} = 3\%$ ). In these equations,  $\bar{F}_1$  and  $\bar{F}_2$  are, respectively, the mean reaction forces along the directions 1 and 2 at the right and top nodes ( $\bar{F}_1 = \frac{\sum_{i=1}^{n_R} F_{1i}}{n_R}$ ,  $\bar{F}_2 = \frac{\sum_{i=1}^{n_T} F_{2i}}{n_T}$ , where  $n_R$  and  $n_T$  are the total numbers of the right and top nodes while  $F_{1i}$  and  $F_{2i}$  are the reaction forces along the directions 1 and 2 at each of the right and top nodes, respectively). To calculate the Poisson's ratio ( $\nu_{12} = \nu_{21} = -\frac{\varepsilon_{trans}}{\varepsilon_{axial}}$ ), the transverse strain was first calculated as the ratio of the mean displacement of the lateral nodes to the initial transversal length of the structure. The transverse strain was then divided by the applied axial strain (in the case of  $\varepsilon_{axial} = \varepsilon_{11} = 3\%$ :  $\varepsilon_{trans} = \varepsilon_{22} = \frac{\sum_{i=1}^{n_T} \delta y_i}{L_2 n_T}$ , and in the case of  $\varepsilon_{axial} = \varepsilon_{22} = 3\%$ :  $\varepsilon_{trans} = \varepsilon_{11} = \frac{\sum_{i=1}^{n_R} \delta x_i}{L_1 n_R}$  where  $L_1$  and  $L_2$  are the initial lengths of the structure along the directions 1 and 2).

### 5.2.2. Deep learning

We implemented two artificial neural networks (ANN) using Tensorflow.keras neural network library<sup>38,39</sup>, namely the 'single unit cell model' and the 'four-tile model'. The single unit cell model predicts the mechanical properties of the lattice structures with three unit cell angles of 60°, 90°, and 120° and a wide range of  $\rho_h$  values (*i.e.*,  $\rho_h$  (%) = 5, 10, 20, 30, 40, 50, 60, 70, 80, 90, and 95). To train the single unit cell model, the FE models were first solved for 18,150,000 lattice structures (16,500,000 structures as the training dataset and 1,650,000 structures as

## 5.2. Materials and methods

the testing dataset) with random assignments of the hard phase within the structure. The inputs to the single unit cell model included 150 material parameters indicating whether each strut was hard or soft (1 = hard, 0 = soft) and one unit cell angle ( $\theta = 60, 90, \text{ and } 120$ ) (151 inputs in total). The outputs of the model included the elastic moduli ( $E_{11}, E_{22}$ ) and Poisson's ratios ( $\nu_{12}, \nu_{21}$ ) in both directions (4 outputs in total) (Figure 1a). The dataset generated for the training of the single unit cell model was also used for the training of the four-tile deep learning model. Towards this aim, we selected 90 single unit cell tiles with mechanical properties uniformly distributed within the achievable range of elastic properties for these single unit cell designs. The mechanical properties of these 90 designs were first calculated by performing the FE simulations. All possible four-combinations of these single tiles (*i.e.*,  $C(90, 4) = 2,555,190$ ) considering the permutation of these four single tiles ( $= 4!$ , which is reduced to 6 due to the symmetry of the structure) were generated and were used for setting up the deep learning models ( $n_2 = 6 \times 2,555,190 = 15,331,140$ ). Our FE code was then used to calculate the overall elastic properties of these structures (Figure 1b). We randomly selected 90% of the dataset as training dataset and the remaining 10% as testing dataset. The four-tile model was then created to map the space of the 16 input parameters (*i.e.*, the elastic properties of the individual tiles) to the space of 4 output parameters (*i.e.*, the elastic properties of the four-tile structures).

We scaled all the outputs of the single unit cell models and all the inputs and outputs of the four-tile model to the range [0-1] (see Table 1 for the scaling method). In post-processing, we scaled the relevant outputs back to the original range to facilitate the interpretation of the results.

For the training of both the single unit cell model and four-tile model, we used a sequential model composed of a linear stack of fully connected layers based on the Tensorflow.keras library. Before training the models, we configured the learning process by defining several parameters, including an optimizer (RMSprop), a list of

metrics (MSE and MAE), and a loss function (MSE) that was the objective that the model would try to minimize. To evaluate the performance of the model with different hyperparameter values and also to detect overfitting during the training process, we assumed 20% of the training dataset as the validation dataset. This means that during each epoch, the model was trained based on the training data, and was tuned with the metrics (MSE, MAE) calculated for the validation dataset. In this way, we tuned the hyperparameters of the model based on the results of the metrics for the validation dataset.

In the single unit cell model, we systematically studied the effects of different hyperparameters (*i.e.*, the number of hidden layers, the number of neurons in each hidden layer, learning rate, and activation function). To design the architecture of the four-tile model, we started with the optimized hyperparameters determined for the single unit cell model. Hyperparameter tuning is discussed in detail in the Supplementary methods (Supplementary Figures 4-7 and Supplementary Tables 6-10). The optimized architecture and hyperparameters of both models together with their optimized accuracy, the type of feature scaling, and the optimization algorithm are presented in Table 1.

**Table 1.** The training parameters of the single unit cell and four-tile deep learning models.

Parameters	Single-tile model	Four-tile model
Hidden layer dimensions	256-128-128-64-32	256-128-64-32-16-8
Activation function	ReLU	ReLU
Learning rate	$10^{-4}$	$10^{-4}$
Number of epochs	200	200
Feature scaling	min-max	min-max
Optimization algorithm	RMSprop	RMSprop

In order to calculate the training error, the prediction results of the deep learning models were compared with the target values (FE simulation results) and MAE as well as MSE were calculated for each training epoch. MSE and MAE graphs for single

## 5.2. Materials and methods

unit cell model and four-tile model are presented in Supplementary Figures 6 and 7, respectively. MAE quantifies the magnitude of the prediction error without considering the error direction:

$$MAE = \frac{1}{n} \sum_{i=1}^n |y_i - \hat{y}_i| \quad (8)$$

where  $n$  is the number of the training samples,  $y_i$  are the predicted values, and  $\hat{y}_i$  are the true values. MSE is the squared mean of the differences between the predicted values,  $y_i$ , and the true values,  $\hat{y}_i$ , and is calculated as:

$$MSE = \frac{1}{n} \sum_{i=1}^n (y_i - \hat{y}_i)^2 \quad (9)$$

### 5.2.3 Experiments

To validate the results of our computational models used for training the single unit cell models, we selected three single unit cell lattice structures (one from each of the cell angles of 60°, 90°, and 120°) (Figure 1a). In addition, we designed three nine-tile structures and four four-tile structures. These structures represented different arrangements of the single unit cell designs (see Section 3.6). The selected designs were 3D printed and mechanically tested.

We used a multi-material 3D printer (Object500 Connex3, Stratasys, US) which uses the jetting of multiple UV-curable polymers (Polyjet technology) for printing multi-material structures. The commercially available polymers VeroCyan™ (hard phase, RGD841) and Agilus30™ white (soft phase, FLX985) were employed (both from Stratasys, USA). The hard and soft phases were selected such that the ratio of the elastic modulus of the hard phase ( $E_h \cong 60$  MPa) to that of the soft phase ( $E_s \cong 0.60$  MPa) was around 100. We designed a pin and gripper system to attach the printed specimens to the mechanical testing machine. These parts were 3D printed using a fused deposition modeling (FDM) 3D printer (Ultimaker 2+, Geldermalsen, the Netherlands) from polylactic acid (PLA) filaments (MakerPoint PLA, 750 gr,

Natural). A mechanical testing machine (LLOYD instrument LR5K, load cell = 100 N) was used to load the specimens under tension (stroke rate = 1 mm/min). The applied displacement and the reaction force were recorded to obtain the stress-strain curve by dividing the force by the initial cross-section area and dividing the displacement by the initial length of the specimen. The slope of the stress-strain curve represents the overall stiffness of the sample. This procedure was repeated for a total of ten specimens. In addition, we used a digital camera to capture the lateral deformations of the specimens at the different steps of the applied longitudinal displacement. We used image analysis (a custom-made MATLAB code) to measure the transverse strain for all the lattice structures. The axial strain was directly measured from the crosshead displacement of the mechanical testing machine. We, then, defined the Poisson's ratio as  $\nu = -\frac{\epsilon_{trans}}{\epsilon_{axial}}$  (the calculation of  $\epsilon_{trans}$  and  $\epsilon_{axial}$  was the same as computational models).

We also used the DIC technique to measure the full-field strain distribution during the uniaxial tensile tests for the selected single unit cell lattice structures. The surface of the specimens was first painted white. A spackle pattern was then applied to the surface using an airbrush. We used a DIC system (Q400-3D-12MP, LIMESS Messtechnik u. Software GmbH, Germany) equipped with two cameras (DCM 12.0 Mpixel, digital monochrome high performance GigE camera) to record a series of image pairs from two different angles that were later analyzed with the help of the associated commercial software (Istra4D, Germany) to establish the correlations in the images and calculate the full-field strain maps (Figure 1a).

## 5.3. Results and discussion

### 5.3.1. Training and performance of the deep learning models

Using a Workstation (CPU = Intel® Core™ i9-8950HK, RAM = 32.0 GB) and one running script, each FE simulation could be performed between  $6.2 \times 10^{-2} \pm 2.7 \times 10^{-3}$  s and  $6.5 \times 10^{-3} \pm 8.2 \times 10^{-4}$  s while each deep learning prediction

### 5.3. Results and discussion

took between  $8.3 \times 10^{-2} \pm 2.9 \times 10^{-3}$  s and  $1.2 \times 10^{-5} \pm 1.2 \times 10^{-6}$  s depending on the number of simultaneously run simulations/predictions (a comparison between the FE simulation time and the deep learning prediction time for the single unit cell model is presented in Supplementary Figure 1). The solution time per design also depends on the number of scripts run in parallel. For instance, for  $10^5$  simultaneously run simulations and  $10^6$  simultaneously run deep learning predictions, each FE simulation could be performed within  $5.0 \times 10^{-3} \pm 4.9 \times 10^{-4}$  s -  $2.5 \times 10^{-3} \pm 1.3 \times 10^{-4}$  s while each deep learning prediction took between  $1.3 \times 10^{-5} \pm 1.8 \times 10^{-7}$  s and  $2.4 \times 10^{-6} \pm 1.2 \times 10^{-7}$  s depending on the number of simultaneously run scripts.

Within 200 epochs of training, the prediction errors (the mean absolute error (MAE) as well as the mean squared error (MSE)) of the single unit cell models reduced from  $6.6 \times 10^{-4}$  and  $1.38 \times 10^{-2}$  to  $1.05 \times 10^{-4}$  and  $6 \times 10^{-3}$ , respectively. Meanwhile, the prediction errors (MSE and MAE) of the validation dataset decreased from  $4.25 \times 10^{-4}$  and  $1.19 \times 10^{-2}$  to  $1.14 \times 10^{-4}$  and  $6.38 \times 10^{-3}$ , respectively. In the case of the four-tile model, the prediction errors (MSE and MAE) corresponding to the training and validation datasets reduced within 200 epochs from (MSE =  $3.1 \times 10^{-4}$ , MAE =  $1.24 \times 10^{-2}$ ) and (MSE =  $1.88 \times 10^{-4}$ , MAE =  $1.02 \times 10^{-2}$ ) to (MSE =  $3.27 \times 10^{-5}$ , MAE =  $4.3 \times 10^{-3}$ ) and (MSE =  $3.68 \times 10^{-5}$ , MAE =  $4.6 \times 10^{-3}$ ). The coefficients of determination of the single unit cell and four-tile deep learning models were respectively  $9.98 \times 10^{-1}$  and  $9.98 \times 10^{-1}$  (Supplementary Table 2), indicating that these models were highly accurate in predicting the mechanical properties of both types of soft-hard lattices. The prediction vs. simulation results and the coefficients of determination for the test datasets are respectively presented in Supplementary Figures 2a and 2b for the single unit cell and four-tile models. Given this high degree of accuracy, the deep learning models were used in the rest of the study for evaluating the mechanical properties of the designed structures.



### 5.3.2. Single unit cell deep learning model

We used the trained ‘single unit cell’ deep learning model to predict the mechanical properties of  $1.5 \times 10^9$  random structures. The predicted ranges of the elastic moduli (*i.e.*,  $E_{11} \in 0$  to 10.94 MPa and  $E_{22} \in 0$  to 0.55 MPa) and Poisson’s ratios (*i.e.*,  $\nu_{12} \in -1.24$  to 1.16 and  $\nu_{21} \in -0.53$  to 0.51) were quite broad (more information is provided in Supplementary Table 3 for the specific subset of data presented in Figure 1). Along direction 1, a wide range of elastic properties (*i.e.*,  $E_{11}$ ,  $\nu_{12}$  duos) were obtained within a conifer cone-like region. In comparison, the range of the elastic properties found for direction 2 (*i.e.*,  $E_{22}$ ,  $\nu_{21}$  duos) was narrower and included several bean-like regions (Figure 1a). High elastic modulus ( $E_{11}$ ) values were achieved when orthogonal unit cells were used, which is expected, given that the deformation of orthogonal unit cells under orthogonal loading is primarily stretch-dominated. Highly negative and highly positive Poisson’s ratios were predicted for the lattices based on the re-entrant and honeycomb unit cells, respectively.  $E_{11}$  and the absolute value of  $\nu_{12}$  were inversely correlated for  $\rho_h$  values up to 80%, after which they were directly correlated (Figure 1a). According to the predictions of the Hashin–Shtrikman theory and the theoretical limits established for composite materials<sup>40,41</sup>, an inverse relationship between the elastic modulus and Poisson’s ratio is expected. However, the direct correlation observed for the  $\rho_h$  values exceeding 80% is caused by the non-affinity imposed by the random distribution of the hard phase within the lattice structures. In another study<sup>42</sup>, we showed that the Poisson’s ratio and the degree of non-affinity ( $\Gamma$ ) are related to each other through a power law for both re-entrant and honeycomb unit cells.

### 5.3. Results and discussion

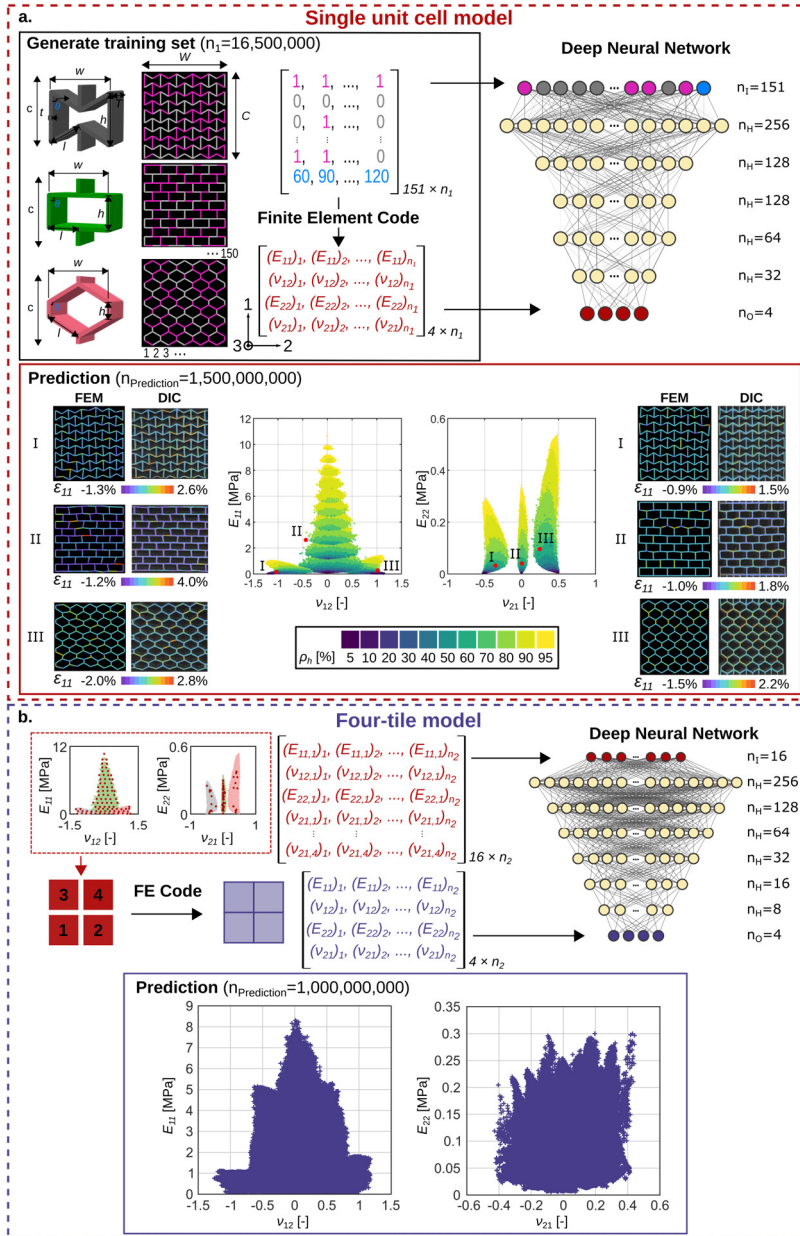


**Figure 1.** The structures of the optimized deep learning models as well as relevant training procedures and the range of attainable mechanical properties for single unit cell model (a) and four-tile model (b). The strain distribution and deformation patterns obtained from FEM and DIC for selected representative designs are presented in (a). Given the very large number of data points which makes the generation of the plots challenging, only the data points for which the FE models were directly solved (i.e., 1% of the data points) are plotted in Figure 1.

Furthermore, it was concluded that regardless of the type of the unit cell and the level of the applied strain, the degree of non-affinity increases with  $\rho_h$  until a maximum value is reached at  $\rho_h = 75\% - 90\%$  after which it decreases to reach  $\Gamma = 0$  for the structures only made from the hard phase (i.e.,  $\rho_h = 100\%$ ). These statements clearly explain the asymmetry in the plot of  $E_{11}$  vs.  $\nu_{12}$  for both re-entrant and honeycomb types of the unit cells.

### 5.3.4. Role of multi-material design

In the single unit cell model, the ranges of both elastic moduli ( $E_{11}$ ,  $E_{22}$ ) monotonically increased with  $\rho_h$  regardless of the type of unit cell (Figure 2a). This is expected, given that increasing the volume ratio of the hard phase to the soft phase simply increases the elastic modulus of the composite lattice structure. The plots of the Poisson's ratios vs.  $\rho_h$  were not monotonic with the absolute values of  $\nu$  initially increasing until a global extremum was reached for  $\rho_h > 50\%$  (i.e., 60 – 80%), followed by a decreasing trend. For all the three types of unit cells, the ranges of the attainable Poisson's ratios were the widest for  $\rho_h = 60 - 80\%$ . This is the range where the multi-material nature of the designs plays the most important role in determining the Poisson's ratio of the lattice structure, given that both phases have comparable effects. For smaller or larger values of  $\rho_h$ , either the soft or the hard phase dominates the mechanical response of the lattice structure, respectively. For a fixed value of the Poisson's ratio (i.e.,  $\nu_{12} = -1 \pm 0.01$ ,  $\nu_{12} = 0 \pm 0.01$ , and  $\nu_{12} = 1 \pm 0.01$ ), a wide range of elastic moduli were achieved, depending on the type of unit cell and  $\rho_h$  (Figure 2b). For fixed values of  $\nu$  and  $\rho_h$ , the largest range of the elastic moduli was achieved for the larger  $\rho_h$ . For example, for the designs with orthogonal unit cells and with a  $\rho_h$  value of 80%, the elastic modulus can change by up to 10.7 folds, depending on how the hard and soft phases are assigned to the lattice structure and without any noticeable change in the Poisson's ratio (i.e.,  $\nu_{12} = 0 \pm 0.01$ ). This highlights the importance of multi-material design aspect in the tunability of the elastic properties of mechanical metamaterials.

#### 5.3.5. Stiff double-auxetic structures

We also studied how the assignment of hard and soft phases in multi-material lattices as well as combining different types of unit cells in a four-tile structure could be used to achieve double-auxetic, yet stiff structures. When combining different types of unit cells, one of the chosen unit cell types should always be the re-entrant unit cell, leading to four possible combinations. To study the probability of finding double-auxetic structures with high stiffness values, we defined a characteristic number (*i.e.*,  $\alpha = \bar{E}_1 \times \bar{E}_2 \times \bar{\nu}_{12} \times \bar{\nu}_{21}$ ) that sums up the effects of both the Poisson's ratios and stiffness in a single number. The overline refers to the fact that all the properties (*i.e.*,  $E_1$ ,  $E_2$ ,  $\nu_{12}$ , and  $\nu_{21}$ ) were normalized between 0 and 1. We calculated  $\alpha$  for all the double-auxetic single unit cell and four-tile model structures (Supplementary Table 4 and Supplementary Figure 3). Among all the single unit cell and four-tile lattice structures plotted in Figure 1, 0.08% and 0.58% (respectively) had  $\alpha$  values that were 5 standard deviations higher than their corresponding mean values. Furthermore, the results indicated that a four-tile combination of unit cells enables us to achieve double-auxetic, yet stiff lattice structures (Figure 2c). Double-auxeticity is a rare event on its own<sup>18</sup>, let alone combined with high stiffness, further underscoring the importance of the implemented design strategies. Furthermore, the presented combinations of different unit cell types enable a better coverage of the  $(E_{11}, E_{22})$  and  $(\nu_{12}, \nu_{21})$  planes.

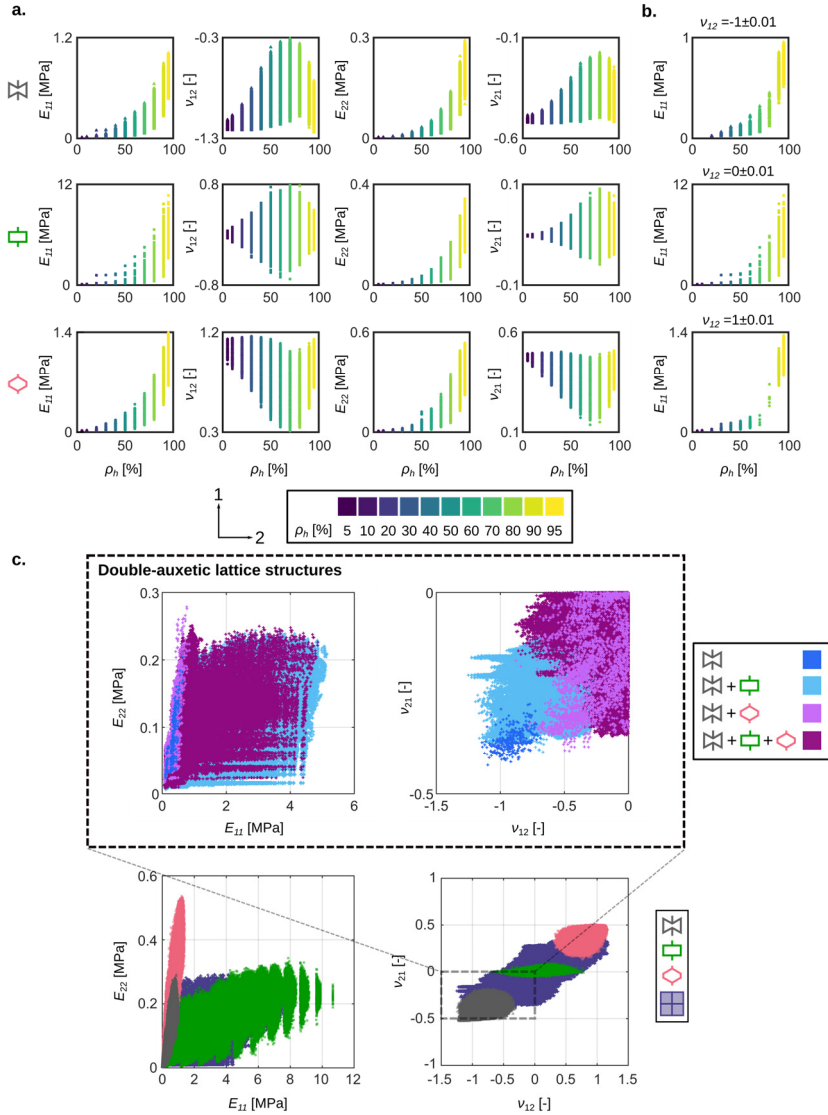


**Figure 2.** The elastic properties of studied lattice structures with a focus on double-auxetic lattices. (a) the elastic properties ( $E_{11}$ ,  $\nu_{12}$ ,  $E_{22}$ , and  $\nu_{21}$ ) of the different types of unit cells for the different values of  $\rho_h$ . (b) the achievable range of the elastic moduli for some specific values of the Poisson's ratio (*i.e.*,  $\nu_{12} = -1 \pm 0.01$ ,  $\nu_{12} = 0 \pm 0.01$ , and  $\nu_{12} = 1 \pm 0.01$ ) considering the different values of  $\rho_h$ . (c) the elastic properties corresponding to the single unit cell and four-tile designs with a focus on double-auxetic lattices. The magnified view shows the distribution of double-auxetic structures by types of unit cells of constituent designs. Given the very large number of data points which makes the generation of the plots challenging, only the data points for which the FE models were directly solved (*i.e.*, 1% of the data points) are plotted in Figure 2.

#### 5.3.6. Tiled and transformed structures

We selected the following single unit cells designs for a more in-depth study: a design with the highest values of  $E_{11}$  and  $E_{22}$  from the orthogonal unit cell group ( $E_{11} = 9.67$  MPa,  $E_{22} = 0.31$  MPa,  $\nu_{12} = -0.04$ , and  $\nu_{21} = 0.00$ ), a design with the most negative value of the Poisson's ratio and almost the highest elastic modulus from the re-entrant unit cell group ( $E_{11} = 0.93$  MPa,  $E_{22} = 0.26$  MPa,  $\nu_{12} = -1.17$ , and  $\nu_{21} = -0.45$ ), and a design with the most positive value of the Poisson's ratio and an almost highest elastic modulus from the honeycomb unit cell group ( $E_{11} = 1.31$  MPa,  $E_{22} = 0.52$  MPa,  $\nu_{12} = 1.05$ , and  $\nu_{21} = 0.47$ ). We then arranged these designs into four-tile (Figure 3) and nine-tile (Figure 4) structures and obtained their mechanical properties and deformation patterns both computationally and experimentally. Moreover, we studied how a 90-degree rotation of a design would affect the mechanical properties of the combined structures (Figure 3). We found that combining the abovementioned designs further expanded the space of achievable elastic properties, filling the gaps in mechanical properties of individual unit cells. For instance, in structure 1 (Figure 3) and structure 5 (Figure 4), the combination of re-entrant and orthogonal unit cells boosted the elastic modulus ( $E_{11}$ ) of the constituent re-entrant unit cell by 75.6% and 91.4%, respectively, while the Poisson's ratio maintained its extreme negative values ( $|\nu_{12}|$  reduced by 6.6% and 9.4%, respectively). In structure 2 (Figure 3) and structure 6 (Figure 4), the combination of honeycomb and orthogonal unit cells boosted the elastic modulus ( $E_{11}$ ) of the constituent honeycomb unit cell by 40% and 40.4%, respectively, while the extreme positive Poisson's ratios did not change much ( $|\nu_{12}|$  reduced only by 1.4% and 2.8%, respectively).

We also showed that with a 90-degree rotation of a design, we could increase the elastic modulus in the weak direction ( $E_{22}$ ) and create structures with a higher level of isotropy. In this way, we could achieve structures with a higher elastic modulus ( $E_{22}$ ) than both types of their constituent designs. For example, the elastic

modulus ( $E_{22}$ ) of structure 3 was 56.2% and 31% higher than the elastic modulus ( $E_{22}$ ) of the constituent re-entrant and orthogonal unit cells, respectively (Figure 3). In structure 4 (Figure 3), the elastic modulus ( $E_{22}$ ) was 4.5% and 75.3% higher than the elastic modulus ( $E_{22}$ ) of the constituent honeycomb and orthogonal unit cells, respectively.

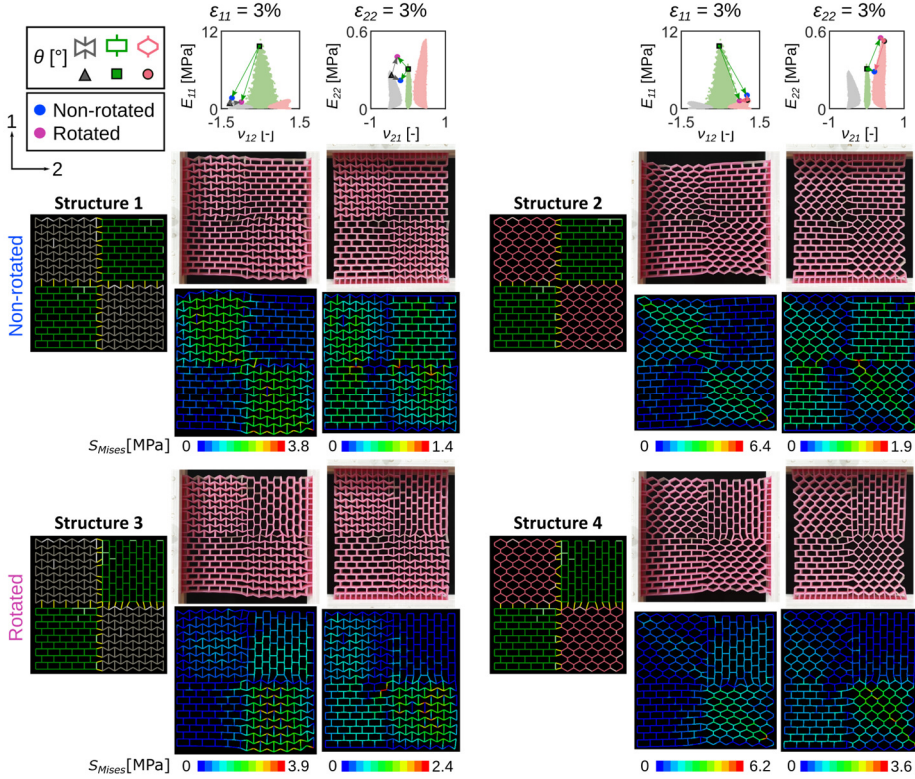


**Figure 3.** Different combinations of designs with extreme mechanical properties which are selected from each group of the unit cells (*i.e.*, a re-entrant structure with a highly negative Poisson's ratio, a honeycomb structure with a highly positive Poisson's ratio, and an orthogonal structure with a high value of the elastic modulus). The mechanical properties of two four-tile structures with non-rotated and rotated tiles and the distribution of the von Mises stresses in these lattice structures. These multi-material 3D printed specimens were mechanically tested in both the 1- and 2-directions under 3% tensile strain and the experimental results were compared with the FE simulation results (Table 2).

### 5.3. Results and discussion

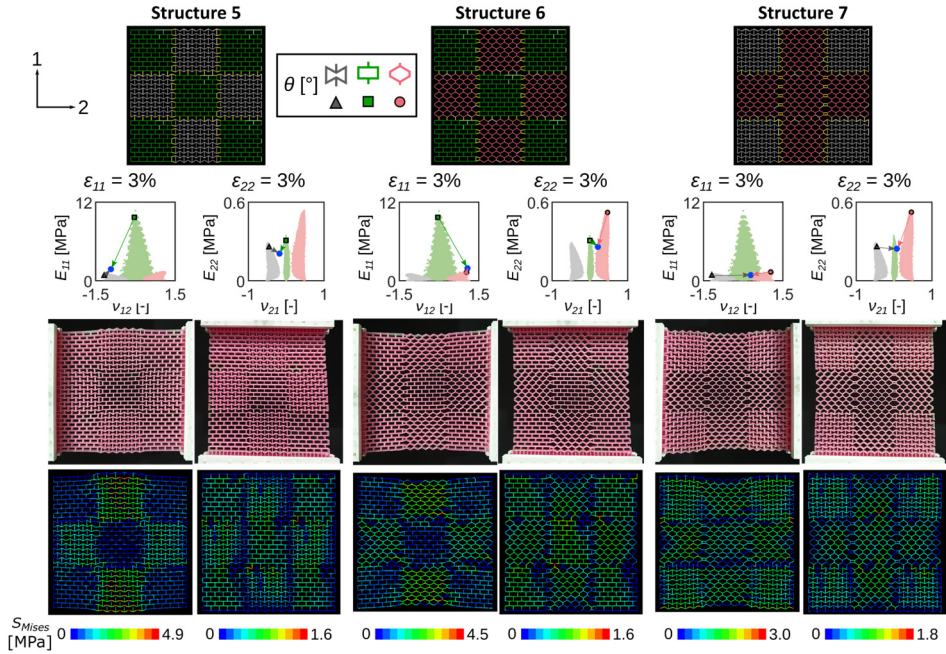


**Figure 4.** Different combinations of designs with extreme mechanical properties which are selected from each group of the unit cells (*i.e.*, a re-entrant structure with a highly negative Poisson's ratio, a honeycomb structure with a highly positive Poisson's ratio, and an orthogonal structure with a high value of the elastic modulus). The mechanical properties of nine-tile combinations and the von Mises stress distribution in these combinations. These multi-material 3D printed specimens were mechanically tested in both the 1- and 2-directions under 3% tensile strain, and the experimental results were compared with the FE simulation results (Table 2).

We also showed how the change of boundary conditions would affect the deformation patterns and also contributed to a more uniform stress distribution within the lattice structure. In all designs, the experimental observations regarding the deformation patterns as well as the experimental values of the mechanical properties clearly agreed with our computational results (Table 2), confirming the validity of the computational approach used here.

Furthermore, the combination of structures with different types of unit cells allows for different functionalities. For instance, the hybrid combination of negative Poisson's ratios with positive values could be used to design orthopedic implants with improved longevity<sup>43</sup>. Combining different types of unit cells could create



action-at-a-distance behavior that enables different patterns of local actuation using a single far-field deformation and has various potential applications in soft robotics<sup>44</sup>. Here, we also showed that combining different unit cells allows for shape-morphing boundaries as well as for specific values of the Poisson's ratio. For instance, different shape-morphing boundaries were observed in structure 7 (Figure 4) when re-entrant and honeycomb unit cells were combined with each other, while the designed structure had a zero value of the Poisson's ratio in both directions. Such properties are of high interest in high added value industries, such as the biomedical and aeronautical industries, as they exhibit improved damping performance<sup>45</sup>.

**Table 2.** Comparisons between the computationally determined and experimentally measured elastic properties of the multi-tile designs.

Type	Structure number	FE simulation				Experimental test			
		$E_{11}$	$E_{22}$	$\nu_{12}$	$\nu_{21}$	$E_{11}$	$E_{22}$	$\nu_{12}$	$\nu_{21}$
		[MPa]	[MPa]			[MPa]	[MPa]		
Four-tile	1	1.63	0.22	-1.10	-0.21	1.64	0.38	-0.96	-0.32
	2	1.83	0.28	1.03	0.22	1.77	0.19	0.95	0.27
	3	1.02	0.41	-0.74	-0.31	0.99	0.57	-0.64	-0.25
	4	1.17	0.54	0.76	0.38	1.08	0.35	0.68	0.26
Nine-tile	5	1.78	0.21	-1.06	-0.17	1.13	0.26	-0.91	-0.21
	6	1.84	0.26	1.08	0.21	1.78	0.24	0.96	0.15
	7	0.83	0.24	0.29	0.08	0.77	0.27	0.26	0.11

### 5.3.7. Uniformity of stress distribution

To date, most studies on mechanical metamaterials have focused on the elastic properties of architected lattices without paying much attention to the structural integrity aspects including the risk of failure due to such phenomena as stress concentrations. Generally speaking, the presence of stress concentration leads to premature failure caused by premature initiation and growth of cracks. It is,

### 5.3. Results and discussion

therefore, desirable to distribute the stresses as uniformly as possible within the lattice structure. An important advantage of having giga-sized databases of possible designs with the corresponding elastic properties is the possibility to apply additional design criteria, such as the one related to the uniformity of the stress distribution.

For example, among all the single unit cell designs with the same range of elastic properties (*i.e.*,  $0.15 < E_{11} < 0.25$ ,  $-1.1 < \nu_{12} < -1$ ,  $0.01 < E_{22} < 0.08$ , and  $-0.45 < \nu_{21} < -0.3$ ), we studied the uniformity of the stress distributions within the lattice structure. In total, 207 tiles with various  $\rho_h$  values (*i.e.*, 50, 60, 70, and 80%) were included (Figure 5a). The maximum values of the von Mises stress in the structural elements of these designs were calculated while these designs were subjected to two different boundary conditions (*i.e.*,  $\varepsilon_{11} = 3\%$  or  $\varepsilon_{22} = 3\%$ ) (Figure 5b). Although the elastic properties of these designs were generally very similar, the maximum von Mises stresses in their struts varied up to 2.5 and 6.5 times along the loading conditions 1 and 2, respectively. This finding indicates the importance of applying an additional design rule regarding the stress uniformity within the structure. For that reason, two designs with  $\rho_h = 70\%$  (one with the minimum and one with the maximum Euclidean distance from the origin) were selected for a more in-depth analysis (Figure 5b and 5c). A closer study of the stress distributions in these two structures showed a clear incident of stress concentration in design 2 while design 1 exhibited more uniform stress distributions (Figure 5d). Such types of stress risers are the primary zones for crack initiation and will ultimately result in premature fracture. It is, therefore, important to consider stress uniformity as an additional design requirement in the design of mechanical metamaterials. It should also be mentioned that the maximum von Mises stresses in soft and hard struts of these selected designs are lower than the tensile strengths of the individual materials in the bulk form.

We also studied the distribution of the compressive or tensile axial stresses ( $S_{11}$ ) in individual struts of the selected designs under the aforementioned boundary

conditions. That included  $S_{11@ \varepsilon_{22}=3\%}$  vs.  $S_{11@ \varepsilon_{11}=3\%}$  values as well as 95% confidence ellipses fitted to the stress values of individual struts for the multi-material designs (Figure 5e). We then compared these results with the axial stresses obtained from a lattice structure with  $\rho_h = 70\%$  and equivalent homogenous material properties (Figure 5e). This comparison highlighted that the lattice design with a lower stress riser point (*i.e.*, design 1) was located inside the confidence ellipse of the design with the equivalent homogenous material (Figure 5e). Such an approach can, therefore, be considered as additional design rule for selecting the optimum multi-material design with target properties.

### 5.3. Results and discussion

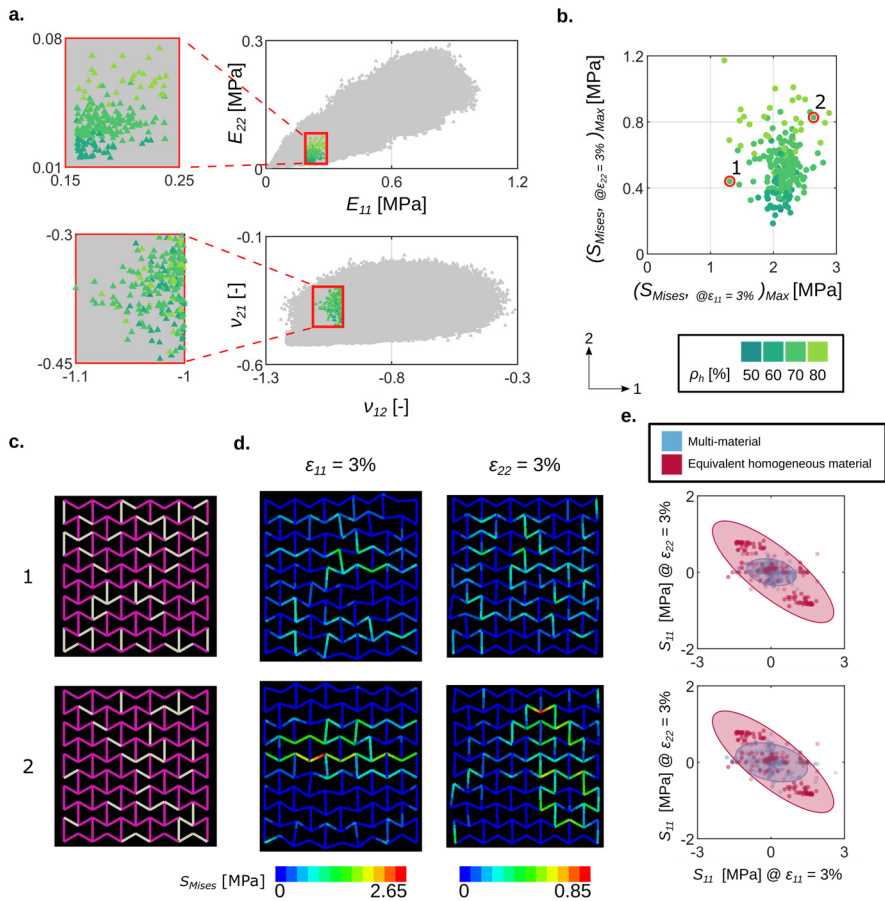
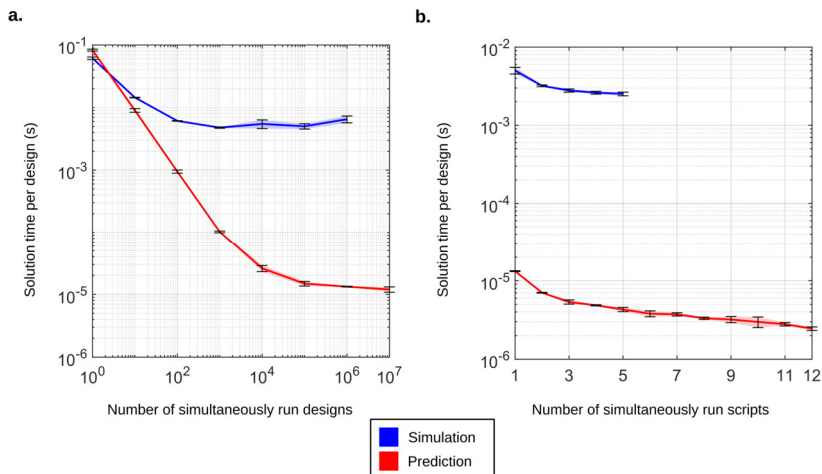


**Figure 5.** Stress distribution within the lattice structure. (a) the selection of a certain range of the elastic properties achieved for the unit cells with a cell angle of  $60^\circ$ . In total, the elastic properties of 207 designs with various  $\rho_h$  values (*i.e.*, 50, 60, 70, and 80) fall within these selected ranges. (b) the maximum values of the von Mises stress in the structural elements of the corresponding lattice structures when these structures were subjected to two boundary conditions (*i.e.*,  $\epsilon_{11} = 3\%$  or  $\epsilon_{22} = 3\%$ ). Two designs were selected, including one with the minimum (node 1) and one (node 3) with the maximum Euclidean distance from the origin (b and c). The distribution of the von Mises stresses in the selected designs and their deformations under two boundary conditions (*i.e.*,  $\epsilon_{11} = 3\%$  and  $\epsilon_{22} = 3\%$ ) are presented in (d). The axial stresses ( $S_{11}$ ) in the struts of each design under two boundary conditions (*i.e.*,  $\epsilon_{11} = 3\%$  or  $\epsilon_{22} = 3\%$ ) are calculated and are compared with the axial stresses of the corresponding struts when the lattice structure is composed of an equivalent homogenous material (e).

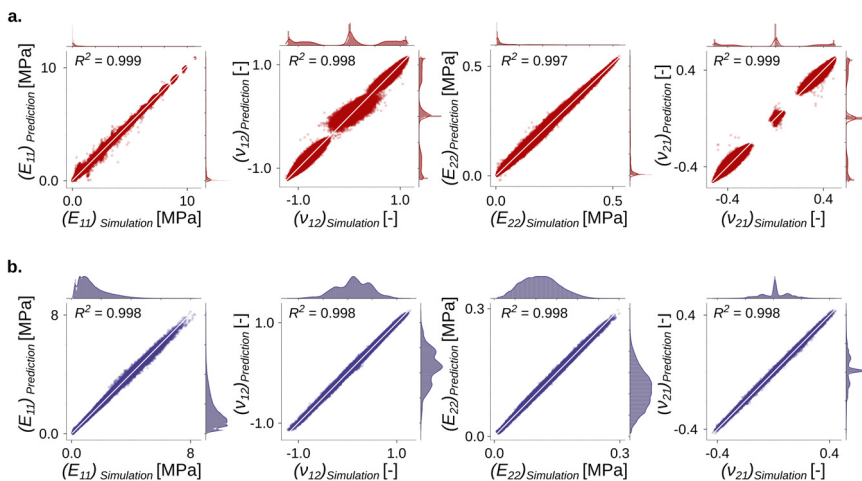
## 5.4. Conclusion

In conclusion, deep learning models can accurately predict the mechanical properties of multi-materials mechanical metamaterials, reduce the speed of evaluating each design, and make parallel computing efficient and straightforward to the point where evaluating  $10^{10} - 10^{20}$  designs is within reach. Our results show that such unprecedented sizes of the design database enable the rational design of multi-material mechanical metamaterials that not only achieve a very wide range of elastic properties but also meet additional design requirements. For example, we demonstrated that double-auxetic yet stiff designs can be realized using this approach. In this study, we examined two essential parameters in the design of multi-material mechanical metamaterials, namely the ratio of the volume of the hard phase to that of the soft phase ( $\rho_h$ ) and the angle of the unit cells. In all simulations, the ratio of the elastic modulus of the hard phase to that of the soft phase was assumed to be constant and equal to 100. As increasing this ratio can increase the degree of non-affinity of the lattice structure<sup>42</sup>, it can have an influence on their overall mechanical properties. Therefore, this parameter can be further studied and considered as an input parameter for the training of the model to explore a broader range of mechanical properties. Another application demonstrated here is the addition of a criterion regarding stress uniformity that can reduce stress concentration in such types of mechanical metamaterials, thereby increasing their fracture and fatigue resistance.

## 5.5. Supplementary document



**Supplementary Figure 1.** The solution time per design. The solution time per design depends on the number of simultaneously run simulations/predictions as well as the number of scripts run in parallel. A comparison between the finite element simulation time (MATLAB) and the deep learning prediction time (Python) for the single unit cell model (a) for the different numbers of simultaneously run simulations/predictions (without any parallelization) and (b) for the different numbers of in-parallel run scripts (105 simultaneously run finite element simulations and 106 simultaneously run deep learning predictions per script). The standard deviation of the reported times was calculated by repeating each experiment three times.



**Supplementary Figure 2.** The evaluation of the trained deep learning models. The prediction vs. simulation results and the coefficients of determination for the test datasets for (a) the single unit cell model and (b) four-tile model.

**Supplementary Table 1.** The total number of possible designs.

Group number	$\rho_h$ [%]	Number of hard elements	Number of possible designs	Number of possible designs considering symmetry
1	5	8	$5.25721 \times 10^{12}$	$1.31400 \times 10^{12}$
2	10	15	$1.62392 \times 10^{20}$	$4.05981 \times 10^{19}$
3	20	30	$3.21988 \times 10^{31}$	$8.04970 \times 10^{30}$
4	30	45	$4.41669 \times 10^{38}$	$1.10417 \times 10^{38}$
5	40	60	$4.62150 \times 10^{42}$	$1.15537 \times 10^{42}$
6	50	75	$9.28261 \times 10^{43}$	$2.32065 \times 10^{43}$
7	60	90	$4.62150 \times 10^{42}$	$1.15537 \times 10^{42}$
8	70	105	$4.41660 \times 10^{38}$	$1.10417 \times 10^{38}$
9	80	120	$3.21988 \times 10^{31}$	$8.04970 \times 10^{30}$
10	90	135	$1.62392 \times 10^{20}$	$4.05981 \times 10^{19}$
11	95	142	$5.25721 \times 10^{12}$	$1.31430 \times 10^{12}$
Sum			$1.02070 \times 10^{44}$	$2.55175 \times 10^{43}$
Total number considering three groups of unit cells with positive, zero, and negative values of the Poisson's ratio				$7.65525 \times 10^{43}$

**Supplementary Table 2.** The coefficients of determination, the mean absolute error (MAE), and the mean squared error (MSE) for the outputs of the single unit cell and four-tile deep learning models.

		Coefficient of determination ( $R^2$ )	MSE	MAE
Single unit cell model	Total	$9.98 \times 10^{-1}$	$1.14 \times 10^{-4}$	$6.38 \times 10^{-3}$
	$E_{11}$	$9.99 \times 10^{-1}$	$2.18 \times 10^{-5}$	$2.65 \times 10^{-3}$
	$E_{22}$	$9.97 \times 10^{-1}$	$8.96 \times 10^{-5}$	$5.51 \times 10^{-3}$
	$\nu_{12}$	$9.98 \times 10^{-1}$	$2.34 \times 10^{-4}$	$1.04 \times 10^{-2}$
	$\nu_{21}$	$9.99 \times 10^{-1}$	$1.11 \times 10^{-4}$	$6.96 \times 10^{-3}$
Four-tile model	Total	$9.98 \times 10^{-1}$	$3.77 \times 10^{-5}$	$4.58 \times 10^{-3}$
	$E_{11}$	$9.98 \times 10^{-1}$	$2.96 \times 10^{-5}$	$3.86 \times 10^{-3}$
	$E_{22}$	$9.98 \times 10^{-1}$	$4.80 \times 10^{-5}$	$5.30 \times 10^{-3}$
	$\nu_{12}$	$9.97 \times 10^{-1}$	$4.92 \times 10^{-5}$	$5.46 \times 10^{-3}$
	$\nu_{21}$	$9.98 \times 10^{-1}$	$2.38 \times 10^{-5}$	$3.69 \times 10^{-3}$

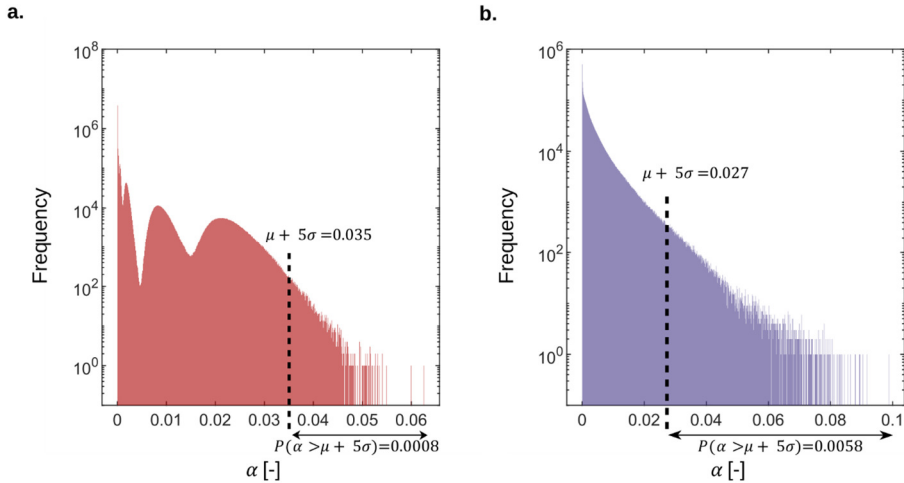
## 5.5. Supplementary document

**Supplementary Table 3.** The range of the elastic properties for the single unit cell lattice structures corresponding to the data presented in Figure 1.

Type of unit cell	$E_{11}$ [MPa]		$E_{22}$ [MPa]		$\nu_{12}$ [-]		$\nu_{21}$ [-]	
	min	max	min	max	min	max	min	max
$\theta = 60^\circ$	0.01	1.02	0.00	0.29	-1.24	-0.31	-0.53	-0.17
$\theta = 90^\circ$	0.11	10.67	0.00	0.34	-0.70	0.78	-0.06	0.09
$\theta = 120^\circ$	0.01	1.39	0.00	0.54	0.31	1.16	0.14	0.51

**Supplementary Table 4.** The probability of finding  $\alpha$  values that are one, two, three, four, or five standard deviations higher than their corresponding mean value. To calculate  $\alpha$ , we first normalized all the properties (i.e.,  $E_1$ ,  $E_2$ ,  $\nu_{12}$ , and  $\nu_{21}$ ) between 0 and 1.

$P(\alpha > \mu + x\sigma)$	Model	$\mu + \sigma$	$\mu + 2\sigma$	$\mu + 3\sigma$	$\mu + 4\sigma$	$\mu + 5\sigma$
	Single unit cell		0.111	0.078	0.041	0.007
Four-tile		0.108	0.047	0.022	0.011	0.0058



**Supplementary Figure 3.** The histogram of  $\alpha$ . These histograms are for the double-auxetic lattice structures plotted in Figure 1: (a) single unit cell and (b) four-tile models.

**Supplementary Table 5.** The geometrical parameters of the designed single unit cell lattices.

$\theta$ [°]	$W$ [mm]	$C$ [mm]	$w$ [mm]	$c$ [mm]	$l$ [mm]	$h$ [mm]	$t$ [mm]	$T$ [mm]
60	56.25	56.25	11.25	12.5	6.50	9.50	1	10
90	56.25	56.25	11.25	12.5	5.63	6.25	1	10
120	56.25	56.25	11.25	12.5	6.50	3.00	1	10



### 5.5.1. Supplementary methods

#### Hyperparameter tuning of single unit cell model:

For the training of the single unit cell model, we used a sequential model composed of a linear stack of fully connected layers. Before training the model, we configured the learning process by defining several parameters, including an optimizer (RMSprop), a list of metrics (Mean Squared Error (MSE) and Mean Absolute Error (MAE)), and a loss function (MSE), which is the objective that the model will try to minimize.

In this model, we systematically studied the effects of different hyperparameters (*i.e.*, the number of hidden layers, the number of neurons in each hidden layer, learning rate, and activation function) on the performance of the deep learning model. To evaluate the performance of the model with different hyperparameter values and also to detect overfitting during the training process, we created a subset of the data known as the validation dataset. Therefore, we generated a dataset of 165,000 samples, and then we randomly selected 20% of this dataset as a testing dataset, 80% as a training dataset, and 20% of the training dataset as a validation dataset for hyperparameter tuning. It should be mentioned that for hyperparameter tuning, we trained each model until 20 epochs. This means that during each epoch, the model was trained based on the training data, and was tuned with the results of the metrics (MSE, MAE) for the validation dataset. Therefore, during the training process, the model did not see the validation dataset, while the validation dataset indirectly affected the model. In this way, we tuned the hyperparameters of the model based on the results of metrics for the validation dataset. The following systematic approach explains how those hyperparameters were selected in our models.

**Number of hidden layers:** At the first step, we studied the effects of the number of the hidden layers (*i.e.*, 1, 2, 3, 4, 5, and 6) on reducing the loss function. Towards this aim, six models with different numbers of hidden layers were analyzed, while the rest of the hyperparameters for these models were kept unchanged.

## 5.5. Supplementary document

The number of neurons per each hidden layer: 128 (since we had 151 input parameters, we assumed the number of neurons in each hidden layer to equal 128).

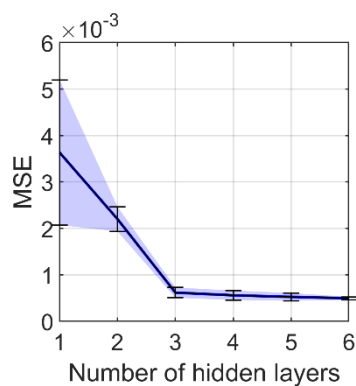
Learning rate: 0.0001.

Activation function: ReLU.

Each model was trained three times to calculate the average and the standard deviation of the loss function (MSE) for each model. Supplementary Table 6 and Supplementary Figure 4 present the comparisons between the six models with different numbers of hidden layers.

**Supplementary Table 6.** The comparison between models with different numbers of hidden layers.

layers	MSE			MSE average	Standard deviation
	Trial 1	Trial 2	Trial 3		
1	0.0034	0.0053	0.0022	0.003633	$1.28 \times 10^{-3}$
2	0.002	0.0021	0.0025	0.0022	$2.16 \times 10^{-4}$
3	0.00049	0.00067	0.00069	0.000616	$9.01 \times 10^{-5}$
4	0.00052	0.00048	0.00067	0.000558	$8.32 \times 10^{-5}$
5	0.00046	0.00049	0.00062	0.000524	$6.81 \times 10^{-5}$
6	0.00046	0.00052	0.00049	0.000494	$2.55 \times 10^{-5}$



**Supplementary Figure 4.** Tuning the number of hidden layers. The comparisons between the MSE of six models with different numbers of hidden layers.

The results of the comparison between the models with different hidden layers showed that the MSE values converged after considering five hidden layers. Also, the low standard deviation indicates that the model is not sensitive to the randomly selected training dataset. Therefore, we selected five hidden layers as an optimum number of hidden layers for our model.

**Number of neurons in each hidden layer:** In the second step, we optimized the number of neurons in each hidden layer using “Hyperparameter Tuning” with the HParams Dashboard of Tensorboard<sup>38</sup>. Towards this aim, we selected the possible number of neurons per layer:

Layer 1: 256 and 128 neurons

Layer 2: 128 and 64 neurons

Layer 3: 128 and 64 neurons

Layer 4: 64 and 32 neurons

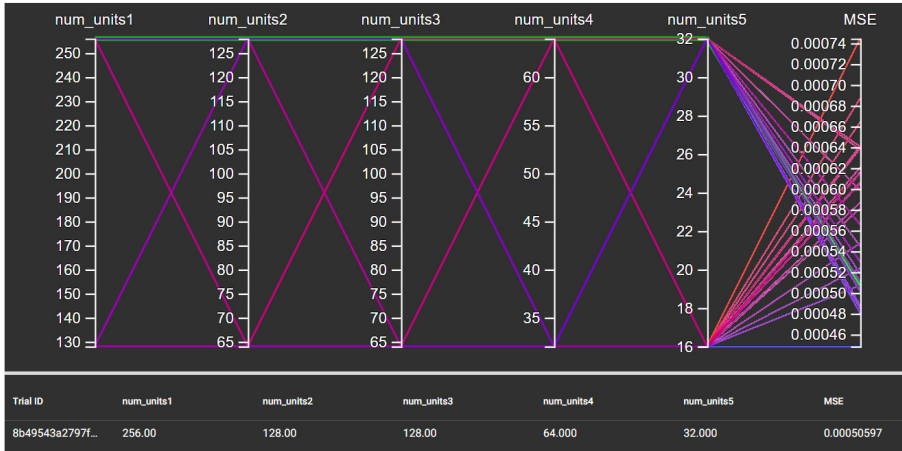
Layer 5: 32 and 16 neurons

Since we had five layers and we assumed two possibilities for each layer, there were  $2^5 = 32$  possible combinations that were studied to find the best combination. The model was trained for each combination, and the loss function (MSE) was calculated for each trained model. Also, we repeated the training process three times, and we compared the average and standard deviation of the loss function (MSE). As an example, Supplementary Figure 5 shows the parallel coordinate plot for the results of the second trial of the optimization of the number of neurons. Supplementary Table 7 summarizes the results of model training for different combinations of neurons per hidden layer. The results in this table were sorted based on the average and standard deviation of MSE. The best combination with the lowest averages of MSE was 256-128-128-64-32. This combination had also the lowest standard deviation of MSE among all the 32 combinations, meaning that the results of this combination were less sensitive to the selected training dataset

## 5.5. Supplementary document

**Supplementary Table 7.** The comparisons between the trained models with different numbers of neurons per hidden layer.

Combination number	Number of neurons in each hidden layer					MSE			MSE average	MSE standard deviation
	1	2	3	4	5	Trial 1	Trial 2	Trial 3		
1	256	128	128	64	32	0.000493	0.000506	0.000502	0.0005	$5.64 \times 10^{-6}$
2	256	128	128	32	32	0.00047	0.00048	0.000444	0.000465	$1.52 \times 10^{-5}$
3	128	128	128	32	32	0.000562	0.000545	0.000606	0.000571	$2.56 \times 10^{-5}$
4	128	64	128	32	32	0.000491	0.000504	0.000444	0.00048	$2.58 \times 10^{-5}$
5	256	128	64	32	32	0.000554	0.000501	0.000486	0.000514	$2.91 \times 10^{-5}$
6	128	64	128	64	16	0.000662	0.000581	0.000611	0.000618	$3.32 \times 10^{-5}$
7	128	128	128	64	16	0.00051	0.000587	0.000579	0.000559	$3.44 \times 10^{-5}$
8	128	64	64	64	16	0.000555	0.000616	0.000533	0.000568	$3.50 \times 10^{-5}$
8	128	128	64	64	16	0.000618	0.000606	0.000686	0.000637	$3.51 \times 10^{-5}$
10	128	64	128	32	16	0.000538	0.000605	0.000619	0.000587	$3.54 \times 10^{-5}$
11	128	128	64	32	16	0.000532	0.000615	0.000619	0.000589	$3.99 \times 10^{-5}$
12	256	128	128	64	16	0.000587	0.000524	0.000485	0.000532	$4.22 \times 10^{-5}$
13	128	64	64	64	32	0.000606	0.000565	0.00049	0.000554	$4.78 \times 10^{-5}$
14	256	64	128	32	32	0.000476	0.00053	0.000595	0.000534	$4.84 \times 10^{-5}$
15	256	64	64	64	32	0.00046	0.00051	0.000585	0.000519	$5.15 \times 10^{-5}$
16	256	128	64	32	16	0.000551	0.000448	0.000564	0.000521	$5.18 \times 10^{-5}$
17	128	128	128	64	32	0.000435	0.000488	0.000572	0.000498	$5.66 \times 10^{-5}$
18	256	64	64	32	32	0.00048	0.000599	0.000469	0.000516	$5.87 \times 10^{-5}$
19	256	64	128	64	16	0.000587	0.000744	0.000677	0.000669	$6.46 \times 10^{-5}$
20	128	128	64	64	32	0.000478	0.000638	0.00058	0.000565	$6.59 \times 10^{-5}$
21	128	64	64	32	32	0.000659	0.00053	0.000497	0.000562	$6.99 \times 10^{-5}$
22	128	128	128	32	16	0.000589	0.000639	0.000461	0.000563	$7.48 \times 10^{-5}$
23	256	128	128	32	16	0.000436	0.000548	0.000637	0.00054	$8.24 \times 10^{-5}$
24	256	64	128	64	32	0.000546	0.000641	0.000435	0.00054	$8.42 \times 10^{-5}$
25	128	128	64	32	32	0.00046	0.000518	0.000683	0.000554	$9.42 \times 10^{-5}$
26	256	128	64	64	16	0.000468	0.000641	0.000707	0.000606	$1.01 \times 10^{-4}$
27	128	64	64	32	16	0.000773	0.00062	0.000517	0.000637	$1.05 \times 10^{-4}$
28	256	128	64	64	32	0.000478	0.000565	0.000752	0.000599	$1.14 \times 10^{-4}$
29	256	64	64	64	16	0.000479	0.000664	0.000763	0.000635	$1.18 \times 10^{-4}$
30	128	64	128	64	32	0.00076	0.000485	0.000539	0.000595	$1.19 \times 10^{-4}$
31	256	64	64	32	16	0.000883	0.000507	0.000586	0.000659	$1.62 \times 10^{-4}$
32	256	64	128	32	16	0.000902	0.000687	0.000474	0.000688	$1.75 \times 10^{-4}$



**Supplementary Figure 5.** Tuning the number of neurons in each hidden layer. The green line shows the following combination of neurons : 256-128-128-64-32.

**Learning rate:** We analyzed the effects of the learning rate on the accuracy of the model. We selected three levels for the learning rate (*i.e.*, 0.01, 0.001, and 0.0001) while keeping other hyperparameters unchanged:

- Number of hidden layers: 5.
- Number of neurons per each hidden layer: 256, 128, 128, 64, 32.
- Activation function: ReLU.
- Number of epochs: 20.

Supplementary Table 8 presents the comparison of models trained with different values of the learning rate. This highlights that the learning rate equal to 0.0001 provided the highest accuracy. It was, therefore, selected in our final model.

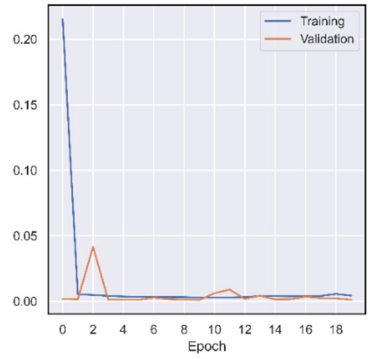
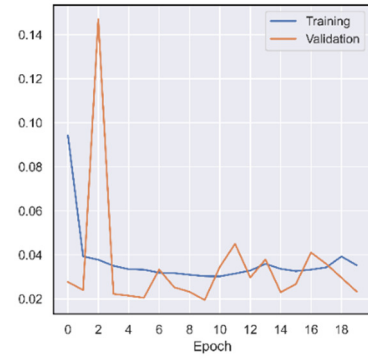
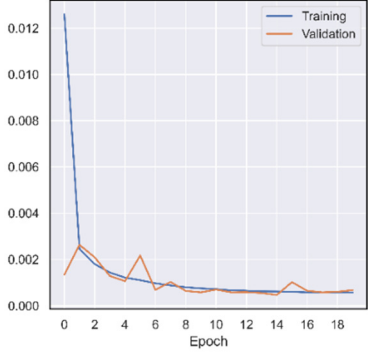
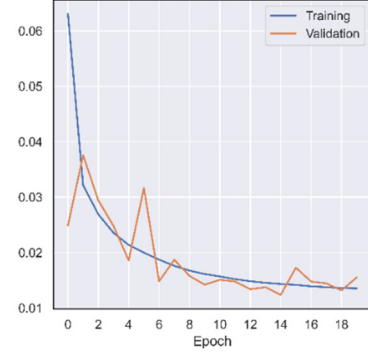
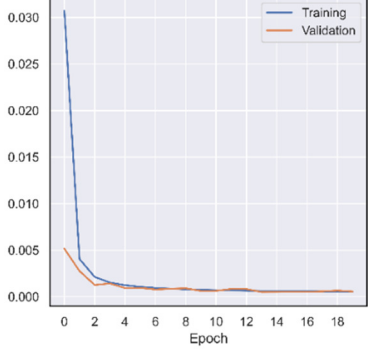
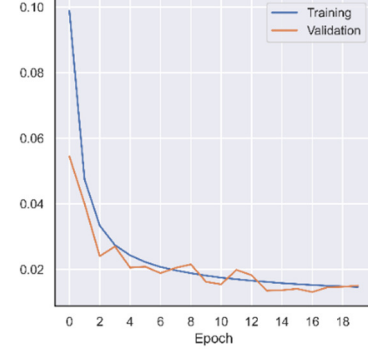
**Activation function:** We also used different activation functions (*i.e.*, ReLU, Sigmoid, and Tanh), while the rest of the hyperparameters were set as follows:

- Number of hidden layers: 5.
- Number of neurons per each hidden layer: 256, 128, 128, 64, 32.
- Learning rate: 0.0001.
- Number of epochs: 20.

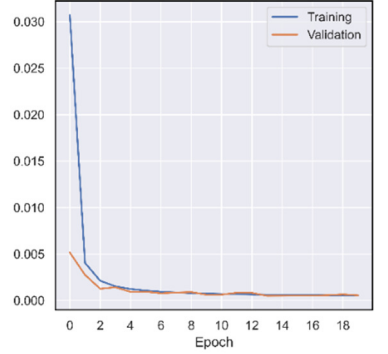
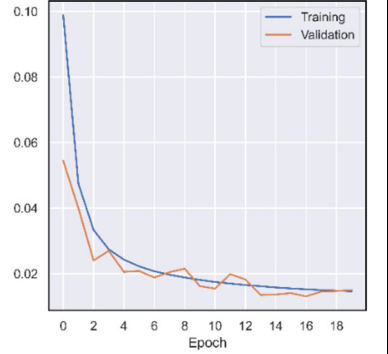
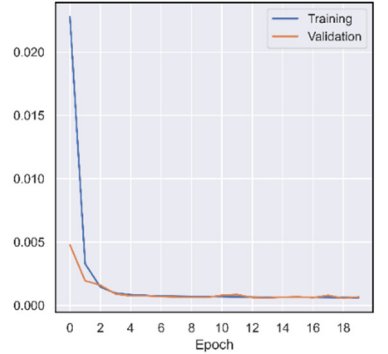
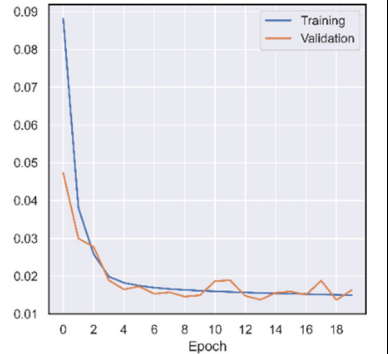
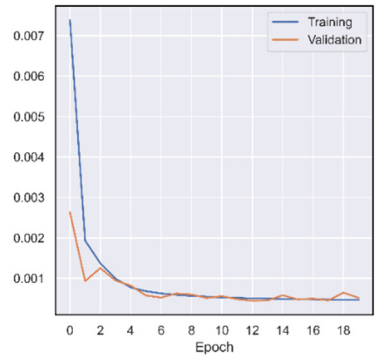
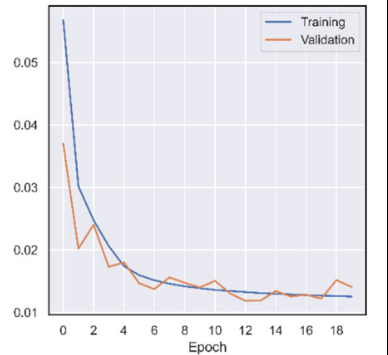
## 5.5. Supplementary document

Supplementary Table 9 shows the results of the comparison between the models trained with different activation functions. Based on these results, we selected the activation function ReLU in our single unit cell models.

**Supplementary Table 8.** The comparison between the models with different values of learning rates.

Learning rate	MSE	MAE	Other parameters
0.01			$R^2$ for testing dataset: $R^2 = 0.958$ $(R^2)_{v_{12}} = 0.991$ $(R^2)_{v_{21}} = 0.995$ $(R^2)_{s_1} = 0.882$ $(R^2)_{s_2} = 0.963$  Training time: 4m, 16s
0.001			$R^2$ for testing dataset: $R^2 = 0.981$ $(R^2)_{v_{12}} = 0.992$ $(R^2)_{v_{21}} = 0.997$ $(R^2)_{s_1} = 0.958$ $(R^2)_{s_2} = 0.975$  Training time: 4m, 18s
0.0001			$R^2$ for testing dataset: $R^2 = 0.986$ $(R^2)_{v_{12}} = 0.992$ $(R^2)_{v_{21}} = 0.997$ $(R^2)_{s_1} = 0.969$ $(R^2)_{s_2} = 0.987$  Training time: 4m, 17s

**Supplementary Table 9.** The results of the comparison between the models trained with different activation functions.

Activation function	MSE	MAE	Other parameters
ReLU			$R^2$ for testing dataset: $R^2 = 0.986$ $(R^2)_{v_{12}} = 0.992$ $(R^2)_{v_{21}} = 0.997$ $(R^2)_{S_1} = 0.969$ $(R^2)_{S_2} = 0.987$  Training time: 4m, 17s
Sigmoid			$R^2$ for testing dataset: $R^2 = 0.982$ $(R^2)_{v_{12}} = 0.993$ $(R^2)_{v_{21}} = 0.995$ $(R^2)_{S_1} = 0.964$ $(R^2)_{S_2} = 0.977$  Training time: 5m, 32s
Tanh			$R^2$ for testing dataset: $R^2 = 0.984$ $(R^2)_{v_{12}} = 0.994$ $(R^2)_{v_{21}} = 0.997$ $(R^2)_{S_1} = 0.962$ $(R^2)_{S_2} = 0.985$  Training time: 5m, 1s

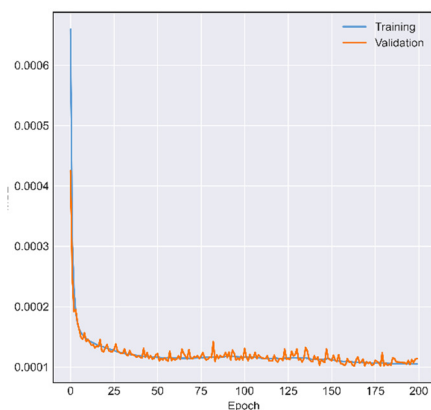
We evaluated the performance of the model based on the coefficient of determination ( $R^2$ ), MSE, and MAE values. The above-mentioned systematic

## 5.5. Supplementary document

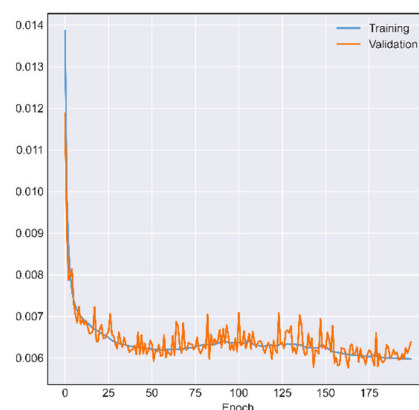
analyses were, therefore, used to determine the optimized architecture and hyperparameters of the model with the highest accuracy (see Table 2).

Once the hyperparameters were set, we increased the size of the training dataset and the number of epochs to improve the accuracy of our model further. Towards this aim, we increased the size of training dataset by 100 times (*i.e.*, a dataset of 16,500,000 lattice structures) and the number of epochs by 10 times (*i.e.*, 200 epochs). Also, we assumed 20% of the training dataset as a validation dataset. In addition, we generated a dataset of 1,650,000 lattice structures as the testing dataset. MSE and MAE graphs for the single unit cell model are presented in Supplementary Figure 6. Quantitatively, the final optimized single unit cell model had a low MSE value of  $1.05 \times 10^{-4}$  and  $1.14 \times 10^{-4}$ , and a low MAE value of  $6 \times 10^{-3}$  and  $6.38 \times 10^{-3}$  for the training and validation datasets, respectively. Moreover, these graphs showed a good agreement between the training and validation datasets, confirming that the model was trained without overfitting.

a.



b.



**Supplementary Figure 6.** a MSE graph and b MAE graph for the single unit cell model.

### Hyperparameter tuning of four-tile model:

To design the architecture of the four-tile model, we selected the optimized hyperparameters obtained from the single unit cell model, namely five hidden layers (the number of neurons: 256-128-128-64-32), ReLU activation function, and a

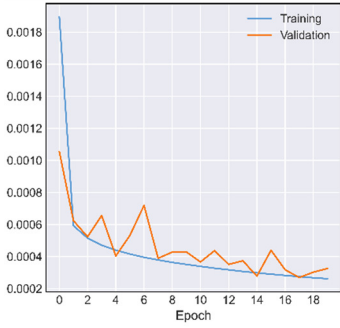
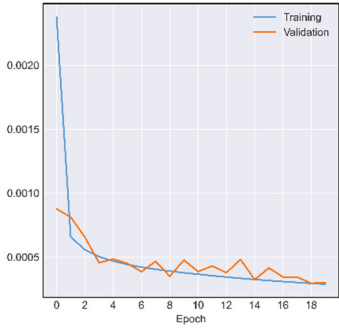


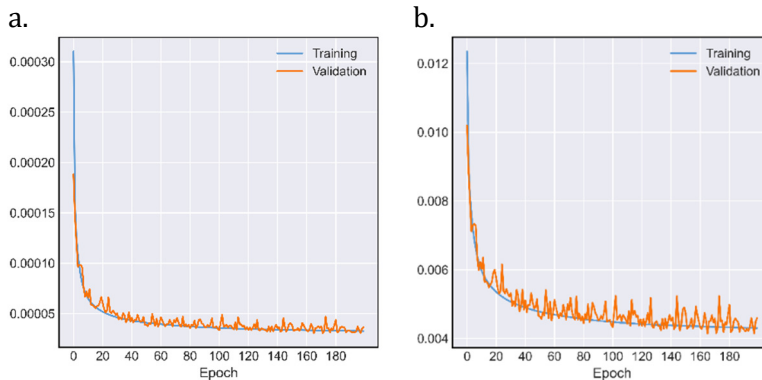
learning rate equal to 0.0001. Furthermore, we trained another model with six hidden layers and the number of neurons was reduced from 256 to 8 (*i.e.*, 256-128-64-32-16-8) to see if we could further improve the accuracy of the model. For these two models, we used a dataset of 250,409 lattice structures, and we randomly selected 20% of the dataset as a testing dataset, 80% as a training dataset, and 20% of the training dataset was randomly selected as a validation dataset. As compared to the model with five hidden layers, the model with six hidden layers had a slightly higher coefficient of determination for the testing dataset and a lower MSE value for the training and validation datasets with 20 epochs (see Supplementary Table 10). Since the six-layer model had low values of MSE and MAE and a high coefficient of determination, and also the MSE graph of this model showed a good agreement between the training and validation datasets to avoid overfitting, we stopped at this model and considered it to be our optimized four-tile model.

Furthermore, we increased the size of the dataset to 15,331,140 lattice structures (60× larger) and the number of epochs by 10 times (*i.e.*, 200 epochs). We randomly selected 90% of the dataset as the training dataset and the remaining 10% as the testing dataset. We also considered 20% of the training dataset for validation. The training procedure took 3569 minutes and 36 seconds. All the training parameters of the final four-tile model are listed in Table 2 of the manuscript. Quantitatively, the four-tile model had a high coefficient of determination of 0.998 and a low MSE value of  $3.77 \times 10^{-5}$  for the testing dataset, and respectively a low MSE value of  $3.27 \times 10^{-5}$  and  $3.68 \times 10^{-5}$  and a low MAE value of  $4.3 \times 10^{-3}$  and  $4.6 \times 10^{-3}$  for the training and validation datasets (see Supplementary Figure 7). Furthermore, the MSE and MAE graphs showed a good agreement between the training and validation datasets, confirming that the model was trained without overfitting.

## 5.5. Supplementary document

**Supplementary Table 10.** The comparison between the four-tile models with five and six hidden layers.

Architecture	5 hidden layers: 256-128-128-64-32	6 hidden layers: 256-128-64-32-16-8
Size of dataset	250,409	250,409
Epochs	20	20
Loss function (MSE)		
Coefficient of determination	$R^2 = 0.982$ $(R^2)_{v_{12}} = 0.967$ $(R^2)_{v_{21}} = 0.994$ $(R^2)_{s_1} = 0.984$ $(R^2)_{s_2} = 0.984$	$R^2 = 0.983$ $(R^2)_{v_{12}} = 0.966$ $(R^2)_{v_{21}} = 0.995$ $(R^2)_{s_1} = 0.983$ $(R^2)_{s_2} = 0.990$
Testing dataset MSE	$3.21 \times 10^{-4}$	$2.98 \times 10^{-4}$
Time	7m, 43s	7m, 21s



**Supplementary Figure 7:** (a) MSE graph and (b) MAE graph for the four-tile model.

## References

1. Al-Ketan, O. *et al.* Microarchitected stretching-dominated mechanical metamaterials with minimal surface topologies. *Adv. Eng. Mater.* **20**, 1800029 (2018).
2. Gibson, L. J. Biomechanics of cellular solids. *J. Biomech.* **38**, 377–399 (2005).
3. Sabet, F. A., Najafi, A. R., Hamed, E. & Jasiuk, I. Modelling of bone fracture and strength at different length scales: a review. *Interface Focus* **6**, 20150055 (2016).
4. Barthelat, F. & Rabiei, R. Toughness amplification in natural composites. *J. Mech. Phys. Solids* **59**, 829–840 (2011).
5. Ritchie, R. O. The conflicts between strength and toughness. *Nat. Mater.* **10**, 817–822 (2011).
6. Zadpoor, A. A. Mechanical meta-materials. *Mater. Horizons* **3**, 371–381 (2016).
7. Mirzaali, M. J. *et al.* Multi-material 3D printed mechanical metamaterials: rational design of elastic properties through spatial distribution of hard and soft phases. *Appl. Phys. Lett.* **113**, 241903 (2018).
8. Mirzaali, M. J. *et al.* Rational design of soft mechanical metamaterials: Independent tailoring of elastic properties with randomness. *Appl. Phys. Lett.* **111**, 051903 (2017).
9. Zied, K., Osman, M. & Elmahdy, T. Enhancement of the in-plane stiffness of the hexagonal re-entrant auxetic honeycomb cores. *Physica Status Solidi B* **252**, 2685–2692 (2015).
10. Barthelat, F., Tang, H., Zavattieri, P. D., Li, C. M. & Espinosa, H. D. On the mechanics of mother-of-pearl: a key feature in the material hierarchical structure. *J. Mech. Phys. Solids* **55**, 306–337 (2007).
11. Sarikaya, M. & Aksay, I. A. Biomimetics. Design and processing of materials. (Department of Materials Science and Engineering, Washington University Seattle, 1995).
12. Su, B.-L., Sanchez, C. & Yang, X.-Y. Hierarchically structured porous materials: from nanoscience to catalysis, separation, optics, energy, and life science. 1st edn (eds Su, B.-L., Sanchez, Clement & Yang, Xiao-Yu) 651 (Wiley-VCH, 2011).
13. Gibson, L. J. The hierarchical structure and mechanics of plant materials. *J. R. Soc. Interface* **9**, 2749–2766 (2012).

## References

14. Liu, Z., Meyers, M. A., Zhang, Z. & Ritchie, R. O. Functional gradients and heterogeneities in biological materials: design principles, functions, and bioinspired applications. *Prog. Mater. Sci.* **88**, 467–498 (2017).
15. Naleway, S. E., Porter, M. M., McKittrick, J. & Meyers, M. A. Structural design elements in biological materials: application to bioinspiration. *Adv. Mater.* **27**, 5455–5476 (2015).
16. Ji, B. & Gao, H. Elastic properties of nanocomposite structure of bone. *Compos. Sci. Technol.* **66**, 1212–1218 (2006).
17. Collins, M. J. *et al.* The survival of organic matter in bone: a review. *Archaeometry* **44**, 383–394 (2002).
18. Mirzaali, M. J., Pahlavani, H. & Zadpoor, A. A. Auxeticity and stiffness of random networks: lessons for the rational design of 3D printed mechanical metamaterials. *Appl. Phys. Lett.* **115**, 3–8 (2019).
19. Köppen, M. The curse of dimensionality. *In Proc. of the 5th Online Conference on Soft Computing in Industrial Applications (WSC5)*, 4–8 (2000).
20. Silver, D. *et al.* Mastering the game of Go with deep neural networks and tree search. *Nat.* **529**, 484–489 (2016).
21. Guo, K., Yang, Z., Yu, C.-H. & Buehler, M. J. Artificial intelligence and machine learning in design of mechanical materials. *Mater. Horizons* **8**, 1153–1172 (2021).
22. Gu, G. X., Chen, C. T. & Buehler, M. J. De novo composite design based on machine learning algorithm. *Extrem. Mech. Lett.* **18**, 19–28 (2018).
23. Bessa, M. A., Glowacki, P. & Houlder, M. Bayesian machine learning in metamaterial design: fragile becomes supercompressible. *Adv. Mater.* **31**, 1–6 (2019).
24. Ma, W., Cheng, F. & Liu, Y. Deep-learning-enabled on-demand design of chiral metamaterials. *ACS Nano* **12**, 6326–6334 (2018).
25. Wilt, J. K., Yang, C. & Gu, G. X. Accelerating auxetic metamaterial design with deep learning. *Adv. Eng. Mater.* **22**, 1–7 (2020).
26. Gu, G. X., Chen, C. T., Richmond, D. J. & Buehler, M. J. Bioinspired hierarchical composite design using machine learning: simulation, additive manufacturing, and experiment. *Mater. Horizons* **5**, 939–945 (2018).
27. Zhang, Z., Zhang, Z., Di Caprio, F. & Gu, G. X. Machine learning for accelerating the design process of double-double composite structures. *Compos. Struct.* **285**, 115233 (2022).

28. Sui, F., Guo, R., Zhang, Z., Gu, G. X. & Lin, L. Deep reinforcement learning for digital materials design. *ACS Mater. Lett.* **3**, 1433–1439 (2021).
29. Yang, Z., Yu, C.-H. & Buehler, M. J. Deep learning model to predict complex stress and strain fields in hierarchical composites. *Sci. Adv.* **7**, eabd7416 (2021).
30. Yang, C., Kim, Y., Ryu, S. & Gu, G. X. Prediction of composite microstructure stress-strain curves using convolutional neural networks. *Mater. Des.* **189**, 108509 (2020).
31. Yang, Z., Yu, C. H., Guo, K. & Buehler, M. J. End-to-end deep learning method to predict complete strain and stress tensors for complex hierarchical composite microstructures. *J. Mech. Phys. Solids* **154**, 104506 (2021).
32. Chen, C. T. & Gu, G. X. Learning hidden elasticity with deep neural networks. *Proc. Natl. Acad. Sci. U. S. A.* **118**, (2021).
33. Gokhale, N. Solving an elastic inverse problem using convolutional neural networks. Preprint at arXiv:2109.07859 (2021).
34. Wang, C., Tan, X. P., Tor, S. B. & Lim, C. S. Machine learning in additive manufacturing: state-of-the-art and perspectives. *Addit. Manuf.* **36**, 101538 (2020).
35. Wang, S. *et al.* Machine-learning micropattern manufacturing. *Nano Today* **38**, 101152 (2021).
36. Austrell, P. E. *et al.* CALFEM - A finite element toolbox, version 3.4. (2004).
37. Reddy, J. N. Introduction to the finite element method. (McGraw-Hill Education, 2019).
38. Abadi, M. *et al.* TensorFlow: large-scale machine learning on heterogeneous distributed systems. Preprint at arXiv:1603.04467 (2016).
39. Chollet, F. *et al.* Keras. Retrieved from <https://github.com/fchollet/keras> (2015).
40. Hashin, Z. & Shtrikman, S. A variational approach to the theory of the elastic behaviour of multiphase materials. *J. Mech. Phys. Solids* **11**, 127–140 (1963).
41. Paul, B. Prediction of elastic constants of multi-phase materials. Technical Report No. 3 (Brown University, 1959).
42. Mirzaali, M. J., Pahlavani, H., Yarali, E. & Zadpoor, A. A. Non-affinity in multi-material mechanical metamaterials. *Sci. Rep.* **10**, 1–10 (2020).
43. Kolken, H. M. A. *et al.* Rationally designed meta-implants: a combination of auxetic and conventional meta-biomaterials. *Mater. Horizons* **5**, 28–35 (2018).

## References

44. Hedayati, R., Mirzaali, M. J. & Vergani, L. Action-at-a-distance metamaterials: distributed local actuation through far-field global forces. *APL Mater.* **6**, 36101 (2018).
45. Naghavi Zadeh, M., Dayyani, I. & Yasae, M. Fish cells, a new zero Poisson's ratio metamaterial—Part I: design and experiment. *J. Intell. Mater. Syst. Struct.* **31**, 1617–1637 (2020).



# 6

## Size-agnostic inverse design of random networks

Published as:

Pahlavani, H., Tsifoutis-Kazolis, K., Mody, P., Zhou, J., Mirzaali, M. J., & Zadpoor, A. A. Deep learning for size-agnostic inverse design of random-network 3D printed mechanical metamaterials. arXiv preprint arXiv:2212.12047 (2022).



## Abstract

Practical applications of mechanical metamaterials often involve solving inverse problems where the objective is to find the (multiple) micro-architectures that give rise to a given set of properties. The limited resolution of additive manufacturing techniques often requires solving such inverse problems for specific sizes. One should, therefore, find multiple micro-architectural designs that exhibit the desired properties for a specimen with given dimensions. Moreover, the candidate micro-architectures should be resistant to fatigue and fracture, meaning that peak stresses should be minimized as well. Such a multi-objective inverse design problem is formidably difficult to solve but its solution is the key to real-world applications of mechanical metamaterials. Here, we propose a modular approach titled “Deep-DRAM” (deep learning for the design of random-network metamaterials) that combines four decoupled models, including two deep learning models (DLM), a deep generative model (DGM) based on conditional variational autoencoders (CVAE), and direct finite element (FE) simulations. The integrated framework first introduces the desired elastic properties to the DGM, which returns a set of candidate designs. The candidate designs, together with the target specimen dimensions are then passed to the DLM which predicts their actual elastic properties considering the specimen size. After a filtering step based on the closeness of the actual properties to the desired ones, the last step uses direct FE simulations to identify the designs with the minimum peak stresses. Using an extensive set of simulations as well as experiments performed on 3D printed specimens, we demonstrate that: (i) the predictions of the deep learning models are in agreement with FE simulations and experimental observations, (ii) an enlarged envelope of achievable elastic properties (including such rare combinations as double-auxetic behavior and high stiffness) is realized using the proposed approach, and (iii) the proposed framework can provide many solutions to the multi-objective inverse design problem posed here.

### 6.1. Introduction

The second and third decades of the 21<sup>st</sup> century have witnessed the emergence of architected materials with bespoke, unusual properties that stem from their small-scale design. At the nexus of rational design techniques, where computational models are used to establish design-property relationships, and additive manufacturing (AM, = 3D printing) techniques, which enable the realization of arbitrarily complex designs, a highly vibrant sub-discipline has emerged that is rapidly pushing such designer materials into applications in medical devices<sup>1-3</sup>, soft robotics<sup>4-6</sup>, and other advanced areas of research<sup>7-9</sup>. Depending on the type of the properties targeted, these architected materials may be referred to as mechanical metamaterials<sup>10-14</sup>, acoustic metamaterials<sup>15-17</sup>, or meta-biomaterials<sup>3,18</sup>, among other types.

Despite their recent academic success, there are two major challenges that hinder the real-world applications of metamaterials in general and mechanical metamaterials in particular. To put these challenges in perspective, let us consider a typical device design scenario where the required elastic properties as well as the dimensions of a device are specified by the device designer. The design problem is then reduced to the problem of finding the micro-architectures that give rise to the required elastic properties while also satisfying the size requirements. The inverse problem of finding the micro-architecture(s) resulting in a specific set of elastic properties is challenging enough in its own right particularly given that the desired combination of properties is often very rare (*e.g.*, high stiffness and highly negative values of the Poisson's ratio<sup>19</sup>). The difficulty of such an inverse design problem is further exacerbated by the fact that most mechanical metamaterials are usually only analyzed in terms of their homogenized or asymptotic properties (*i.e.*, when the number of the constituting unit cells approaches infinity). Such homogenized solutions are only valid at their convergence limits and may significantly deviate from the actual elastic properties when the number of unit cells is not large enough<sup>20</sup>.

Given the limited resolution of AM techniques, it is often impossible to fit a very large number of unit cells within a given set of dimensions. Homogenized solutions may, therefore, not offer too much help when dealing with real-world design problems. The inverse design problem should, therefore, not be solved for the asymptotic case of an infinite number of unit cells but for the actual case of a finite number of unit cells in each spatial direction. Here, we use deep learning (DL) models and deep generative models to tackle such a size-agnostic inverse design problem within the context of random-network (RN) mechanical metamaterials.

Most of the mechanical metamaterials developed to date are composed of periodic unit cells. Previous studies have, however, shown that RN units cells, consisting of stretch- and bending-dominated beam-like structures, allow for a wide range of conventional and auxetic elastic properties<sup>21-25</sup>, which may go beyond the limits achieved by geometrically-ordered mechanical metamaterials, particularly when seeking after rare combinations of elastic properties<sup>26</sup>. We will, therefore, use RN designs to increase the chance of finding accurate solutions for the inverse design problems targeted here. A facet of such nonlinear inverse problems relevant to micro-architecture design of mechanical metamaterials concerns the non-uniqueness of the solution. It is important to realize that different solutions to the inverse problem posed in the previous paragraph are not equal in many other aspects. That is because designs with similar effective properties could have highly different stress distributions and, thus, highly different degrees of resistance to fatigue and fracture. We are, therefore, interested in finding as many solutions to the posed inverse problem as possible so that additional design requirements, such a uniform stress distribution or a minimum stress peak, can be applied. This further increases the practical utility of the approach presented here.

The existing DL models used for such inverse design problems are often deterministic in nature. Such models are not well equipped to regress a single input to multiple outputs and may converge to the average of the solutions instead. We will, therefore, model the aforementioned inverse design problem in a probabilistic,

## 6.1. Introduction

generative manner because such approaches have been shown to enable investigations of the structure–response relationship and can resolve the one-to-many mapping problem that deterministic models are unable to cope with<sup>27–30</sup>. Generative adversarial networks (GAN)<sup>31</sup> and variational autoencoders (VAE)<sup>32</sup>, which seek to understand the underlying relationship between design features and targets/labels and generate new designs from a low-dimensional latent space, are popular deep generative models used for the inverse design of materials<sup>28,33–36</sup>. In contrast to VAE, which provides a straightforward mapping from the observed dataset to a continuous latent space, a continuous latent space with a meaningful structure is intractable for GAN models<sup>28</sup>.

To achieve the goals presented above, we take a modular approach, hereafter referred to as “Deep-DRAM”. Deep-DRAM (deep learning for the design of random-network metamaterials) is composed of a sequence of DL and generative models that not only collectively solve the size-agnostic, inverse design problem but can also be (individually) used for many other purposes. First, we create a DL-based forward predictor model that predicts the anisotropic elastic properties of a specific type of RN unit cells. Second, we present a generative model based on conditional variational autoencoder (CVAE) that generates the micro-architecture of RN unit cells with a given set of anisotropic elastic properties. The third module is a DL-based forward predictor model that receives the micro-architecture of the RN unit cells and the desired dimensions of the specimen (*i.e.*, the number of RN unit cells along each spatial direction) and predicts its elastic properties. The developed models are then combined to solve the size-agnostic design problem with the additional requirement that the maximum stresses are minimized (see Supplementary Movies 1, 2, and 3). While the data required for training and testing the DL models are all generated using finite element (FE) models, we also present several experiments in which actual mechanical metamaterials are 3D printed and mechanically tested to compare their measured elastic properties and deformation patterns with our computational results.

## 6.2. Materials and methods

We studied restricted RN unit cells in which the nodal points of the beam-like elements were fixed at specific locations. The design of these unit cells was inspired by our previous research<sup>21</sup> that computationally explored the auxeticity and stiffness of random networks and demonstrated a wide range of elastic moduli and Poisson's ratios for this type of mechanical metamaterials. For this work, we first studied RN unit cells composed of different node numbers (*i.e.*,  $n_x = n_y = 3, 4, 5, 6, 7,$  and  $8$ ) to find out the least number of nodes that corresponds to the broadest range of elastic properties. We assumed the internodal distances of  $\Delta x$  and  $\Delta y$  in directions 1 and 2, respectively. The overall size of a unit cell is, therefore, given by:  $L \times W$  ( $L = n_y \times \Delta y$  and  $W = n_x \times \Delta x$ ) (Figure 1a). Also we assumed the in-plane ( $t = 1$  mm) and out-of-plane ( $T = 10$  mm) thicknesses for the RN unit cells. The beam-like elements were randomly distributed to connect the whole grid. We studied unit cells with the network connectivity values of  $Z_g = 2.5, 3, 3.5, 4,$  and  $4.5$  (Figure 1a). We further studied combinatorial designs that are composed of different numbers of rows and columns of RN unit cells.

### 6.2.1. Computational models

All the FE models were created using MATLAB (MATLAB R2018b, MathWorks, USA) codes. Custom codes were used to design the structures by randomly connecting each node to its surrounding nodes and to perform the FE simulations that estimate the elastic properties of the resulting structures (*i.e.*, the elastic moduli and Poisson's ratios in both orthogonal in-plane directions). The random distribution of beams resulted in 'loose designs' where some nodes were not connected to the overall grid. To exclude such designs, we used a graph-based search method (breadth-first search<sup>37</sup>) for filtering and discarding such invalid unit cell designs. The applied graph-based algorithm sped up the process by nearly 900 times as compared to an image-based filtering method used previously<sup>21</sup> (more information

## 6.2. Materials and methods

is provided in Supplementary Figure 1). Our codes were further extended to incorporate the RN unit cells into the combinatorial designs (Figure 3a).

We employed three-node quadratic beam elements (Timoshenko beam elements) with rectangular cross-sections ( $t \times T$ ) and with two translational (*i.e.*,  $u_{11}$  and  $u_{22}$ ) and one rotational (*i.e.*,  $u_{33}$ ) degrees of freedom (DOF) at each node. An elastic material with a Young's modulus of  $E_b = 0.6$  MPa and a Poisson's ratio of  $\nu_b = 0.3$  was then assigned to elements. For each structure, two FE models were created to separately apply a strain of 5% along 1- and 2-directions. In the first model, the top nodes were subjected to a strain of 5% along the 2-direction ( $u_{11} = u_{33} = 0$  and  $u_{22} = 0.05 \times L$ ) while all the DOF of the bottom nodes were constrained ( $u_{11} = u_{22} = u_{33} = 0$ ). In the second model, the right nodes were subjected to 5% strain along the 1-direction ( $u_{22} = u_{33} = 0$  and  $u_{11} = 0.05 \times W$ ) while all the DOF of the left nodes were constrained ( $u_{11} = u_{22} = u_{33} = 0$ ). More information about the FE equations used for the numerical simulations are provided in the supplementary document.

To calculate the elastic moduli of the structures ( $E_{11} = \sigma_{11}/\varepsilon_{11}$  and  $E_{22} = \sigma_{22}/\varepsilon_{22}$ ), the normal stresses along directions 1 and 2 ( $\sigma_{11} = \overline{F_{11}}/(L \times T)$ ,  $\sigma_{22} = \overline{F_2}/(W \times T)$  (Figure 1a)) were divided by the strain applied along the same direction ( $\varepsilon_{11} = \varepsilon_{22} = 5\%$ ). In these equations,  $\overline{F_{11}}$  and  $\overline{F_2}$  are the mean reaction forces along directions 1 and 2 at the right and top nodes, respectively ( $\overline{F_{11}} = \frac{\sum_{i=1}^{n_R} F_{11,i}}{n_R}$ ,  $\overline{F_2} = \frac{\sum_{i=1}^{n_T} F_{22,i}}{n_T}$ , where  $n_R$  and  $n_T$  are the total numbers of the right and top nodes while  $F_{11,i}$  and  $F_{22,i}$  are the reaction forces along directions 1 and 2 at each of the right and top nodes, respectively). We then calculated the transverse strain as the ratio of the average displacement of the lateral nodes to the initial transversal length of the structure (in the case of  $\varepsilon_{axial} = \varepsilon_{11} = 5\%$ :  $\varepsilon_{trans} = \varepsilon_{22} = \frac{\sum_{i=1}^{n_T} \delta y_i}{L \times n_T}$ , and in

the case of  $\varepsilon_{axial} = \varepsilon_{22} = 5\%$ :  $\varepsilon_{trans} = \varepsilon_{11} = \frac{\sum_{i=1}^{n_R} \delta x_i}{W \times n_R}$ ). The transverse strain was then divided by the applied axial strain to calculate the Poisson's ratio ( $\nu = -\frac{\varepsilon_{trans}}{\varepsilon_{axial}}$ ).

## 6.2.2. Deep learning

**Unit cell elastic properties model:** We trained a predictor model that we refer to as the “unit cell elastic properties model” which aims to learn the mapping from the space of RN unit cell designs to that of their elastic properties. This model takes as input a binary vector representing the RN unit cells (*i.e.*, a binary vector of 0 and 1 values, where 1 indicates the presence of an element and 0 indicates its absence) and returns the elastic properties ( $E_{11}$ ,  $E_{22}$ ,  $\nu_{12}$ , and  $\nu_{21}$ ) of the unit cells as output. Before training the model, we performed an initial data analysis process followed by a hyperparameter tuning study. To select the options and parameters for both data analysis and hyperparameter tuning, we used a pipeline training technique (Supplementary Figure 5) which combined data analysis options and model hyperparameters in its search space. Pipeline training automates the training process including data analysis and hyperparameter tuning and optimizes the model considering different configurations of the parameters of the search space of the pipeline.

We used a workstation (CPU = Intel® Xeon® W-2295, RAM = 256 GB) and a Python script (Python 3.9.7) to tune the parameters of the pipeline's search space. Through this, 10,368 combinations of parameters were investigated (Supplementary Table 5) and the best pipeline parameters were selected. For data analysis, we selected data resampling and data scaling to be investigated since the size and distribution of both inputs and outputs are important for the success of the model training step. As for the model hyperparameters, we selected the parameters describing the design of the DL models (*i.e.*, the width and depth of the hidden layers as well as the trend of the variation of the number of hidden neurons per layer), the regularization terms, the type of the optimizer algorithm, the activation functions of

## 6.2. Materials and methods

the hidden layers and output layer, and the application of batch normalization. We used the search methods of cross-validation grid search from scikit-learn (version 1.1.1) to systematically iterate over the predefined values of the search space parameters (see the supplementary document for a more in-depth discussion of the methods).

The overall performance of the model was assessed by characterizing its ability to generalize from the training dataset to the test dataset to avoid both under- and overfitting. To avoid overfitting, we used  $k$ -fold cross validation (CV) that divides the training dataset into  $k$  smaller sets. We used 3-fold CV, meaning that each set equals 33% of the training dataset. Note that 10% of the overall dataset was kept as the test dataset for final model evaluation.

We selected MSE (Equation (1)) as the loss function of the model to ensure that the regression line changes only slightly for a modest change in the data point. For the evaluation of the model training, we used the coefficient of determination ( $R^2$ ) (Equation (2)) which indicates the amount of target variance explained by the model's independent variables.

$$\text{MSE} = \frac{1}{n} \sum_{i=1}^n (y_i - \hat{y}_i)^2, \quad (1)$$

$$R^2 = 1 - \frac{\sum_{i=1}^n (y_i - \hat{y}_i)^2}{\sum_{i=1}^n (y_i - \bar{y})^2}, \quad (2)$$

where  $n$  is the size of the dataset,  $y_i$  is the  $i^{\text{th}}$  real target,  $\hat{y}_i$  is the corresponding predicted value, and  $\bar{y}$  is the mean value of  $y$  ( $\bar{y} = \frac{1}{n} \sum_{i=1}^n y_i$ ).

**Deep generative model:** We trained a deep generative model that allows for the inverse design of RN unit cells. This model is based on CVAE and follows a similar approach as in a number of previous studies<sup>27,38</sup>. The key difference between CVAE and VAE is that CVAE can incorporate certain conditions into the training process<sup>38,39</sup>. Here, the additional conditions concern the elastic properties of the RN unit cells. Two deep neural networks were utilized as the sub-models of the CVAE,



each with a structure purposefully built for their specialized roles. More specifically, they are a recognition network and a reconstruction network which are coupled in an encoder-decoder format (Figure 2a). The recognition model transfers the designs of the RN unit cells as well as their corresponding elastic properties into a low-dimensional, continuous, and ordered latent space<sup>28</sup>. The reconstruction model uses the four elastic properties and the latent variables to recreate the binary vector representing the metamaterial design. After the successful training of the CVAE, the reconstruction model was separated and used as the deep generative model. The input to this deep generative model was the desired elastic properties of the RN unit cell as well as a random sampling from a normal distribution with the same dimensions as the latent space.

The loss function that we utilized to train the CVAE ( $\mathcal{L}_{CVAE}$ ) was obtained from the loss function of a standard VAE ( $\mathcal{L}_{VAE}$ ) with conditional information included. The loss function of VAE consists of two terms, the reconstruction error and the Kullback-Leibler (KL) term, and is given as<sup>32,38,39</sup>:

$$\mathcal{L}_{VAE} = E[\log P(x|z)] - D_{KL}[Q(z|x) \parallel P(z)], \quad (3)$$

where  $E$  represents an expectation value,  $P$  and  $Q$  are probability distributions,  $D_{KL}$  represents the KL divergence,  $x$  is the binary vector representing the RN unit cells, and  $z$  represents the latent variables.  $Q(z|x)$  and  $P(x|z)$  are approximated by the recognition and reconstruction models, respectively. The incorporation of the conditional information into the loss function of the VAE modifies the loss function of CVAE as follows<sup>38,39</sup>:

$$\mathcal{L}_{CVAE} = E[\log P(x|z,y)] - D_{KL}[Q(z|x,y) \parallel P(z|y)], \quad (4)$$

where  $y$  is a condition vector that plays an active role in both the encoding and decoding operations. The condition vector in our model contains the elastic properties of the RN unit cells.

## 6.2. Materials and methods

To assess the elastic properties of the generated RN unit cells and as a regularisation term to the overall loss function<sup>30</sup>, the pre-trained “unit cell elastic properties model” that predicts the elastic properties of the RN unit cells was incorporated into the overall loss function ( $\mathcal{L}_{all}$ ).  $\mathcal{L}_{all}$  for the training of the deep generative model contains the terms that account for the configuration of the latent space, the reconstruction of the input metamaterial design, and the retrieval of the desired elastic properties from the generated RN unit cells. For the retrieval of the desired mechanical properties from the reconstructed RN unit cells, MSE is considered as the loss function,  $\mathcal{L}_{MSE}$ . Therefore, the total loss function for the deep generative model (Equation (5)) include those corresponding to the CVAE ( $\mathcal{L}_{CVAE}$ ) and the MSE ( $\mathcal{L}_{MSE}$ ) between the target and predicted elastic properties of the reconstructed RN unit cells.

$$\mathcal{L}_{all} = \mathcal{L}_{CVAE} + \mathcal{L}_{MSE} \quad (5)$$

To train a CVAE with an optimal fitting and a lower dimension of the latent space, we used the same hyperparameter tuning pipeline as for the unit cell elastic properties model. Some assumptions were made based on the best resulting parameters for the unit cell properties model. Identical hyperparameters as for the unit cell elastic properties model were used in the data processing steps. Additionally, the Adam optimizer was preselected, having outperformed the RMSprop optimizer in the training of the "unit cell properties model". In total, 6144 combinations of parameters were tested through the hyperparameter optimization method with a running time of approximately 1341 minutes (~23 hours) (Supplementary Table 7). For the validation of the elastic properties arising from the generated RN unit cells and as a regularization term to the overall loss, the pre-trained unit cell elastic properties model was used as a forward predictor of the elastic properties of the RN unit cells ( $E_{11}$ ,  $E_{22}$ ,  $\nu_{12}$ , and  $\nu_{21}$ ).

For the evaluation of the trained CVAE (Supplementary Figure 8) with the help of the test dataset, we visualized the latent space to see if it is well-clustered.

Moreover, we used the relevant performance metrics (*i.e.*, Confusion matrix, Precision, Recall, and  $F_1$  score) for the same purpose. To visualize the latent space (Supplementary Figure 9a) where the metamaterial design is encoded, the  $t$ -distributed stochastic neighbor embedding ( $t$ -SNE) approach was used to reduce its dimension to two. In addition to capturing the relevant information regarding the design of RN structures, the latent variables need to capture some information regarding the elastic properties of the designs. As a result, elastic properties are examined and distributed inside each geometric cluster. Because elastic properties are continuous and, thus, cannot be split into categories, they were manually classified according to certain specific criteria to investigate if the latent space can identify distinct Poisson's ratios to a satisfactory degree. The targets of the elastic properties are assigned to three classes: 0 for auxetic metamaterials, 1 for conventional metamaterials, and 2 for double-auxetic metamaterials. The binary multilabel class output is assessed in the case of unit cell representation reconstruction. This is accomplished by calculating the weighted average of the actual and predicted classes for each sample in the test dataset. The confusion matrix shows, in a sample-wise manner, the summary of the prediction results of the classification problem with each row corresponding to the actual class and each column corresponding to the predicted one. This matrix was then used to assess the classification accuracy of the model.

For the evaluation of the model training, the  $F_1$  score (Supplementary Figure 9b) was chosen as the evaluation index of the introduced RN reconstruction, and the predicted elastic responses of the returned structures were evaluated using  $R^2$ . The  $F_1$  score is mainly established for binary classification tasks with the values 1 and 0 corresponding to the best and worst performances, respectively. The  $F_1$  score may be considered a weighted harmonic mean of the precision and recall, where the recall and precision are both equally essential (Equation (6)). Intuitively, precision is the proportion of the true positive cases among those labelled as positive by the

## 6.2. Materials and methods

model and recall is the proportion of the positive instances among the total number of positive examples including :

$$F_1 = \frac{2 \times \text{recall} \times \text{precision}}{\text{recall} + \text{precision}}, \text{ where recall} = \frac{\text{TP}}{\text{TP} + \text{FN}}, \text{ precision} = \frac{\text{TP}}{\text{TP} + \text{FP}}, \quad (6)$$

where TP is true positive, FN is false negative, and FP is false positive.

**Size-agnostic model:** To predict the elastic properties of the combinatorial designs composed of RN unit cells with given dimensions, we trained a forward predictor model referred to as the “size-agnostic model”. This model aims to learn the mapping from the space of combinatorial designs composed of  $D_1 \times D_2$  repetitions of RN unit cells (where  $D_1$  and  $D_2$  are the number of the repetitions of a RN unit cell along directions 1 and 2, respectively, and are assumed to be an even value in the range of (2 – 20)) to the space of their elastic properties (*i.e.*,  $E_{11}$ ,  $E_{22}$ ,  $\nu_{12}$ , and  $\nu_{21}$ ). A binary vector representing the RN unit cells combined with the vectors  $D_1$  and  $D_2$  were introduced to the model as inputs. The model returned the elastic properties of the combinatorial design as its output. Before training the model, we used the same hyperparameter tuning pipeline as described above for the unit cell elastic properties model to optimize the hyperparameters of the model (Supplementary Table 11). We assumed MSE (Equation (1)) as the loss function of the model and used  $R^2$  (Equation (2)) and MSE (Equation (1)) for the evaluation of the trained model.

### 6.2.3. Experiments

We selected six RN unit cells (Figure 1b and 1c) and four combinatorial designs (Figure 3d) to be 3D printed and mechanically tested. We used selective laser sintering (SLS) for printing these lattices using a commercially available material (*i.e.*, Oceansz Flexible TPU). We attached the 3D printed specimens to the testing machine using a designed pin and gripper system that was 3D printed using a fused deposition modeling (FDM) 3D printer (Ultimaker 2+, Geldermalsen, the

Netherlands) from polylactic acid (PLA) filaments (MakerPoint PLA, 750 gr, Natural). We used a mechanical testing machine (LLOYD instrument LR5K, load cell = 100 N) to perform axial tensile loading test on the specimens (stroke rate = 1 mm/min) along directions 1 and 2. The stress-strain curves were then obtained based on the applied displacements and the recorded reaction forces. Stress and strain values were calculated by dividing the force by the initial cross-section area and dividing the crosshead displacements by the initial length of the specimen, respectively. The overall stiffness of the specimens along directions 1 and 2 (*i.e.*,  $E_{11}$  and  $E_{22}$ ) were then calculated as the slope of the stress-strain curves. To calculate the Poisson's ratios (*i.e.*,  $\nu_{12}$  and  $\nu_{21}$ ) of the specimens, we performed image analysis using a custom-made MATLAB code. Towards this aim, we used a digital camera to capture the lateral deformations of the specimens to measure the transverse strain at the different steps of the applied longitudinal displacement. Finally, the Poisson's ratio was calculated as  $\nu = -\frac{\epsilon_{trans}}{\epsilon_{axial}}$ , where  $\epsilon_{trans}$  and  $\epsilon_{axial}$  were calculated in the same way as in the computational models.

## 6.3. Results and discussion

### 6.3.1. Elastic properties of RN unit cells

For the first module, we considered RN unit cells composed of 16 nodes ( $n_x \times n_y$ ,  $n_x = n_y = 4$ ) because this number of nodes allows for a broader range of elastic properties when compared to larger sizes of RN unit cells (Supplementary Figure 2 and Supplementary Table 1), as well as a higher chance of extreme negative and extreme positive Poisson's ratios (Supplementary Table 2). For this number of nodes, it is possible to generate unit cells with average nodal connectivity values of  $Z_g = 2.5, 3, 3.5, 4,$  and  $4.5$ . Depending on the  $Z_g$  value, the number of beam-like elements in the RN unit cells varied between 20 and 42 (Figure 1a). It should be noted that the total estimated number of unit cells that can be generated, whether they abide by the design limitations or not, considering the above-mentioned values

### 6.3. Results and discussion

of  $Z_g$  is  $\approx 9.22 \times 10^{11}$  (Supplementary Table 3). Assuming that the average simulation time per design equals  $\approx 5.42 \times 10^{-4}$  s (Supplementary Figure 3), it takes approximately 497 million seconds (= 5761 days) (Supplementary Table 3) to perform FE analysis on all these RN unit cells. The huge number of possible designs highlights the need to have an ultra-fast model to predict the elastic properties of the RN unit cells.

We performed FE analysis on 6 million randomly generated RN unit cells (*i.e.*, 1.2 million unit cells from each group of  $Z_g$ ) as the training group. The elastic properties in directions 1 and 2, which were calculated by FE modeling of these unit cells, cover a cone-like region with a range of (0, 0.25) and (-1.5, 1.2) for the relative elastic moduli ( $E_{11}/E_b$  and  $E_{22}/E_b$ , where  $E_b$  is the elastic modulus of the bulk material) and Poisson's ratios ( $\nu_{12}$  and  $\nu_{21}$ ), respectively (Figure 1b). The distributions of the relative elastic modulus and Poisson's ratio in directions 1 and 2 had similar ranges of values. Moreover, the results show that the RN unit cells are highly anisotropic. The broad range of the elastic properties is due to the possibility to generate both stretching- and bending-dominated structures using random distributions of elements as well as by changing  $Z_g$ . These results confirm that it is possible to devise RN unit cells with extreme positive and extreme negative values of the Poisson's ratio as well as rare-event<sup>19</sup> double-auxetic unit cells.

We selected six unit cells from the different groups of elastic properties, *i.e.*, almost extreme positive and negative values of the Poisson's ratio in one direction, almost extreme double-auxeticity, almost extreme elastic moduli in both directions, and moderate positive and negative values of the Poisson's ratio as well as moderate values of the elastic moduli in both directions (Figure 1b). To validate the results of our simulations, we 3D printed and experimentally evaluated the elastic properties and deformation patterns of these six unit cells. The experimentally obtained values of the elastic moduli (see the stress-strain curves in Supplementary Figure 4) and Poisson's ratios show a good agreement with FE simulations (Supplementary Table

4). Moreover, the deformation patterns follow similar trends in both simulations and experiments (Figure 1c). In some elements within the FE models, we see higher levels of deformations predicted by FE models as compared to those observed experimentally. These small differences may be explained by the assumptions of the FE models, including a linear elastic constitutive behavior and fully fixed boundary conditions.

We trained a DL model, hereafter referred to as the “unit cell elastic properties model” that predicted the four elastic properties of any RN unit cell given its design (Figure 1d). Based on the results of our hyperparameter tuning pipeline, the applications of an undersampling process and a MinMaxScaler to the cross-validation data resulted in the best model performance. The hyperparameter tuning suggested a model with four hidden layers (500, 376, 252, and 128 hidden neurons in subsequent layers) without a regularization term, with Adam optimizer<sup>40</sup>, and with ReLU activation functions throughout the layers (Supplementary Table 5). Within 200 epochs of model training with the optimized hyperparameters, the mean squared error (MSE) and the mean absolute error (MAE) reduced for the training dataset from  $9.5 \times 10^{-4}$  and  $2.0 \times 10^{-2}$  to  $1.5 \times 10^{-5}$  and  $2.7 \times 10^{-3}$ , respectively. For the validation dataset, the values of MSE and MAE reduced from  $3.7 \times 10^{-4}$  and  $1.4 \times 10^{-2}$  to  $1.6 \times 10^{-5}$  and  $2.6 \times 10^{-3}$ , respectively (Supplementary Figure 6). The evaluation of the trained model using the test dataset resulted in a coefficient of determination ( $R^2$ ) of  $>0.993$  and  $>0.999$  for the Poisson’s ratios and elastic moduli, respectively (Supplementary Table 6 and Supplementary Figure 7). In general, the trained model exhibited a high degree of accuracy in predicting the elastic properties of the RN unit cells with an overall coefficient of determination ( $R^2$ ) of 0.997, an MAE of  $3.6 \times 10^{-3}$ , and an MSE of  $6.0 \times 10^{-5}$  (Supplementary Table 6 and Supplementary Figure 7).

### 6.3. Results and discussion

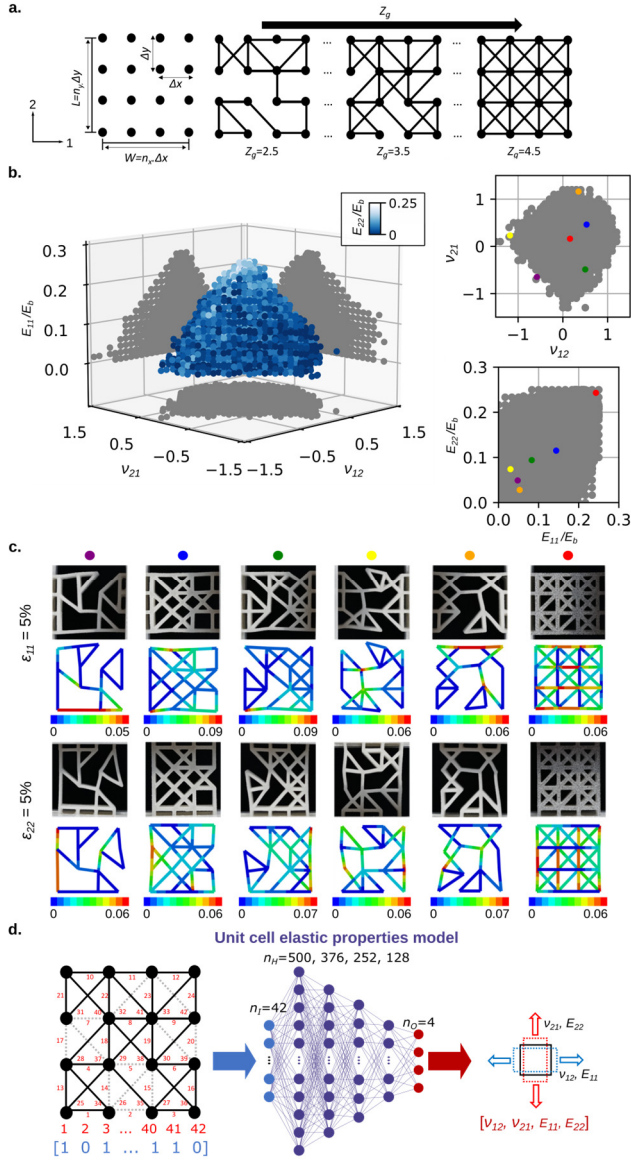


**Figure 1.** A schematic illustration and elastic properties of the RN unit cells. (a) Each RN unit cell has a fixed horizontal and vertical distance of  $\Delta x = \Delta y = 7.5$  mm. Assuming a grid of  $4 \times 4$  nodes, the overall dimensions of each unit cell is  $L = W = 22.5$  mm. Based on the defined overall connectivity,  $Z_g$ , the applicable number of beam-like elements were randomly distributed within the structure. (b) The elastic properties (*i.e.*,  $E_{11}/E_b$ ,  $E_{22}/E_b$ ,  $v_{12}$ , and  $v_{21}$ ) calculated for the RN unit cells using FE analysis. (c) The deformation patterns of six RN unit cells under two loading conditions of  $\epsilon_{11} = 5\%$  and  $\epsilon_{22} = 5\%$  as predicted by FE analysis and observed in the mechanical tests on the 3D printed specimens. (d) The network architecture of the trained unit cell elastic properties model, which maps the design of the unit cell to their elastic properties.



All these results show that the model is well trained without underfitting and overfitting and can, therefore, be further used for highly accurate, deterministic prediction of the elastic properties of various RN unit cell designs. The availability of such a model allows for the ultrafast prediction of the elastic properties associated with any design of RN unit cells with the evaluation of the DL model taking  $\approx 2.44 \times 10^{-5}$  s per design (for prediction of  $10^6$  specimens), which is  $> 20$  times faster than the corresponding FE simulation.

### 6.3.2. Generative inverse design framework

For the inverse design of RN unit cells, we trained a deep generative model based on the CVAE that was paired with the pretrained forward predictor (*i.e.*, the unit cell elastic properties model) (Figure 2a). Based on the results of the hyperparameter tuning, the size of the latent space was chosen to be 8. For both recognition and reconstruction models of the CVAE, we selected two hidden layers with 512 and 260 neurons, an Adam optimizer, and ReLU activation functions throughout both hidden layers. ReLU and Sigmoid were selected as the activation functions of the output layer for the recognition and reconstruction models, respectively (Supplementary Table 7 and Supplementary Figure 8).

The reconstruction model of the trained CVAE was separated and called “unit cell generative model”. To assess the generative ability of this model, the elastic properties of the test dataset and a random sampling from a normal distribution ( $\varepsilon \sim N(0,1)$ ) were passed as inputs to this model. The predicted unit cell structures were passed as inputs to the unit cell elastic properties model and the predicted elastic properties were compared with the initially requested elastic properties of the test dataset. The results of this comparison showed an overall coefficient of determination ( $R^2$ ) of 0.865, an MAE of  $5.1 \times 10^{-2}$ , and an MSE of  $8.5 \times 10^{-3}$  (Supplementary Figure 9c and Supplementary Table 8). To assess the best achievable accuracy among the designs generated by the unit cell generative model, one hundred possible designs were generated for each set of elastic properties present

### 6.3. Results and discussion

in the test dataset. Then, the elastic properties of the generated unit cells were compared with the desired mechanical response provided to the model through the calculation of the regression metrics  $R^2$ , MSE, MAE, and RMSE. The best candidates were then selected among the 100 possible designs. Based on the proposed approach, the final evaluation of the unit cell generative model showed an overall  $R^2$  of 0.977, an MAE of  $1.2 \times 10^{-2}$ , and an MSE of  $3.0 \times 10^{-4}$  (Supplementary Figure 9d and Supplementary Table 9). In addition, the high accuracy of the unit cell generative model in generating new RN unit cells was demonstrated by comparing the DL-predicted elastic properties of the generated unit cells with their corresponding FE results (Supplementary Figure 10). Based on this comparison,  $R^2$  of 0.98, 0.98, 0.99, and 0.99 were calculated for  $\nu_{12}$ ,  $\nu_{21}$ ,  $E_{11}$ , and  $E_{22}$ , respectively (Supplementary Figure 10).

#### 6.3.3. Unit cells with requested rare elastic properties

To demonstrate the generative ability of the unit cell generative model, grid-sampled values of double-auxetic elastic properties, which are rare occurrences in the natural sampling of random networks<sup>21</sup>, were created and fed to the deep generative model. For each request, the elastic properties were defined as a combination of  $\nu_{12}$  and  $\nu_{21}$  in the range of  $(-1, -0.1)$  and an equal elastic modulus along both directions with values within the range of  $E_{11}/E_b = E_{22}/E_b = (0, 0.25)$ . For each input, the best design out of a 100 designs was selected. The four elastic properties of the generated unit cells predicted by the unit cell properties model are reported in a 3D scatterplot incorporating color coding for the fourth property (Figure 2b). To explore the expansion offered by the deep generative model over the observed elastic properties in the initial library (*i.e.*, the training and test datasets), the existing elastic properties in the dataset and the non-duplicate values from the generative process were compared (Figure 2b). From the 3D scatterplot, we can see that the envelope of the achievable elastic properties is expanded in all three planes (*i.e.*, planes of  $\nu_{12} - \nu_{21}$ ,  $E_{11}/E_b - \nu_{12}$ , and  $E_{11}/E_b - \nu_{21}$ ). The top view of the 3D

scatterplot, which shows the expansion of the envelope in the  $\nu_{12} - \nu_{21}$  plane, reveals the possibility of generating unit cells with extreme double-auxetic properties (Figure 2b). In general, these results confirm the ability of the deep generative model to generate unit cells with new elastic properties that were not within the envelope of the elastic properties covered by the initial (*i.e.*, training) library. The deep generative model is, therefore, of value for the efficient generation of unit cells with predefined elastic properties, specially rare-event properties, such as double-auxeticity.

As case studies, we selected four sets of elastic properties (I, II, III, and IV) with negative values of the Poisson's ratio and different Young's moduli (see the top views in Figure 2b) to illustrate the generated unit cells corresponding to these cases. For the elastic properties of case IV, three generated candidates are displayed to demonstrate the possibility of generating different designs exhibiting similar sets of elastic properties. The deformation patterns of these unit cells (when subjected to 5% strain along directions 1 and 2) were compared to the initial state of the generated unit cell (Figure 2c). The calculated error values averaged over the four components of the elastic properties were 8.3%, 8.6%, 3.6%, and 3.1% for unit cells I, II, III, and IV, respectively (Supplementary Table 10). These case studies show a high degree of accuracy of the deep generative model when used for the design of double-auxetic unit cells with elastic properties that were not seen before in the training or test datasets.

### 6.3. Results and discussion

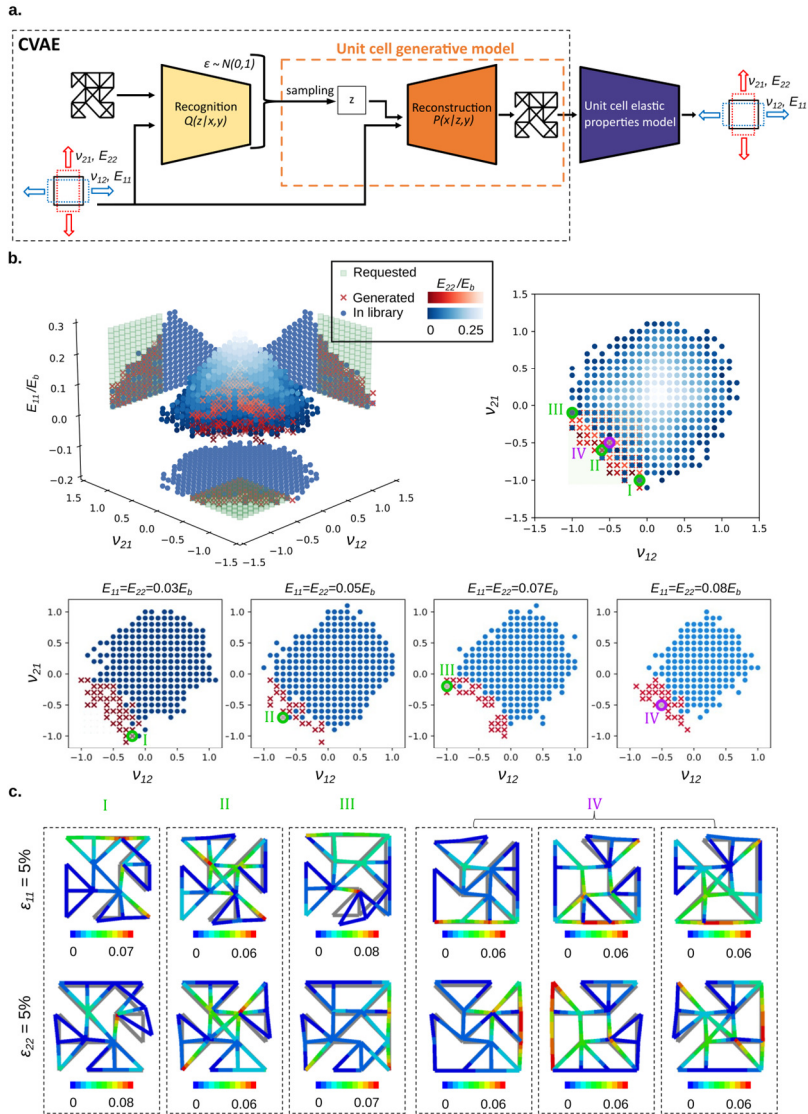


**Figure 2.** The unit cell generative model and its ability to generate new RN unit cells. (a) The reconstruction part of CVAE is referred to as the “unit cell generative model” to generate RN unit cells given the target elastic properties. The elastic properties of the generated unit cells are further predicted by the unit cell elastic properties model for final filtering. (b) A demonstration of the ability of the unit cell generative model to generate new unit cells with given elastic properties which were not present in the initial library. Cross-sections are presented to more clearly visualize the generated unit cells with new elastic properties. (c) The deformation pattern of three specimens (*i.e.*, I, II, III) with new elastic properties not present in the original library. Moreover, a group of specimens (*i.e.*, IV) are presented to show the ability of the trained model to generate specimens with similar elastic properties.

### 6.3.4. Elastic properties of combinatorial designs

We studied combinatorial designs composed of  $D_1 \times D_2$  repetitions of RN unit cells (Figure 3a). Assuming  $D_1$  and  $D_2$  are values varying in a range of (2, 20), we studied a total of 100 combinatorial designs from each RN unit cell. We used the undersampled dataset of RN unit cells (dataset size = 81,569), which was used for the training of the unit cell elastic properties model and performed numerical simulations for all the 100 combinatorial designs composed of these RN unit cells (size of dataset = 8,156,900). The generated dataset was further used to train a forward predictor called “size-agnostic model” that predicts the elastic properties of the combinatorial designs (Figure 3a).

To train the model, we assumed MinMaxScaler as the scaling method, ReLU as the activation function of all the hidden layers as well as of the output layer, and Adam as the optimizer with a learning rate of 0.0001, which were adopted from the hyperparameter tuning step of the unit cell elastic properties model. The hyperparameter tuning step of the deep generative model resulted in 6 hidden layers with 512, 428, 343, 258, 174, and 89 neurons, respectively (Supplementary Table 11). Within 200 epochs, the prediction errors (MSE, MAE) reduced from  $\text{MSE} = 4.7 \times 10^{-3}$  and  $\text{MAE} = 2.9 \times 10^{-2}$  to  $\text{MSE} = 1.6 \times 10^{-5}$  and  $\text{MAE} = 2.9 \times 10^{-3}$  for the training dataset and from  $\text{MSE} = 4.1 \times 10^{-3}$  and  $\text{MAE} = 1.4 \times 10^{-2}$  to  $\text{MSE} = 1.7 \times 10^{-5}$  and  $\text{MAE} = 3.0 \times 10^{-3}$  for the validation dataset (Supplementary Figure 11). The trained model had an overall  $R^2$  of 0.995 for the test dataset (10% of the original dataset), confirming that it can accurately predict the elastic properties of the combinatorial designs (Supplementary Table 12 and Supplementary Figure 12).

Combinatorial designs showed a wide range of elastic properties. The relative elastic moduli ( $E_{11}/E_b$  and  $E_{22}/E_b$ ) and Poisson’s ratios ( $\nu_{12}$  and  $\nu_{21}$ ) calculated by the numerical simulations were in the ranges of (0, 0.3) and (-2, 3), respectively (Figure 3b). The 3D distribution of the elastic properties of the combinatorial designs

### 6.3. Results and discussion

resembled a square pyramid with inwardly curved faces whose base is placed within the  $v_{12} - v_{21}$  plane. The distribution of the elastic properties in the  $v_{12} - v_{21}$  plane was bounded by two hyperbolas, one with openings in the first and third quadrants and the other one with openings in the second and fourth quadrants.

To study how the elastic properties vary with  $D_1$  and  $D_2$ , we selected one of the RN unit cells and depicted the evolution of the four elastic properties as a function of changes in  $D_1$  and  $D_2$  (Figure 3c). We found a nonlinear relationship between the elastic properties and dimensions of the combinatorial designs of this unit cell that, as expected, saturates for large enough numbers of unit cells along each spatial direction (Figure 3c and Supplementary Figure 13). For this selected RN unit cell,  $E_{11}/E_b$ ,  $E_{22}/E_b$ ,  $v_{12}$ , and  $v_{21}$  converge towards 0.020, 0.048, 0.05, and 0.5, respectively (Supplementary Figure 13). Based on a preliminary study we performed on the combinations of RN unit cells, we selected  $D_1 = D_2 = 20$  as the maximum size of combinatorial designs due to the saturation of the elastic properties for larger numbers of unit cells (Supplementary Figure 13). To validate the results of our simulations, the elastic properties and deformation patterns of four selected combinatorial designs were determined experimentally (Figure 3d). The mechanical tests on these specimens indicated that the deformation patterns follow the same trends as observed in the simulations. The mismatches between the simulations and mechanical tests can be attributed to the assumptions used in the simulations (*e.g.*, a linear elastic constitutive equation), the differences between the experimental and simulated boundary conditions, and manufacturing imperfections.

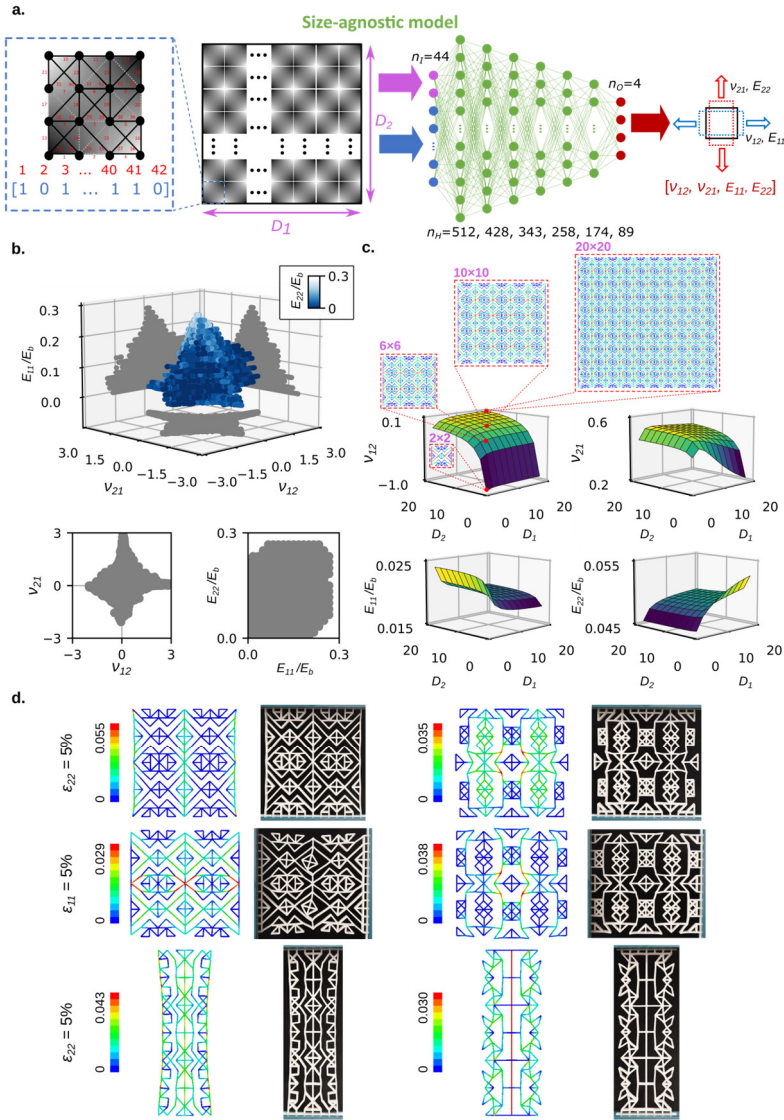


**Figure 3.** A schematic illustration and elastic properties of the combinatorial designs as well as the network architecture of the size-agnostic model. (a) Each combinatorial design with a given dimension ( $D_1 \times D_2$ ) is created by repeat filling a specific RN unit cell  $D_1$  times vertically (along direction 1) and  $D_2$  times horizontally (along direction 2). The vectors containing  $D_1$  and  $D_2$  and the binary vectors representing the design of the unit cells are introduced to the size-agnostic model as input. The model then returns the predicted elastic properties of the combinatorial design as output. (b) The envelope of the elastic properties achieved by the combinatorial designs, according to direct FE simulations. (c) The evolution of the elastic properties as functions of  $D_1$  and  $D_2$  for a specific case study. (d) The deformation patterns of four combinatorial designs subjected to the following loading conditions:  $\epsilon_{11} = 5\%$  and  $\epsilon_{22} = 5\%$  using FE analysis and experimental tests.

### 6.3.5. Inverse design of lattice structures with requested elastic properties and dimensions

We combined the unit cell generative model and the size-agnostic model to develop a comprehensive and powerful framework called Deep-DRAM, which can inversely design lattice structures with given elastic properties and dimensions. Given the requested elastic properties, we first used the deep generative model to generate  $10^5$  RN unit cells. It takes the deep generative model  $5.7 \pm 0.1$  s on a workstation (see the Methods section for the specifications) to generate these unit cells. Since the returned unit cell structures would vary in their design and mechanical response, they can deviate from the requested set of elastic properties. This is, in fact, an advantage of such a generative model because the actual elastic properties of a lattice structure with a finite (anisotropic) number of unit cells along each spatial direction may be quite different from the unit cell properties. The presence of such natural variations in the elastic properties of the generated unit cells enables us to feed a large number of designs created by the deep generative model to the size-agnostic model that is trained to account for the effects of size along each direction. Then, all these generated unit cells together with the desired dimensions are introduced to the size-agnostic model to predict the elastic properties of these combinatorial designs. Finally, the MSE values showing the difference between the target properties and the final elastic properties of the generated combinatorial designs are calculated. Based on the error values, we selected the designs that best matched the target elastic properties for the given dimensions (Figure 4a).

To demonstrate the functionality of Deep-DRAM, we assumed a constant value for the elastic modulus (*i.e.*,  $E_{11}/E_b = E_{22}/E_b = 0.03$ ) and a range of  $(-1, 1.6)$  for the Poisson's ratios with a step size of 0.2 (*i.e.*, 14 groups of values for the Poisson's ratios). In total, we studied 196 (*i.e.*,  $14 \times 14$ ) sets of elastic properties. We also predefined a dimension of  $D_1 = D_2 = 4$  for the generated combinatorial designs. Using these predefined values,  $1.96 \times 10^7$  combinatorial designs were generated



and filtered based on their MSE values. The whole design procedure including the inverse design of the RN unit cells, combining the unit cells into combinatorial designs, prediction of the elastic properties of the combinatorial designs, and finding the best candidates based on the calculated MSE values took  $\approx 38$  min (for all the  $1.96 \times 10^7$  designs) using the same, above-described computer. A few examples of generated RN lattice structures with predefined elastic properties and dimensions are presented in Supplementary Movie 1 (RN lattice structures with negative Poisson's ratio) and Supplementary Movie 2 (RN lattice structures with positive Poisson's ratio).

To quantify the expected error values for the design of combinatorial designs with different elastic properties and dimensions, we repeated the aforementioned procedure for 196 selected sets of elastic properties considering two groups of dimensions. In the first group, we predefined equal dimensions (*i.e.*,  $D_1 = D_2 = [2, 4, 6, 8, 10, 12, 14, 16, 18, 20]$ ) while in the second group we assumed  $D_2 = 2$  and  $D_1 = [2, 4, 6, 8, 10, 12, 14, 16, 18, 20]$ . We defined the envelope of successful designs such that it was bounded by the designs corresponding to an MSE value of 0.1. The heat maps of the MSE values depict the expected error values for generating combinatorial designs when the elastic properties and dimensions are provided as input (Figure 4b). The gray regions represent the designs whose elastic properties are associated with MSE values exceeding the acceptance threshold (Figure 4b). Upon closer inspection, we found that the gray regions primarily correspond to the property-size combinations that simply cannot arise from the considered random network. As expected, the envelopes of successful design generations converge for large enough values of  $D_1$  and  $D_2$  (Figure 4b). For larger sizes, the heat maps of MSE values for combinatorial designs with  $D_1 = D_2$  are symmetrical around the  $\nu_{12} = \nu_{21}$  line. This increased symmetry indicates a more isotropic behavior of RN combinatorial designs as their dimensions increase. In the other group of the combinatorial designs with  $D_2 = 2$  and varying  $D_1$  values, we do not expect isotropy because the ratio of  $D_1/D_2$  increases and the geometry is not symmetric anymore.

### 6.3. Results and discussion

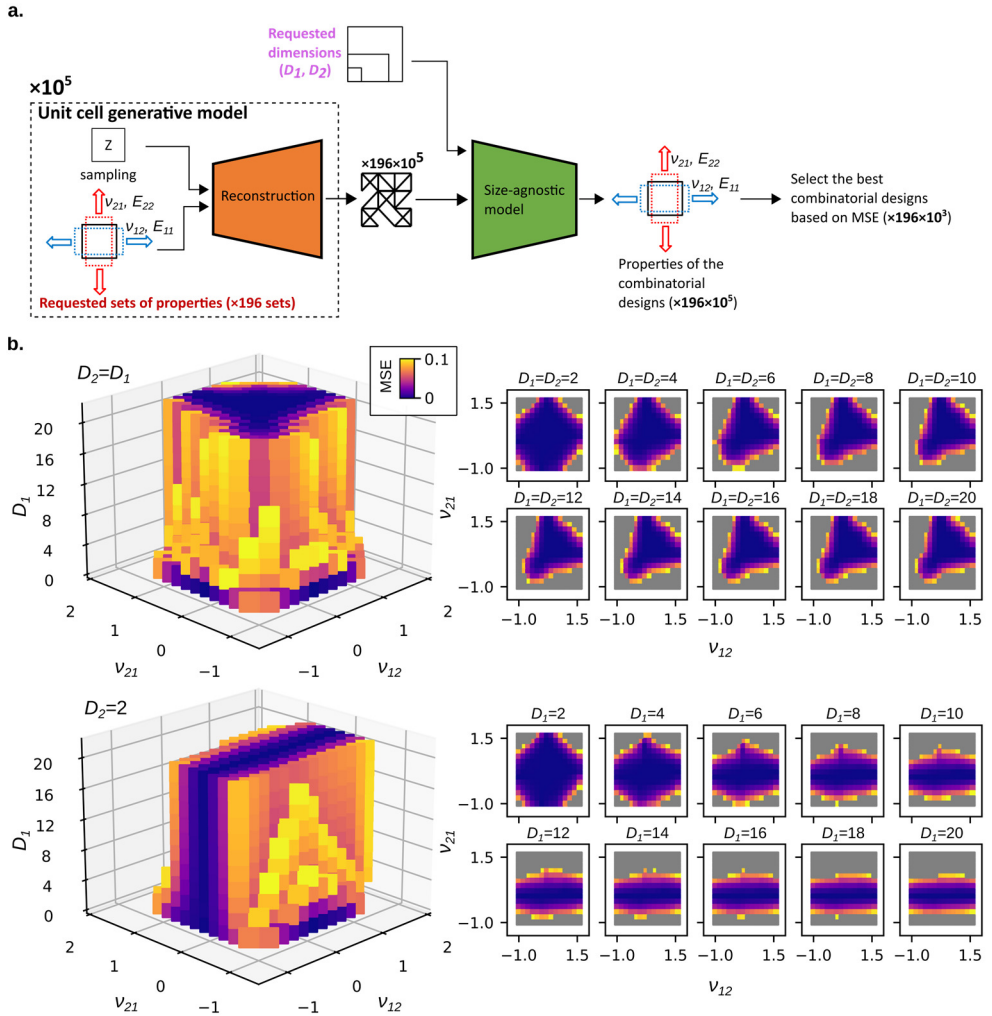


**Figure 4.** The structure of Deep-DRAM as a size-agnostic inverse design framework. (a) In this framework, the deep generative model and the size-agnostic model are combined to generate combinatorial designs with desired elastic properties and dimensions. The best candidates among the generated combinatorial designs are then selected based on their MSE values. (b) The heat maps of the MSE values indicating the expected error values for generating combinatorial designs with predefined elastic properties and dimensions.

#### 6.3.6. Stress distribution

Deep-DRAM provides many solutions to the design problem of finding RN lattice structures with pre-defined dimensions and elastic properties. It is, therefore,

possible to apply additional design requirements, such as criteria regarding the stress distributions observed within the generated structures under various types of loading conditions. One such criterion is to choose the design with the minimum peak stress, thereby enhancing their resistance against fatigue and failure. To demonstrate the utility of our size-agnostic inverse design framework within this context, we first generated combinatorial designs with predefined elastic properties and dimensions. We then filtered the generated designs based on their maximum von Mises stress (Figure 5a) (see Supplementary Movie 3). As representative cases, we studied three groups of combinatorial designs with predefined specifications: (i)  $D_1 = D_2 = 4$ ,  $\nu_{12} = -0.2$ , and  $\nu_{21} = 0.2$ , (ii)  $D_1 = 10$ ,  $D_2 = 4$ ,  $\nu_{12} = \nu_{21} = 0.5$ , and (iii)  $D_1 = D_2 = 10$ ,  $\nu_{12} = \nu_{21} = -0.2$ , while the elastic modulus was assumed to be the same for these three groups (*i.e.*,  $E_{11}/E_b = E_{22}/E_b = 0.03$ ). From each group, the first 1000 designs with  $MSE < 0.1$  were further analyzed using FE simulations to determine the stress distribution within their elements under two loading conditions (*i.e.*,  $\varepsilon_{11} = 5\%$  or  $\varepsilon_{22} = 5\%$ ). The normalized peak values of the von Mises stress in directions 1 and 2 were then calculated (Figure 5b). From each group, we selected two specimens with almost the same MSE but with either the minimum or maximum Euclidean distance from the origin. The stress distributions corresponding to these case studies clearly show stress concentrations in some regions within the specimens with the maximum Euclidean distances (*i.e.*, specimens 2, 4, and 6) while the stress distribution are comparatively more uniform within specimens 1, 3, and 5 (Figure 5c). The specimens with high peak stresses are prone to premature crack initiation and growth and should be avoided in the design of mechanical metamaterials aimed for practical applications. Further analysis of these results shows 310%, 250%, and 270% differences between the maximum and minimum values of the von Mises stresses of the three study groups, which are very substantial numbers within the context of peak stress reduction analysis.

### 6.3. Results and discussion

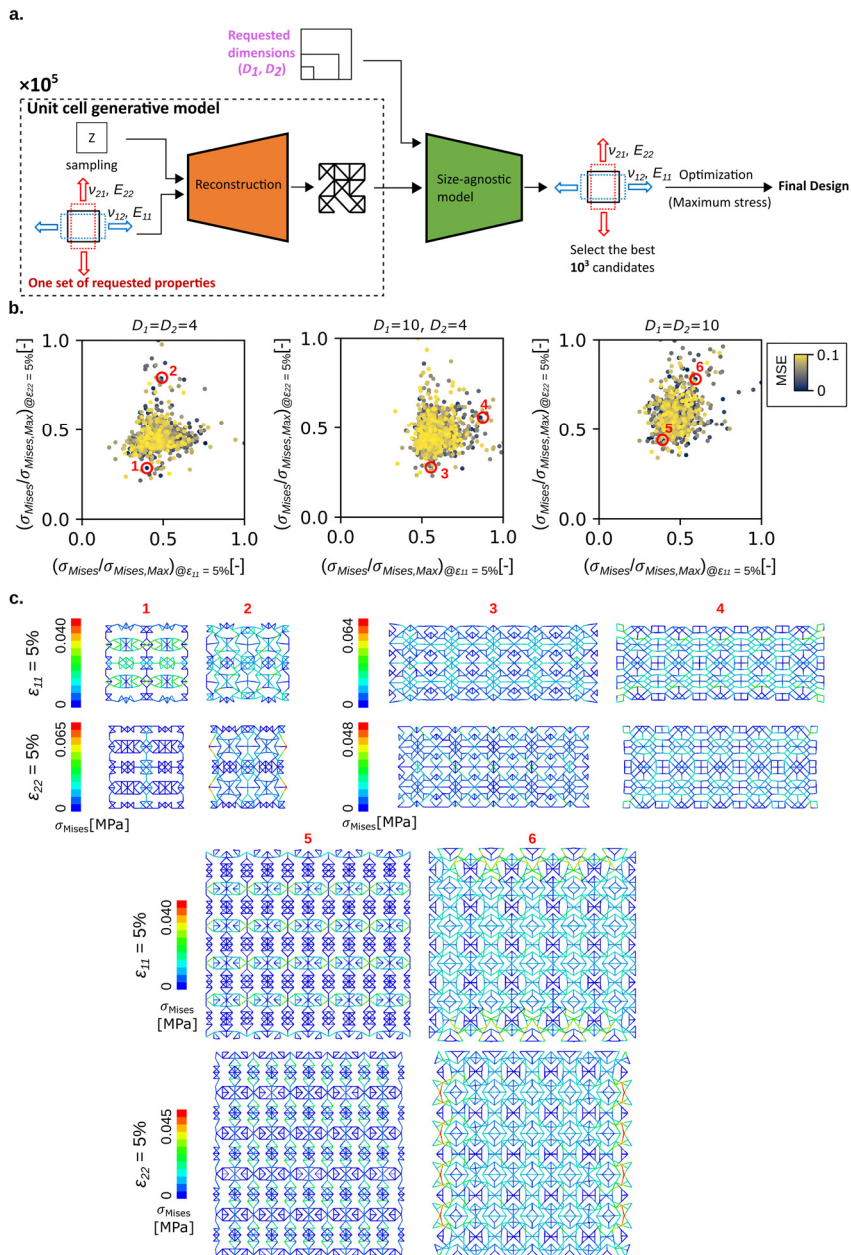


**Figure 5.** Multi-objective design where the minimization of peak von Mises stresses is considered as an additional design requirement. (a) Finding the optimized combinatorial designs based on the stress values of the elements of the lattice structure (see Supplementary Movie 3). (b) For each group of representative cases, the normalized peak von Mises stresses when the structure was subjected to a strain of  $\epsilon_{11} = 5\%$  are plotted against the same type of stress when the applied strain is  $\epsilon_{22} = 5\%$ . (c) The stress distributions of the elements of some selected combinatorial designs.

## 6.4. Discussion and future outlook

The Deep-DRAM framework presented here is a combination of four modules and provides many opportunities for the design of mechanical metamaterials for practical use in the design of advanced functional devices. In addition, the presented modular approach allows the individual modules to be combined with other tools available elsewhere to provide solutions for the many challenges encountered in the design of designer materials. To a degree, the modularity of this approach and the probabilistic nature of the CVAE allows us to decouple some of the problems encountered in the design and optimization of mechanical metamaterials, thereby enabling multi-objective design optimization with minimum development and computational costs. For example, the multiple objectives of achieving a certain set of elastic properties and minimizing the peak stress within the structure can be handled in-series with minimum computational costs. That is partially due to the extremely high speeds of both generating and evaluating individual designs, which are in the range of micro-seconds.

There are a number of points that need to be discussed regarding the broader use of Deep-DRAM. First, while we focused on a specific choice of RN for this study, the same methodology can also be used for any underlying design paradigm including any other types (*i.e.*, size, organization) of random structures as well as ordered structures and a combination thereof. Second, the modular design of our approach as well as its *ad hoc* combination with direct FE modeling affords it a high degree of flexibility in terms of taking design requirements into account and tackling multiple types of problems that are challenging in their own right. For example, the problem of finding rare combinations of elastic properties is treated independently in multiple other studies<sup>19,41</sup> but can also be studied, within the confines of the selected RN design, using the modules developed here. Third, our focus on the linear elastic properties meant that we used linear elastic constitutive models everywhere in the current study. However, the same approach can be used to study the nonlinear properties of RN designs or to consider any other aspects of their constitutive

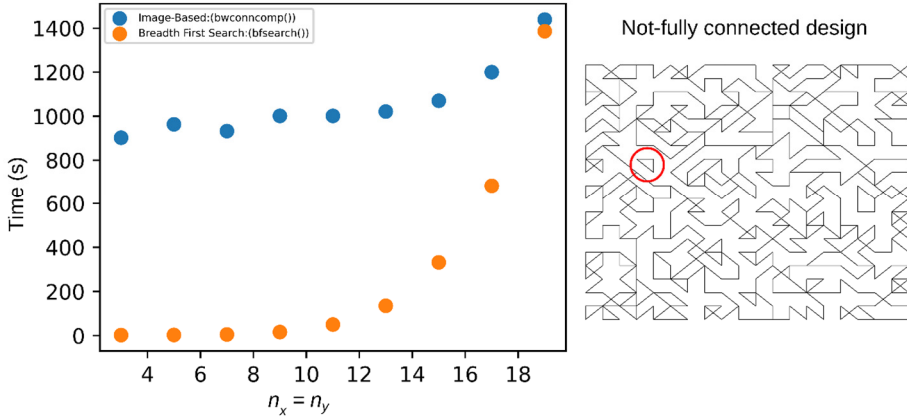
## 6.5. Conclusion

behavior (*e.g.*, viscoelasticity). The only difference would be that the FE models need to be modified to reflect the more complex constitutive behavior. Indeed, the relative advantage of the presented approach would be even more evident when the simulation time is longer, such as the case of nonlinear or viscoelastic constitutive behaviors. Fourth, the compact and computationally efficient nature of the final models means that they can be implemented in low-resource settings to power edge computing<sup>42,43</sup> applications. Finally, some elements of the developed modulus (*i.e.*, even individual layers) can be used for more advanced machine learning approaches, such as transfer learning, to further generalize the domain of application of our models.

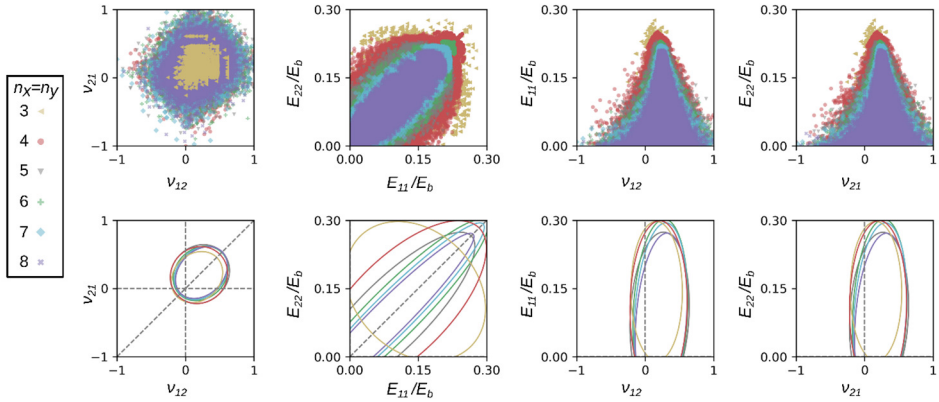
## 6.5. Conclusion

In summary, we developed a size-agnostic inverse design framework, Deep-DRAM, which can generate RN lattice structures not only with predefined elastic properties but also with predefined dimensions suitable for any intended application. We showed that combining deep generative models with forward predictors is successful in generating bespoke mechanical metamaterials while also satisfying additional design requirements, such as minimum peak stresses, to improve the endurance of designer materials for real-world applications.

## 6.6. Supplementary document



**Supplementary Figure 1.** Random network design filtering. This figure illustrates how the connectivity of RN unit cells are checked. A comparison between two different algorithms for the detection of non-connected nodes and their time efficiency. The analysis is performed for different node sizes ( $n_x = n_y$ ).



**Supplementary Figure 2.** The elastic properties (top row) and the confidence ellipses (bottom row) for RN unit cells with different node numbers (*i.e.*,  $n_x = n_y = 3, 4, 5, 6, 7$ , and  $8$ ).  $E_b$  is the elastic modulus of the bulk material

6.6. Supplementary document

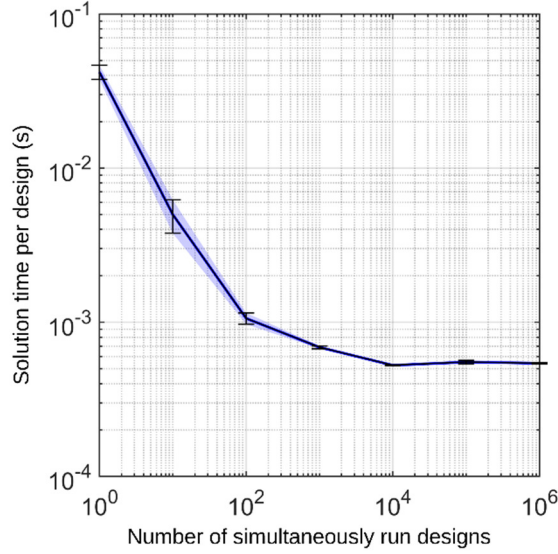
**Supplementary Table 1.** The principal radii ( $r_1$  and  $r_2$ ) as well as the areas ( $A$ ) of the confidence ellipses presented in Supplementary Figure 2.

$n_x$ = $n_y$	$\nu_{12}, \nu_{21}[-]$			$E_{11}/E_b, E_{22}/E_b[-]$			$\nu_{12}, E_{11}/E_b[-]$			$\nu_{21}, E_{22}/E_b[-]$		
	$r_1$	$r_2$	$A$	$r_1$	$r_2$	$A$	$r_1$	$r_2$	$A$	$r_1$	$r_2$	$A$
3	0.43	0.41	0.55	0.17	0.15	0.08	0.38	0.16	0.19	0.38	0.16	0.19
4	0.46	0.41	0.59	0.24	0.11	0.08	0.42	0.19	0.24	0.42	0.19	0.24
5	0.45	0.37	0.52	0.25	0.08	0.06	0.43	0.18	0.25	0.43	0.18	0.25
6	0.43	0.34	0.46	0.27	0.06	0.05	0.41	0.19	0.25	0.41	0.19	0.25
7	0.43	0.32	0.43	0.29	0.05	0.04	0.39	0.2	0.24	0.39	0.2	0.25
8	0.41	0.35	0.45	0.27	0.04	0.03	0.38	0.18	0.22	0.38	0.18	0.22

**Supplementary Table 2.** The probability of finding different ranges of the Poisson's ratio (%) for datasets with different  $n_x$  and  $n_y$  values.

$n_x$ = $n_y$	$\nu_{12} \cdot \nu_{21} < -0,5$	$-0,5 \leq \nu_{12} \cdot \nu_{21} < 0$	$0 \leq \nu_{12} \cdot \nu_{21} < 0,5$	$(\nu_{12} \cdot \nu_{21} \geq 0,5)$
3	0.00	6.75	92.75	0.50
4	0.05	6.63	90.47	2.84
5	0.05	6.01	91.43	2.50
6	0.04	6.00	91.47	2.49
7	0.03	5.43	92.51	2.02
8	0.03	5.17	93.02	1.78



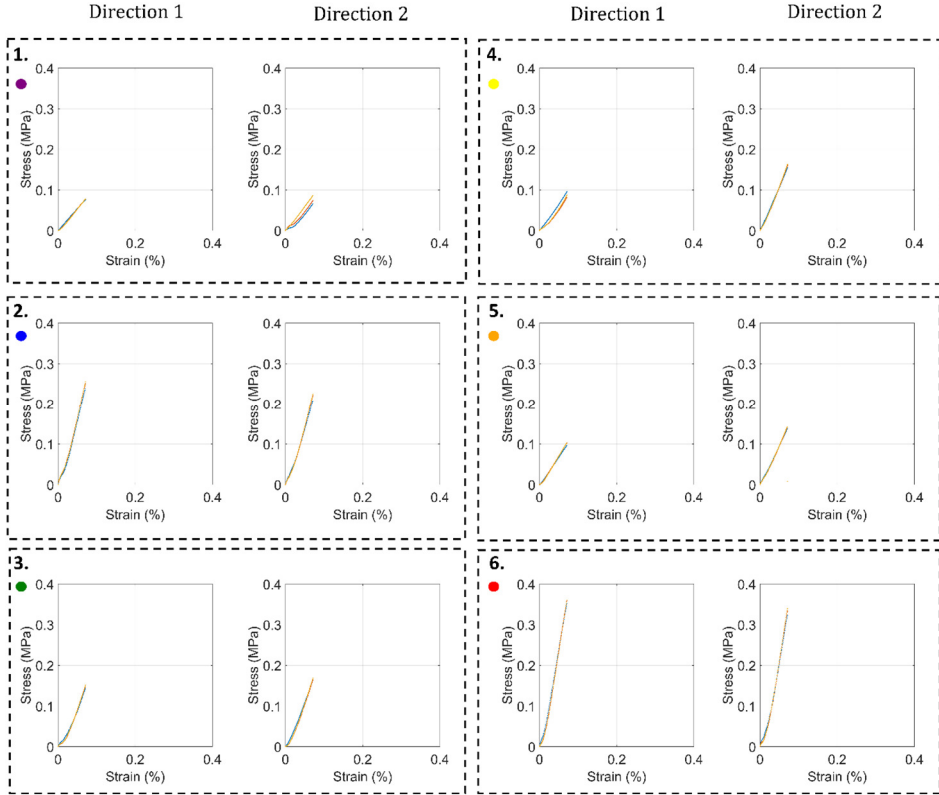


**Supplementary Figure 3.** Time comparison for the direct FE simulations aimed at determining the elastic properties of the RN unit cells.

**Supplementary Table 3.** The estimated time (considering  $5.4 \times 10^{-4}$  s for each RN unit cell) to generate all possible RN unit cells with  $n_x = n_y = 4$ . The estimated number of RN unit cells is calculated as  $C_{El_{placed}}^{El_{all}} = \frac{El_{all}!}{(El_{all}-El_{placed})!El_{placed}!}$ , where,  $El_{all} = n_x(n_y - 1) + n_y(n_x - 1) + 2(n_x - 1)(n_y - 1)$ ,  $El_{placed} = \frac{1}{2}Z_g \times n_x \times n_y$ .

$Z_g$	The estimated number of RN unit cells	Estimated Time [s]
2,5	$C_{20}^{42} \approx 5.14 \times 10^{11}$	277.447.468
3	$C_{24}^{42} \approx 3.54 \times 10^{11}$	190.996.445
3,5	$C_{28}^{42} \approx 5.29 \times 10^{10}$	28.544.524
4	$C_{32}^{42} \approx 1.47 \times 10^9$	794.579
4,5	$C_{36}^{42} \approx 5.25 \times 10^6$	2.832
Total	$9.22 \times 10^{11}$	497.785.848

## 6.6. Supplementary document



**Supplementary Figure 4.** The stress-strain curves for the experimental results of the RN unit cells. For the color code of each specimen see Figures 1b and 1c.

**Supplementary Table 4.** The numerical simulations and experimental results for the elastic properties of the RN unit cells. The numerically calculated elastic moduli are normalized to the elastic modulus of the bulk material assumed in the FE analysis ( $E_{b,FE} = 0.6$  MPa) while the experimentally obtained elastic moduli are normalized with respect to the elastic modulus of the bulk material from which the samples were printed ( $E_{b,EXP} = 25$  MPa).

Samp le	Numerical Simulations				Experimental Results			
	$v_{12}[-]$	$v_{21}[-]$	$E_{11}/E_{b,FE}[-]$	$E_{22}/E_{b,FE}[-]$	$v_{12}[-]$	$v_{21}[-]$	$E_{11}/E_{b,EXP}[-]$	$E_{22}/E_{b,EXP}[-]$
1	-0.58	-0.65	0.048	0.049	-0.39	-0.48	0.048	0.045
2	0.53	0.46	0.144	0.115	0.59	0.41	0.152	0.133
3	0.50	-0.49	0.083	0.094	0.20	-0.41	0.091	0.104
4	-1.18	0.23	0.030	0.074	-0.88	0.54	0.053	0.097
5	0.35	1.16	0.053	0.028	0.39	0.86	0.084	0.063
6	0.16	0.16	0.243	0.243	0.31	0.27	0.229	0.209

## 6.6.1. Supplementary methods

### Finite Element modeling

The element stiffness matrix was transferred to the global coordinate ( $K^e$ ) and was calculated as<sup>44,45</sup>:

$$K^e = Q^T \bar{K}^e Q, \quad (1)$$

$$\bar{K}^e = \frac{E_b}{(1+\mu)} \begin{bmatrix} A(1+\mu)/L_e & 0 & 0 & -A(1+\mu)/L_e & 0 & 0 \\ 0 & 12I/L_e^3 & 6I/L_e^2 & 0 & -12I/L_e^3 & 6I/L_e^2 \\ 0 & 6I/L_e^2 & 4I(1+\mu/4)/L_e & 0 & -6I/L_e^2 & 2I(1-\mu/2)/L_e \\ -A(1+\mu)/L_e & 0 & 0 & A(1+\mu)/L_e & 0 & 0 \\ 0 & -12I/L_e^3 & -6I/L_e^2 & 0 & 12I/L_e^3 & -6I/L_e^2 \\ 0 & 6I/L_e^2 & 2I(1-\mu/2)/L_e & 0 & -6I/L_e^2 & 4I(1+\mu/4)/L_e \end{bmatrix}, \quad (2)$$

$$\mu = \frac{12E_b I}{L_e^2 G_b A K_s}, \quad (3)$$

$$Q = \begin{bmatrix} n_{x\bar{x}} & n_{y\bar{x}} & 0 & 0 & 0 & 0 \\ n_{x\bar{y}} & n_{y\bar{y}} & 0 & 0 & 0 & 0 \\ 0 & 0 & 1 & 0 & 0 & 0 \\ 0 & 0 & 0 & n_{x\bar{x}} & n_{y\bar{x}} & 0 \\ 0 & 0 & 0 & n_{x\bar{y}} & n_{y\bar{y}} & 0 \\ 0 & 0 & 0 & 0 & 0 & 1 \end{bmatrix}, \quad (4)$$

where  $\bar{K}^e$  is the local element stiffness matrix, and  $E_b$ ,  $A$ ,  $I$ , and  $L_e$  are the elastic modulus of the bulk material, the cross-section area ( $A = Tt$ ) of the element, the moment of inertia ( $I = Tt^3 / 12$ ) of the element, and the length of the element, respectively.  $\mu$  is a dimensionless coefficient that characterizes the importance of shear-related parameters including  $G_b$  (shear modulus of the bulk material) and  $K_s$  (shear correction factor = 0.85).  $Q$  is the transformation matrix and contains the direction cosines:

$$n_{x\bar{x}} = n_{y\bar{y}} = \frac{x_2 - x_1}{L_e}, n_{y\bar{x}} = -n_{x\bar{y}} = \frac{y_2 - y_1}{L_e} \quad (5)$$

where  $x_1, y_1, x_2$ , and  $y_2$  are the element nodal coordinates. The stiffness matrix was calculated for all the elements and was assembled into a global stiffness matrix ( $K$ ).

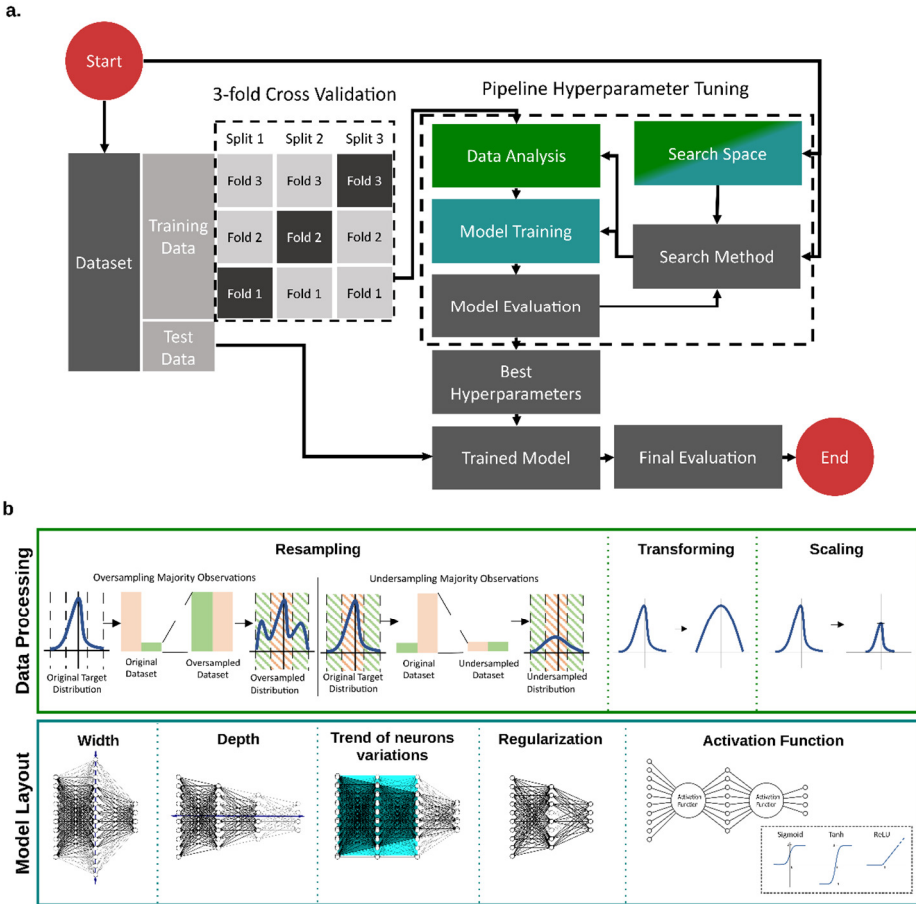
## 6.6. Supplementary document

The predefined boundary conditions for our displacement control ( $f = 0$ ) analysis are applied as the following boundary condition matrix:

$$bc = \begin{bmatrix} DOF_1 & (u_{11})_{node\_1} \\ DOF_2 & (u_{22})_{node\_1} \\ DOF_3 & (u_{33})_{node\_1} \\ \vdots & \vdots \\ DOF_{3 \times n} & (u_{33})_{node\_n} \end{bmatrix} \quad (6)$$

where the first column shows the number of DOF and the second column shows the corresponding predefined displacements. Considering  $n$  as the total number of nodes and three DOF for each node, we had  $3 \times n$  DOF in total. Finally, we used solveq function ( $[a, r] = solveq(K, f, bc)$ ) of CALFEM finite element toolbox<sup>45</sup> to calculate reaction forces ( $r$ ) and displacements ( $a$ ) in all DOF.

Hyperparameter tuning pipeline



**Supplementary Figure 5.** The training pipeline. a) The suggested methodology for the training of deep learning models while avoiding the pitfalls of common practice and introducing an extra step of optimization in the search of best parameters, b) The data analysis and model hyperparameter options for the search space of the hyperparameter tuning procedure.

**Data processing**

Various data processing methods can aid in the successful training of a deep learning model. The features have binary values and no further analysis is, therefore, required. The distributions of the targets were acquired. It is noticeable that the distribution of the Poisson's ratio for both directions have heavy tails, explained by the rarity of the specimens with extreme negative and positive values of the Poisson's

## 6.6. Supplementary document

ratios. Furthermore, the Poisson's ratios and elastic moduli have different ranges of values (*i.e.*,  $\nu_{12}, \nu_{21} = [-1.5, 1.5]$  and  $E_{11}/E_b, E_{22}/E_b = [0, 0.25]$ ).

Model training on highly skewed data tends to be misleading and leads to poor model performance<sup>46</sup>. These observations within the tail of the distributions refer to rare but useful data samples, such as double-auxeticity or strong auxeticity. In this case, the dataset is imbalanced with some data of interest underrepresented. To balance out the dataset based on the targets, a data resampling process is proposed. Prior to training a deep learning model, the input and output data can be prepared by utilizing transformation/rescaling techniques<sup>46</sup>. Models commonly work more efficiently when the inputs have a normal distribution, and it is also shown that the transformation of the outputs could help in improving the performance of the model<sup>46</sup>. An input with a variance that is orders of magnitude greater than others may dominate the objective function and prevent the estimator from learning from other inputs. Output transformation may also aid in the training of the model. Some form of output scaling is also suggested to make the model converge more easily, as unscaled output variables can cause exploding gradients when dealing with regression problems<sup>46</sup>. Taking into consideration the distribution and the range of the targets, the training dataset could be processed accordingly by including the option of target-based data resampling and transformation/rescaling options (either as output for the forward models or as input for the inverse model) in the search space of the hyperparameter tuning pipeline.

**Data resampling:** Addressing classification issues for imbalanced data is well-documented. However, regression training on imbalanced data is not as widely studied. Using the same techniques as in other cases is often problematic. Pre-processing approaches are primarily concerned with oversampling the minority samples, undersampling the majority ones, or a combination of both before training the regression model<sup>47</sup>. Oversampling depends on duplicating some data that do not have enough representation or fabricating similar data. The simplest technique for oversampling is to produce new samples by randomly sampling and replacing

existing samples<sup>47</sup>. Undersampling cuts down the total number of the available data points, selecting a roughly similar size of each type of data that needs to be represented<sup>47</sup>. For oversampling, we used the Synthetic Minority Over-Sampling Technique for Regression with Gaussian Noise (SMOGRN)<sup>48</sup>, which is beneficial for regression problems where the prediction of rare values is of great importance.

By undersampling the dataset, the model can be trained faster while having equivalent information to work with. Undersampling for classification is a much easier work due to the explicit segmentation of classes that is specified from the beginning. However, in the case of a continuous variable, the areas of resampling are more difficult to specify. The binning of the dataset was performed by manually selecting the number of “classes” to obtain datasets with a similar number of data points. As a preliminary inspection of bin-based undersampling, three bins were created for the following ranges of the Poisson’s ratio:  $-1.5 < \nu < 0$ ,  $0 < \nu < 0.3$ , and  $0.3 < \nu < 1.5$ . The second class appeared to be the most common while the other two were underrepresented. The results revealed that the initial dataset was greatly downsized. To better classify the dataset, samples with relatively similar elastic properties were grouped together. The number of samples per each group was then kept constant. The values of  $E$  and  $\nu$  were rounded to the first and second decimals respectively, as smaller variations of the elastic properties can be neglected. In that way, multiple tiles can be grouped to have similar elastic properties. The frequency of each unique combination of the four elastic properties was then calculated. It is clear that there are more duplicates for specific elastic properties. Finally, we kept five unit cells for each pair of the elastic properties when available. Consequently, a dataset of six million-unit cells reduced to eighty thousand unit cells. Both oversampling and undersampling were included in the search space considered for hyperparameter tuning.

**Data transformation/scaling:** Scaling features to be confined in the range between specific minimum and maximum values is an alternative standardization method. In the case of multitask regression, normalizing all the targets aids in

## 6.6. Supplementary document

balancing the training loss from various individual tasks. The rescaling through `MinMaxScaler` and the quantile transformation were included in the search space of the hyperparameter tuning pipeline applied before training the model. `MinMaxScaler` transforms features by scaling each feature such that it is in the range of  $[0,1]$ . `QuantileTransformer` is a class that transforms features and targets to fit a uniform or normal distribution, given enough training examples.

### **Model hyperparameters**

Training of a deep learning model requires the modification of several hyperparameters. Here, we tuned the architecture of the model (including the number of hidden layers, the number of hidden neurons per each layer, and the trend of the changes of the neurons of different hidden layers), the activation function, the optimizer, and the regularization terms as hyperparameters. Then, we created the models with the use of Keras TensorFlow API for Sequential Models. The search methods of cross-validation grid search from `scikit-learn`<sup>46</sup> were then used to systematically iterate among a library of predefined values for the hyperparameters.

**Capacity/architecture of the model:** Each model was created from scratch. The architecture of a neural network model is modified (i) by the width, determined by the number of neurons in each layer and (ii) the depth that is determined by the number of layers, and (iii) the trend of the changes of the neurons of different hidden layers. The number of neurons in the input layer equals the number of features in the data and the number of neurons in the output layer for supervised learning equals the number of targets/labels. As there is no predefined formula that guarantees the high accuracy of a model without overfitting, we systematically studied different combinations of hyperparameters. The parameterized sequential model was built based on a function that takes the following as its inputs: the number of hidden layers, the input and output size, the width of the first hidden layer, and the trend of the variation of the number of hidden neurons per layer (whether the number of neurons remains the same throughout the hidden layers or is it gradually decreasing). The



width of the other hidden layers is declining by a specific step that is defined as the difference between the number of neurons of the first hidden and output layer, divided by the number of hidden layers. For the CVAE, a final parameter that affects the capacity of the models is the dimension of the latent space. The bottlenecking was expected to affect the ability of the reconstruction/inverse model. Therefore, various values [2, 8, and 16] were considered for the dimension of the latent space.

**Regularization:** When there is no way to expand the data, overfitting can be combated by regularization, which is a way to constrain the amount and kind of information that the model can hold, forcing the model to focus on the most essential parameters to achieve generalization. The most prevalent regularization approaches are weight regularization and dropout. Batch normalization can also operate as a regulator, decreasing and, in certain cases, eliminating the requirement for dropout. The option of batch normalization inclusion after each hidden layer was, thus, included in the hyperparameter optimization pipeline.

**Optimizers:** Optimizers are the algorithms that are used to minimize losses by adjusting the characteristics of the neural network, such as weights and learning rate. An optimization algorithm called gradient descent is frequently used to train deep learning models. In current deep learning algorithms, three forms of gradient descent learning algorithms are used: batch gradient descent, stochastic gradient descent, and small batch gradient descent. The simplest, yet widely used optimization approach is batch gradient descent. It is extensively utilized in linear regression and classification techniques. However, for big datasets, batch gradient descent performs redundant computations since it recomputes gradients for comparable cases before each parameter change. By completing one update at a time, stochastic gradient descent (SGD) eliminates this redundancy. As a result, it is significantly faster. Many methods have been proposed for optimizing SGD, among which we selected Adam and RMSprop optimizers to be evaluated through the hyperparameter tuning pipeline.

## 6.6. Supplementary document

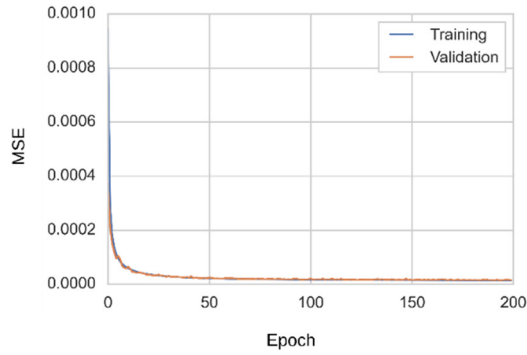
**Activation function:** Activation functions are widely utilized because of a few desired properties: non-linearity, range, and differentiability. For a universal function approximator, nonlinear activations are desirable. Moreover, the function should be continuously differentiable for gradient-based optimization approaches to be possible. The model's stability and efficiency are influenced by whether the function's range is finite or not. Sigmoid, tanh, and ReLU are the examples of popular activation functions that fit the selection criteria and were included as options in the search space for creating the sequential neural network models. The activation functions of hidden layers and the output layer were defined separately. If the range of the output activation function is shorter than the range of the dataset values, a value cut-off can be detected. For the output layer of the reconstruction model of the CVAE, the activation function was pre-set to sigmoid, to output a binary probabilistic representation of the vector that describes the designs, which would allow the reconstruction part of the overall CVAE loss to be approximated with the binary cross entropy.

**Batch size:** The batch size is an important hyperparameter, as there is a relation between the batch size on the one hand and the speed and stability of the learning process on the other. The recommended batch size varies depending on whether the learning method uses batch, stochastic, or minibatch gradient descent. Stochastic gradient descent algorithms that are selected work in a small-batch mode, sampling a subset of the training data, typically 32 to 512 data points. In fact, it has been shown that employing a bigger batch dramatically lowers the model's quality as measured by its capacity to generalize<sup>49</sup>. Thus, the batch size was set at 32.

**Supplementary Table 5.** The search space of the hyperparameter tuning pipeline as applied to the unit cell elastic properties model.

Step	Process	Search Space	Selected
Data Analysis	Resampling	Undersampling, Oversampling	Undersampling
	Rescaling/transforming	None, MinMaxScaler, Quantiletransformer	MinMaxScaler
Model Tuning	Hidden layers	2 – 5	4
	Neurons 1 <sup>st</sup> hidden layer	20, 100, 500	500
	Trend of neurons variations	Rectangle, Triangle	Triangle
	Activation function	None, Relu, Tanh	Relu
	Last layer activation function	None, Relu, Tanh	Relu
	Optimizer	Adam, RMSprop	Adam
	Step size	0.0001	
	Loss function	MSE	
	Batch normalization	Yes, No	No
	Targets	4	
Fitting	Batch size	32 (Default)	
	Epochs	200	
Cross-validation	K-folds	3	
	Data split	60 – 30 – 10	
	Scoring	$R^2$	

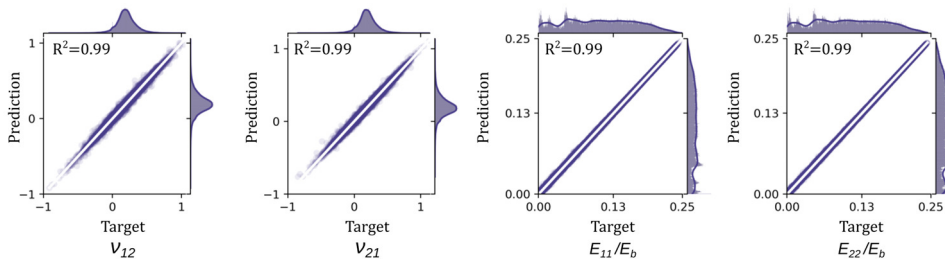
## 6.6. Supplementary document



**Supplementary Figure 6.** The MSE graph for the unit cell elastic properties model.

**Supplementary Table 6.** The regression metrics. The evaluation of the unit cell elastic properties model using the test dataset. In this table,  $R^2$  is the coefficient of determination ( $R^2 = 1 - \frac{\sum_{i=1}^n (y_i - \hat{y}_i)^2}{\sum_{i=1}^n (y_i - \bar{y})^2}$ ),  $MSE$  is the mean squared error ( $MSE = \frac{1}{n} \sum_{i=1}^n (y_i - \hat{y}_i)^2$ ),  $MAE$  is the mean absolute error ( $MAE = \frac{1}{n} \sum_{i=1}^n |y_i - \hat{y}_i|$ ), and  $RMSE$  is the root mean squared error ( $RMSE = \sqrt{MSE}$ ), where  $n$  is the size of the dataset,  $y_i$  is the  $i^{\text{th}}$  real target,  $\hat{y}_i$  is the corresponding predicted value, and  $\bar{y}$  is the mean value of  $y$  ( $\bar{y} = \frac{1}{n} \sum_{i=1}^n y_i$ ).

Index	$\nu_{12}$	$\nu_{21}$	$E_{11}$	$E_{22}$	Overall
$R^2$	0.9934	0.9945	0.9997	0.9997	0.9968
MSE	0.0001	0.0001	0.0000	0.0000	0.0000
MAE	0.0071	0.0065	0.0004	0.0004	0.0036
RMSE	0.0114	0.0104	0.0005	0.0005	0.0057

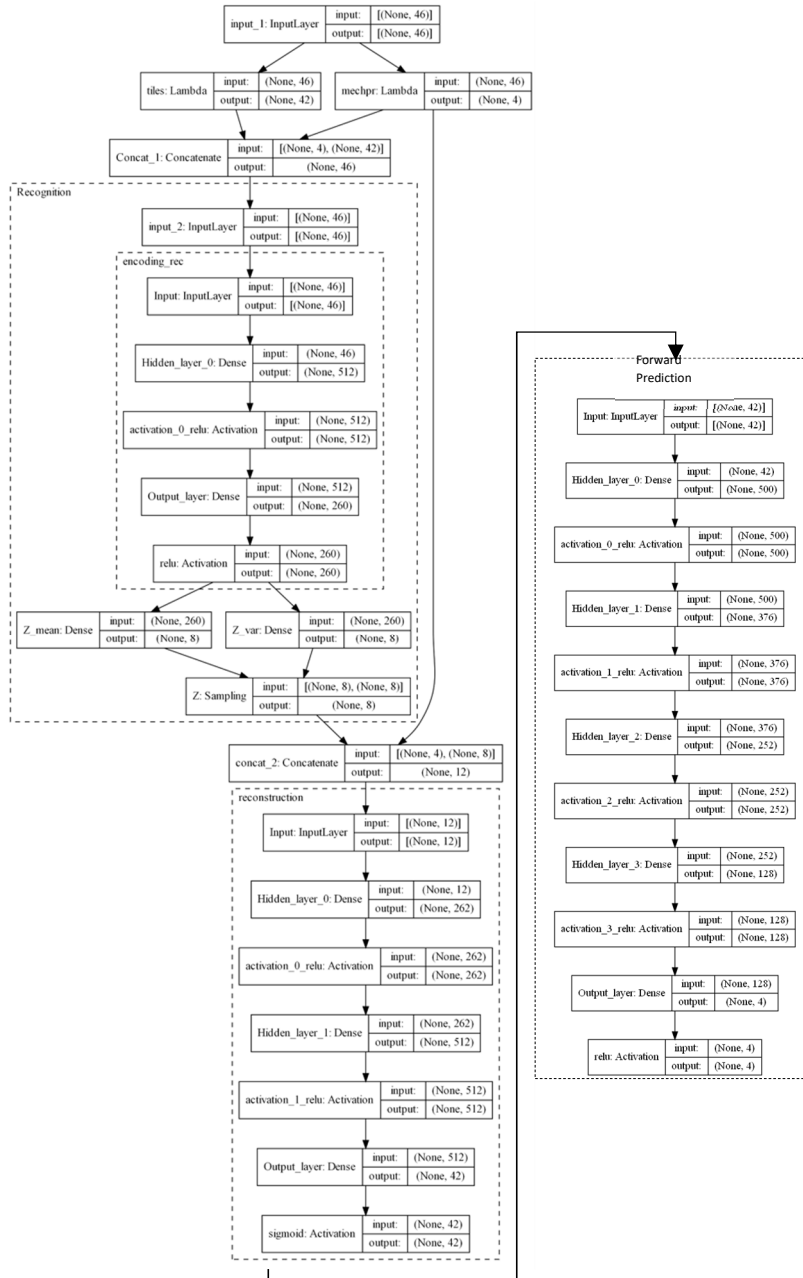


**Supplementary Figure 7.** The evaluation of the unit cell elastic properties model. The prediction vs. target values and the coefficients of determination for the test datasets.

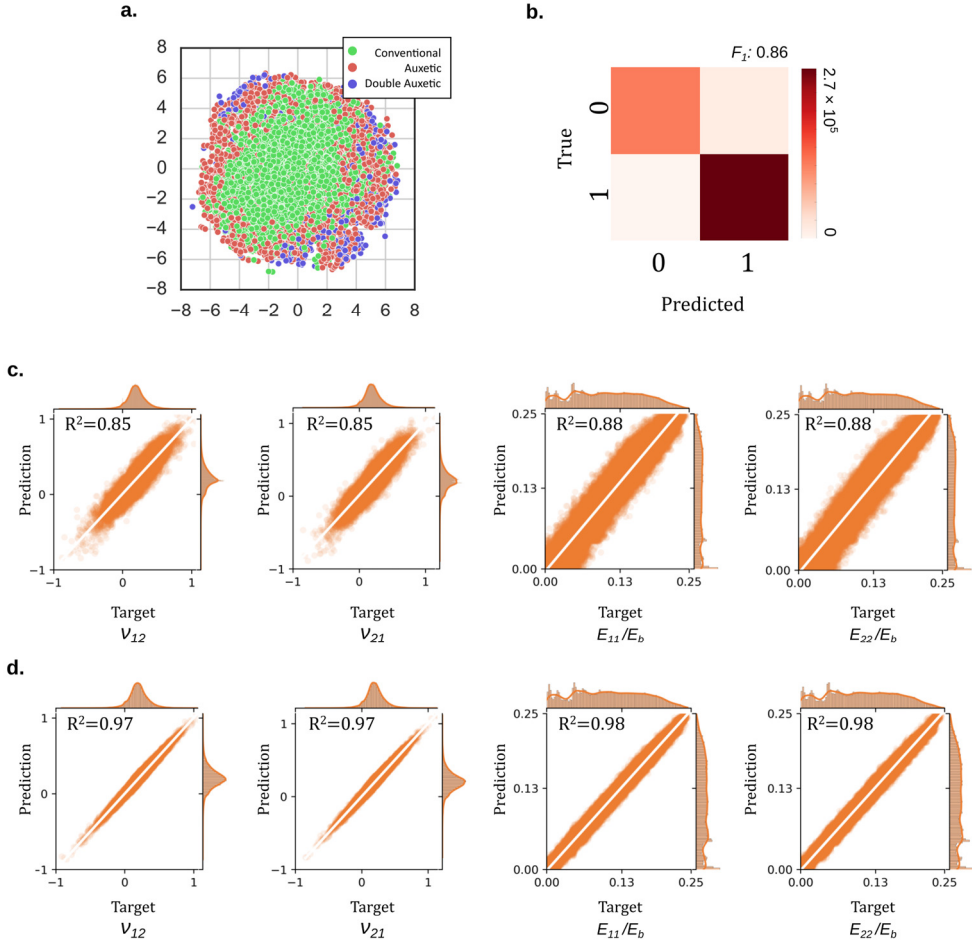
**Supplementary Table 7.** The search space for the training of the CVAE model and the selected parameters.

Step	Parameter	Search Space	Selected
	Inputs	Structures + elastic properties	
	Neurons 1 <sup>st</sup> hidden layer	128,512	512
	Hidden layers	1 – 4	2
Recognition Model	Trend of neurons variations	Rectangle, Triangle	Triangle
	Activation function	Relu, Sigmoid	Relu
	Last layer activation function	Relu, Sigmoid	Relu
	Outputs	Latent dimensions	
Latent Space Dimension	Size	2,8,16	8
	Inputs	Latent Dimensions + elastic properties	
	Neurons 1 <sup>st</sup> hidden layer	128,512	512
	Hidden layers	1 – 4	2
	Trend of neurons variations	Rectangle, Triangle	Triangle
	Activation function	Relu, Sigmoid	Relu
Reconstruction Model	Last layer activation function	Sigmoid	
	Outputs	Structure	
	Optimizer	Adam	
	Step size	0.0001	
	Loss function	$\mathcal{L}_{all} = \mathcal{L}_{CVAE} + \mathcal{L}_{MSE}$	
	Batch normalization	No	
		Batch size	32 (Default)
Fitting	Epochs	2000	
	K-folds	3	
Cross-validation	Data split	60 – 30 – 10	
	Scoring	$\mathcal{L}_{all} = \mathcal{L}_{CVAE} + \mathcal{L}_{MSE}$	

## 6.6. Supplementary document



**Supplementary Figure 8.** The network architecture and selected hyperparameters of the CVAE model and forward prediction unit cell elastic properties model. The reconstruction model of the CVAE is then used to generate unit cells with given elastic properties.



**Supplementary Figure 9.** The evaluation of the trained CVAE and the unit cell generative model. a) The  $t$ -SNE plot of the latent space created by the CVAE, displaying the placement of conventional, auxetic, and double auxetic metamaterials. b) The confusion matrix and  $F_1$  score for the reconstruction of the unit cell through the reconstruction model of the CVAE (*i.e.*, the unit cell generative model). c) The prediction error plot and  $R^2$  for the predicted elastic properties of the designs generated by the unit cell generative model. d) The prediction error plot and  $R^2$  for the predicted elastic properties of the best unit cell candidates from the unit cell generative model.

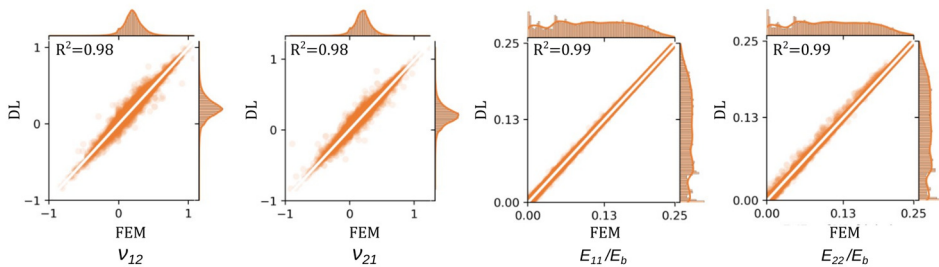
## 6.6. Supplementary document

**Supplementary Table 8.** The regression metrics corresponding to the unit cell generative model for the test dataset, as displayed in Supplementary Figure 9c.

Index	$v_{12}$	$v_{21}$	$E_{11}$	$E_{22}$	Overall
$R^2$	0.8460	0.8489	0.8878	0.8772	0.8650
MSE	0.0170	0.0168	0.0001	0.0001	0.0085
MAE	0.0935	0.0932	0.0086	0.0090	0.0511
RMSE	0.1305	0.1297	0.0011	0.0012	0.0710

**Supplementary Table 9.** Test regression metrics for the unit cell generative model as applied to the test dataset, displayed in Supplementary Figure 9d.

Index	$v_{12}$	$v_{21}$	$E_{11}$	$E_{22}$	Overall
$R^2$	0.9672	0.9665	0.9870	0.9868	0.9769
MSE	0.0006	0.0006	0.0000	0.0000	0.0003
MAE	0.0207	0.0208	0.0033	0.0033	0.0120
RMSE	0.0257	0.0258	0.0041	0.0042	0.0151



**Supplementary Figure 10.** The error plot and  $R^2$  values for the FEM validation of the DL-predicted elastic properties presented in Supplementary Figure 9d.

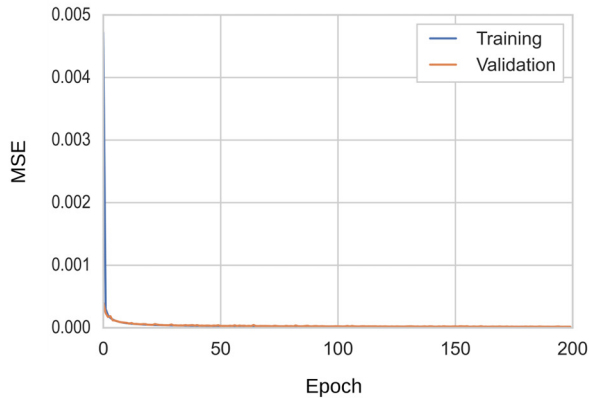
**Supplementary Table 10.** The target, forward predicted, and numerically simulated elastic properties of the generated samples displayed in Fig. 2.

Sample	Target				Forward Predicted				FEM simulated			
	$v_{12}$	$v_{21}$	$\frac{E_{11}}{E_b}$	$\frac{E_{22}}{E_b}$	$v_{12}$	$v_{21}$	$\frac{E_{11}}{E_b}$	$\frac{E_{22}}{E_b}$	$v_{12}$	$v_{21}$	$\frac{E_{11}}{E_b}$	$\frac{E_{22}}{E_b}$
I	-0.2	-1.0	0.03	0.03	-0.2	-1.0	0.02	0.03	-0.2	-1.1	0.02	0.03
II	-0.7	-0.7	0.05	0.05	-0.7	-0.6	0.05	0.04	-0.7	-0.7	0.04	0.04
III	-1.0	-0.2	0.07	0.07	-1.0	-0.2	0.07	0.06	-0.9	-0.2	0.07	0.07
IV	-0.5	-0.5	0.08	0.08	-0.5	-0.5	0.08	0.09	-0.5	-0.5	0.09	0.09



**Supplementary Table 11.** The search space of the hyperparameter tuning pipeline for the size-agnostic model.

Step	Process	Search Space	Selected
Data analysis	Rescaling/transforming	MinMaxScaler	
Model Tuning	Hidden layers	1 – 7	6
	Neurons 1 <sup>st</sup> hidden layer	128,256,512,1024	512
	Network shape	Triangle	
	Activation function	ReLU	
	Last layer activation function	ReLU	
	Optimizer	Adam	
	Step size	0.0001	
	Loss function	MSE	
	Batch normalization	No	
	Targets	4	
Fitting	Batch size	32, 64,128,256	128
	Epochs	200	
Cross-validation	K-folds	3	
	Data split	60 – 30 – 10	
	Scoring	MSE, R <sup>2</sup>	

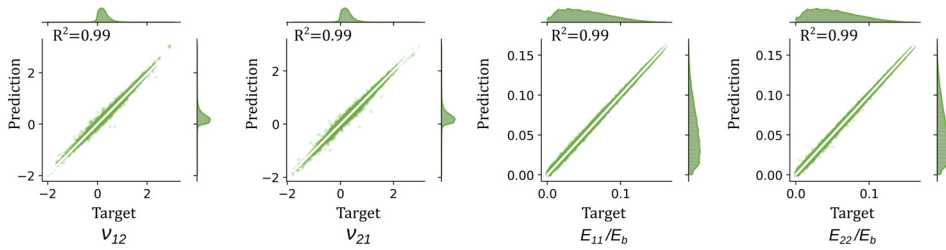


**Supplementary Figure 11.** The MSE graph for the size-agnostic model.

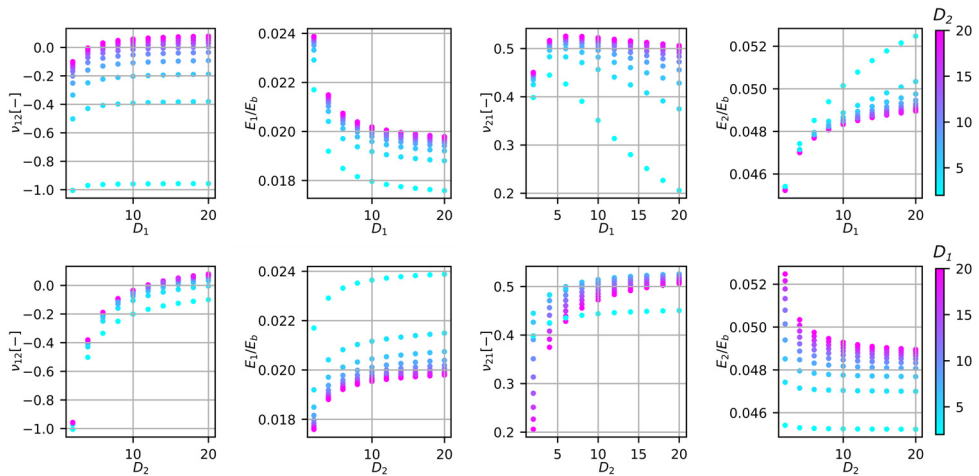
## 6.6. Supplementary document

**Supplementary Table 12.** Regression metrics. The evaluation of the size-agnostic model using the test dataset.

Index	$\nu_{12}$	$\nu_{21}$	$E_{11}$	$E_{22}$	Overall
$R^2$	0.9911	0.9915	0.9996	0.9995	0.9954
MSE	0.0005	0.0004	0.0000	0.0000	0.0002
MAE	0.0151	0.0144	0.0005	0.0005	0.0076
RMSE	0.0214	0.0208	0.0007	0.0007	0.0109



**Supplementary Figure 12.** The evaluation of the size agnostic model. The prediction vs. target values and the coefficients of determination for the test datasets are presented.



**Supplementary Figure 13.** 2D plots showing the evolution of the elastic properties based on changes in  $D_1$  and  $D_2$  for a representative case.

### 6.6.2. Supplementary movies

**Supplementary Movie 1.** Generating random-network metamaterials with negative Poisson's ratio.

**Supplementary Movie 2.** Generating random-network metamaterials with positive Poisson's ratio.

**Supplementary Movie 3.** Deep-DRAM: Generating RN metamaterials with desired elastic properties and dimensions considering the minimization of peak von Mises stresses as an additional design requirement.

## References

1. Kolken, H. M. A. *et al.* Rationally designed meta-implants: a combination of auxetic and conventional meta-biomaterials. *Mater. Horizons* **5**, 28–35 (2018).
2. Koons, G. L., Diba, M. & Mikos, A. G. Materials design for bone-tissue engineering. *Nat. Rev. Mater.* **5**, 584–603 (2020).
3. Zadpoor, A. A. Meta-biomaterials. *Biomater. Sci.* **8**, 18–38 (2020).
4. Rafsanjani, A., Bertoldi, K. & Studart, A. R. Programming soft robots with flexible mechanical metamaterials. *Sci. Robot.* **4**, 2–5 (2019).
5. Lee, H. *et al.* 3D-printed programmable tensegrity for soft robotics. *Sci. Robot.* **5**, 1–12 (2020).
6. Wu, S. *et al.* Symmetry-breaking actuation mechanism for soft robotics and active metamaterials. *ACS Appl. Mater. Interfaces* **11**, 41649–41658 (2019).
7. Surjadi, J. U. *et al.* Mechanical metamaterials and their engineering applications. *Adv. Eng. Mater.* **21**, 1800864 (2019).
8. Wu, W. *et al.* Mechanical design and multifunctional applications of chiral mechanical metamaterials: a review. *Mater. Des.* **180**, 107950 (2019).
9. Mirzaali, M. J. *et al.* Curvature induced by deflection in thick meta-plates. *Adv. Mater.* **33**, 2008082 (2021).
10. Zadpoor, A. A. Mechanical meta-materials. *Mater. Horizons* **3**, 371–381 (2016).
11. Barchiesi, E., Spagnuolo, M. & Placidi, L. Mechanical metamaterials: a state of the art. *Math. Mech. Solids* **24**, 212–234 (2019).
12. Greaves, G. N., Greer, A. L., Lakes, R. S., & Rouxel, T. Poisson’s ratio and modern materials. *Nat. Mater.* **10**, 823–837 (2011).
13. Bertoldi, K., Vitelli, V., Christensen, J. & Van Hecke, M. Flexible mechanical metamaterials. *Nat. Rev. Mater.* **2**, 1–11 (2017).
14. Zheng, X. *et al.* Ultralight, ultrastiff mechanical metamaterials. *Sci.* **344**, 1373–1377 (2014).
15. Ma, G. & Sheng, P. Acoustic metamaterials: from local resonances to broad horizons. *Sci. Adv.* **2**, e1501595 (2016).
16. Cummer, S. A., Christensen, J. & Alù, A. Controlling sound with acoustic

- metamaterials. *Nat. Rev. Mater.* **1**, 1–13 (2016).
17. Kadic, M., Bückmann, T., Schittny, R. & Wegener, M. Metamaterials beyond electromagnetism. *Rep. Prog. Phys.* **76**, 126501 (2013).
  18. Yavari, S. A. *et al.* Relationship between unit cell type and porosity and the fatigue behavior of selective laser melted. *J. Mech. Behav. Biomed. Mater.* **43**, 91–100 (2015).
  19. Pahlavani, H. *et al.* Deep learning for the rare-event rational design of 3D printed multi-material mechanical metamaterials. *Commun. Mater.* **3**, 1–11 (2022).
  20. Maraghechi, S. *et al.* Experimental full-field analysis of size effects in miniaturized cellular elastomeric metamaterials. *Mater. Des.* **193**, 1–10 (2020).
  21. Mirzaali, M. J., Pahlavani, H. & Zadpoor, A. A. Auxeticity and stiffness of random networks: lessons for the rational design of 3D printed mechanical metamaterials. *Appl. Phys. Lett.* **115**, 3–8 (2019).
  22. Hanifpour, M., Petersen, C. F., Alava, M. J. & Zapperi, S. Mechanics of disordered auxetic metamaterials. *Eur. Phys. J. B* **91**, 1–8 (2018).
  23. Rayneau-Kirkhope, D., Bonfanti, S. & Zapperi, S. Density scaling in the mechanics of a disordered mechanical meta-material. *Appl. Phys. Lett.* **114**, 111902 (2019).
  24. Hagh, V. F. & Thorpe, M. F. Disordered auxetic networks with no reentrant polygons. *Phys. Rev. B* **98**, 100101 (2018).
  25. Reid, D. R. *et al.* Auxetic metamaterials from disordered networks. *Proc. Natl. Acad. Sci. U. S. A.* **115**, E1384–E1390 (2018).
  26. Mirzaali, M. J., Pahlavani, H. & Zadpoor, A. A. Auxeticity and stiffness of random networks: lessons for the rational design of 3D printed mechanical metamaterials. *Appl. Phys. Lett.* **115**, 021901 (2019).
  27. Ma, W., Cheng, F., Xu, Y., Wen, Q. & Liu, Y. Probabilistic representation and inverse design of metamaterials based on a deep generative model with semi-supervised learning strategy. *Adv. Mater.* **31**, 1901111 (2019).
  28. Wang, L. *et al.* Deep generative modeling for mechanistic-based learning and design of metamaterial systems. *Comput. Methods Appl. Mech. Eng.* **372**, 1–41 (2020).

## References

29. Kollmann, H. T., Abueidda, D. W., Koric, S., Guleryuz, E. & Sobh, N. A. Deep learning for topology optimization of 2D metamaterials. *Mater. Des.* **196**, 109098 (2020).
30. Kumar, S., Tan, S., Zheng, L. & Kochmann, D. M. Inverse-designed spinodoid metamaterials. *npj Comput. Mater.* **6**, 1–10 (2020).
31. Goodfellow, I. *et al.* Generative adversarial networks. *Commun. ACM* **63**, 139–144 (2020).
32. Kingma, D. P. & Welling, M. Auto-encoding variational bayes. Preprint at arXiv:1312.6114 (2013)
33. Pathak, Y., Juneja, K. S., Varma, G., Ehara, M. & Deva Priyakumar, U. Deep learning enabled inorganic material generator. *ChemRxiv* **22**, 26935-26943 (2020).
34. Dan, Y. *et al.* Generative adversarial networks (GAN) based efficient sampling of chemical composition space for inverse design of inorganic materials. *npj Comput. Mater.* **6**, 1–7 (2020).
35. Xue, T., Wallin, T. J., Menguc, Y., Adriaenssens, S. & Chiaramonte, M. Machine learning generative models for automatic design of multi-material 3D printed composite solids. *Extrem. Mech. Lett.* **41**, 100992 (2020).
36. Sanchez-Lengeling, B. & Aspuru-Guzik, A. Inverse molecular design using machine learning: generative models for matter engineering. *Sci.* **361**, 360–365 (2018).
37. Cormen, T. H. Leiserson, C. E. Rivest, R. L. & Stein, C. Introduction to algorithms. *MIT press* (2022).
38. Lim, J., Ryu, S., Kim, J. W. & Kim, W. Y. Molecular generative model based on conditional variational autoencoder for de novo molecular design. *J. Cheminform.* **10**, 1–9 (2018).
39. Sohn, K., Yan, X. & Lee, H. Learning structured output representation using deep conditional generative models. *Adv. Neural Inf. Process. Syst.* **28**, (2015)
40. Kingma, D. P. & Ba, J. Adam: A method for stochastic optimization. Preprint at arXiv:1412.6980 (2014).
41. Zheng, X. *et al.* Ultralight, ultrastiff mechanical metamaterials. *Sci.* **344**, 1373–1377 (2014).

42. Shi, W., Cao, J., Zhang, Q., Li, Y. & Xu, L. Edge computing: vision and challenges. *IEEE Internet Things J.* **3**, 637–646 (2016).
43. Chen, J. & Ran, X. Deep learning with edge computing: a review. *Proc. IEEE* **107**, (2019).
44. Reddy, J. N. An introduction to the finite element method. McGraw-Hill (1993).
45. Austrell, P. E. et al. CALFEM - A finite element toolbox, version 3.4. (2004).
46. Pedregosa, F. et al. Scikit-learn: machine learning in python. *J. Mach. Learn. Res.* **12**, 2825–2830 (2011).
47. Lemaître, G., Nogueira, F. & Aridas char, C. K. Imbalanced-learn: a python toolbox to tackle the curse of imbalanced datasets in machine learning. *J. Mach. Learn. Res.* **18**, 1–5 (2017).
48. Branco, P., Ribeiro, R. P., Torgo, L., Krawczyk, B. & Moniz, N. SMOGN: a pre-processing approach for imbalanced regression. *Proc. Mach. Learn. Res.* **74**, 36–50 (2017).
49. Keskar, N. S. et al. On large-batch training for deep learning: generalization gap and sharp minima. Preprint at arXiv:1609.04836 (2016).

# 7

## General discussion and future outlook



## 7.1. General discussion

The central theme of this thesis was the rational design of mechanical metamaterials to meet specific design requirements, such as rare-event elastic properties, predefined dimensions that fit particular applications, and minimized peak stress throughout the lattice structure. We introduced two sources of randomness in the design of such materials (i.e., random distribution of hard and soft phases in multi-material architected materials and a random arrangement of beam-like elements in random-network (RN) lattices). To achieve the goal of this thesis, a combination of rational design techniques, computational modeling approaches, machine learning (ML) models, advanced additive manufacturing technologies, and mechanical experiments was employed. The key findings and results of the research presented in the previous chapters will be summarized in the following sections followed by a general outlook and some recommendations for future research.

### 7.1.1. Multi-material mechanical metamaterials

In the design of mechanical metamaterials, a crucial objective is to separately tune both the elastic modulus and Poisson's ratio<sup>1</sup>. We demonstrated that by rationally distributing different materials with different mechanical properties (*e.g.*, a soft and a hard phase) in a cellular structure with an auxetic<sup>2</sup>, zero Poisson's ratio, or conventional unit cells, it is possible to adjust the elastic properties (*i.e.*, elastic modulus and Poisson's ratio) of architected materials. The possibility of tuning the Poisson's ratio in a wide range of values from extremely negative to extremely positive opens the door to an extensive set of new functionalities<sup>3,4</sup>. Through the spatial distribution materials with different mechanical properties, it is also possible to independently tailor the elastic properties of the material in different directions. We can, therefore, use this approach for the rational design of anisotropic mechanical metamaterials, allowing them to be optimized for a particular application.

Our findings, as revealed by the computational models, indicate that the non-homogeneous strain distributions and localized deformations at the micro-scale are

## 7.1. General discussion

the driving forces behind the macro-level observations, including the effective elastic properties and asymmetric deformations. Most importantly, adding a hard phase to a lattice structure can disrupt the flow of deformation in a lattice structure. The stiffer the hard phase is, the stronger this disruption will be. In lattice structures with a large positive or negative Poisson's ratio, such a disruption of deformation is unlikely to further increase the absolute value of the Poisson's ratio. However, in the case of lattice structures with orthogonal unit cells and near-zero Poisson's ratios, any (random) disruption of the deformation flow will likely increase the absolute value of the Poisson's ratio. There is an equal chance that this random disruption of the deformation flow results in a positive or a negative Poisson's ratio. That is why the elastic modulus-Poisson's ratio duos exhibited by random multi-material lattice structures with orthogonal unit cells are more or less symmetric.

The rational positioning of the hard phase in a mechanical metamaterials structure can result in significant changes to its Poisson's ratio. The inclusion of a hard phase increases the resistance to deformation, resulting in a higher elastic modulus. However, the extent of this increase depends on how effectively the hard phase is utilized to enhance the load-bearing capacity of the lattice structure in a particular direction. By adjusting the load-bearing effectiveness of the hard phase in a specific direction, it is possible to tune the elastic modulus of the lattice structure. These mechanisms enable independent tailoring of the elastic modulus and Poisson's ratio of the lattice structure, regardless of its geometric design.

Our findings reveal that the spatial distribution of materials within the lattice structure can result in a wide range of elastic properties and non-affine deformations. The degree of non-affinity, which is a measure of deviation from a homogeneous deformation field, was shown to be strongly influenced by design parameters, such as  $\theta$ ,  $\rho_h$ , and  $E_h/E_s$ . The degree of non-affinity increased with  $\rho_h$  and reached a maximum value before decreasing to zero for a monolithically hard material, regardless of the type of the unit cell and applied strain. In addition, the degree of non-affinity increases with  $E_h/E_s$  until a saturation point is reached at around

$E_h/E_s = 10^4$ . Hard phases with higher stiffness disrupt stress flow more, but for extremely large values of  $E_h/E_s$ , the hard phase behaves like a rigid material and further increases in  $E_h/E_s$  do not affect stress flow, resulting in the observed saturation. There is, therefore, a theoretical ceiling to the extent by which deformations in heterogeneous structures can deviate more from those of equivalent homogeneous structures.

Our results show that the degree of non-affinity is also highly correlated to the mechanical properties, particularly the Poisson's ratio. A power law relationship was observed between the degree of non-affinity and Poisson's ratio in auxetic and honeycomb unit cells, which was stronger at higher levels of applied strain. However, no such relationship was observed for lattice structures with near-zero Poisson's ratios. This observation suggests that achieving high absolute values of the Poisson's ratio in multi-material mechanical metamaterials requires highly affine deformations. It was also found that achieving high values of the elastic modulus with multi-material mechanical metamaterials is associated with high levels of non-affine deformations, creating a new type of incompatibility between high values of the elastic modulus and high absolute values of the Poisson's ratio.

We found that lattice structures composed of auxetic unit cells are more susceptible to inhomogeneous deformations caused by the presence of high-stiffness struts. This is due to the fact that deformations in auxetic unit cells are dominated by high stresses concentrated around sharp corners, while stresses are more homogeneously distributed in honeycomb and orthogonal unit cells. The high-stress concentration zones created by non-affine deformations could accelerate crack initiation and lead to premature structural failure<sup>5</sup>. These effects could potentially be alleviated through the use of functional gradients.

### **7.1.2. RN mechanical metamaterials**

Another source of randomness in the design of mechanical metamaterials that we studied in this thesis was the geometrical randomness manifested in RN

## 7.1. General discussion

mechanical metamaterials. We studied the elastic properties of random networks, both lattice-restricted and unrestricted, with varying levels of connectivity. Our results showed a wide range of elastic properties achieved by these random networks, and similar trends for both types of networks. Moreover, the changes of the elastic modulus with the relative density ( $\phi$ ) followed a similar nonlinear trend for both types of networks. The range of the elastic moduli achieved was within the theoretical limits given by the Hashin-Shtrikman bounds<sup>6-9</sup> for the positive values of the Poisson's ratio. In general, the lattice-restricted networks had higher values of the elastic modulus, while unrestricted networks had larger variations in their elastic properties. Auxetic behavior was only observed for the smaller values of connectivity. The maximum level of connectivity for auxetic behavior was higher for unrestricted networks than restricted networks. In the case of lattice-restricted networks, all auxetic structures were bending-dominated based on the Maxwell's stability number<sup>10,11</sup>. In the case of unrestricted networks, however, auxetic structures could be found even for networks with high connectivity values and positive Maxwell numbers, indicating that they were stretch-dominated<sup>10,12</sup>. Given that stretch-dominated networks exhibit higher stiffness values, unrestricted random networks are useful for expanding the range of elastic properties of auxetic structures.

Our results state that the level of anisotropy decreases as the size of networks increases, which is expected due to the random nature of the networks. The anisotropy of the stiffness values of lattice-restricted and unrestricted networks showed different types of dependency on the degree of connectivity. The maximum level of stiffness anisotropy in lattice-restricted networks was observed for the intermediate values of connectivity. In unrestricted networks, stiffness anisotropy increased up to a certain point after which it remained constant. The opposite was observed for the Poisson's ratio, which decreased with connectivity for both types of networks. In addition, the probability of finding auxetic networks decreased as the size of the networks increased. This probability was also higher in unrestricted

networks than lattice-restricted networks. Moreover, our finding showed a low probability of finding networks with double-auxetic behavior (*i.e.*, ranging between 0.4% and 1.62%), which further decreased as the size of the networks increased. Some of the most negative values of the Poisson's ratio were observed for networks with large lateral openings. Upon closer inspection, we found that diverse movement trajectories could be achieved using RN designs. Therefore, these RN designs can also be seen as a type of compliant mechanism<sup>13-15</sup>, particularly when multiple networks are combined to create complex movement patterns.

In general, the results of our study show that unrestricted networks have multiple benefits compared to lattice-restricted networks. These advantages include a wider coverage of elastic modulus-Poisson's ratio plane and a higher probability of auxetic and double-auxetic behavior. Additionally, unrestricted networks can exhibit auxetic behavior even in the stretch-dominated domain, while lattice-restricted networks do not. This makes unrestricted networks useful for designing stiff auxetic metamaterials.

### **7.1.3. Deep learning for the design of rare-event multi-material mechanical metamaterials**

Due to the vast range of possible designs, the introduction of randomness into mechanical metamaterials makes it challenging to optimize their design particularly with regard to rare-event combinations of mechanical properties. Conventional computational models are usually not fast enough to allow for a thorough canvassing of the entire design space. We, therefore, used ML techniques to create an efficient computational approach that could more effectively handle the vastness of the design space. The use of ML methods in the development of composites and metamaterials<sup>16-23</sup> and to the prediction of material properties<sup>24-26</sup> has recently drawn the attention of many researchers. However, this potential is not yet fully explored for the design of multi-material mechanical metamaterials. This thesis demonstrated how a combination of computational models and DL algorithms can be used for

## 7.1. General discussion

ultrafast prediction of the mechanical properties of multi-material mechanical metamaterials with randomly distributed hard and soft phases within their structures. Specifically, we investigated how the distribution of the hard and soft phases affects the elastic properties of the resulting structures. The research presented in this thesis demonstrated that DL techniques can be used to effectively predict the elastic properties of multi-material mechanical metamaterials, speeds up the evaluation of each design, and facilitate efficient parallel computing. The developed DL-based approach allows us to evaluate multiple designs quickly and efficiently in parallel, with each evaluation taking approximately  $2.4 \times 10^{-6}$  seconds. This approach makes it possible to evaluate an extremely large number of possible designs. Therefore, it enables us to identify designs with highly desirable combinations of elastic properties, such as high stiffness and a highly negative Poisson's ratio.

In addition, having such a vast design database makes it possible to apply additional design criteria. For example, our results showed a wide range of variations in the peak von Mises stresses observed in the various structures with similar elastic properties. This highlights the need to consider the uniformity of stress within the lattice structure as a key factor in the design process to prevent failure caused by cracks initiated in the high-stress regions<sup>5</sup>. Our proposed approach showed the possibility to identify designs with desired elastic properties while also minimizing the risk of premature failure due to high peak stress values.

Finally, by combining the studied multi-material tiled designs into structures made of four such tiles, we demonstrated that by combining unit cells, it is possible to increase the range of elastic properties that can be achieved and create lattice structures that are both double-auxetic and stiff. On the other hand, combining different types of unit cells allows for various functionalities. For instance, these combinations can be used to design orthopedic implants with improved longevity<sup>27</sup>. A potential use for soft robotics is the ability to generate various patterns of local actuation through a single far-field deformation<sup>4</sup>. Combining different unit cells also

allows for shape-morphing boundaries and the possibility to fit the design to different surfaces<sup>28</sup>.

#### **7.1.4. Deep-DRAM framework: Deep learning for the design of random-network mechanical metamaterials**

The inverse design of mechanical metamaterials with predefined design requirements, such as elastic properties (particularly rare-event properties), and dimensions is crucial when considering their real-world applications. Given the demonstrated capability of DL techniques in predicting the elastic properties of multi-material mechanical metamaterials with random distributions of hard and soft phases within their structure (as presented in Chapter 5), we applied the same technique to predict the elastic properties of RN mechanical metamaterials. Additionally, we employed variational autoencoders (VAE)<sup>29</sup> as a probabilistic deep generative model for the inverse design of these RN mechanical metamaterials with desired elastic properties and dimensions.

We developed a size-agnostic inverse design framework, titled "Deep-DRAM", that utilizes DL for the design of RN mechanical metamaterials. Deep-DRAM can inversely design RN mechanical metamaterials with specific elastic properties and dimensions that are customized for different intended applications. The combination of deep generative models, forward predictors, and finite element modeling enables the creation of tailored mechanical metamaterials that also meet additional design requirements. While the Deep-DRAM framework combines four modules, each individual module can be also used either independently or be combined with other tools to address various challenges in the design process. In addition, the probabilistic nature of Deep-DRAM allows for finding many solutions to the multi-objective inverse design problem mentioned above. For instance, this size-agnostic inverse design framework allows for the simultaneous pursuit of structures with specific elastic properties and dimensions, while also minimizing the peak stress within the structure. All this can be done efficiently due to the high speeds of design

## 7.2. Future outlook

generation and evaluation. The approach proposed in this study paves ways for the development of mechanical metamaterials with well-defined elastic properties (including rare properties) corresponding to a structure with pre-defined overall dimensions. In this thesis, RN mechanical metamaterials were used a case study due to their wide range of achievable elastic properties. However, the same methodology can be also used for the multi-objective inverse design of many other types of (multi-material) mechanical metamaterials.

### 7.2. Future outlook

Looking ahead, the potential of mechanical metamaterials in general and randomness-incorporated architected materials in particular for pushing the boundaries of knowledge in multiple fields is considerable. Advances in rational design, computational methods, ML techniques, and additive manufacturing technologies have created numerous opportunities for the real-world applications of mechanical metamaterials in various industries. As we move forward, it is important to continue to push the boundaries of achievable properties and functionalities and explore new ideas to further progress in this field. Although this thesis made significant strides in the design of mechanical metamaterials with rare-event properties, there remain several unresolved questions that, if answered, could greatly expand the practical applications of these materials. This concluding section outlines a number of suggestions for future studies that could help to address these outstanding issues and further advance the field of mechanical metamaterials.

1. In this thesis, we used linear elastic constitutive models and focused on the elastic properties of the designed lattices. The same method can be applied to investigate nonlinear properties or other characteristics of the designed structures. The most important change needed would be to adjust the FE models to reflect the more complex constitutive behavior. The benefits of using DL techniques for ultra-fast predictions would be then even more apparent when



simulation time is longer, such as when investigating nonlinear or viscoelastic behaviors.

2. In our study, we carried out monotonic quasi-static tensile tests to investigate the elastic properties of the designed structures. However, to gain a comprehensive understanding of the failure and fatigue mechanisms in these structures, a more comprehensive set of tests would be required. This would include mechanical testing at various strain rates as well as fatigue tests to investigate how these structures behave under cyclic loading. Such tests would provide valuable insights into the durability and long-term performance of these structures. Additionally, fatigue testing would also help to identify any potential weak points or areas within structures that are more susceptible to failure under cyclic loading.
3. Designing multi-material lattice structures using materials with different mechanical properties, such as soft and hard phases, can lead to stress concentrations at the local interfaces of soft and hard phases. These stress concentrations can become more pronounced as the difference between the mechanical properties of the hard and soft phases increases. This can ultimately lead to premature failure, especially under cyclic loading. To mitigate this, it may be beneficial to incorporate intermediate phases with gradually changing mechanical properties to decrease the impact of such stress concentrations.
4. To extend the design space and explore a wider range of mechanical properties, additional parameters can be incorporated into the training of DL models. For instance, we previously concentrated on two main parameters in the training of a DL model for multi-material mechanical metamaterials. These parameters were the ratio of the volume of the hard phase to that of the soft phase ( $\rho_h$ ) and the angle of the unit cells, while the ratio of the elastic moduli of both phases was kept constant. However, varying this ratio can impact the mechanical

## 7.2. Future outlook

properties of the material. It would, therefore, be beneficial to include this in our model training to expand the potential design options.

5. The Deep-DRAM platform has the potential to be adapted and applied to a wide range of structures beyond the specific type of random structures that were studied in this thesis. This could include lattice-unrestricted random networks, multi-material structures, and any other variations of mechanical metamaterials. Furthermore, the Deep-DRAM can also be used to optimize the generated structures based on other design parameters than peak stress values, stress uniformity, and energy absorption. The flexibility of the Deep-DRAM methodology allows for its use in a variety of fields and industries, including soft robotic, automotive, and biomedical engineering.
6. The trained deep learning models are very compact and computationally efficient, which makes them ideal for use in edge computing applications.

This thesis showcases the impressive potential of ML techniques in the design of mechanical metamaterials and the discovery of rare-event designs. The results underscore the need for further research into utilizing ML techniques to broaden the design space of mechanical metamaterials with unprecedented mechanical properties. Overall, this study represents a significant step forward in the field of mechanical metamaterials and offers exciting possibilities for the development of innovative structures with enhanced functionality.

## References

1. Mirzaali, M. J. *et al.* Rational design of soft mechanical metamaterials: independent tailoring of elastic properties with randomness. *Appl. Phys. Lett.* **111**, 51903 (2017).
2. Alderson, A. & Alderson, K. L. Auxetic materials. *Proc. Inst. Mech. Eng. Part G J. Aerosp. Eng.* **221**, 565–575 (2007).
3. Kolken, H. M. A. *et al.* Rationally designed meta-implants: a combination of auxetic and conventional meta-biomaterials. *Mater. Horizons* **5**, 28–35 (2018).
4. Hedayati, R., Mirzaali, M. J., Vergani, L. & Zadpoor, A. A. Action-at-a-distance metamaterials: distributed local actuation through far-field global forces. *APL Mater.* **6**, 036101 (2018).
5. Sangid, M. D. The physics of fatigue crack initiation. *Int. J. Fatigue* **57**, 58–72 (2013).
6. Berger, J. B., Wadley, H. N. G. & McMeeking, R. M. Mechanical metamaterials at the theoretical limit of isotropic elastic stiffness. *Nature* **543**, 533 (2017).
7. Hashin, Z. The elastic moduli of heterogeneous materials. *J. Appl. Mech.* **29**, 143–150 (1962).
8. Hashin, Z. & Shtrikman, S. A variational approach to the theory of the elastic behaviour of multiphase materials. *J. Mech. Phys. Solids* **11**, 127–140 (1963).
9. Ostanin, I., Ovchinnikov, G., Tozoni, D. C. & Zorin, D. A parameteric class of composites with a large achievable range of effective elastic properties. *J. Mech. Phys. Solids* (2018).
10. Deshpande, V. S., Ashby, M. F. & Fleck, N. A. Foam topology: bending versus stretching dominated architectures. *Acta Mater.* **49**, 1035–1040 (2001).
11. Ashby\*, M. F. Hybrids to fill holes in material property space. *Philos. Mag.* **85**, 3235–3257 (2005).
12. Buxton, G. A. & Clarke, N. “Bending to stretching” transition in disordered networks. *Phys. Rev. Lett.* **98**, 238103 (2007).
13. Ion, A. *et al.* Metamaterial mechanisms. *Proceedings of the 29th Annual Symposium on User Interface Software and Technology* 529–539 (2016).
14. Lee, J., Kim, K., Ju, J. & Kim, D.-M. Compliant cellular materials with elliptical holes for extremely high positive and negative Poisson’s ratios. *J. Eng. Mater. Technol.* **137**, 11001 (2015).
15. Meza, L. R. *et al.* Resilient 3D hierarchical architected metamaterials. *Proc.*

## References

- Natl. Acad. Sci.* **112**, 11502–11507 (2015).
16. Guo, K., Yang, Z., Yu, C.-H. & Buehler, M. J. Artificial intelligence and machine learning in design of mechanical materials. *Mater. Horizons* **8**, 1153–1172 (2021).
  17. Gu, G. X., Chen, C. T. & Buehler, M. J. De novo composite design based on machine learning algorithm. *Extrem. Mech. Lett.* **18**, 19–28 (2018).
  18. Bessa, M. A., Glowacki, P. & Houlder, M. Bayesian machine learning in metamaterial design: fragile becomes supercompressible. *Adv. Mater.* **31**, 1–6 (2019).
  19. Ma, W., Cheng, F. & Liu, Y. Deep-learning-enabled on-demand design of chiral metamaterials. *ACS Nano* **12**, 6326–6334 (2018).
  20. Wilt, J. K., Yang, C. & Gu, G. X. Accelerating auxetic metamaterial design with deep learning. *Adv. Eng. Mater.* **22**, 1–7 (2020).
  21. Gu, G. X., Chen, C. T., Richmond, D. J. & Buehler, M. J. Bioinspired hierarchical composite design using machine learning: simulation, additive manufacturing, and experiment. *Mater. Horizons* **5**, 939–945 (2018).
  22. Zhang, Z., Zhang, Z., Di Caprio, F. & Gu, G. X. Machine learning for accelerating the design process of double-double composite structures. *Compos. Struct.* **285**, 115233 (2022).
  23. Sui, F., Guo, R., Zhang, Z., Gu, G. X. & Lin, L. Deep reinforcement learning for digital materials design. *ACS Mater. Lett.* **3**, 1433–1439 (2021).
  24. Yang, Z., Yu, C.-H. & Buehler, M. J. Deep learning model to predict complex stress and strain fields in hierarchical composites. *Sci. Adv.* **7**, eabd7416 (2021).
  25. Yang, C., Kim, Y., Ryu, S. & Gu, G. X. Prediction of composite microstructure stress-strain curves using convolutional neural networks. *Mater. Des.* **189**, 108509 (2020).
  26. Yang, Z., Yu, C. H., Guo, K. & Buehler, M. J. End-to-end deep learning method to predict complete strain and stress tensors for complex hierarchical composite microstructures. *J. Mech. Phys. Solids* **154**, 104506 (2021).
  27. Kolken, H. M. A. *et al.* Rationally designed meta-implants: a combination of auxetic and conventional meta-biomaterials. *Mater. Horizons* **5**, 28–35 (2018).
  28. Mirzaali, M. J., Janbaz, S., Strano, M., Vergani, L. & Zadpoor, A. A. Shape-matching soft mechanical metamaterials. *Sci. Rep.* **8**, 965 (2018).
  29. Kingma, D. P. & Welling, M. Auto-encoding variational bayes. Preprint at

arXiv:1312.6114 (2013).

# Acknowledgements

The completion of a PhD is a truly memorable and immensely challenging journey that surpasses the realms of individual effort. As I stand at the culmination of this arduous path, I am acutely aware that my achievement is not solely my own but rather the result of the collaborative efforts of numerous individuals. It is time to pause here and express my heartfelt gratitude to these wonderful people, even though many deserve much more than that.

I would like to express my deepest appreciation to my promoters, **Amir** and **Jie**, and my daily supervisor, **Mohammad** for their invaluable guidance, support, and dedication throughout my doctoral research. Thank you for giving me the opportunity to work on this Ph.D. project. I am truly grateful for your constant availability, patience, and willingness to engage in intellectual discussions, which have enriched my understanding and broadened my perspectives in the field. **Amir**, I had the pleasure of initially encountering you through the captivating pages of an article. As I delved deeper into your articles, my excitement for the opportunity to conduct research within your research group increased. Fortuitously, a twist of fate brought me to the Netherlands, where I seized the opportunity to join your research group. I will never forget the overwhelming joy I experienced when I first stepped into your office, realizing that my dream was finally becoming a reality. Your remarkable intelligence and boundless creativity have continuously served as an inspiration to me. Your expertise, encouragement, and insightful feedback have been instrumental in shaping this thesis and my overall growth as a researcher. I want to acknowledge the profound impact you have had on my life, both professionally and personally. **Jie**, you are undoubtedly one of the most outstanding supervisors throughout my academic journey. In the face of challenges, I consistently turned to you, and without fail, you emerged as my guide and pillar of support. I am deeply

grateful to you for your exceptional assistance during these years. I am grateful for your support, mentorship, and commitment to my success. **Mohammad**, as your first Ph.D. student, I am deeply grateful for the immense amount of energy you devoted to guiding me through my doctoral journey. Your unwavering support was evident in the fact that you were always available to answer my questions and for brainstorming sessions. Your genuine passion for research was truly inspiring, and your ability to complete tasks promptly served as a valuable lesson for me. I would like to sincerely thank you for your support and commendable contributions throughout my doctoral journey.

I am grateful to the numerous individuals within the faculty who played an instrumental role in supporting me throughout my doctoral journey, enabling me to achieve successful completion. **Sander**, I sincerely thank you for all your technical support and training. **Sabrina, Angelique, Marjolijn, and Amanda**, thank you very much for your invaluable assistance with the administrative affairs. **Paul, Lidy, and Julian**, I am so thankful for the nice discussions and moments we have shared. I would also like to thank **Anneke, Costanza, Dirk, Ebrahim, Edwin, Eline, Esther, Fabian, Françoise, Gerwin, Ingmar, Jelle, Jette, Jiahui, Jinlai, Judith, Katerina, Keyu, Khashayar and Sara, Kirsten, Lorenzo, Mahdiyeh, Mahya, Maryam, Mauricio, Merle, Monika, Mostafa, Nazli, Niko, Pier, Pedro, Sara, Sebastien, Shahram, Teunis, Vahid, Vera, Yageng, Yujiang, and Zahra** and all my colleagues at the department of biomechanical engineering for all great and enjoyable moments we have shared during the last five years. I would like to express my heartfelt gratitude to my dear friend, **Mahya**, who has consistently provided me with invaluable advice and experiences. I am truly grateful for all the beautiful memories we have created together, and I feel incredibly blessed to have such a wonderful friend like you in my life.

I would like to thank my office mates **Ebrahim, Jelle, Jiahui, Jinlai, Khashayar, Mahdiyeh, Niko, Pedro, Shima, and Vahid** for the nice moments and memories we have shared over the past few years. **Jiahui**, We started our PhD in

almost the same time, and I am very happy that I got to know you right from the very beginning of my PhD and had a companion and empathetic friend like you. Despite our distinct areas of expertise, it has always been a delight to engage in conversations about our work. I will never forget the late evenings we spent working in the office, which often concluded with learning Persian and Chinese words. I am incredibly thankful for all these wonderful moments we shared. **Shima**, although we were office mates for a short time, your energy and friendliness quickly made you one of my closest friends. I would like to express my gratitude for the beautiful memories we have created together and for our friendship. **Vahid**, we had excellent collaboration on the 3DMed project, which enabled us to successfully complete it. Additionally, working together to supervise master students was both productive and enjoyable. **Saeede** and **Vahid**, I would also like to thank you for our wonderful friendship, the cherished memories we share, and for your unwavering support during both joyful and challenging times.

Living abroad, far from our families, would not be possible without having close friends. **Maede** and **Javad**, I would like to express my heartfelt gratitude to you for your constant presence in our lives, providing us with unwavering support during both joyful and challenging moments. **Maede**, you are the kindest and most companionable friend that anyone would be fortunate to have. I would also like to extend my sincere appreciation to you for beautifully designing the cover of my doctoral thesis. **Jos**, you have been one of our best teachers, guiding us in learning the Dutch language and immersing us in the richness of Dutch culture. Through our weekly classes and personal conversations, we have had the privilege of discussing various aspects of life, work, and experiences. Your valuable advice has accompanied us through different stages of life. I am genuinely thankful to you for your dedicated efforts and for imparting so much knowledge to us. I am thankful to our friends **Azar** and **Ali**, **Arezoo** and **Babak**, **Artemis**, **Banafsheh** and **Masoud**, **Delaram** and **Nima**, **Fatima** and **Erfan**, **Helga**, **Khatereh** and **Siamak**, **Maryam** and **Hadi**, **Mathilde**, **Nasibe** and **Amir**, **Pooyan**, **Romina** and **Amirhossein**, **Saeed**,



**Samaneh, Shokufeh and Milad, Somayeh and Behnam, Zahra and Hamidreza, Zahra and Sara**, with whom we shared numerous delightful memories. You made our stay in Delft truly memorable. Thank you for being such wonderful friends and for enriching our lives with your warmth and kindness.

I would like to extend my deepest gratitude to the most important individuals in my life. Every step I have taken is driven by their love and a sincere desire for their happiness. **My father**, who embodies kindness and unwavering dedication, has been my pillar of support through all stages of my life. **My mother**, a true role model in perseverance and effort, has taught me how to think, be resilient, and nurture ambitious dreams. She has always wanted the best for me and instilled in me the determination to strive for my aspirations. My husband, my beloved **Amirhossein**, my constant companion and supporter. Without a doubt, reaching this stage would not have been possible without his unwavering help and support. Last but Not Least, my little sister, **Lida**, who is the most sympathetic and companionable sister in the world.

*It is good and right to express gratitude towards the One who created this wonderful world and bestowed upon me the strength to pursue my aspirations diligently.*

# Publications

## A. Journals

- **Pahlavani, H.**, Tsifoutis-Kazolis, K., Mody, P., Zhou, J., Mirzaali, M. J. and Zadpoor, A. A. Deep learning for size-agnostic inverse design of random network 3D printed mechanical metamaterials, Submitted (2023). (<https://arxiv.org/abs/2212.12047>)
- Saldívar, M. C., Tay, E., **Pahlavani, H.**, Mirzaali, M. J., Doubrovski, E.L. and Zadpoor, A. A. Mimicking living bones to optimize hierarchical, multi-material 3D printed auxetic metamaterials, Submitted (2023).
- **Pahlavani, H.**, Amani, M., Saldívar, M. C., Zhou, J., Mirzaali, M. J. and Zadpoor, A. A. Deep learning for the rare-event rational design of 3D printed multi-material mechanical metamaterials, *Communications Materials* 3(1), 1-11 (2022).
- Kubo, Y., Gonzalez, J. A. H., Beckmann, R., Weiler, M., **Pahlavani, H.**, Saldivar, M. C., ... & Jahr, H. Nuclear factor erythroid 2–related factor 2 (Nrf2) deficiency causes age-dependent progression of female osteoporosis. *BMC Musculoskeletal Disorders* 23(1), 1-13 (2022).
- Van Kootwijk, A., Moosabeiki, V., Saldivar, M. C., **Pahlavani, H.**, *et al.* Semi-automated digital workflow to design and evaluate patient-specific mandibular reconstruction implants, *Journal of the Mechanical Behaviour of Biomedical Materials* 132, 105291 (2022).
- Yu, K., Balasubramanian, S., **Pahlavani, H.**, Mirzaali, M. J., Zadpoor, A. A. and Aubin-Tam, M. E. Spiral honeycomb microstructured bacterial cellulose for increased strength and toughness, *ACS Applied Materials & Interfaces* 12(45), 50748-50755 (2021).
- Mirzaali, M. J., **Pahlavani, H.**, Yarali, E. and Zadpoor, A. A. "Non-affinity in multi-material mechanical metamaterials, *Scientific Reports* 10(1), 1-10 (2020).

- Mirzaali, M. J., **Pahlavani, H.** and Zadpoor, A. A. Auxeticity and stiffness of random networks: lessons for the rational design of 3D printed mechanical metamaterials, *Applied Physics Letters* 115(2), 021901 (2019).
- Mirzaali, M. J., Caracciolo, A., **Pahlavani, H.**, Janbaz, S., Vergani, L. and Zadpoor, A. A. Multi-material 3D printed mechanical metamaterials: rational design of elastic properties through spatial distribution of hard and soft phases, *Applied Physics Letters* 113(24), 241903 (2018).

## B. Conferences

- **Pahlavani, H.**, Amani, M., Saldívar, M. C., Zhou, J., Mirzaali, M. J. and Zadpoor, A. A. AI-based 3D-printed multi-material mechanical metamaterials, Netherlands Society for Biomaterials and Tissue Engineering (NBTE), Lunteren, The Netherlands (2022, poster presentation).
- **Pahlavani, H.**, Mirzaali, M. J., Zhou, J. and Zadpoor, A. A. 3D printable optimized design for orthotic and prosthetic medical devices, 3D Medical Conference, 3D Medical Printing Series, Eindhoven, The Netherlands (2022, oral presentation).
- **Pahlavani, H.**, Mirzaali, M. J. and Zadpoor, A. A. Randomness in mechanical metamaterials, The American Society of Mechanical Engineers (ASME), Fully Virtual (2021, oral presentation).
- **Pahlavani, H.**, Mirzaali, M. J., Zhou, J. and Zadpoor, A. A. Additive manufacturing of patient-specific prosthetic medical devices, The 31<sup>st</sup> Annual Conference of the European Society for Biomaterials (ESB), Fully Virtual (2021, poster presentation).

# Curriculum Vitae

Helda Pahlavani was born on 29 May 1993 in Torbatehedarieh, Iran. She earned her B.Sc. and M.Sc. degrees in Civil Engineering from Sharif University of Technology in Tehran, Iran, in 2015 and 2017, respectively. During her master's studies, she focused on conducting probabilistic-based analyses of mechanically stabilized earth (MSE) retaining walls using the finite element method. In June 2018, she joined the structural engineering department at the Faculty of Civil Engineering and Geosciences of Delft University of Technology in The Netherlands as a researcher. Her research primarily involved performing finite element analyses on a masonry structure subjected to seismic loading. This research project was part of the "Damage Sensitivity of Groningen Masonry Structures: Experimental and Computational Studies" project. In October 2018, she embarked on her Ph.D. journey in the Biomechanical Engineering department at the Faculty of Mechanical, Maritime, and Materials Engineering of Delft University of Technology in The Netherlands. She did her Ph.D. under the supervision of Prof. Amir A. Zadpoor, Dr. Jie Zhou and Dr. Mohammad Mirzaali. During her Ph.D., she focused on incorporating finite element analysis, machine learning, big data analytics, computer-aided design (CAD), and 3D printing into design of mechanical metamaterials with rare-event mechanical properties. Additionally, she participated in a European project (Interreg 2 Seas 3DMed project) with the main responsibility of development of a semi-automated workflow for the patient-specific design of selected prosthetic and orthotic medical devices.

